

Ministry of Science and Higher Education of the Russian Federation
ITMO University

ISSN 2220-8054

NANOSYSTEMS:
PHYSICS, CHEMISTRY, MATHEMATICS

2024, volume 15 (5)

Наносистемы: физика, химия, математика

2024, том 15, № 5



NANOSYSTEMS:

PHYSICS, CHEMISTRY, MATHEMATICS

ADVISORY BOARD MEMBERS

Chairman: V.N. Vasiliev (*St. Petersburg, Russia*),
V.M. Buznik (*Moscow, Russia*); V.M. Ievlev (*Voronezh, Russia*), P.S. Kop'ev (*St. Petersburg, Russia*), V.N. Parmon (*Novosibirsk, Russia*), A.I. Rusanov (*St. Petersburg, Russia*),

EDITORIAL BOARD

Editor-in-Chief: I.Yu. Popov (*St. Petersburg, Russia*)

Section Co-Editors:

Physics – V.M. Uzdin (*St. Petersburg, Russia*),

Material science – V.V. Gusarov (*St. Petersburg, Russia*); O.V. Al'myasheva (*St. Petersburg, Russia*);

Chemistry – V.K. Ivanov (*Moscow, Russia*),

Mathematics – I.Yu. Popov (*St. Petersburg, Russia*).

Editorial Board Members:

V.M. Adamyan (*Odessa, Ukraine*); A.P. Alodjants (*St. Petersburg, Russia*); S. Bechta (*Stockholm, Sweden*); J. Behrndt (*Graz, Austria*); A. Chatterjee (*Hyderabad, India*); A.V. Chizhov (*Dubna, Russia*); A.N. Enyashin (*Ekaterinburg, Russia*), P.P. Fedorov (*Moscow, Russia*); E.A. Gudilin (*Moscow, Russia*); H. Jónsson (*Reykjavik, Iceland*); A.A. Kiselev (*Durham, USA*); Yu.S. Kivshar (*Canberra, Australia*); S.A. Kozlov (*St. Petersburg, Russia*); P.A. Kurasov (*Stockholm, Sweden*); A.V. Lukashin (*Moscow, Russia*); I.V. Melikhov (*Moscow, Russia*); G.P. Miroshnichenko (*St. Petersburg, Russia*); I.Ya. Mittova (*Voronezh, Russia*); H. Najjar (*Monastir, Tunisia*), Nguyen Anh Tien (*Ho Chi Minh, Vietnam*); V.V. Pankov (*Minsk, Belarus*); K. Pankrashkin (*Orsay, France*); A.V. Ragulya (*Kiev, Ukraine*); V. Rajendran (*Tamil Nadu, India*); A.A. Rempel (*Ekaterinburg, Russia*); A.A. Rogachev (*Minsk, Belarus*); V.Ya. Rudyak (*Novosibirsk, Russia*); H.M. Sedighi (*Ahvaz, Iran*); D Shoikhet (*Karmiel, Israel*); M.N. Smirnova (*Moscow, Russia*); P. Stovicek (*Prague, Czech Republic*); V.M. Talanov (*Novocherkassk, Russia*); A.Ya. Vul' (*St. Petersburg, Russia*); A.V. Yakimansky (*St. Petersburg, Russia*), V.A. Zagrebnoy (*Marseille, France*).

Editors:

I.V. Blinova; A.I. Popov; A.I. Trifanov; E.S. Trifanova (*St. Petersburg, Russia*),

R. Simoneaux (*Philadelphia, Pennsylvania, USA*).

Address: ITMO University, Kronverkskiy pr., 49, St. Petersburg 197101, Russia.

Phone: +7(812)607-02-54, **Journal site:** <http://nanojournal.ifmo.ru/>,

E-mail: nanojournal.ifmo@gmail.com

AIM AND SCOPE

The scope of the journal includes all areas of nano-sciences. Papers devoted to basic problems of physics, chemistry, material science and mathematics inspired by nanosystems investigations are welcomed. Both theoretical and experimental works concerning the properties and behavior of nanosystems, problems of its creation and application, mathematical methods of nanosystem studies are considered.

The journal publishes scientific reviews (up to 30 journal pages), research papers (up to 15 pages) and letters (up to 5 pages). All manuscripts are peer-reviewed. Authors are informed about the referee opinion and the Editorial decision.

CONTENT

MATHEMATICS

A. Harshitha, S. Nayak, S. D'Souza
Eccentricity Laplacian energy of a graph 567

M.M. Rahmatullaev, D.O. Egamov
Translation-invariant Gibbs measures for the mixed spin- $\frac{1}{2}$ and spin-1 Ising model with an external field on a Cayley tree 576

Z.A. Sobirov, A.A. Turemuratova
Inverse source problem for the subdiffusion equation with edge-dependent order of time-fractional derivative on the metric star graph 586

PHYSICS

S. Navarro-Vilca, S. Urcia-Romero, H. Vigo-Cotrina
Skyrmionium – semicircular magnetic defect interaction on a racetrack 597

Yu.V. Luniakov
Magnesium based tin-silicon alloys under pressure: first-principles evolution search results 621

Suman Dahiya, Siddhartha Lahon, Rinku Sharma
Tuning the nonlinear optical properties of a 1D excitonic GaAs quantum dot system under a semi-parabolic potential with a detailed comparison with the experimental results: interplay of hydrostatic pressure and temperature 632

O.M. Gorbenko, S.Y. Lukashenko, S.V. Pichakhchi, I.D. Sapozhnikov, M.L. Felshtyn, A.O. Golubok
Inertial nanostep piezoelectric drive: modeling and experiment 643

I.Z. Latypov, V.V. Chistyakov, M.A. Fadeev, D.V. Sulimov, A.K. Khalturinsky, S.M. Kynev, V.I. Egorov
Hybrid quantum communication protocol for fiber and atmosphere channel 654

Mahmoud Ali, Mohammad Elsaid
Effect of structural parameters, and spin-orbit interaction on the electronic properties of double quantum wire systems in the presence of external magnetic field 658

Nguyen Pham Quynh Anh
**Simulation of Bessel plasmon polariton field formation
in a dielectric-metal structure** 670

CHEMISTRY AND MATERIAL SCIENCE

D.D. Kolmanovich, M.V. Romanov, S.A. Khaustov, V.K. Ivanov,
A.E. Shemyakov, N.N. Chukavin, A.L. Popov
**Proton beam-induced radiosensitizing effect of Ce_{0.8}Gd_{0.2}O_{2-x}
nanoparticles against melanoma cells *in vitro*** 675

E.A. Zamyatina, O.A. Goryacheva, N.R. Popova
**Physicochemical properties and biological activity of novel cerium
oxide nanoparticles modified with pyrroloquinoline quinone** 683

O.N. Kondrat'eva, M.N. Smirnova, G.E. Nikiforova,
A.D. Yapryntsev, D.F. Kondakov, L.D. Yagudin
**Ceramic materials prepared from nanocrystalline InFeZnO₄
powder: optical and mechanical properties, and evaluation
of radiation tolerance** 693

A.S. Zakharova, S.V. Kuznetsov, A.A. Alexandrov, D.V. Pominova,
V.V. Voronov, P.P. Fedorov, V.K. Ivanov
**Highly dispersed anti-Stokes phosphors based on KGd₂F₇:Yb,Er
single-phase solid solutions** 702

M.A. Jafarov, V.M. Salmanov, R.M. Mamedov,
E.F. Nasirov, T.A. Mammadova
Synthesis of CdSTe nanoparticles by laser ablation 710

V.T. Lebedev, V.S. Kozlov, M.V. Remizov, Yu.V. Kulvelis,
O.N. Primachenko, E.A. Marinenko, G.S. Peters
**Ionic channel structure in perfluorinated membranes studied
by small angle X-ray scattering, optical and Mössbauer
spectroscopy** 716

Information for authors 726

Eccentricity Laplacian energy of a graph

A. Harshitha^{1,a}, S. Nayak^{1,b}, S. D'Souza^{1,c}

¹Manipal Institute of Technology, Manipal Academy of Higher Education, Manipal, India, 576104

^aharshuarao@gmail.com, ^bswati.nayak@manipal.edu, ^csabitha.dsouza@manipal.edu

Corresponding author: S. D'Souza, sabitha.dsouza@manipal.edu

PACS 05C50.90E10

ABSTRACT Let G be a simple, finite, undirected and connected graph. The eccentricity of a vertex v is the maximum distance from v to all other vertices of G . The eccentricity Laplacian matrix of G with n vertices is a square matrix of order n , whose elements are el_{ij} , where el_{ij} is -1 if the corresponding vertices are adjacent, el_{ii} is the eccentricity of v_i for $1 \leq i \leq n$, and el_{ij} is 0 otherwise. If $\epsilon_1, \epsilon_2, \dots, \epsilon_n$ are the eigenvalues of the eccentricity Laplacian matrix, then the eccentricity Laplacian energy of G is $ELE(G) = \sum_{i=1}^n |\epsilon_i - \text{avec}(G)|$, where $\text{avec}(G)$ is the average eccentricities of all the vertices of G . In this study, some properties of the eccentricity Laplacian energy are obtained and comparison between the eccentricity Laplacian energy and the total π -electron energy is obtained.

KEYWORDS distance, eccentricity, Laplacian energy

FOR CITATION Harshitha A., Nayak S., D'Souza S. Eccentricity Laplacian energy of a graph. *Nanosystems: Phys. Chem. Math.*, 2024, **15** (5), 567–575.

1. Introduction

Let G be a simple, finite, undirected and connected graph. The degree of a vertex is the number of edges incident on the vertex. The distance between two vertices is the number of edges in the shortest path between them. Eccentricity of a vertex is the maximum distance from a vertex to all other vertices of a graph. Minimum and maximum among the eccentricities of all the vertices is the radius and diameter of the graph, respectively. If the eccentricity of a vertex is equal to radius of the graph, then the vertex is called a central vertex. The set of all central vertices is called the center of the graph.

The degree of a vertex v of a graph G is denoted by $\deg_G(v)$. The notation $d_G(v_i, v_j)$ represents distance between the vertices v_i and v_j of G . Eccentricity of a vertex v is denoted by $e_G(v)$. The notations $r(G)$ and $d(G)$ represent the radius and the diameter of the graph respectively. The center of the graph is denoted by $C(G)$.

The average eccentricity of a graph is as follows

$$\text{avec}(G) = \frac{1}{n} \sum_{i=1}^n e_G(v_i).$$

The status of a vertex v_i is given by

$$\sigma_G(v_i) = \sum_{v_j \in V(G)} d_G(v_i, v_j).$$

A clique of a graph is an induced subgraph which is complete. The size of the largest clique is the clique number of the graph, denoted by ω . The independent set of a graph is the subset of the set of vertices in which no two vertices are adjacent. The independent number of a graph is the cardinality of the maximum independent set of vertices, denoted by α .

The energy of a graph was introduced by I. Gutman [1] in 1978 as sum of the absolute eigenvalues of the adjacency matrix associated with the graph. That is, if $\lambda_1, \lambda_2, \dots, \lambda_n$ are the eigenvalues of the adjacency matrix of the graph G , then the energy of G is as follows

$$E(G) = \sum_{i=1}^n |\lambda_i|.$$

The spectrum of the graph G with distinct eigenvalues $\lambda_1, \lambda_2, \dots, \lambda_k$ having multiplicity m_1, m_2, \dots, m_k , respectively, is denoted by

$$\text{Spec}(G) = \begin{pmatrix} \lambda_1 & \lambda_2 & \lambda_3 & \dots & \lambda_k \\ m_1 & m_2 & m_3 & \dots & m_k \end{pmatrix}.$$

In 2006, I Gutman and B. Zhou [2] introduced the Laplacian energy of a graph. The Laplacian matrix of a graph on n vertices is the square matrix of order n , whose diagonal entries are degrees of the corresponding vertices and non-diagonal entries are -1 if the corresponding vertices are adjacent and 0 if the corresponding vertices are non-adjacent. If $\mu_1, \mu_2, \dots, \mu_n$ are the eigenvalues of the Laplacian matrix, then the Laplacian energy of G of order n and size m is given by the expression

$$LE(G) = \sum_{i=1}^n \left| \mu_i - \frac{2m}{n} \right|.$$

Motivated by the works on Laplacian energy [3–7], in this paper, the eccentricity Laplacian matrix is considered and its spectral properties are studied.

The eccentricity Laplacian matrix of a connected graph G on n vertices, denoted by $EL(G)$ [8], is a square matrix of order n , whose elements are given by el_{ij} , where

$$el_{ij} = \begin{cases} -1 & \text{if } v_i \sim v_j \text{ and } i \neq j \\ e_G(v_i) & \text{if } i = j \\ 0 & \text{otherwise.} \end{cases}$$

The trace of the matrix $EL(G)$ is $Tr(EL(G)) = \sum_{i=1}^n e_G(v_i) = n(avec(G))$. If $\epsilon_1, \epsilon_2, \dots, \epsilon_n$ are the eigenvalues of the matrix $EL(G)$, then the eccentricity Laplacian energy is defined as

$$ELE(G) = \sum_{i=1}^n |\epsilon_i - avec(G)|.$$

It is well known that the energy of a graph coincides with the total π -electron energy of conjugated hydrocarbon molecule. Also, few comparisons between different energies and total π -electron energy can be found in [9–11]. In a similar manner, in this study, comparison between the eccentricity Laplacian energy and the total π -electron energy of hydrocarbons are made. The result of which gives the strong correlation between the two energies.

2. Preliminaries

Theorem 1. [12] For any connected graph G ,

$$avec(G) \leq \frac{1}{n} \sigma_G(C(G)) + r(G).$$

The equality holds for any tree.

Theorem 2. [12] For a connected graph of order n ,

$$avec(G) \leq \frac{1}{n} \left[\frac{3}{4}n^2 - \frac{1}{2}n \right].$$

The equality holds if and only if $G \cong P_n$.

Theorem 3. [13] Let $G(\cong K_n)$ be a connected graph of order n with clique number ω and independent number α . Then

$$avec(G) \geq \frac{1}{n}(\omega + 2\alpha - 1).$$

Theorem 4. [13] Let $G(\cong K_n)$ be a connected graph of order n with clique number ω . Then $\sum_{i=1}^n e_G^2(v_i) \geq 4n - 3\omega + 3$.

3. Main Results

Lemma 1. The matrix $EL(G)$ is positive semi-definite if $e_G(v_i) \geq deg_G(v_i)$ for all $i = 1, 2, \dots, n$.

Proof. In a graph G of order n , if $e_G(v_i) \geq deg_G(v_i)$ for all $i = 1, 2, \dots, n$, then $EL(G)$ is symmetrically diagonally dominant matrix and therefore a positive semi-definite matrix. \square

Lemma 2. Let G be a connected graph on n vertices. Then $ELE(G) = E(G)$ if $e_G(v_i) = k$ for all $v_i \in V(G)$ and $k \in \mathbb{Z}$.

Proof. If $e_G(v_i) = k$ for all $v_i \in V(G)$, then $EL(G) = -A(G) + kI_n$ and $e_i(G) = -\lambda_i(G) + k$ and $avec(G) = k$

$$\begin{aligned} ELE(G) &= \sum_{i=1}^n |-\lambda_i(G) + k - k| \\ &= \sum_{i=1}^n |\lambda_i(G)| = E(G). \end{aligned}$$

□

Table 3 gives one some graphs with equal adjacency energy and eccentricity Laplacian energy.

TABLE 1. Graphs with equal adjacency energy and eccentricity Laplacian energy

Graph	Eccentricities of all the vertices
complete graph K_n	1
cycle C_n	$\lfloor \frac{n}{2} \rfloor$
complete bipartite graph $K_{m,n}$, $m \leq n$, $m > 1$	2
cocktail party graph $K_{n \times 2}$	2
crown graph S_n^0	3

Remark. $ELE(G) = LE(G) = E(G)$ if $e_G(v_i) = \deg_G(v_i)$ for all $v_i \in V(G)$.

For instance, among the graphs in table 3 complete graph K_2 , cycle C_4 , complete bipartite graph $K_{2,2}$, cocktail party graph $K_{2 \times 2}$, and crown graph S_4^0 have equal energy, Laplacian energy, and eccentricity Laplacian energy.

Theorem 5. Let G be a connected graph of order n , size m with clique number ω and independent number α . Then

$$ELE \geq \sqrt{2mn + Mn + N^2 - 2 \left\{ \left\lfloor \frac{3}{4}n^2 - \frac{1}{2}n \right\rfloor \right\}^2}.$$

Here $M = 4n - 3\omega + 3$ and $N = \omega + 2\alpha - 1$.

Proof. Let $\epsilon_1 \geq \epsilon_2 \geq \dots \geq \epsilon_n$ be the eigenvalues of $EL(G)$. Consider the Cauchy-Schwartz inequality,

$$\left(\sum_{i=1}^n a_i b_i \right)^2 \leq \left(\sum_{i=1}^n a_i^2 \right) \left(\sum_{i=1}^n b_i^2 \right).$$

Set $a_i = 1$ and $b_i = |\epsilon_i - avec(G)|$, then

$$(ELE(G))^2 = \left(\sum_{i=1}^n |\epsilon_i - avec(G)| \right)^2 \leq n \sum_{i=1}^n |\epsilon_i - avec(G)|^2.$$

However,

$$\sum_{i=1}^n |\epsilon_i - avec(G)|^2 = \sum_{i=1}^n \epsilon_i^2 + \sum_{i=1}^n (avec(G))^2 - 2avec(G) \sum_{i=1}^n \epsilon_i. \tag{1}$$

Now we will find the values of $\sum_{i=1}^n \epsilon_i^2$, $\sum_{i=1}^n (avec(G))^2$ and $avec(G) \sum_{i=1}^n \epsilon_i$. Consider

$$\begin{aligned} \sum_{i=1}^n \epsilon_i^2 &= \sum_{i=1}^n (EL(G))_{ii}^2 \\ &= 2m + \sum_{i=1}^n e_G^2(v_i). \end{aligned}$$

But, $\sum_{i=1}^n e_G^2(v_i) \geq 4n - 3\omega + 3$ (by Theorem 4). Therefore,

$$\sum_{i=1}^n \epsilon_i^2 \geq 2m + 4n - 3\omega + 3. \tag{2}$$

By Theorem 3, $avec(G) \geq \frac{\omega + 2\alpha - 1}{n}$ and therefore,

$$\sum_{i=1}^n (avec(G))^2 \geq \frac{(\omega + 2\alpha - 1)^2}{n}. \tag{3}$$

and by Theorem 2 and noting the fact that $\sum_{i=1}^n \epsilon_i = n(avec(G))$, one obtains

$$-2avec(G) \sum_{i=1}^n \epsilon_i \geq \frac{-2}{n} \left\{ \left[\frac{3}{4}n^2 - \frac{1}{2}n \right] \right\}^2. \tag{4}$$

Theorem 5 follows by substituting the values of equations 2, 3, and 4 in equation 1. □

Theorem 6. Let G be a connected graph of order n , size m with clique number ω , independent number α , and radius $r(G)$. Then

$$ELE(G) \leq \left\{ 2mn + n^2(r(G)^2) + r(G) + 2r(G)\sigma_G(C(G)) + n \sum_{i=1}^n (d_G(u, C(G)))^2 + (\sigma_G(C(G)))^2 - 2R^2 \right\}^{\frac{1}{2}}.$$

Here $R = \omega + 2\alpha - 1$ and $\sigma_G(C(G))$ is the status of the center of G .

Proof. Let v be a vertex of a connected graph G . Note that $e_G(v) \leq nr(G) + \sigma_G(C(G))$ and the equality holds for any tree [12]. Let $\epsilon_1 \geq \epsilon_2 \geq \dots \geq \epsilon_n$ be the eigenvalues of $EL(G)$. Then by the Cauchy-Schwartz inequality,

$$\begin{aligned} (ELE(G))^2 &= \left(\sum_{i=1}^n |\epsilon_i - avec(G)| \right)^2 \\ &\leq n \sum_{i=1}^n |\epsilon_i - avec(G)|^2 \\ &= \sum_{i=1}^n \epsilon_i^2 + \sum_{i=1}^n (avec(G))^2 - 2avec(G) \sum_{i=1}^n \epsilon_i. \end{aligned} \tag{5}$$

Now we will find the values of $\sum_{i=1}^n \epsilon_i^2$, $\sum_{i=1}^n (avec(G))^2$ and $avec(G) \sum_{i=1}^n \epsilon_i$. Consider

$$\sum_{i=1}^n \epsilon_i^2 = 2m + \sum_{i=1}^n e_G^2(v_i).$$

Noting the fact that $e_G(v_i) \leq r(G) + d_G(v_i, C(G))$, one comes to the inequality

$$\sum_{i=1}^n \epsilon_i^2 \leq 2m + n(r(G))^2 + 2r(G)\sigma_G(C(G)) + \sum_{i=1}^n (d_G(u, C(G)))^2. \tag{6}$$

Also

$$\sum_{i=1}^n (avec(G))^2 \leq \frac{(nr(G) + \sigma_G(C(G)))^2}{n}. \tag{7}$$

By lemma 3, $avec(G) \geq \omega + 2\alpha - 1$ which implies that

$$-2avec(G) \sum_{i=1}^n \epsilon_i \leq \frac{-2}{n} (\omega + 2\alpha - 1)^2. \tag{8}$$

Theorem 6 follows by substituting the values of 6, 7 and 8 in 5. □

4. Eccentricity Laplacian matrix of a tree

Theorem 7. Let T be a tree on n vertices. Let $f_n(T, \lambda) = a_0\lambda^n + a_1\lambda^{n-1} + a_2\lambda^{n-2} + \dots + a_n$ be the characteristic polynomial of $EL(T)$. Then,

- (1) $a_0 = 1$.
- (2) $a_1 = -(nr(T) + \sigma_T(C(T)))$.
- (3) $a_2 = \frac{(r(T))^2 n(n-1)}{2} - (n-1) + \sum_{i=1}^{n-1} x_i(x_{i+1} + x_{i+2} + \dots + x_n) + \sum_{i=1}^n (n-1)x_i$, where, $x_i = r(T) + d(v_i, C(T))$.

Proof. (1) By the definition of $f_n(T, \lambda)$, $a_0 = 1$.

(2) The value of a_1 is (-1) times the sum of the determinants of all 1×1 principal sub-matrices of $EL(T)$. By lemma 1, $avec(T) = \frac{1}{n}\sigma_T(C(T)) + r(T)$. Therefore, $a_1 = -(nr(T) + \sigma_T(C(T)))$.

(3) The value of a_2 is sum of the determinants of all 2×2 principal sub-matrices of $EL(T)$. That is,

$$a_2 = \sum_{1 \leq i < j \leq n} \begin{vmatrix} el_{ii} & el_{ij} \\ el_{ji} & el_{jj} \end{vmatrix} = \sum_{1 \leq i < j \leq n} el_{ii}el_{jj} - \sum_{1 \leq i < j \leq n} el_{ij}^2.$$

But, $\sum_{1 \leq i < j \leq n} el_{ii}el_{jj} = \frac{(r(T))^2 n(n-1)}{2} + \sum_{i=1}^{n-1} x_i(x_{i+1} + x_{i+2} + \dots + x_n) + \sum_{i=1}^n (n-1)x_i$ and $\sum_{1 \leq i < j \leq n} el_{ij}^2 = n-1$ and Theorem 7 follows by substitution. □

Theorem 8. Let T be a tree on n vertices with radius $r(T)$ and center $C(T)$. Then

$$ELE(T) \leq \left\{ n(nr^2(T) + (d_T(u_i, C(T)))^2 + 2r(T)\sigma_T(C(T)) + 2n - 2) - (nr(T) + \sigma_T(C(T)))^2 \right\}^{\frac{1}{2}}.$$

Proof. Let $\epsilon_1 \geq \epsilon_2 \geq \dots \geq \epsilon_n$ be the eigenvalues of $EL(T)$. Consider the Cauchy-Schwartz inequality

$$\left(\sum_{i=1}^n a_i b_i \right)^2 \leq \left(\sum_{i=1}^n a_i^2 \right) \left(\sum_{i=1}^n b_i^2 \right).$$

Set $a_i = 1$ and $b_i = |\epsilon_i - avec(T)|$, then

$$\begin{aligned} (ELE(T))^2 &= \left(\sum_{i=1}^n |\epsilon_i - avec(T)| \right)^2 \\ &\leq n \sum_{i=1}^n |\epsilon_i - avec(T)|^2 \\ &= n \left(\sum_{i=1}^n \epsilon_i^2 \right) + \sum_{i=1}^n (avec(T))^2 - 2avec(T) \sum_{i=1}^n \epsilon_i. \end{aligned}$$

But $e_T(u_i) = r(T) + d_T(u_i, C(T))$ and therefore, $avec(T) = nr(T) + \sigma_T(C(T))$ and $\epsilon_i^2 = nr^2(T) + 2r(T)\sigma_T(C(T)) + \sum_{i=1}^n d_T^2(u_i, C(T)) + 2n - 2$. Therefore,

$$\begin{aligned} (ELE(T))^2 &\leq n(nr^2(T) + 2r(T)\sigma_T(C(T)) + (d_T(u_i, C(T)))^2 + 2m) \\ &\quad - (nr(T) + \sigma_T(C(T)))^2 \end{aligned}$$

and the proof follows. □

Theorem 9. Let S_n be a star graph on n vertices. Then,

$$ELE(S_n) = \frac{n-2}{n} + \sqrt{4n-3}.$$

Proof. The average eccentricity of star graph S_n is $2n - 1$. Consider

$$|\gamma I - EL(S_n)| = \left| \begin{pmatrix} \gamma - 1 & 1 & 1 & 1 & \dots & 1 & 1 \\ 1 & \gamma - 2 & 0 & 0 & \dots & 0 & 0 \\ 1 & 0 & \gamma - 2 & 0 & \dots & 0 & 0 \\ 1 & 0 & 0 & \gamma - 2 & \dots & 0 & 0 \\ \vdots & \vdots & \vdots & \vdots & \ddots & \vdots & \vdots \\ 1 & 0 & 0 & 0 & \dots & \gamma - 2 & 0 \\ 1 & 0 & 0 & 0 & \dots & 0 & \gamma - 2 \end{pmatrix} \right|.$$

The characteristic polynomial of $EL(S_n)$ is $(\gamma - 2)^{n-2}(\gamma^2 - 3\gamma - (n - 3))$ and the eccentric Laplacian spectrum of S_n is

$$\left(\begin{array}{ccc} 2 & \frac{3 + \sqrt{4n-3}}{2} & \frac{3 - \sqrt{4n-3}}{2} \\ n-2 & 1 & 1 \end{array} \right).$$

Therefore,

$$ELE(S_n) = \frac{n-2}{n} + \sqrt{4n-3}.$$

□

5. Chemical significance of the eccentric Laplacian energy

The eccentric Laplacian energies of Polyenes, Vinyl compounds, Polyacenes and Cyclobutadienes listed in the Dictionary of π -electron calculation [14] are calculated and compared with the respective total π -electron energies when $S = 0$, where S is a overlap integral. Refer [14] for more details regarding terminologies related to total π -electron energy (Figs. 1, 2).

When the eccentric Laplacian energy of Polyenes and Vinyl compounds are compared with the total π -electron energy, very strong correlation has been found with correlation coefficient 0.96 (Figs. 3, 4).

Similarly, the eccentric Laplacian energies of Polyacenes and Cyclobutadienes are compared with the total π -electron energy, which gives correlation coefficient 0.98 (Figs. 5, 6).

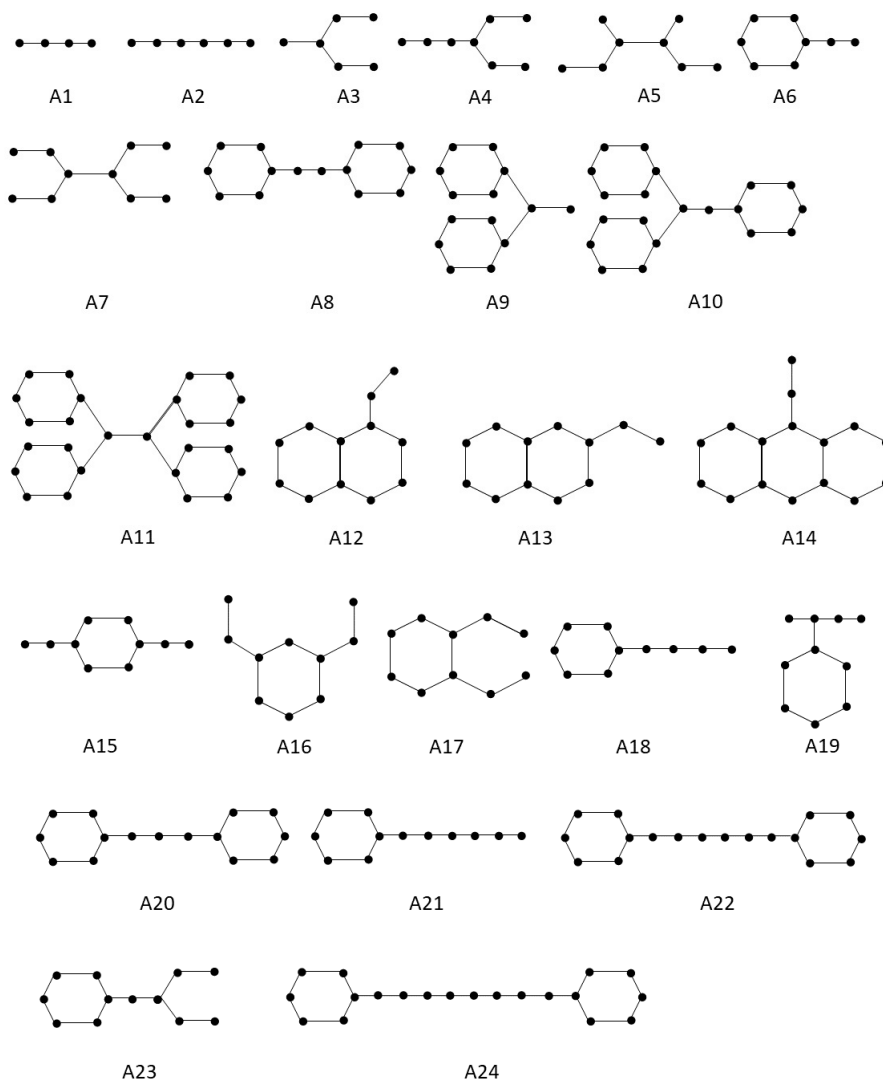


FIG. 1. Polyenes and vinyl compounds

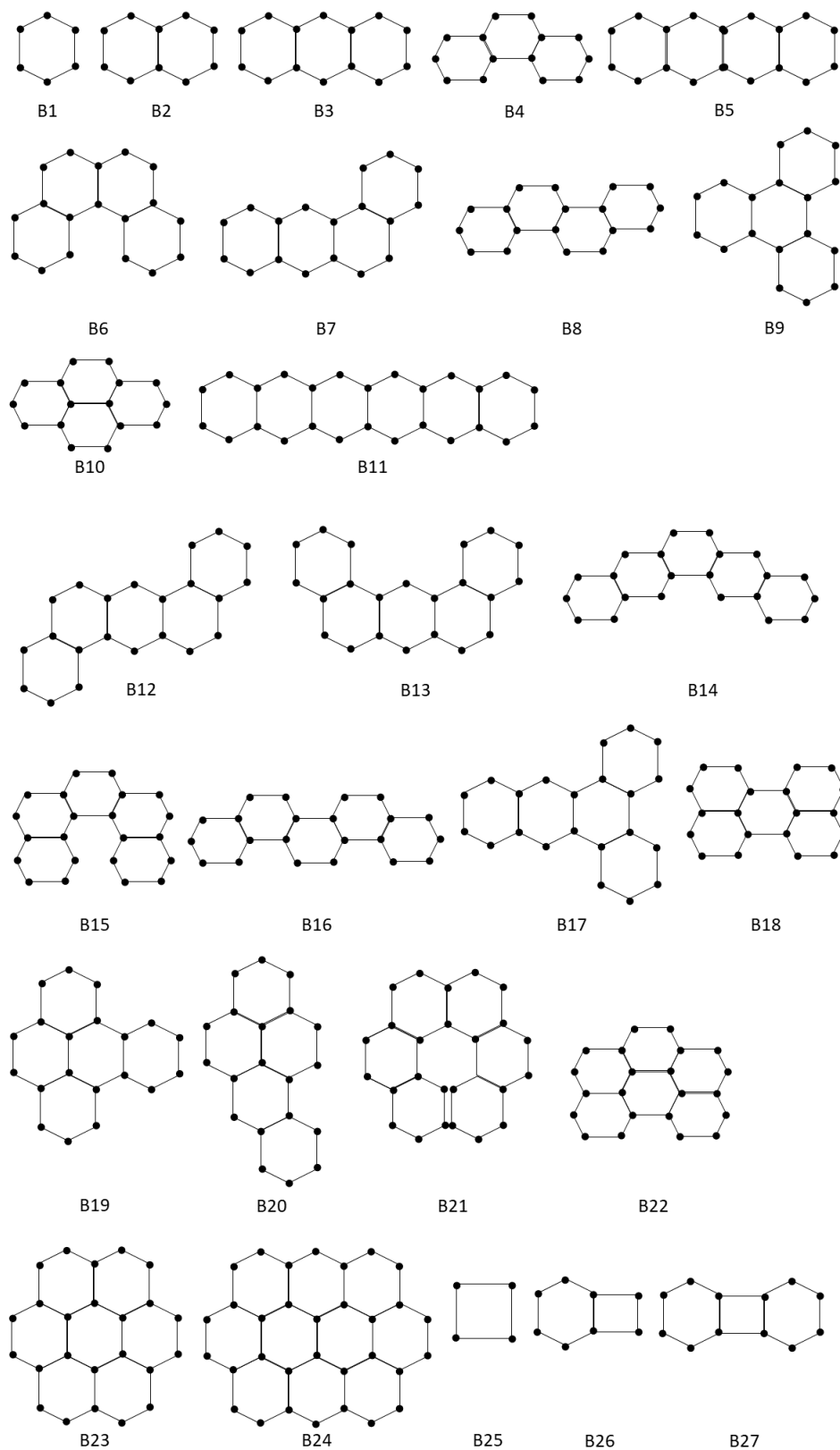


FIG. 2. Polyacenes and Cyclobutadienes

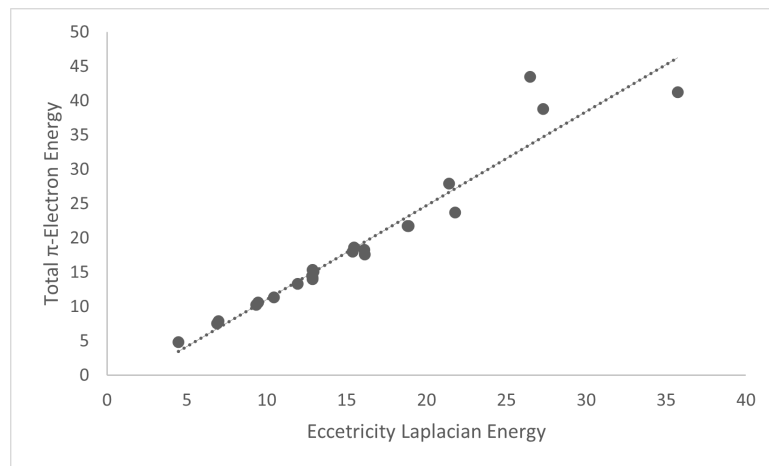


FIG. 3. Scatter plot of $ELE(G)$ and total π -electron energy of Polyenes and Vinyl compounds

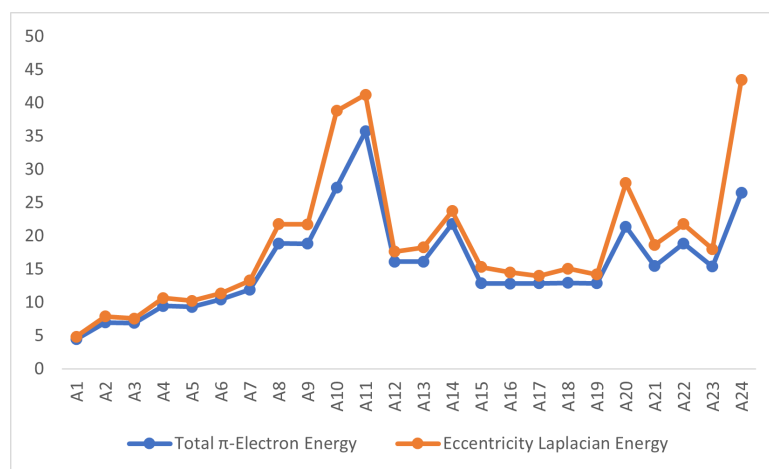


FIG. 4. Comparison between $ELE(G)$ and total π -electron energy of Polyenes and Vinyl compounds

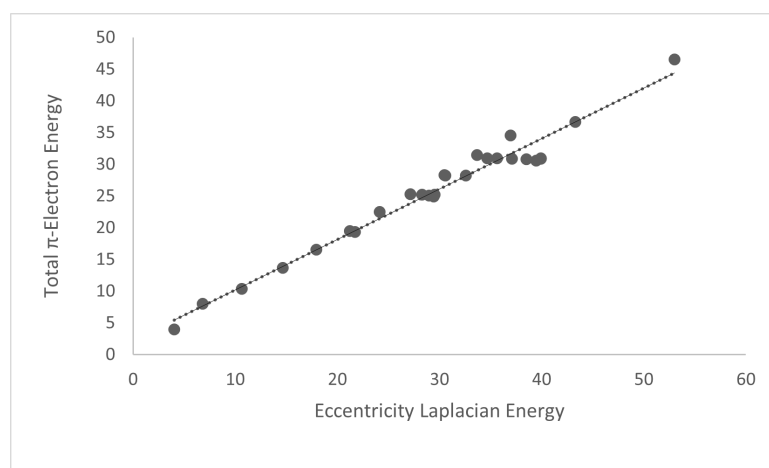


FIG. 5. Scatter plot of $ELE(G)$ and total π -electron energy of Polyacenes and Cyclobutadienes

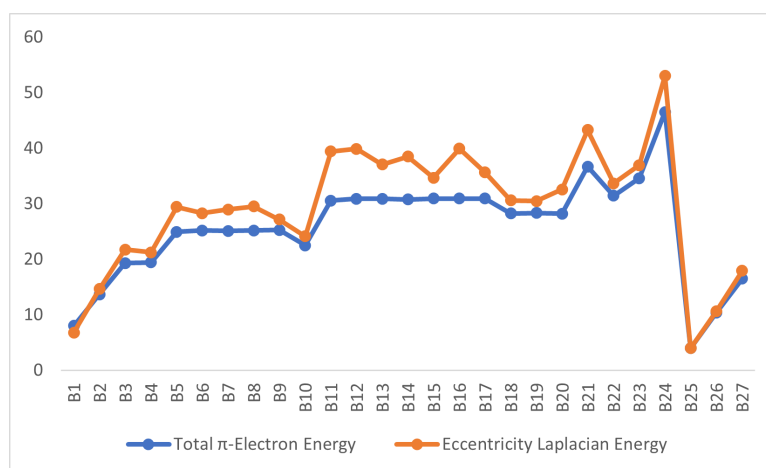


FIG. 6. Comparison between $ELE(G)$ and total π -electron energy of Polyacenes and Cyclobutadienes

6. Conclusion

In this study, the eccentricity Laplacian matrix $EL(G)$ of a graph G is explored and the corresponding eccentricity Laplacian energy $ELE(G)$ is derived. This analysis includes conditions under which $EL(G)$ is positive semi-definite and scenarios where $ELE(G)$ matches the ordinary and the Laplacian energies of the graph. We also established several bounds for $ELE(G)$ in relation with various graph parameters, such as the number of vertices and edges, the clique number, the independent number, the radius, and the status of the center.

Additionally, we characterized the eccentricity Laplacian matrix and its energy specifically for trees. As an intriguing application, we compared the eccentricity Laplacian energy of specific polyenes, vinyl compounds, polyacenes, and cyclobutadienes with their total π -electron energies. Remarkably, the correlation coefficient between $ELE(G)$ and the total π -electron energies is found to be 0.96 for polyenes and vinyl compounds, and 0.98 for polyacenes and cyclobutadienes, demonstrating a very strong correlation.

References

- [1] I. Gutman, The energy of a graph. *Ber. Math. Stat. Sect. Forschungsz. Graz.*, 1978, **103**, P. 1–22.
- [2] I. Gutman, B. Zhou, Laplacian energy of a graph. *Linear Algebra and its Applications*, 2006, **414**, P. 29–37.
- [3] M. Lazić, On the Laplacian energy of a graph. *Czechoslovak Mathematical Journal*, 2006, **56**, P. 1207–1213.
- [4] B. Zhou, More on energy and Laplacian energy. *MATCH Commun. Math. Comput. Chem.*, 2010, **64**, P. 75–84.
- [5] K.C. Das, S.A. Mojjallal and I. Gutman. On energy and Laplacian energy of bipartite graphs. *Applied Mathematics and Computation*, 2016, **273**, P. 795–766.
- [6] P. G. Bhat and S. D'souza. Color Laplacian energy of a graph. *Proceedings of the Jangjeon Mathematical Society*, 2015, **18**, P. 321–330.
- [7] D. Anchan, H.J. Gowtham, S. D'souza and P.G. Bhat. Laplacian Energy of a Graph with Self-Loops. *MATCH Commun. Math. Comput. Chem.*, 2023, **90**, P. 247–258.
- [8] N. De. On Eccentricity Version of Laplacian Energy of a Graph. *Mathematics Interdisciplinary Research*, 2017, **2**, P. 131–139.
- [9] S. Radenković and I. Gutman. Total π -electron energy and Laplacian energy: How far the analogy goes?. *Journal of the Serbian Chemical Society*, 2007, **72**, P. 1343–1350.
- [10] I. Redzepovic and I. Gutman. Comparing energy and Sombor energy—An empirical study. *MATCH Commun. Math. Comput. Chem*, 2022, **88**, P. 133–140.
- [11] K. Zemljič and P. Žigert Pleteršek. Smoothness of Graph Energy in Chemical Graphs. *Mathematics*, 2023, **11**, P. 1–14.
- [12] P. Dankelmann, W. Goddard and C.S. Swart. The average eccentricity of a graph and its subgraphs. *Utilitas Mathematica*, 2004, **65**, P. 41–52.
- [13] K.C. Das, A.D. Maden, I.N. Cangül and A.S. Çevik. On average eccentricity of graphs. *Proceedings of the National Academy of Sciences, India Section A: Physical Sciences*, 2017, **87**, P. 23–30.
- [14] C.A. Coulson and A. Streitwieser, *Dictionary of π -electron calculations*, W.H. Freeman, San Francisco, 1965.

Submitted 4 April 2024; revised 9 September 2024; accepted 10 September 2024

Information about the authors:

A. Harshitha – Department of Mathematics, Manipal Institute of Technology, Manipal Academy of Higher Education, Manipal, India, 576104; harshuarao@gmail.com

S. Nayak – Department of Mathematics, Manipal Institute of Technology, Manipal Academy of Higher Education, Manipal, India, 576104; swati.nayak@manipal.edu

S. D'Souza – Department of Mathematics, Manipal Institute of Technology, Manipal Academy of Higher Education, Manipal, India, 576104; sabitha.dsouza@manipal.edu

Conflict of interest: the authors declare no conflict of interest.

Translation-invariant Gibbs measures for the mixed spin-1/2 and spin-1 Ising model with an external field on a Cayley tree

Muzaffar M. Rahmatullaev^{1,2,3,a}, Dilshod O. Egamov^{1,3,b}

¹V. I. Romanovskiy Institute of Mathematics, Uzbekistan Academy of Sciences, 100174, Tashkent, Uzbekistan

²New Uzbekistan University, 100000, Tashkent, Uzbekistan

³Namangan state University, Namangan, Uzbekistan

^amrahmatullaev@rambler.ru, ^bdilshodbekegamov87@gmail.com

Corresponding author: M. M. Rahmatullaev, mrahmatullaev@rambler.ru

PACS 82B23, 82B26, 60G70

ABSTRACT Phase transitions of the mixed spin-1/2 and spin-1 Ising model under the presence of an external field on the general order Cayley tree are investigated within the framework of the tree-indexed Markov chains. We find the conditions that ensure the existence of at least three translation-invariant Gibbs measures for the model on the Cayley tree of order k . We are able to solve the model exactly on the binary tree ($k = 2$) under the specific external field. The main attention is paid to the systematic study of the structure of the set of the Gibbs measures. We find the extremality and non-extremality regions of the disordered phase of the model on the binary tree.

KEYWORDS mixed-spin Ising model; external field; Cayley tree; Gibbs measures.

ACKNOWLEDGEMENTS We thank Professor F. M. Mukhamedov for his participation in discussions of the results. We also thank the anonymous referee for reading the manuscript carefully and for making valuable suggestions.

FOR CITATION Rahmatullaev M.M., Egamov D.O. Translation-invariant Gibbs measures for the mixed spin-1/2 and spin-1 Ising model with an external field on a Cayley tree. *Nanosystems: Phys. Chem. Math.*, 2024, **15** (5), 576–585.

1. Introduction

In recent years, the theoretical study of mixed-spin Ising models has received significant attention. Unlike their single-spin counterparts, mixed-spin Ising models possess less translational symmetry, making them primarily subjects of experimental study, with a considerable gap in theoretical research. To the best of the authors' knowledge, the first paper to rigorously study mixed-spin Ising models with mathematical precision is [1]. This paper investigates the model using a measure-theoretic approach and proves the existence of phase transitions. Subsequent papers [2–6] continue the investigation, exploring various properties of mixed-type Ising models on Cayley trees.

The impact of an external field is evident from the outset of the theory. For instance, the classical Ising model on the cubic lattice \mathbb{Z}^d ($d \geq 2$) exhibits a phase transition in the absence of an external field, but no phase transition occurs when a non-zero external field is applied. Introducing an external field to such models typically results in the loss of symmetry, making it more challenging to study the model's properties. In this paper, we employ the exact recursion equations technique to investigate the phase transition of the mixed spin-1/2 and spin-1 Ising model with an external field on the Cayley tree. The aim of this work is to elucidate the influence of the external field on the model's physical properties.

In [7], the mixed spin-1/2 and spin-1 Ising model in the absence of an external field on the arbitrary order Cayley tree is studied. It is shown that this particular model exhibits a phase transition phenomena in both the ferromagnetic and antiferromagnetic regions. In that paper, the authors also investigate the extremality of disordered phases employing a Markov chain indexed by a tree on a semi-infinite Cayley tree. Utilizing the Kesten-Stigum condition [8], they delve into the non-extremality aspects of disordered phases by scrutinizing the eigenvalues of the stochastic matrix associated with the (1,1/2) mixed-spin Ising model on Cayley trees with order k ($k \geq 3$). One of the main contributions of the present paper is to show the existence of a phase transition for the (1,1/2) mixed-spin Ising model under the external field on the general order Cayley tree.

In [9], the author studies the one-dimensional Ising model with mixed spins $(s, \frac{2t-1}{2})$ under the influence of nearest-neighbor interactions and an external magnetic field. By analyzing the iterative equations related to the model, the phase transition problem is explored using the cavity approach. Furthermore, various thermodynamic quantities for the model

are calculated, and precise formulas are provided to determine the free energy, entropy, magnetization, and susceptibility. For the case $s = 1$ and $t = 1$, our results extend the findings of [9] to higher-order Cayley trees.

Numerous numerical methods also have been applied to the study of mixed-spin models. We mention some of them: One of the earliest, simplest, and most extensively studied mixed-spin Ising models is the spin-1/2 and spin-1 mixed system. This system has been investigated using a variety of techniques, including the renormalization-group technique [10], high-temperature series expansions [11], the free-fermion approximation, the recursion method on the Bethe lattice, and the Bethe-Peierls approximation [12–15]. Additionally, studies have employed the effective-field theory framework [16, 17], the mean-field approximation [18, 19], the finite cluster approximation [20], Monte Carlo simulations [21], the mean-field renormalization-group technique, numerical transfer matrix studies [7], and the cluster variation method in pair approximation [22].

It is known [23–26] that for all $\beta > 0$, the set of Gibbs measures forms a non-empty, convex, and compact subset in the space of probability measures. Moreover, any Gibbs measure can be expressed as an integral over extreme Gibbs measures, known as the extreme decomposition [25]. Consequently, the extreme points are of fundamental importance for describing the entire convex set of Gibbs measures. The extreme disordered phases of models on lattices are particularly significant in the context of information flow theory [27–30]. In the present paper, we provide a non-trivial adaptation of well-known methods, including the Kesten-Stigum criterion [8] for assessing the non-extremality of translation-invariant Gibbs measures, as well as the Martinelli-Sinclair-Weitz method [31] for evaluating the extremality of translation-invariant Gibbs measures.

In this paper, we derive a system of functional equations based on the compatibility condition. We show the presence of a phase transition for the mixed-spin Ising model under the external field on the general order Cayley tree. On the binary tree, solving the model exactly under a constant external field, we demonstrate that the model possesses either one or three Gibbs measures depending on the temperature. Additionally, we investigate the conditions for extremality and non-extremality of the disordered phase of the model.

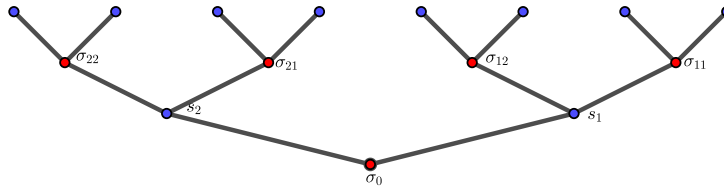


FIG. 1. Some generations of a second order Cayley tree of with a σ_0 spin in the root.

2. Preliminaries

Let $\Gamma^k = (V, L)$ be a semi-infinite Cayley tree of order $k \geq 1$, with a designated root vertex $x^{(0)}$. In this tree, each vertex has exactly $k + 1$ adjacent edges, except for the root $x^{(0)}$, which has only k adjacent edges. The set V represents the vertices of the tree, while L represents the edges.

Two vertices x and y are called *nearest neighbors*, denoted by $l = \langle x, y \rangle$, if there exists an edge in L that connects them. A sequence of edges $\langle x, x_1 \rangle, \langle x_1, x_2 \rangle, \dots, \langle x_{d-1}, y \rangle$ is called a *path* from the vertex x to the vertex y . The distance $d(x, y)$ between two vertices x and y in the Cayley tree is defined as the length of the shortest path connecting them.

We denote

$$W_n = \{x \in V \mid d(x, x^{(0)}) = n\}, V_n = \bigcup_{m=0}^n W_m, L_n = \{l = \langle x, y \rangle \in L \mid x, y \in V_n\}.$$

The set of direct successors of a vertex x is defined as

$$S(x) = \{y \in W_{n+1} : d(x, y) = 1\}$$

where $x \in W_n$.

Denote

$$\Gamma_+^k = \{x \in V : d(x^{(0)}, x) - \text{even}\}, \quad \Gamma_-^k = \{x \in V : d(x^{(0)}, x) - \text{odd}\}.$$

In this paper, we consider the following spin state spaces: $\Phi = \{-1, 0, 1\}$ and $\Psi = \{-\frac{1}{2}, \frac{1}{2}\}$. The corresponding configuration spaces are defined as $\Omega_+ = \Phi^{\Gamma_+^k}$ and $\Omega_- = \Psi^{\Gamma_-^k}$, where Γ_+^k and Γ_-^k represent two disjoint semi-infinite Cayley trees of order k .

Additionally, the finite-volume configuration spaces are denoted by $\Omega_{+,n} = \Phi^{\Gamma_+^k \cap V_n}$ and $\Omega_{-,n} = \Psi^{\Gamma_-^k \cap V_n}$, where V_n is the set of vertices at distance n from the root.

The overall configuration space of the model is given by $\Xi = \Omega_+ \times \Omega_-$. An element of Ω_+ is denoted by $\sigma(x)$ for $x \in \Gamma_+^k$, and an element of Ω_- is denoted by $s(x)$ for $x \in \Gamma_-^k$.

For the configuration $\xi \in \Xi$, the associated sites are assigned to successive generations of the tree (see Fig. 1). Specifically, at the odd-numbered levels of the tree, the vertices are occupied by spins taking values from the set Ψ . Conversely, at the even-numbered levels, the vertices are occupied by spins taking values from the set Φ . This is formally expressed as follows:

$$\xi(x) = \begin{cases} \sigma(x) & \text{if } x \in \Gamma_+^k; \\ s(x) & \text{if } x \in \Gamma_-^k, \end{cases} \tag{1}$$

where $\sigma(x) \in \Phi = \{-1, 0, 1\}$ and $s(x) \in \Psi = \{-\frac{1}{2}, \frac{1}{2}\}$. This arrangement ensures that spins from Ψ are located at odd levels, while spins from Φ are located at even levels of the tree.

The Hamiltonian of (1/2-1) mixed spin Ising model with an external field is defined by

$$H(\xi) = -J \sum_{\langle x,y \rangle} \xi(x)\xi(y) - \sum_{x \in V} \alpha_{\xi(x)}(x), \quad \xi \in \Xi \tag{2}$$

where

$$\alpha_{\xi(x)}(x) = \begin{cases} \alpha_{\sigma(x)}(x) & \text{if } x \in \Gamma_+^k; \\ \tilde{\alpha}_{s(x)}(x) & \text{if } x \in \Gamma_-^k, \end{cases} \tag{3}$$

is the external field.

We denote $\mathbf{h} = (\mathbf{h}_{\xi(x)}(x))_{x \in \Gamma^k}$, where

$$h_{\xi(x)}(x) = \begin{cases} h_{\sigma(x)}(x), & x \in \Gamma_+^k; \\ \tilde{h}_{s(x)}(x), & x \in \Gamma_-^k, \end{cases}$$

and $\mathbf{h}(x) = (h_{-1}(x), h_0(x), h_{+1}(x))$, $\tilde{\mathbf{h}}(x) = (\tilde{h}_{-\frac{1}{2}}(x), \tilde{h}_{\frac{1}{2}}(x))$.

Now, for each $n \geq 1$, we define the Gibbs measure $\mu_n^{\mathbf{h}}$ by

$$\mu_n^{\mathbf{h}}(\xi) = \frac{e^{-\beta H_n(\xi) + \sum_{x \in W_n} h_{\xi(x)}(x)}}{Z_n}, \tag{4}$$

where $\xi \in \Xi_n := \Omega_{+,n} \times \Omega_{-,n}$, Z_n is the partition function.

The sequence of measures $\{\mu_n^{\mathbf{h}}\}$ is compatible, if for all $n \geq 1$ and $\xi_{n-1} \in \Xi_{n-1}$ one has

$$\sum_{w \in \Xi W_n} \mu_n^{\mathbf{h}}(\xi_{n-1} \vee w) = \mu_{n-1}^{\mathbf{h}}(\xi_{n-1}), \quad \text{for all } n \geq 1, \tag{5}$$

$$\Xi W_n = \begin{cases} \Phi^{W_n}, & n - \text{even}; \\ \Psi^{W_n}, & n - \text{odd}. \end{cases}$$

Here $\xi_{n-1} \vee w$ is the concatenation of the configurations. In this setting, there is a unique measure μ on Ω such that for all n and $\xi_n \in \Xi_n$

$$\mu(\{\xi|V_n = \xi_n\}) = \mu_n^{\mathbf{h}}(\xi_n).$$

Such a measure is called a *splitting Gibbs measure (SGM)* corresponding to the model (2).

The following result describes the condition on \mathbf{h} ensuring that the sequence $\{\mu_n^{\mathbf{h}}\}$ is compatible.

Theorem 1. The sequence of measures $\{\mu_n^{\mathbf{h}}\}$, $n = 1, 2, \dots$ given by (5) is compatible if and only if for any $x \in V$ the following equations hold:

$$e^{h_{-1}(x) - h_0(x)} = \prod_{y \in S(x)} \left(\frac{e^{\frac{1}{2}J\beta + \beta\tilde{\alpha}_{-\frac{1}{2}}(y) + \tilde{h}_{-\frac{1}{2}}(y)} + e^{-\frac{1}{2}J\beta + \beta\tilde{\alpha}_{\frac{1}{2}}(y) + \tilde{h}_{\frac{1}{2}}(y)}}{e^{\beta\tilde{\alpha}_{-\frac{1}{2}}(y) + \tilde{h}_{-\frac{1}{2}}(y)} + e^{\beta\tilde{\alpha}_{\frac{1}{2}}(y) + \tilde{h}_{\frac{1}{2}}(y)}} \right), \tag{6}$$

$$e^{h_1(x) - h_0(x)} = \prod_{y \in S(x)} \left(\frac{e^{-\frac{1}{2}J\beta + \beta\tilde{\alpha}_{-\frac{1}{2}}(y) + \tilde{h}_{-\frac{1}{2}}(y)} + e^{\frac{1}{2}J\beta + \beta\tilde{\alpha}_{\frac{1}{2}}(y) + \tilde{h}_{\frac{1}{2}}(y)}}{e^{\beta\tilde{\alpha}_{-\frac{1}{2}}(y) + \tilde{h}_{-\frac{1}{2}}(y)} + e^{\beta\tilde{\alpha}_{\frac{1}{2}}(y) + \tilde{h}_{\frac{1}{2}}(y)}} \right), \tag{7}$$

$$e^{\tilde{h}_{\frac{1}{2}}(x) - \tilde{h}_{-\frac{1}{2}}(x)} = \prod_{y \in S(x)} \left(\frac{e^{-\frac{1}{2}J\beta + \beta\alpha_{-1}(y) + h_{-1}(y)} + e^{\beta\alpha_0(y) + h_0(y)} + e^{\frac{1}{2}J\beta + \beta\alpha_1(y) + h_1(y)}}{e^{\frac{1}{2}J\beta + \beta\alpha_{-1}(y) + h_{-1}(y)} + e^{\beta\alpha_0(y) + h_0(y)} + e^{-\frac{1}{2}J\beta + \beta\alpha_1(y) + h_1(y)}} \right). \tag{8}$$

Proof. The proof can be carried out using the standard argument presented in [7].

3. Translation-invariant Gibbs measures

In this section, we deal with the existence of translation-invariant splitting Gibbs measures (TISGMs) corresponding to the Ising model with mixed spin-1 and spin-1/2 by analyzing the the equations (6)-(8). Recall that the vector-valued functions $\tilde{\mathbf{h}} = \{\tilde{h}_{-\frac{1}{2}}(x), \tilde{h}_{\frac{1}{2}}(x)\}$ and $\mathbf{h}(x) = (h_{-1}(x), h_0(x), h_{+1}(x))$ are called *translation-invariant* if $\tilde{h}_i(x) = \tilde{h}_i(y) =: \tilde{h}_i$ and $h_j(x) = h_j(y) =: h_j$ for all $y \in S(x)$ (see [7]). The measures corresponding to the vector valued functions $\tilde{\mathbf{h}}$ and \mathbf{h} are called TISGMs. We assume that external field $\alpha(x)$ is also translation-invariant, i.e., $\alpha(x) := \alpha \forall x \in \Gamma^k$.

Denote $\mathbf{h}_j := \mathbf{h}_j(x)$ for all $x \in \Gamma_+^k, j \in \Phi, \tilde{\mathbf{h}}_i := \tilde{\mathbf{h}}_i(x), x \in \Gamma_-^k, i \in \Psi$. Introducing the notations $U_1 = h_{-1} - h_0, U_2 = h_1 - h_0, V = \tilde{h}_{\frac{1}{2}} - \tilde{h}_{-\frac{1}{2}}, T_1 = \beta(\alpha_{-1} - \alpha_0), T_2 = \beta(\alpha_1 - \alpha_0), F = \beta(\alpha_{\frac{1}{2}} - \alpha_{-\frac{1}{2}})$, we have the following

$$e^{U_1} = \prod_{y \in S(x)} \left(\frac{\theta^2 + e^V \cdot e^F}{\theta \cdot (1 + e^V \cdot e^F)} \right), \tag{9}$$

$$e^{U_2} = \prod_{y \in S(x)} \left(\frac{1 + \theta^2 \cdot e^V \cdot e^F}{\theta \cdot (1 + e^V \cdot e^F)} \right), \tag{10}$$

$$e^V = \prod_{y \in S(x)} \left(\frac{e^{U_1} \cdot e^{T_1} + \theta^2 \cdot e^{U_2} \cdot e^{T_2} + \theta}{\theta^2 \cdot e^{U_1} \cdot e^{T_1} + e^{U_2} \cdot e^{T_2} + \theta} \right). \tag{11}$$

Denoting $e^{U_1} = X, e^{U_2} = Y, e^V = Z, e^{T_1} = M, e^{T_2} = N, e^F = L$, we obtain the following system of equations:

$$\begin{cases} X = \left(\frac{\theta^2 + LZ}{\theta(1 + LZ)} \right)^k, \\ Y = \left(\frac{1 + \theta^2 LZ}{\theta(1 + LZ)} \right)^k, \\ Z = \left(\frac{MX + \theta^2 NY + \theta}{\theta^2 MX + NY + \theta} \right)^k. \end{cases} \tag{12}$$

3.1. Stability of a fixed point

We consider the system of equations (12). For simplicity, we assume that $L = 1, M = N = m$. In this case, the model possesses the disordered phase [32], i.e., $Z = 1, X = Y = \left(\frac{\theta^2 + 1}{2\theta} \right)^k$ is always a solution to the system (12).

We study the stability of this solution.

To investigate the dynamics of (12), we find the eigenvalues of the following Jacobian matrix J_F :

$$J_F = \begin{pmatrix} 0 & 0 & -\frac{k(\theta^2 - 1)}{4\theta} \cdot \left(\frac{\theta^2 + 1}{2\theta} \right)^{k-1} \\ 0 & 0 & \frac{k(\theta^2 - 1)}{4\theta} \cdot \left(\frac{\theta^2 + 1}{2\theta} \right)^{k-1} \\ -\frac{k \cdot m \cdot (\theta^2 - 1)}{m \cdot \theta^2 \left(\frac{\theta^2 + 1}{2\theta} \right)^2 + m \cdot \left(\frac{\theta^2 + 1}{2\theta} \right)^2 + \theta} & \frac{k \cdot m \cdot (\theta^2 - 1)}{m \cdot \theta^2 \left(\frac{\theta^2 + 1}{2\theta} \right)^2 + m \cdot \left(\frac{\theta^2 + 1}{2\theta} \right)^2 + \theta} & 0 \end{pmatrix} \tag{13}$$

After some algebraic manipulations, we obtain that the eigenvalues of the matrix are: $\lambda_1 = 0,$

$$\lambda_2 = \frac{2\sqrt{(\theta^8 m + 4\theta^6 m + 4\theta^5 + 6\theta^4 m + 4\theta^3 + 4\theta^2 m + m)2^{-k} \left(\frac{\theta^2 + 1}{\theta} \right)^k m(\theta + 1)(\theta - 1)\theta k}}{\theta^8 m + 4\theta^6 m + 4\theta^5 + 6\theta^4 m + 4\theta^3 + 4\theta^2 m + m},$$

$$\lambda_3 = -\frac{2\sqrt{(\theta^8 m + 4\theta^6 m + 4\theta^5 + 6\theta^4 m + 4\theta^3 + 4\theta^2 m + m)2^{-k} \left(\frac{\theta^2 + 1}{\theta} \right)^k m(\theta + 1)(\theta - 1)\theta k}}{\theta^8 m + 4\theta^6 m + 4\theta^5 + 6\theta^4 m + 4\theta^3 + 4\theta^2 m + m}.$$

Remark 1. From Fig. 2, it can be seen that, at some values of parameters θ and k , we have

$$|\lambda_3(\theta, k, m)| > 1,$$

which shows that the fixed point $\left(\left(\frac{\theta^2 + 1}{2\theta} \right)^2, \left(\frac{\theta^2 + 1}{2\theta} \right)^2, 1 \right)$ is saddle [33]. This fact indicates that there is a phase transition.

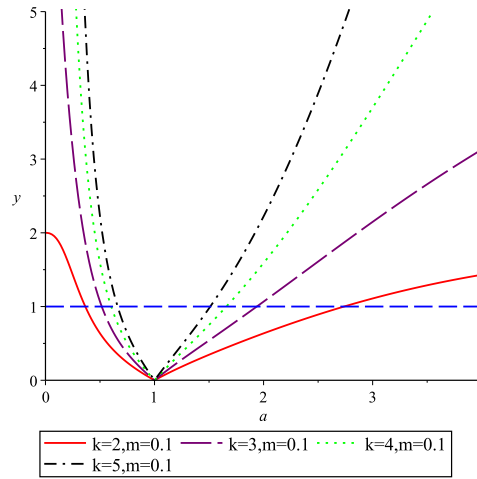


FIG. 2. Plots of the function $|\lambda_3(\theta, k, m)|$ for $k = 2, 3, 4, 5$ and $m = 0, 1$.

3.2. The existence of the phase transition

On substituting the first and second equations of (12) into the third equation, we obtain

$$Z = \left(\frac{M(\theta^2 + LZ)^k + (1 + \theta^2 LZ)^k + \theta^{k+1}(1 + LZ)^k}{\theta^2 M(\theta^2 + LZ)^k + N(1 + \theta^2 LZ)^k + \theta^{k+1}(1 + LZ)^k} \right)^k = F(Z). \tag{14}$$

It follows from (14) that solving (12) is reduced to finding the fixed points of the function $F(Z)$. It is clear that the function $F(Z)$ is an increasing, bounded function with $F(0) > 0$ and $F(\infty) < \infty$. It follows from properties of the function $F(Z)$ that the function has at least one fixed point, say, Z^* . We have

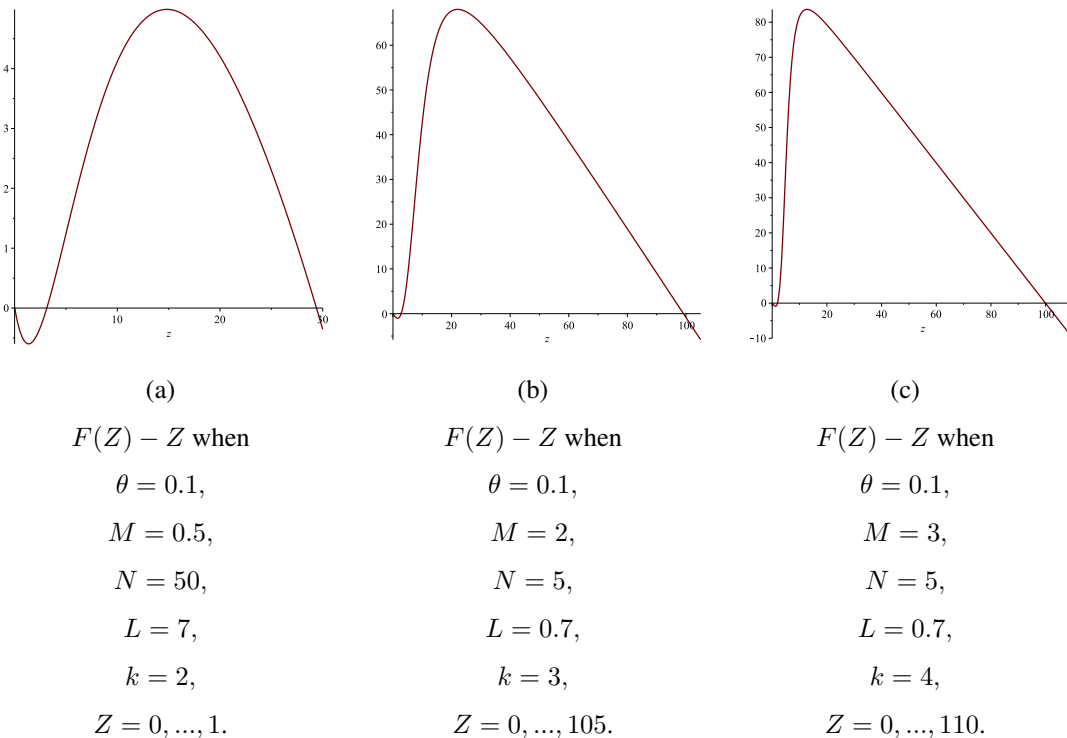


FIG. 3. The plots of the function $F(Z) - Z$ at some values of parameters

Theorem 2. For the mixed-spin Ising model with external field on the Cayley tree of order $k \geq 2$ if the condition $F'(Z^*) > 1$ is satisfied, then there exist at least three distinct SGMs, i.e. the phase transition occurs.

Proof. The condition $F'(Z^*) > 1$ implies the existence of at least three solutions of Equation (14). Let Z^* be the fixed point of $F(Z)$. When $F'(Z^*) > 1$, Z^* is unstable. Consequently, there exists a small neighborhood $(Z^* - \varepsilon, Z^* + \varepsilon)$ of Z^* such that for $Z \in (Z^* - \varepsilon, Z^*)$ $F(Z) < Z$, and for $Z \in (Z^*, Z^* + \varepsilon)$ $F(Z) > Z$. Since $F(0) > 0$, there exists

a solution Z_-^* between 0 and Z^* . Similarly, since $F(+\infty) < +\infty$, there is another solution Z_+^* between Z^* and $+\infty$. Given that there is a bijection between the solution of Eq.(14) and SGMs, it follows that there exist at least three SGMs, which implies the existence of a phase transition.

Remark 2. Note that the set of parameters which satisfy $F'(Z^*) > 1$ is not empty, e.g., see Fig. 3.

3.3. The case $k = 2$

In what follows, we restrict ourselves to the case $k = 2, L = 1, M = N = m$ in (12). Then the system of equations (12) can be reduced to the following equation:

$$(Z - 1)(AZ^4 + BZ^3 + CZ^2 + BZ + A) = 0 \tag{15}$$

where

$$\begin{aligned} A &= \theta^8 m^2 + 2\theta^7 m + 2\theta^6 m^2 + \theta^6 + 2\theta^5 m + \theta^4 m^2, \\ B &= -\theta^{12} m^2 - 2\theta^9 m + 5\theta^8 m^2 + 10\theta^7 m + 8\theta^6 m^2 + 4\theta^6 + 10\theta^5 m + 5\theta^4 m^2 - 2\theta^3 m - m^2, \\ C &= -\theta^{12} m^2 - 2\theta^{10} m^2 - 4\theta^9 m + 7\theta^8 m^2 + 16\theta^7 m + 16\theta^6 m^2 + 6\theta^6 + 16\theta^5 m + 7\theta^4 m^2 - 4\theta^3 m - 2\theta^2 m^2 - m^2. \end{aligned}$$

We obtain that $Z = 1$ is a solution of (15) independent of remaining parameters, and we denote it by z_1 . We consider the second factor in (15). After some algebraic operations, we have

$$A\left(Z^2 + \frac{1}{Z^2}\right) + B\left(Z + \frac{1}{Z}\right) + C = 0.$$

Introducing the new variable

$$t = Z + \frac{1}{Z}, \tag{16}$$

we have

$$f(t) = At^2 + Bt + (C - 2A) = 0. \tag{17}$$

The solutions of (17) are

$$t_1 = \frac{-B - \sqrt{8A^2 + B^2 - 4AC}}{2A}, \quad t_2 = \frac{-B + \sqrt{8A^2 + B^2 - 4AC}}{2A}. \tag{18}$$

Taking into account $t = Z + \frac{1}{Z}$, we consider the following two cases: $t_1 < 2 < t_2$ or $2 < t_1 < t_2$.

Case 1. Let $t_1 < 2 < t_2$. In this case, the parabola defined in (17) should satisfy $Af(2) < 0$. Since $A > 0$ we have that

$$2(A + B) + C < 0$$

or

$$m(\theta^2 + 1)(\theta^2 - 3)\left(\theta^2 - \frac{1}{3}\right) > \frac{4}{3}\theta^3. \tag{19}$$

Taking into account that $\theta > 0$, we solve the inequality (19) with respect to the parameter m :

$$m > \frac{4\theta^3}{3(\theta^2 + 1)(\theta^2 - 3)\left(\theta^2 - \frac{1}{3}\right)}$$

where $\theta \in (0; \frac{1}{\sqrt{3}}) \cup (\sqrt{3}; \infty)$. Under these conditions, we obtain the solutions of the second factor of the equation (15):

$$z_2 = \frac{t_2 + \sqrt{t_2^2 - 4}}{2}, \quad z_3 = \frac{t_2 - \sqrt{t_2^2 - 4}}{2}.$$

Case 2. $2 < t_1 < t_2$. In this case, it suffices to consider $\frac{1}{\sqrt{3}} < \theta < \sqrt{3}$. Since $A > 0$ from properties of the (17), we have $f(2) > 0$. It follows that $-\frac{B}{2A} > 2$ or $B + 4A < 0$ which is equivalent to

$$m(\theta^2 + 1)(\theta^4 - 4\theta^2 + 1) > 2\theta^3.$$

Solving this equality, we have

$$m > \frac{2\theta^3}{(\theta^2 + 1)(\theta^4 - 4\theta^2 + 1)}$$

where $\theta \in (0; \sqrt{2 - \sqrt{3}}) \cup (\sqrt{2 + \sqrt{3}}; \infty)$. However, the obtained solution does not satisfy the condition $\frac{1}{\sqrt{3}} < \theta < \sqrt{3}$, thus, in this case, we do not obtain any solution.

Introduce

$$\Upsilon_1 = \{(\theta, m) : m(\theta^2 + 1)(\theta^4 - 4\theta^2 + 1) > 2\theta^3 \text{ and } \theta \in (0; \sqrt{2 - \sqrt{3}}) \cup (\sqrt{2 + \sqrt{3}}; \infty)\}$$

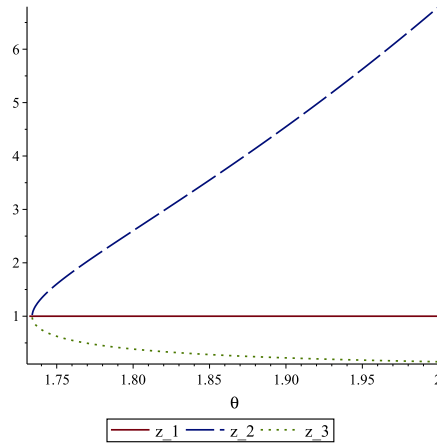
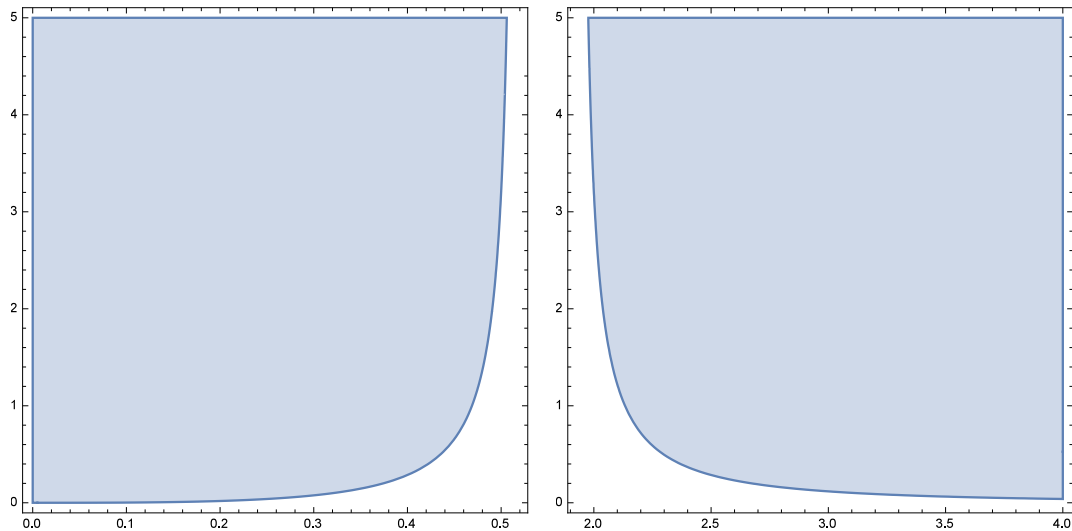


FIG. 4. The plot of the solutions z_1, z_2, z_3 at $m = 100$ and $\theta \in [1.75;2]$.

(see e.g., Fig. 5).

Theorem 3. Assume that $J \neq 0$. If $(\theta, m) \in \Upsilon_1$ then there is a phase transition for the mixed-spin Ising model on the Cayley tree of order two.



(a)The plot of Υ_1 is drawn for $\theta \in (0, \sqrt{2 - \sqrt{3}})$ and $m \in (0, 5)$.

(b)The plot of Υ_1 is drawn for $\theta \in (\sqrt{2 + \sqrt{3}}, 4)$ and $m \in (0, 5)$.

FIG. 5. The plot of Υ_1 is drawn for $\theta \in (0, \sqrt{2 - \sqrt{3}}) \cup (\sqrt{2 + \sqrt{3}}, 4)$ and $m \in (0, 5)$.

4. Extremality of disordered phase

In this section, we check the non-extremality of the obtained Gibbs measures: Let us consider the following stochastic matrix $\mathbb{P} = (P_{ij})$:

$$P_{ij} = \frac{e^{ij\beta J + \tilde{h}_j + \beta \tilde{\alpha}_j}}{\sum_{u=\mp \frac{1}{2}} e^{iu\beta J + \tilde{h}_u + \beta \tilde{\alpha}_u}}$$

where $i \in \{-1, 0, 1\}$ va $j \in \{-\frac{1}{2}, \frac{1}{2}\}$.

Using our notations $Z = e^{\tilde{h}_{\frac{1}{2}} - \tilde{h}_{-\frac{1}{2}}}$ and $L = e^{\beta(\tilde{\alpha}_{\frac{1}{2}} - \tilde{\alpha}_{-\frac{1}{2}})}$, introduced in Section 2, we have the following matrix

$\mathbb{P} = (P_{ij})$:

$$\mathbb{P} = \begin{pmatrix} P_{(-1,-\frac{1}{2})} & P_{(-1,\frac{1}{2})} \\ P_{(0,-\frac{1}{2})} & P_{(0,\frac{1}{2})} \\ P_{(1,-\frac{1}{2})} & P_{(1,\frac{1}{2})} \end{pmatrix} = \begin{pmatrix} \frac{\theta^2}{\theta^2 + LZ} & \frac{LZ}{\theta^2 + LZ} \\ \frac{1 + LZ}{1} & \frac{1 + LZ}{\theta^2 LZ} \\ \frac{1}{1 + \theta^2 LZ} & \frac{1}{1 + \theta^2 LZ} \end{pmatrix} \tag{20}$$

Similarly, we introduce the following stochastic matrix $\mathbb{Q} = (Q_{ij})$:

$$Q_{ij} = \frac{\exp(ij\beta J + h_j + \beta\alpha_j)}{\sum_{u \in \{-1,0,1\}} \exp(iu\beta J + h_u + \beta\alpha_u)}$$

where $i \in \{-\frac{1}{2}, \frac{1}{2}\}$ and $j \in \{-1, 0, 1\}$.

Using the notations $e^{h_{-1}-h_0} = X$, $e^{h_1-h_0} = Y$, $e^{\beta(\alpha_{-1}-\alpha_0)} = M$ and $e^{\beta(\alpha_1-\alpha_0)} = N$, we have $\mathbb{Q} = (Q_{ij})$:

$$\mathbb{Q} = \begin{pmatrix} Q_{(-\frac{1}{2},-1)} & Q_{(-\frac{1}{2},0)} & Q_{(-\frac{1}{2},1)} \\ Q_{(\frac{1}{2},-1)} & Q_{(\frac{1}{2},0)} & Q_{(\frac{1}{2},1)} \end{pmatrix} = \begin{pmatrix} \frac{\theta^2 MX}{\theta^2 MX + \theta + NY} & \frac{\theta}{\theta^2 MX + \theta + NY} & \frac{NY}{\theta^2 MX + \theta + NY} \\ \frac{MX}{MX + \theta + \theta^2 NY} & \frac{\theta}{MX + \theta + \theta^2 NY} & \frac{\theta^2 NY}{MX + \theta + \theta^2 NY} \end{pmatrix} \tag{21}$$

For the solution $Z = 1$, $X = Y = \left(\frac{\theta^2 + 1}{2\theta}\right)^2$, the matrices \mathbb{P} and \mathbb{Q} have the following forms:

$$\mathbb{P} = \begin{pmatrix} \frac{\theta^2}{1 + \theta^2} & \frac{1}{1 + \theta^2} \\ \frac{1}{2} & \frac{2}{\theta^2} \\ \frac{1}{1 + \theta^2} & \frac{1}{1 + \theta^2} \end{pmatrix}, \tag{22}$$

$$\mathbb{Q} = \begin{pmatrix} \frac{m\theta^2(\theta^2 + 1)^2}{4\theta^3 + m(\theta^2 + 1)^3} & \frac{4\theta^3}{4\theta^3 + m(\theta^2 + 1)^3} & \frac{m(\theta^2 + 1)^2}{4\theta^3 + m(\theta^2 + 1)^3} \\ \frac{m(\theta^2 + 1)^2}{4\theta^3 + m(\theta^2 + 1)^3} & \frac{4\theta^3}{4\theta^3 + m(\theta^2 + 1)^3} & \frac{m\theta^2(\theta^2 + 1)^2}{4\theta^3 + m(\theta^2 + 1)^3} \end{pmatrix}. \tag{23}$$

It is easy to see that $\mathbb{P} \cdot \mathbb{Q}$ is again a stochastic matrix:

$$\mathbb{H} = \mathbb{P} \cdot \mathbb{Q} = \frac{1}{4\theta^3 + m(\theta^2 + 1)^3} \begin{pmatrix} m(\theta^2 + 1)(\theta^4 + 1) & 4\theta^3 & 2m\theta^2(\theta^2 + 1) \\ \frac{m(\theta^2 + 1)^3}{2} & 4\theta^3 & \frac{m(\theta^2 + 1)^3}{2} \\ 2m\theta^2(\theta^2 + 1) & 4\theta^3 & m(\theta^2 + 1)(\theta^4 + 1) \end{pmatrix}. \tag{24}$$

The eigenvalues of the stochastic matrix \mathbb{H} are:

$$\left\{0, \frac{m(\theta^6 - \theta^4 - \theta^2 + 1)}{\theta^6 m + 3\theta^4 m + 4\theta^3 + 3\theta^2 m + m}, 1\right\}.$$

After some calculation, one can show that the second eigenvalue in terms of the absolute value is

$$\lambda_{max} = \frac{m(\theta^6 - \theta^4 - \theta^2 + 1)}{\theta^6 m + 3\theta^4 m + 4\theta^3 + 3\theta^2 m + m} \tag{25}$$

According to the Kesten-Stigum criterion [8], in order to check the non-extremality of the measure, we should consider the following inequality

$$2\lambda_{max}^2 - 1 = 2 \left(\frac{m(\theta^6 - \theta^4 - \theta^2 + 1)}{\theta^6 m + 3\theta^4 m + 4\theta^3 + 3\theta^2 m + m} \right)^2 - 1 = \frac{A \cdot m^2 + B \cdot m + C}{(\theta^6 m + 3\theta^4 m + 4\theta^3 + 3\theta^2 m + m)^2}$$

$$A := \theta^{12} - 10\theta^{10} - 17\theta^8 - 12\theta^6 - 17\theta^4 - 10\theta^2 + 1,$$

$$B := -8\theta^9 - 24\theta^7 - 24\theta^5 - 8\theta^3, \quad C := -16\theta^6.$$

Denote

$$K(\theta, m) = A \cdot m^2 + B \cdot m + C. \tag{26}$$

Thus, the inequality $2\lambda_{max}^2 - 1 > 0$ is reduced to $K(\theta, m) > 0$.

Theorem 4. If $K(\theta, m) > 0$ then the disordered phase is non-extreme.

Remark 3. Note that the set $\Upsilon_2 = \{(\theta, m) \in \mathbb{R}_+^2 : K(\theta, m) > 0\}$ is not empty, see, for example Fig. 4(a).

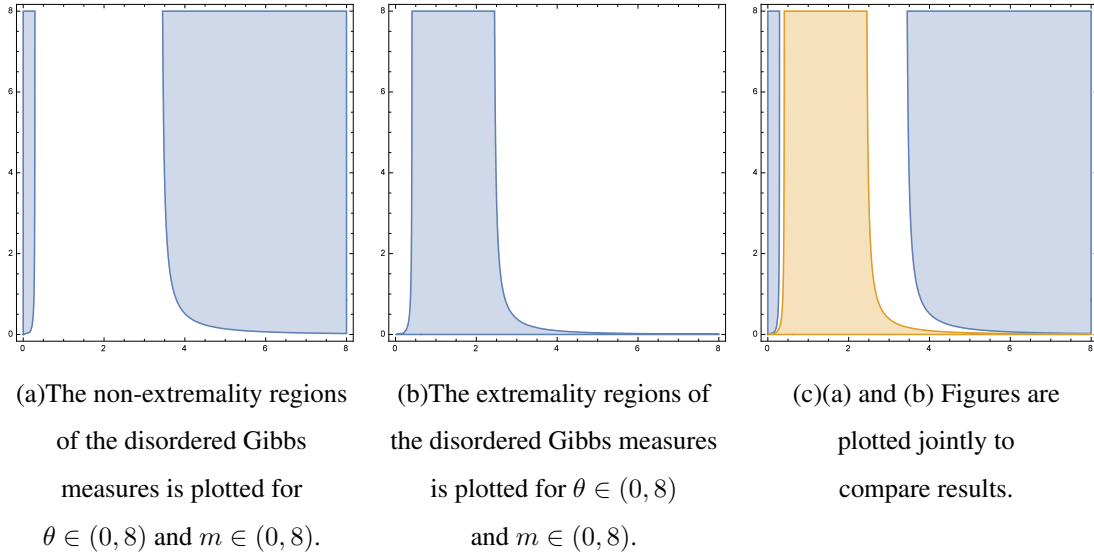


FIG. 6. The extremality vs non-extremality regions of the obtained Gibbs measures are plotted.

In the subsection, we check the extremality of the measures.

Definition. [31] For a set of Gibbs distributions $\mu_{T_x}^s$, the quantities $\kappa \equiv \kappa(\{\mu_{T_x}^s\})$ and $\gamma \equiv \gamma(\{\mu_{T_x}^s\})$ are defined by

- (1) $\kappa = \sup_{z \in \Gamma^k} \max_{z, s, s'} \|\mu_{T_z}^s - \mu_{T_z}^{s'}\|_z$
- (2) $\gamma = \sup_{z \subset \Gamma^k} \max_{z, s, s'} \|\mu_A^{\eta^{y,s}} - \mu_A^{\eta^{y,s'}}\|_z$, where the maximum is taken over all boundary conditions η , all sites $y \in \partial A$, all neighbors $x \in A$ of y , and all spins $s, s' \in \{-1, 0, 1\}$.

It is known [1, 7, 31] that to check the extremality of the translation-invariant Gibbs measures, we should consider the following inequality:

$$2\kappa\gamma < 1, \tag{27}$$

where $\kappa = \sqrt{\tau_{\mathbb{P}}\tau_{\mathbb{Q}}}$ and $\tau_{\mathbb{H}} = \frac{1}{2} \max_{i,j} \left\{ \sum_{l=1}^3 |H_{i,l} - H_{j,l}| \right\}$. From (22) and (23), we have

$$\tau_{\mathbb{P}} = \frac{|\theta^2 - 1|}{\theta^2 + 1}, \quad \tau_{\mathbb{Q}} = \frac{m(\theta^2 + 1)^2 |\theta^2 - 1|}{4\theta^3 + m(\theta^2 + 1)^3}.$$

As in [1, 7, 34] we assume that $\kappa = \gamma$. Then,

$$\begin{aligned} \kappa^2 &= \frac{m(\theta^2 - 1)^2(\theta^2 + 1)}{4\theta^3 + m(\theta^2 + 1)^3}, \\ 2\kappa^2 - 1 &= \frac{2m(\theta^2 - 1)^2(\theta^2 + 1)}{4\theta^3 + m(\theta^2 + 1)^3} - 1 < 0. \end{aligned} \tag{28}$$

Simplifying the above expression, we have

$$m(\theta^6 - 5\theta^4 - 5\theta^2 + 1) < 4\theta^3.$$

Introduce

$$\Upsilon_3 = \{(\theta, m) : m(\theta^6 - 5\theta^4 - 5\theta^2 + 1) < 4\theta^3 \text{ and } \theta \in (0, \sqrt{2} - 1) \cup (\sqrt{2} + 1, \infty)\}.$$

We can deduce that

Theorem 5. 1. If $\theta^6 - 5\theta^4 - 5\theta^2 + 1 \leq 0$ or $(\theta, m) \in \Upsilon_3$, then the disordered phase is extreme.

Remark 4. Note that the set Υ_3 is not empty, see, for example Fig. 4(b).

5. Conclusion

In the present work, we have investigated the phase transition of the mixed type Ising model on the Cayley tree under the non-zero external field. We showed that under some conditions on parameters the model exhibits a phase transition on the general order Cayley tree. On the binary tree, we solved the model exactly under the specific external field, i.e., we find all regions where the phase transition occurs. Moreover, we checked the extremality and non-extremality of one of obtained translation-invariant Gibbs measures on the binary tree.

References

- [1] Akin H., Mukhamedov F.M. Phase transition for the Ising model with mixed spins on a Cayley tree. *J. Stat. Mech.*, 2022, P. 053204.
- [2] Akin H. The classification of disordered phases of mixed spin $(2,1/2)$ Ising model and the chaoticity of the corresponding dynamical system. *Chaos Solutions Fractals*, 2023, **167**, P. 113086
- [3] Akin H. Quantitative behavior of $(1,1/2)$ -MSIM on a Cayley tree. *Chin. J. Phys.*, 2023, **83**, P. 501–14
- [4] Karimou M., Yessoufou R.A., Oke T.D., Kpadonou A., Hontinfinde F. Bethe approach study of the mixed spin-1/2 and spin-5/2 Ising system in the presence of an applied magnetic field. *Condensed Matter Physics*, 2016, **19**, P. 33003.
- [5] Akin H. Exploring the Phase Transition Challenge by Analyzing Stability in a 5-D Dynamical System Linked to $(2,1/2)$ -MSIM. *Chinese Journal of Physics*, 2024, **91**, P. 494–504.
- [6] Akin H. Investigation of Thermodynamic Properties of Mixed-Spin $(2,1/2)$ Ising and Blum-Capel Models on a Cayley Tree. *Chaos, Solitons Fractals*, 2024, **184**, P. 1149980.
- [7] Akin H. and Mukhamedov F.M. The extremality of disordered phases for the mixed spin- $(1,1/2)$ Ising model on a Cayley tree of arbitrary order. *J. Stat. Mech.*, 2024, P. 013207.
- [8] Kesten H., Stigum B.P. Additional limit theorems for indecomposable multidimensional Galton-Watson processes. *The Annals of Mathematical Statistics*, 1996, **37**, P. 1463–1481.
- [9] Akin H. Exploring the Phase Transition Challenge by Analyzing Stability in a 5-D Dynamical System Linked to $(2,1/2)$ -MSIM. *Chinese Journal of Physics*, 2024, **91**, P. 494–504.
- [10] Schofield S.L., and Bowers R.G. Renormalization group calculations on a mixed-spin system in 2 dimensions. *J. Phys. A: Math. Gen.*, 1980, **13**, P. 3697.
- [11] Schofield S.L., and Bowers R.G. High-temperature series expansion analyses of mixed-spin Ising-models. *J. Phys. A: Math. Gen.*, 1981, **14**, P. 2163.
- [12] Albayrak E., The study of mixed spin-1 and spin-1/2: Entropy and isothermal entropy change, *Physica A*, 2020, **559**, P. 125079.
- [13] da Silva N.R., Salinas S.R. Mixed-spin Ising model on the Bethe lattice. *Phys. Rev. B*, 1991, **44**, P. 852–855.
- [14] Bleher P.M., Ganikhodjaev N.N. On pure phases of the Ising model on the Bethe lattice, *Theor. Probab. Appl.*, 1990, **35**, P. 216–227.
- [15] Baxter R.J. *Exactly Solved Models in Statistical Mechanics*. Academic Press, London/New York 1982.
- [16] Kaneyoshi T. Role of single-ion-anisotropy in amorphous ferrimagnetic alloys, *Phys. Rev.*, 1986, **B34**, P. 7866.
- [17] Kaneyoshi T. A new disordered phase and its physical contents of a mixed Ising system with a random crystal-field. *Solid State Commun.*, 1989, **70**, P. 975.
- [18] Kaneyoshi T., Sarmiento E.F. and Fittipaldi I.F. An effective-field theory of mixed Ising spin systems in transverse fields. *Phys. Stat. Sol. (b)*, 1988, **150**, P. 261.
- [19] Kaneyoshi T. and Chen J.C. Mean-field analysis of a ferrimagnetic mixed spin system. *J. Magn. Magn. Mater.*, 1991, **98**, P. 201.
- [20] Benayad N., Klümper A., Zittartz J. and Benyoussef A. Re-entrant ferromagnetism in a two-dimensional mixed spin Ising-model with random nearest-neighbour interactions. *Phys.B. Condens. Matter*, 1989, **77**, P. 333–339.
- [21] Zhang G.M., and Yang C.L. Monte-Carlo study of the 2-dimensional quadratic Ising ferromagnet with spin $s = 1/2$ and $s = 1$ and with crystal-field interactions. *Phys. Rev.*, 1993, **B48**, P. 9452.
- [22] Tucker J.W. The ferrimagnetic mixed spin 1/2 and spin 1 Ising system. *Magn. Magn. Mater.*, 1999, **195**, P. 733.
- [23] Mukhamedov F.M., Pah C.H., Jamil H., Rahmatullaev M.M. On Ground states and phase transition for λ -model with the competing Potts interactions on Cayley trees. *Physica A*, 2020, **549**, P. 124184.
- [24] Mukhamedov F. Extremality of disordered phase of λ -model on Cayley trees. *Algorithms*, 2022, **15**, P. 18.
- [25] Georgii H.O. *Gibbs Measures and Phase Transitions*, de Gruyter, Berlin, 1988.
- [26] Sinai Ya.G. *Theory of phase transitions: Rigorous Results*. Pergamon, Oxford 1982.
- [27] Rozikov U.A. *Gibbs measures on a Cayley tree*. World Scientific Publishing, Singapore 2013.
- [28] Mossel E., *Reconstruction on trees: beating the second eigenvalue*, Ann. Appl. Probab. 2001, **11(1)**, P. 285–300.
- [29] Mossel E., Peres Y. *Information flow on trees*. Ann. Appl. Probab., 2003, **13(3)**, P. 817–844.
- [30] Mossel E. *Survey: information flow on trees*. Graphs. morphisms and statistical physics, 155-170 DI-MACS Ser. Discrete Math. Theoret. Comput. Sci., 63, Amer. Math. Soc., Providence, RI, 2004.
- [31] Martinelli F., Sinclair A., Weitz D. Fast mixing for independent sets, coloring, and other models on trees. *Random Struct. Algor.*, 2007, **31**, P. 134–172.
- [32] Bleher P.M. Extremity of the disordered phase in the Ising model on the Bethe lattice. *Commun.Math. Phys.*, 1990, **128**, P. 411–419.
- [33] Alligood K., Sauer T., Yorke J.A. *Chaos-an introduction to dynamical systems*, Springer-Verlag, New York, 1996, 603 p.
- [34] Rozikov U.A., Khakimov R.M., Khaidarov F.K. Extremality of the translation-invariant Gibbs measures for the Potts model on the Cayley tree. *Theor. Math. Phys.*, 2018, **196**, P. 1043–1058.
- [35] Rahmatullaev M.M., Rasulova M.A. Extremality of translation-invariant Gibbs measures for the Potts-SOS model on the Cayley tree. *J. Stat. Mech.*, 2021, **7**, P. 073201.

Submitted 1 August 2024; revised 4 September 2024; accepted 9 September 2024

Information about the authors:

Muzaffar M. Rahmatullaev – V.I. Romanovskiy Institute of Mathematics, Uzbekistan Academy of Sciences, 4-b, University str, 100174, Tashkent, Uzbekistan; New Uzbekistan University, 100000, Tashkent, Uzbekistan; Namangan state University, 316, Uychi str, Namangan, Uzbekistan; ORCID 0000-0003-2987-7714; mrahmatullaev@rambler.ru

Dilshod O. Egamov – V.I. Romanovskiy Institute of Mathematics, Uzbekistan Academy of Sciences, 4-b, University str, 100174, Tashkent, Uzbekistan; Namangan state University, 316, Uychi str, Namangan, Uzbekistan; ORCID 0000-0002-0133-0883; dilshodbekegamov87@gmail.com

Conflict of interest: the authors declare no conflict of interest.

Inverse source problem for the subdiffusion equation with edge-dependent order of time-fractional derivative on the metric star graph

Zarifboy A. Sobirov^{1,2,a}, Ariukhan A. Turemuratova^{1,3,b}

¹National University of Uzbekistan, 100174, Tashkent, Uzbekistan

²V. I. Romanovskiy Institute of Mathematics, Uzbekistan Academy of Science, 100174, Tashkent, Uzbekistan

³Branch of Russian Economic University named after G. V. Plekhanov in Tashkent, 100164, Tashkent, Uzbekistan

^az.sobirov@nuu.uz, ^bariuxanturemuratova@gmail.com

Corresponding author: Z. A. Sobirov, z.sobirov@nuu.uz

PACS 02.30.Jr, 02.30.Zz

ABSTRACT The paper discusses the inverse source problem for the subdiffusion equation in the Sobolev space. The direct and inverse problems are transformed into operator equations to derive solutions. The uniqueness and existence of a strong solution to the direct problem are proven. The inverse problem is reduced to an operator equation, and the well-definedness and continuity of the corresponding resolvent operator are proven.

KEYWORDS subdiffusion equation, star metric graph, inverse problem, generalized solution, resolvent operator

FOR CITATION Sobirov Z.A., Turemuratova A.A. Inverse source problem for the subdiffusion equation with edge-dependent order of time-fractional derivative on the metric star graph. *Nanosystems: Phys. Chem. Math.*, 2024, **15** (5), 586–596.

1. Introduction

The theory of differential equations on graphs has significant implications in various fields, including mathematics, physics, biology and engineering. There are numerous studies dedicated to the differential operators and differential equations on branched structures and networks [1–5]. In [6], a metric graph model is developed for Stokes flow in three-dimensional spaces, addressing the complexities of fluid dynamics in networks with varying viscosity and density. The study examines quantum graphs, where the absence of reflection is linked to the transparency of the graph vertices [7–9]. In [7], the researchers investigated the issue of reflectionless soliton transport in network branching points by modeling soliton dynamics in networks using the nonlinear Schrödinger equation on metric graphs. Paper [9] emphasizes the importance of boundary conditions in quantum graphs and proposes a method to achieve low reflection, a crucial factor for effective electron transport in nanosystems. In graphs, various differential equations are studied with a set of methods of solving. In particular, the linearized KdV equation [10], a pseudo-subdiffusion equation involving the Hilfer time-fractional derivative [11], the Schrödinger operator on the quantum graph [12], the Fokas method for the heat equation [13] are investigated. In [14], authors consider construction of the matrix-Green's functions of initial-boundary value problems for the time-fractional diffusion equation on the metric star graph with equal bonds. It is investigated how magnetic boundary control can be utilized to solve inverse problems for Schrödinger operators on metric graphs in [15].

The study of fractional diffusion equations on metric graphs is motivated by practical and important problems such as anomalous heat transport in mesoscopic networks, subdiffusion processes in nanoscale network structures, molecular wires, different lattices and discrete structures. The interest in fractional diffusion equations is fueled by the close connection between anomalous diffusion and fractional derivatives. This link has been explored in the works of Luchko [16] and Metzler and Klafter [17], among others. The well-posedness of some time-fractional parabolic equations has been investigated, as referenced in the works of Sakamoto and Yamamoto [18], Kubica and Yamamoto [19]. Additionally, space-time fractional diffusion equations have also been the subject of investigation by various authors.

The application of fractional derivatives in fractional Sobolev spaces is essential for introducing weak or generalized solutions to fractional differential equations. Just as in the theory of partial differential equations, various approaches can be employed to address this problem. In [20], Gorenflo et. al investigated the maximal regularity of solutions to the time-fractional diffusion equation with the Caputo derivative in the fractional Sobolev spaces. We mention also the recent work [21], it provides rigorous treatments for time-fractional derivatives in the Sobolev spaces and solutions to initial boundary value problems for time-fractional partial differential equations.

Inverse problems are recognized as one of the most important mathematical challenges in science and mathematics. This area of study has been the focus of extensive research by numerous scholars, leading to significant advancements in understanding and solving inverse problems in differential equations. In a specific instance, researchers have investigated

the uniqueness and stability of the solution to the inverse problem of determining the order of the Caputo time-fractional derivative for a subdiffusion equation, as documented in [22]. Additionally, R. Ashurov et al. [23] have concentrated on an inverse problem related to determining the orders of systems of fractional pseudo-differential equations.

The integral overdetermination condition has been leveraged in various research works to address inverse problems associated with differential equations. Notably, Kamynin utilized the integral overdetermination condition for the solution of the inverse problem related to a degenerate parabolic equation, as referenced in [24, 25]. Also, we refer to work [26].

2. Preliminary materials

In this section, we introduce some notations, provide the function spaces necessary for studying our problem.

2.1. Fractional integrals and derivatives

Definition 1. [27] *The left and right fractional integrals of order $0 < \alpha < 1$ for a function $y(t) \in L_1(0, T)$ are, respectively, defined by*

$$I_{0,t}^\alpha y(t) \equiv D_{0,t}^{-\alpha} y(t) := \frac{1}{\Gamma(\alpha)} \int_0^t \frac{y(\tau)}{(t-\tau)^{1-\alpha}} d\tau,$$

$$I_{t,T}^\alpha y(t) \equiv D_{t,T}^{-\alpha} y(t) := \frac{1}{\Gamma(\alpha)} \int_t^T \frac{y(\tau)}{(\tau-t)^{1-\alpha}} d\tau.$$

Definition 2. [27] *The left and right Caputo fractional derivatives of order $0 < \alpha < 1$ for a function $y(t)$ on $[0, T]$ are, respectively, defined by*

$$d_{0,t}^\alpha y(t) = \frac{1}{\Gamma(1-\alpha)} \int_0^t \frac{y'(\tau)}{(t-\tau)^\alpha} d\tau, \quad d_{t,T}^\alpha y(t) = \frac{-1}{\Gamma(1-\alpha)} \int_t^T \frac{y'(\tau)}{(\tau-t)^\alpha} d\tau,$$

provided that the integrals in the right-hand sides of these expressions exist.

Definition 3. [27] *The left and right Riemann-Liouville fractional derivatives of order $0 < \alpha < 1$ for a function $y(t)$ on $[0, T]$ are, respectively, defined by*

$$D_{0,t}^\alpha y(t) = \frac{1}{\Gamma(1-\alpha)} \frac{d}{dt} \int_0^t \frac{y(\tau)}{(t-\tau)^\alpha} d\tau,$$

$$D_{t,T}^\alpha y(t) = \frac{-1}{\Gamma(1-\alpha)} \frac{d}{dt} \int_t^T \frac{y(\tau)}{(\tau-t)^\alpha} d\tau,$$

provided that the integrals in the right-hand sides of these expressions exist.

2.2. Fractional Sobolev spaces and weak Caputo derivative

We introduce some functional spaces that are helpful in solving the studied problem. The fractional derivatives defined above are pointwise derivatives. It's necessary to provide a definition of the generalized (weak) fractional derivative, which is well-defined within a subspace of a fractional order Sobolev space. This particular derivative is defined in [21].

Following to [21], by $H^\alpha(0, T)$, $0 < \alpha < 1$, we denote the fractional Sobolev - Slobodeskii space governed by the norm (see [20], [21])

$$\|u\|_{H^\alpha(0,T)} := \left(\|u\|_{L_2(0,T)}^2 + \int_0^T \int_0^T \frac{|u(t) - u(s)|^2}{(t-s)^{1+2\alpha}} ds dt \right)^{\frac{1}{2}}.$$

We put ${}_0H^\alpha(0, T) = \{u \in H^\alpha(0, T) : u(0) = 0\}$ for $\frac{1}{2} < \alpha \leq 1$,

$$H_\alpha(0, T) = \begin{cases} H^\alpha(0, T), & 0 \leq \alpha < \frac{1}{2}, \\ \{v \in H^{\frac{1}{2}}(0, T) : \int_0^T \frac{|v(t)|^2}{t} dt < \infty\}, & \alpha = \frac{1}{2}, \\ {}_0H^\alpha(0, T), & \frac{1}{2} < \alpha \leq 1. \end{cases}$$

The space $H_\alpha(0, T)$ is a Banach space with the norm [21]

$$\|v\|_{H_\alpha(0,T)} = \begin{cases} \|v\|_{H^\alpha(0,T)}, & 0 < \alpha < 1, \alpha \neq \frac{1}{2}, \\ \left(\|v\|_{H^{\frac{1}{2}}(0,T)}^2 + \int_0^T \frac{|v(t)|^2}{t} dt \right)^{\frac{1}{2}}, & \alpha = \frac{1}{2}. \end{cases}$$

According to [21], the space ${}_0C^1[0, T] = \{v \in C^1[0, T] : v(0) = 0\}$ is dense in $H_\alpha(0, T)$.

Theorem 1. [21] *Let $0 < \alpha < 1$.*

(i) $I_{0,t}^\alpha : L_2(0, T) \rightarrow H_\alpha(0, T)$ *is injective and surjective.*

(ii) *There exists a constant $C > 0$ such that*

$$C^{-1} \|I_{0,t}^\alpha u\|_{H_\alpha(0,T)} \leq \|u\|_{L_2(0,T)} \leq C \|I_{0,t}^\alpha u\|_{H_\alpha(0,T)}$$

for all $u \in L_2(0, T)$.

From Theorem 1, it follows that the inverse operator $(I_{0,t}^\alpha)^{-1}$ exists. We put $I_{0,t}^{-\alpha} = (I_{0,t}^\alpha)^{-1}$.

Corollary 1. [21] Let $0 < \alpha < 1$. Then

$$I_{0,t}^{-\alpha} I_{0,t}^\alpha u = u, \quad u \in L_2(0, T),$$

and

$$I_{0,t}^\alpha I_{0,t}^{-\alpha} u = u, \quad u \in H_\alpha(0, T).$$

Definition 4. [21] For $0 \leq \alpha \leq 1$, we set

$$\partial_{0,t}^\alpha u := I_{0,t}^{-\alpha} u, \quad u \in H_\alpha(0, T)$$

with the domain $\mathcal{D}(\partial_{0,t}^\alpha) = H_\alpha(0, T)$.

We consider the classical Caputo derivative $d_{0,t}^\alpha$ as an operator from $\mathcal{D}(d_{0,t}^\alpha) = {}_0C^1[0, T] \subset L_2(0, T)$ to $L_2(0, T)$. By $\overline{d_{0,t}^\alpha}$, we denote the closure in $L_2(0, T)$ of $d_{0,t}^\alpha$ with $\mathcal{D}(d_{0,t}^\alpha) = {}_0C^1[0, T]$ which is the smallest closed extension of $d_{0,t}^\alpha$.

Theorem 2. [21] We have $\mathcal{D}(\overline{d_{0,t}^\alpha}) = H_\alpha(0, T)$, and

$$\overline{d_{0,t}^\alpha} = \partial_{0,t}^\alpha = D_{0,t}^\alpha, \quad \text{on } H_\alpha(0, T).$$

This theorem means that our definition of $\partial_{0,t}^\alpha$ is consistent with the classical Caputo derivative by considering the closure of the operator.

Furthermore, the following norms are equivalent in $H_\alpha(0, T)$ (see [21])

$$\|\partial_{0,t}^\alpha v\|_{L_2(0, T)} \sim \|v\|_{H_\alpha(0, T)}.$$

We notice, that in the case $\frac{1}{2} < \alpha < 1$ for any $v(t) \in H^\alpha(0, T)$, the weak Caputo derivative can be defined by the equality $\partial_{0,t}^\alpha v(t) = \partial_{0,t}^\alpha(v(t) - v(0))$ (see [21]).

2.3. Metric star graph. The star metric graph Γ is a graph with n bonds, consisting of a finite set of vertices $V = \{\nu_i\}_0^n$ and a finite set of edges $E = \{e_i\}_1^n$, where e_i connects the vertices ν_0 and $\nu_i, i = \overline{1, n}$ [28]. Each bond e_i is assigned the interval $(0, l_i)$, and coordinates x_i are defined on each bond. The vertex ν_0 of the graph has a coordinate of 0 on each bond. Further, without loss of generality, we will use x instead of x_i . For the function, $u : \Gamma \rightarrow R$, defined on the graph, we put $u|_{e_i} = u_i$.

We define some functional spaces in the metric star graph. For the functions defined on the graph, we also use

vector-type notations $u = (u_1, \dots, u_n), u_x = \left(\frac{\partial u_1}{\partial x}, \dots, \frac{\partial u_n}{\partial x}\right), u_{xx} = \left(\frac{\partial^2 u_1}{\partial x^2}, \dots, \frac{\partial^2 u_n}{\partial x^2}\right), \int_\Gamma u d\Gamma = \sum_{i=1}^n \int_0^{l_i} u_i dx$. For

$u : \Gamma \rightarrow R, v : \Gamma \rightarrow R$ we put $uv = (u_1 v_1, u_2 v_2, \dots, u_n v_n)$.

Let $\alpha = (\alpha_1, \alpha_2, \dots, \alpha_n), 0 < \alpha_i < 1, i = \overline{1, n}, G_\tau = \{(x, t) : x \in \Gamma, t \in (0, \tau)\}, 0 < \tau \leq T$. We put $\partial_{0,t}^\alpha u = (\partial_{0,t}^{\alpha_1} u_1, \partial_{0,t}^{\alpha_2} u_2, \dots, \partial_{0,t}^{\alpha_n} u_n)$.

Definition 5. [28] The space $L_2(\Gamma)$ on Γ consists of functions that are measurable and square-integrable on each edge $e_i, i = \overline{1, n}$ with the scalar product and the norm:

$$(u(x), v(x))_{L_2(\Gamma)} = \int_\Gamma u(x) \cdot v(x) d\Gamma,$$

$$\|u\|_{L_2(\Gamma)}^2 = \sum_i \|u\|_{L_2(e_i)}^2.$$

In other words, $L_2(\Gamma)$ is the orthogonal direct sum of spaces $L_2(e_i), i = \overline{1, n}$.

Definition 6. The Hilbert space $W_2^l(\Gamma), l = 1, 2$ defined by

$$W_2^l(\Gamma) = \bigoplus_{i=1}^n W_2^l(e_i), \quad l = 1, 2,$$

and with the scalar products

$$(u, v)_{W_2^1(\Gamma)} = \int_\Gamma (uv + u_x v_x) d\Gamma,$$

$$(u, v)_{W_2^2(\Gamma)} = \int_\Gamma (uv + u_x v_x + u_{xx} v_{xx}) d\Gamma.$$

Definition 7. Let the space $Q = \{u : u_i(x) \in C^\infty(\bar{e}_i), u|_\nu = 0, \nu \in \partial\Gamma\}$. $\overset{\circ}{W}_2^1(\Gamma)$ is a subspace of the space $W_2^1(\Gamma)$ that is the closure of Q with respect to the norm $\|u\|_{W_2^1(\Gamma)} = \sqrt{(u, u)_{W_2^1(\Gamma)}}$.

Definition 8. Let $L_2(G_\tau) = L_2(0, \tau; L_2(\Gamma))$.

$W_2^{1,\alpha}(G_\tau) = \{u : u(x, \cdot) \in W_2^1(\Gamma), u, u_x, \partial_{0,t}^\alpha u \in L_2(G_\tau)\}$ is a subspace of $L_2(G_\tau)$ with the scalar product

$$(u, v)_{W_2^{1,\alpha}(G_\tau)} = \int_0^\tau \int_\Gamma (uv + u_x v_x + \partial_{0,t}^\alpha u \partial_{0,t}^\alpha v) d\Gamma dt,$$

and with the norm

$$\|u\|_{W_2^{1,\alpha}(G_\tau)} = \left(\int_0^\tau \int_\Gamma (u^2 + u_x^2 + (\partial_{0,t}^\alpha u)^2) d\Gamma dt \right)^{\frac{1}{2}}.$$

$W_{2,0}^{1,\alpha}(G_\tau) = \{u \in W_2^{1,\alpha}(G_\tau) : u|_\nu = 0, \nu \in \partial\Gamma\}$ is a subset of $W_2^{1,\alpha}(G_\tau)$.

Definition 9. $W_2^{2,\alpha}(G_\tau)$ is the Hilbert space consisting of all elements of $L_2(G_\tau)$ that have generalized derivatives $\partial_{0,t}^\alpha u, u_x$ and u_{xx} from $L_2(G_\tau)$. The scalar product in it is defined by the equality

$$(u, v)_{W_2^{2,\alpha}(G_\tau)} = \int_0^\tau \int_\Gamma (uv + u_x v_x + \partial_{0,t}^\alpha u \partial_{0,t}^\alpha v + u_{xx} v_{xx}) d\Gamma dt$$

and the norm is denoted as follows: $\|\cdot\|_{W_2^{2,\alpha}(G_\tau)}$.

Definition 10. $W_{2,0}^{2,\alpha}(G_\tau)$ is a subspace of $W_2^{2,\alpha}(G_\tau)$, which is the intersection of $W_2^{2,\alpha}(G_\tau)$ with $W_{2,0}^{1,\alpha}(G_\tau)$.

Also, we need arithmetic inequality

$$|ab| \leq \frac{\varepsilon}{2} a^2 + \frac{1}{2\varepsilon} b^2, \text{ for all } \varepsilon > 0. \tag{1}$$

3. Problem setting

The main physical purpose for adopting and investigating fractional order diffusion equations to describe phenomena of anomalous diffusion usually met in transport processes through complex and/or disordered systems including fractal media [29]. Fractional diffusion equations appears in nano-sized systems due to the fact, that majority of such systems demonstrate anomalous flow through the branched nanotubes with memory and viscoelasticity effects [5, 6, 29].

In this paper, we consider the time fractional diffusion (subdiffusion) equation on the graph Γ . The correct formulation of the problem on the metric graph requires consideration of the flux (current) conservation rule on the branching points. For the subdiffusion equation

$$\partial_{0,t}^{\alpha_i} U_i(x, t) = U_{i,xx}(x, t) + \mathcal{F}_i(x, t), \quad i = \overline{1, n},$$

where $\partial_{0,t}^{\alpha_i}$ denotes the Caputo fractional derivative of order $\alpha_i \in (0, 1)$ defined by Definition 4, the flux is defined as follows

$$F[U_i(x, t)] = -\frac{\partial}{\partial x} (D_{0,t}^{1-\alpha_i} U_i(x, t)).$$

So, the vertex conditions should be defined as

$$\sum_{i=1}^n D_{0,t}^{1-\alpha_i} U_{i,x}(0, t) = 0, \quad U_i(0, t) = U_j(0, t), \quad i \neq j, \quad i, j = \overline{1, n}, \quad t \in (0, T]. \tag{2}$$

Condition (2) is disadvantageous due to the presence of a mixed derivative. To exclude of the mixed derivative in condition (2), we put $U_i = I_{0,t}^{1-\alpha_i} u_i(x)$ and obtain

$$\sum_{i=1}^n u_{i,x}(0, t) = 0, \quad I_{0,t}^{1-\alpha_i} u_i(0, t) = I_{0,t}^{1-\alpha_j} u_j(0, t), \quad i \neq j, \quad i, j = \overline{1, n}, \quad t \in (0, T], \tag{3}$$

where $I_{0,t}^{1-\alpha_i} u = (I_{0,t}^{1-\alpha_1} u_1, I_{0,t}^{1-\alpha_2} u_2, \dots, I_{0,t}^{1-\alpha_n} u_n)$. The vertex conditions (3) are more advantageous for our further consideration.

So, we investigate subdiffusion equation on each edge of the graph Γ

$$\partial_{0,t}^{\alpha_i} u_i(x, t) - u_{i,xx}(x, t) = f(t)g_i(x, t) + h_i(x, t), \quad x \in e_i, \quad t \in (0, T], \quad i = \overline{1, n}. \tag{4}$$

We need to establish the following initial conditions

$$u_i(x, 0) = 0, \quad x \in \bar{e}_i, \quad i = \overline{1, n}, \tag{5}$$

the vertex conditions (3) and the boundary conditions

$$u_i(l_i, t) = 0, \quad t \in (0, T], \tag{6}$$

where $g_i(x, t), h_i(x, t), i = \overline{1, n}$, are given functions, $f(t)$ is an unknown function.

The main aim is to find the pair of functions $\{u(x, t), f(t)\}$. To find the solution $f(t)$ to the inverse problem, an additional condition is needed. Therefore, we introduce an additional integral overdetermination condition in the form of

$$\int_\Gamma \eta(x) I_{0,t}^{1-\alpha} u(x, t) d\Gamma = \psi(t), \quad t \in [0, T], \tag{7}$$

where $\eta_i(x), i = \overline{1, n}$, and $\psi(t)$ are known functions.

Here we should mention, that by Mehandiratta et al. [30], the existence and uniqueness of the weak solution of the time-fractional diffusion equation on a metric star graph were investigated. This equation involved the same fractional orders of derivatives in each of the edges. The Cauchy problem for the subdiffusion equation with edge-dependent order of the Riemann-Liouville time-fractional derivatives on a metric star graph with semi-infinite bonds was studied in another work [31].

In the current work, the focus is on the strong solution for initial-boundary value problem in the star graph. The approach to solving this problem involves the method introduced by Ladyzhenskaya [32], which entails reducing the given problem to an operator equation and using a-priori estimates.

We represent the solution of the problem as $u(x, t) = v(x, t) + w(x, t)$, where v satisfies the following equation

$$\partial_{0,t}^{\alpha_i} v_i(x, t) - v_{i,xx}(x, t) = h_i(x, t)$$

with (3), (5), (6) conditions. This problem we call *the direct problem*. Also, we define *the inverse problem* looking for $f(t)$ in the following way

$$\partial_{0,t}^{\alpha_i} w_i(x, t) - w_{i,xx}(x, t) = f(t)g_i(x, t), \tag{8}$$

with (3), (5), (6) conditions and an additional condition given by

$$\int_{\Gamma} \eta(x) I_{0,t}^{1-\alpha} w(x, t) d\Gamma = E(t) = \psi(t) - \int_{\Gamma} \eta(x) I_{0,t}^{1-\alpha} v(x, t) d\Gamma, \quad t \in (0, T]. \tag{9}$$

4. Well-posedness of the direct problem

Theorem 3. Let $h(x, t) \in L_2(G_T)$ and $g(x, t) = 0$. Then the problem (3)–(6) has a unique strong solution in $W_{2,0}^{2,\alpha}(G_T)$.

Proof. According to [32], the direct problem can be represented as the problem of solving the operator equation $Av = h$. The domain of A is denoted as

$$D(A) = \left\{ v \in W_{2,0}^{2,\alpha}(G_T) : v_i|_{t=0} = 0, \sum_{i=1}^n v_{i,x}(0, t) = 0, \right. \\ \left. I_{0,t}^{1-\alpha_i} v_i(x, t) = I_{0,t}^{1-\alpha_j} v_j(x, t), i \neq j, i, j = \overline{1, n} \right\}$$

and the range $R(A) \subset L_2(G_T)$.

Proposition 1. Operator $A : D(A) \rightarrow L_2(G_T)$ is continuous.

Proof. Continuity of the operator A is a consequence of the following inequality

$$\|Av\|_{L_2(G_T)} = \|\partial_{0,t}^{\alpha} v - v_{xx}\|_{L_2(G_T)} \leq \|\partial_{0,t}^{\alpha} v\|_{L_2(G_T)} + \|v_{xx}\|_{L_2(G_T)} \leq \|v\|_{W_{2,0}^{2,\alpha}(G_T)}. \tag{10}$$

Further, we suppose that the space $R(A)$ is equipped with the norm of $L_2(G_T)$.

Proposition 2. The inverse operator $A^{-1} : R(A) \rightarrow W_{2,0}^{2,\alpha}(G_T)$ is well-defined and continuous.

Proof. We square Av and integrate over Γ :

$$\int_{\Gamma} (Av)^2 d\Gamma = \int_{\Gamma} (\partial_{0,t}^{\alpha} v - v_{xx})^2 d\Gamma = \int_{\Gamma} [(\partial_{0,t}^{\alpha} v)^2 + (v_{xx})^2] d\Gamma \\ - 2 \int_{\Gamma} \partial_{0,t}^{\alpha} v \cdot (v_{xx}) d\Gamma = \int_{\Gamma} [(\partial_{0,t}^{\alpha} v)^2 + (v_{xx})^2] d\Gamma \\ - 2 \sum_{i=1}^n \frac{\partial}{\partial t} I_{0,t}^{1-\alpha_i} v_i \cdot v_{i,x} \Big|_{x=0}^{x=l_i} + 2 \int_{\Gamma} v_x \partial_{0,t}^{\alpha} v_x d\Gamma.$$

The sum in the final line equals zero according to the vertex conditions (3) and boundary conditions (6). Integrating the last equality with respect to t and taking into account the inequality [33]

$$\int_{\Gamma} y \partial_{0,t}^{\alpha} y d\Gamma \geq \frac{1}{2} \int_{\Gamma} \partial_{0,t}^{\alpha} y^2 d\Gamma, \tag{11}$$

we obtain

$$\int_0^t \int_{\Gamma} (Av)^2 d\Gamma d\tau = \int_0^t \int_{\Gamma} [(\partial_{0,\tau}^{\alpha} v)^2 + (v_{xx})^2] d\Gamma d\tau + 2 \int_0^t \int_{\Gamma} v_x \partial_{0,\tau}^{\alpha} v_x d\Gamma d\tau \\ \geq \int_0^t \int_{\Gamma} [(\partial_{0,\tau}^{\alpha} v)^2 + (v_{xx})^2] d\Gamma d\tau + \int_0^t \int_{\Gamma} \partial_{0,\tau}^{\alpha} (v_x)^2 d\Gamma d\tau.$$

Then we obtain

$$\int_0^t \int_{\Gamma} [(\partial_{0,\tau}^{\alpha} v)^2 + (v_{xx})^2] d\Gamma d\tau + \int_{\Gamma} I_{0,t}^{1-\alpha} v_x^2 d\Gamma \leq \int_0^t \int_{\Gamma} (Av)^2 d\Gamma d\tau. \tag{12}$$

Now we estimate $\|v\|_{L_2(G_t)}$ and $\|v_x\|_{L_2(G_t)}$. By utilizing Proposition 2.1 in [34], we have $\|I_{0,t}^\alpha f\|_{L_p(0,T)} \leq \frac{T^\alpha}{\Gamma(\alpha+1)} \|f\|_{L_p(0,T)}$, for all $f \in L_p(0,T)$ and $\alpha > 0, 1 \leq p \leq \infty$. Using this inequality and the estimate (12), by the Definition 4. and Corollary 1. we obtain the following

$$\begin{aligned} \|v\|_{L_2(G_t)}^2 &= \sum_{i=1}^n \int_0^{l_i} \|I_{0,t}^{\alpha_i}(\partial_{0,t}^{\alpha_i} v_i)\|_{L_2(0,t)}^2 dx \\ &\leq \sum_{i=1}^n \left(\frac{t^{\alpha_i}}{\Gamma(\alpha_i+1)}\right)^2 \|\partial_{0,t}^{\alpha_i} v_i\|_{L_2(G_t)}^2 \leq C_1 \|\partial_{0,t}^\alpha v\|_{L_2(G_t)}^2 \leq \int_0^t \int_\Gamma (Av)^2 d\Gamma d\tau, \end{aligned} \tag{13}$$

where $C_1 = \max_{0 \leq i \leq n} \left\{ \left(\frac{T^{\alpha_i}}{\Gamma(\alpha_i+1)}\right)^2 \right\}$. For each edge of the graph, taking into account (12), we come to the following estimate

$$\begin{aligned} \int_0^t \int_0^{l_i} v_{i,x}^2(x, \tau) dx d\tau &= I_{0,t}^1 \int_0^{l_i} v_{i,x}^2(x, t) dx = I_{0,t}^{\alpha_i} \left(I_{0,t}^{1-\alpha_i} \int_0^{l_i} v_{i,x}^2 dx \right) \leq \\ &\leq I_{0,t}^{\alpha_i} 1 \cdot \operatorname{ess\,sup}_{0 \leq \tau \leq t} I_{0,\tau}^{1-\alpha_i} \int_0^{l_i} v_{i,x}^2 dx = \frac{t^{\alpha_i}}{\Gamma(\alpha_i+1)} \operatorname{ess\,sup}_{0 \leq \tau \leq t} \sum_{i=1}^n I_{0,\tau}^{1-\alpha_i} \int_0^{l_i} v_{i,x}^2 dx \leq \\ &\leq \frac{t^{\alpha_i}}{\Gamma(\alpha_i+1)} \operatorname{ess\,sup}_{0 \leq \tau \leq t} \int_0^\tau \int_\Gamma (Av(x, s))^2 d\Gamma ds = \frac{t^{\alpha_i}}{\Gamma(\alpha_i+1)} \int_0^t \int_\Gamma (Av(x, s))^2 d\Gamma ds. \end{aligned}$$

Summarizing the above estimate, we obtain

$$\int_0^t \int_\Gamma v_x^2 d\Gamma d\tau \leq C_2 \int_0^t \int_\Gamma (Av)^2 d\Gamma d\tau, \tag{14}$$

where $C_2 = \sum_{i=1}^n \frac{T^{\alpha_i}}{\Gamma(\alpha_i+1)}$.

Finally, from (12), (13), (14), we conclude that

$$\|v\|_{W_{2,0}^{2,\alpha}(G_t)} \leq C_3 \|Av\|_{L_2(G_t)}.$$

The last estimate shows that the inverse operator A^{-1} exists and is continuous.

From Proposition 1. and Proposition 2, we can conclude the following result.

Corollary 2. The range $R(A)$ of the operator A is a closed linear subspace of $L_2(G_T)$.

To demonstrate the solvability of the direct problem, we need to establish that the range $R(A)$ of the operator A in $L_2(G_T)$ does not have an orthogonal complement.

Lemma 1. If for some $\varphi \in L_2(G_T)$ it holds $(Av, \varphi) = 0$ for all $v \in D(A)$, then $\varphi = 0$.

Proof. We must show that if for all $v \in D(A)$ the following equality

$$\int_0^t \int_\Gamma (\partial_{0,\tau}^\alpha v - v_{xx}) \varphi d\Gamma d\tau = 0, \tag{15}$$

is satisfied then $\varphi = 0$.

Below, we construct a test function v .

Let $0 < t_1 < T, v(x, t) = 0$ for $0 < t \leq t_1$. We consider the following auxiliary problem:

$$v_{i,xx}(x, t) = \varphi_i(x, t), \quad x \in e_i, \quad t_1 < t < T, \quad v_{xx}|_{t=t_1} = 0, \quad x \in \bar{e}_i \quad i = \overline{1, n},$$

$$v_i(l_i, t) = 0, \quad \sum_{i=1}^n v_{i,x}(0, t) = 0, \quad I_{0,t}^{1-\alpha_i} v_i(0, t) = I_{0,t}^{1-\alpha_j} v_j(0, t), \quad i \neq j, \quad i, j = \overline{1, n}, \quad t_1 < t < T]. \tag{16}$$

The solution to this equation is in the following form

$$v_i(x, t) = \int_0^x (x - \xi) \tilde{\varphi}_i(x, t) d\xi + a_i x + b_i, \tag{17}$$

where $\tilde{\varphi}_i(x, t) = \int_{t_1}^t \varphi_i(x, \tau) d\tau$.

The unknown coefficients $a_i = a_i(t)$, $b_i = b_i(t)$ can be found using the boundary and vertex conditions in (16) as follows

$$\begin{cases} \int_0^{l_i} (l_i - \xi)\tilde{\varphi}(\xi, t)d\xi + a_i l_i + b_i = 0, \quad i = \overline{1, n}, \\ I_{0,t}^{1-\alpha_1} b_1 = I_{0,t}^{1-\alpha_2} b_2 = \dots = I_{0,t}^{1-\alpha_n} b_n, \\ \sum_{i=1}^n a_i = 0. \end{cases}$$

Without loss of generality, we take $\alpha_1 = \min_{1 \leq i \leq n} \{\alpha_i\}$. So, we obtain

$$\begin{cases} a_i = \zeta_i(t) - \frac{1}{l_i} b_i, \quad i = \overline{1, n}, \\ b_i = I_{0,t}^{\alpha_i - \alpha_1} b_1, \quad i = \overline{2, n}, \end{cases} \tag{18}$$

$$\sum_{i=1}^n \frac{1}{l_i} I^{\alpha_i - \alpha_1} b_1(t) = \tilde{\zeta}(t). \tag{19}$$

where $\zeta_i(t) = -\frac{1}{l_i} \int_0^{l_i} (l_i - \xi)\tilde{\varphi}(\xi, t)d\xi$, $\tilde{\zeta}(t) = \sum_{i=1}^n \zeta_i(t)$. The equation (19) is called the generalized Abel integral equation. Following the results of [35], we use the following notations to describe the solution of the generalized Abel integral equation (19). We put

$$w_\mu(t) = l_1 G_n^\mu \left(t; -\frac{l_1}{l_2}, \dots, -\frac{l_1}{l_n}; \alpha_1, \dots, \alpha_n \right),$$

where $\mu = \sum_{i=1}^n \mu_i$, $\mu_i > 0$,

$$G_n^\mu(t; \gamma_1, \dots, \gamma_n; \rho_1, \dots, \rho_n) = \int_0^{+\infty} e^{-\tau} S_n^\mu(t; \gamma_1 \tau, \dots, \gamma_n \tau; \rho_1, \dots, \rho_n) d\tau,$$

$$S_n^\mu(t; z_1, \dots, z_n; \rho_1, \dots, \rho_n) = (y_1 * y_2 * \dots * y_n)(t),$$

$$y_i = y_i(t) = t^{\mu_i - 1} \phi(\rho_i, \mu_i; z_i t^{\rho_i}).$$

By $f * g$, we denoted the Laplace convolution of functions defined by $(f * g)(t) = \int_0^t f(\tau)g(t - \tau)d\tau$.

The function $w_\mu(t)$ has the following properties.

Lemma 2. [35]

- (a) The function $w_\mu(t)$ is independent of the distribution of parameters μ_i but depends only on their sum μ .
- (b) The function $w_\mu(t)$ satisfies the following relations

$$w_\mu(t) = O(t^{\mu-1}) \text{ as } t \rightarrow 0, \quad D_{0,t}^\beta w_\mu(t) = w_{\mu-\beta}(t) \text{ for } \mu > \beta > 0.$$

According to [35], Theorem 6, the solution of equation (19) for $\tilde{\zeta}(t) \in L_1(0, T)$ is given by

$$b_1(t) = D_{0,t}^\mu (\tilde{\zeta}(t) * w_\mu)(t), \tag{20}$$

where $\mu > 0$. Substituting the found function $b_1(t)$ into (18) we obtain the values of the coefficients in (17). So, we find the solution of the auxiliary problem.

Also, we notice that as $\varphi \in L_2(G_T)$, it follows that $\zeta(t) \in H^1(t_1, T)$. According to general theory of integral equations, from (19), it follows that the solution $b_1(t)$ smoothness is such as the right-hand side of the equation $\zeta(t)$.

This way, we construct the test function. Now, from (15), we obtain

$$\begin{aligned} 0 &= \int_{t_1}^t \int_\Gamma (\partial_{0,\tau}^\alpha v - v_{xx}) v_{xx\tau} d\Gamma d\tau = \int_{t_1}^t \int_\Gamma \partial_{0,\tau}^\alpha v \cdot v_{xx\tau} d\Gamma d\tau - \int_{t_1}^t \int_\Gamma v_{xx} v_{xx\tau} d\Gamma d\tau \\ &= \int_{t_1}^t \sum_{i=1}^n \frac{\partial}{\partial \tau} I_{0,\tau}^{1-\alpha_i} v_i \cdot v_{i,x\tau} \Big|_{x=0}^{x=l_i} d\tau - \int_{t_1}^t \int_\Gamma \partial_{0,\tau}^\alpha v_x \cdot v_{x\tau} d\Gamma d\tau - \int_{t_1}^t \int_\Gamma \frac{1}{2} \frac{\partial}{\partial \tau} (v_{xx})^2 d\Gamma d\tau. \end{aligned}$$

Considering the vertex conditions (3) and boundary conditions (6) for the second integral in the last equation, it is evident that the sum equals zero. From the construction of $v(x, t)$, it follows that $v_{xx}(x, t_1) = 0$. Hence, we obtain

$$0 = \mathcal{I}_1 + \frac{1}{2} \int_\Gamma v_{xx}^2 \Big|_{\tau=t} d\Gamma, \tag{21}$$

where considering (11), and according to Theorem 1, Theorem 2, Corollary 1 and Definition 4, we can write as follows

$$\begin{aligned} \mathcal{I}_1 &= \int_{t_1}^t \int_{\Gamma} \partial_{0,\tau}^\alpha v_x \cdot v_{x\tau} d\Gamma d\tau = \int_{t_1}^t \int_{\Gamma} I_{0,\tau}^{1-\alpha} v_{x\tau} v_{x\tau} d\Gamma d\tau \\ &= \int_{t_1}^t \int_{\Gamma} I_{0,\tau}^{1-\alpha} v_{x\tau} \cdot \partial_{0,t}^{1-\alpha} (I_{0,\tau}^{1-\alpha} v_{x\tau}) d\Gamma d\tau \geq \frac{1}{2} \int_{t_1}^t \int_{\Gamma} \partial_{0,\tau}^{1-\alpha} (I_{0,\tau}^{1-\alpha} v_{x\tau})^2 d\Gamma d\tau \\ &= \frac{1}{2} \int_{\Gamma} \left(I_{0,t}^\alpha (I_{0,t}^{1-\alpha} v_{xt})^2 - I_{0,t_1}^\alpha (I_{0,t}^{1-\alpha} v_{xt})^2 \right) d\Gamma. \end{aligned}$$

Substitute the final estimate for \mathcal{I}_1 into equation (21) to obtain the following result

$$0 \geq \frac{1}{2} \int_{\Gamma} I_{t_1,t}^\alpha (I_{0,t}^{1-\alpha} v_{xt})^2 d\Gamma + \frac{1}{2} \int_{\Gamma} v_{xx}^2(x, t) d\Gamma.$$

We obtain from the last inequality that $v_{xx} = 0, I_{0,t}^{1-\alpha} v_{xt} = 0$ for $t_1 < t \leq T, x \in \Gamma$. Taking into consideration the construction of the function v , that t_1 is arbitrary number in $(0, T)$, we obtain $\varphi = v_{xxt} = 0$ in $L_2(G_T)$. The lemma is proven.

We can conclude from this that the direct problem has a unique solution in $W_{2,0}^{2,\alpha}(G_T)$.

5. Solvability of the inverse problem

Now, we show that the inverse problem has a solution. Let the following conditions be satisfied

$$\begin{aligned} (K1) \quad &g(x, t) \in L_\infty(0, T, L_2(\Gamma)), \\ &\eta(x) \in W_2^1(\Gamma), \eta(x) \text{ is continuous in } \Gamma, \eta|_\nu = 0, \nu \in \partial\Gamma, i = \overline{1, n}, \\ &\|\eta_x(x)\|_{L_2(\Gamma)} = m > 0, E(t) \in W_2^1(0, T), |g^*(t)| \geq q > 0, \end{aligned}$$

where

$$g^*(t) = \int_{\Gamma} \eta(x)g(x, t) d\Gamma, \quad t \in (0, T].$$

We multiply the both sides of equation (8) by the function $\eta(x)$ and integrate over Γ , we obtain

$$\int_{\Gamma} \eta(x) \partial_{0,t}^\alpha \omega(x, t) d\Gamma - \int_{\Gamma} \eta(x) \omega_{xx}(x, t) d\Gamma = f(t) \int_{\Gamma} g(x, t) \eta(x) d\Gamma.$$

Using conditions (3), (6), (7) and (K1), we obtain

$$\int_{\Gamma} \eta(x) \partial_{0,t}^\alpha \omega(x, t) d\Gamma + \int_{\Gamma} \eta_x(x) \omega_x(x, t) d\Gamma = f(t) g^*(t).$$

Taking into account (9), we can find $f(t)$ in such form

$$f(t) = (Bf)(t) + \frac{E_t(t)}{g^*(t)}, \tag{22}$$

where $E(t)$ is defined in (9) and

$$(Bf)(t) = \frac{1}{g^*(t)} \left\{ \int_{\Gamma} \eta_x(x) \omega_x(x, t) d\Gamma \right\}, \quad B : L_2(0, T) \rightarrow L_2(0, T).$$

The operator B can be considered as a result of combining two operators: $Bf = M(Kf)$, where $\omega = Kf := A^{-1}(fg)$, where operator A and the proof of existence of its inverse can be found in the previous section, and

$$(M\omega)(t) := \frac{1}{g^*(t)} \left\{ \int_{\Gamma} \eta_x(x) \omega_x(x, t) d\Gamma \right\}.$$

If the conditions known as (K1) are met, then we can substitute the overdetermination condition represented by equation (9) with equation (22). This substitution is equivalent and does not change the meaning or outcome of the conditions.

Theorem 4. *Let conditions (K1) hold. If $h(x, t) \in L_2(G_T)$, then the inverse problem (3)–(7) has a unique generalized solution $\{u, f\} \in W_{2,0}^{2,\alpha}(G_T) \times L_2(0, T)$.*

Proof. It is sufficient to demonstrate that the resolvent operator $(\mathcal{I} - B)^{-1}$ is bounded and continuous when mapping from $L_2(0, T)$ to $L_2(0, T)$, where \mathcal{I} is the identity operator. This then implies that f belongs to $L_2(0, T)$ and $h(x, t) + f(t)g(x, t) \in L_2(G_T)$. Consequently, according to Theorem 3., $u(x, t) \in W_{2,0}^{2,\alpha}(G_T)$.

First, we need to obtain some a-priory estimate. We multiply each of equations (8) by the corresponding $\partial_{0,t}^\alpha \omega(x, t)$ and integrate over G_t to get

$$\begin{aligned} & \int_0^t \int_\Gamma (\partial_{0,\tau}^\alpha \omega(x, \tau))^2 d\Gamma d\tau - \int_0^t \int_\Gamma \omega_{xx}(x, \tau) \partial_{0,\tau}^\alpha \omega(x, \tau) d\Gamma d\tau \\ & = \int_0^t f(\tau) d\tau \int_\Gamma g(x, \tau) \partial_{0,\tau}^\alpha \omega(x, \tau) d\Gamma. \end{aligned}$$

Integrating the second integral by parts, we obtain

$$\begin{aligned} & \int_0^t \int_\Gamma (\partial_{0,\tau}^\alpha \omega(x, \tau))^2 d\Gamma d\tau - \int_0^t \sum_{i=1}^n \left(\frac{\partial}{\partial \tau} I_{0,\tau}^{1-\alpha_i} \omega_i \right) \cdot (\omega_{i,x}) \Big|_{x=0}^{x=l_i} d\tau \\ & + \int_0^t \int_\Gamma \omega_x(x, \tau) \partial_{0,\tau}^\alpha \omega_x(x, \tau) d\Gamma d\tau = \int_0^t f(\tau) d\tau \int_\Gamma g(x, \tau) \partial_{0,\tau}^\alpha \omega(x, \tau) d\Gamma. \end{aligned}$$

Based on conditions (3) and (6), the sum in the last equation becomes zero. Considering the inequality (11) and inequality (1) with $\varepsilon = 1$ on the right hand side of the equation, we can express it as

$$\|\partial_{0,t}^\alpha \omega\|_{L_2(G_t)}^2 + \frac{1}{2} \sum_{i=1}^n I_{0,t}^{1-\alpha_i} \|\omega_x\|_{L_2(e_i)}^2 \leq \frac{1}{2} c^2 \int_0^t f^2(\tau) d\tau + \frac{1}{2} \|\partial_{0,t}^\alpha \omega\|_{L_2(G_t)}^2,$$

where $c = \text{ess sup}_{0 \leq t \leq T} \|g(\cdot, t)\|_{L_2(\Gamma)}$. Then we have

$$\|\partial_{0,t}^\alpha \omega\|_{L_2(G_t)}^2 + \sum_{i=1}^n I_{0,t}^{1-\alpha_i} \|\omega_x\|_{L_2(e_i)}^2 \leq c^2 \int_0^t f^2(\tau) d\tau.$$

From the last inequality, we obtain

$$\sum_{i=1}^n I_{0,t}^{1-\alpha_i} \|\omega_x\|_{L_2(e_i)}^2 \leq c^2 \int_0^t f^2(\tau) d\tau. \tag{23}$$

Taking into account conditions (K1), we have

$$\begin{aligned} \|(Bf)(\tau)\|_{L_2(0,t)}^2 & = \int_0^t |(Bf)(t)|^2 d\tau \leq \frac{m^2}{q^2} \int_0^t \|\omega_x\|_{L_2(\Gamma)}^2 d\tau \\ & = \frac{m^2}{q^2} \sum_{i=1}^n I_{0,t}^1 \|\omega_x\|_{L_2(e_i)}^2 = \frac{m^2}{q^2} \sum_{i=1}^n I_{0,t}^{\alpha_i} \left(I_{0,t}^{1-\alpha_i} \|\omega_x\|_{L_2(e_i)}^2 \right). \end{aligned} \tag{24}$$

If $f(t) \geq 0, t \in (0, T], \rho > \beta$, then the following estimate holds

$$\begin{aligned} I_{0,t}^\rho f(t) & = \frac{1}{\Gamma(\rho)} \int_0^t \frac{1}{(t-\tau)^{1-\rho}} f(\tau) d\tau = \frac{1}{\Gamma(\rho)} \int_0^t \frac{1}{(t-\tau)^{1-\beta}} f(\tau) (t-\tau)^{\rho-\beta} d\tau \\ & \leq \frac{\Gamma(\beta)}{\Gamma(\rho)} t^{\rho-\beta} I_{0,t}^\beta f(t) \leq \frac{\Gamma(\beta)}{\Gamma(\rho)} T^{\rho-\beta} I_{0,t}^\beta f(t). \end{aligned} \tag{25}$$

Accordingly, from (24) and (25), we obtain

$$\|(Bf)(t)\|_{L_2(0,t)}^2 \leq \frac{m^2}{q^2} \sum_{i=1}^n \frac{\Gamma(\alpha_{\min})}{\Gamma(\alpha_i)} T^{\alpha_i - \alpha_{\min}} I_{0,t}^{\alpha_{\min}} \left(I_{0,t}^{1-\alpha_i} \|\omega_x\|_{L_2(e_i)}^2 \right),$$

or

$$\|(Bf)(t)\|_{L_2(0,t)}^2 \leq C_1 I_{0,t}^{\alpha_{\min}} \left(\sum_{i=1}^n I_{0,t}^{1-\alpha_i} \|\omega_x\|_{L_2(e_i)}^2 \right), \tag{26}$$

where $\alpha_{\min} = \min\{\alpha_1, \alpha_2, \dots, \alpha_n\}, C_1 = \frac{m^2}{q^2} \cdot \max_{1 \leq i \leq n} \left\{ \frac{\Gamma(\alpha_{\min})}{\Gamma(\alpha_i)} T^{\alpha_i - \alpha_{\min}} \right\}$.

From (23) and (26), we come to

$$\|(Bf)(t)\|_{L_2(0,t)}^2 \leq C I_{0,t}^{\alpha_{\min}} \|f\|_{L_2(0,t)}^2, \tag{27}$$

where $C = c^2 \cdot C_1$. Now, iterating the inequality (27) k times we obtain

$$\|(B^k f)(t)\|_{L_2(0,t)}^2 \leq C I_{0,t}^{\alpha_{\min}} \|B^{k-1} f\|_{L_2(0,t)}^2 \leq C^k I_{0,t}^{k\alpha_{\min}} \|f\|_{L_2(0,t)}^2, \quad k = 1, 2, 3, \dots$$

From the last inequality, taking into account that the function $\tilde{f}(t) = \|f\|_{L_2(0,t)}^2$ is a nonnegative and non-decreasing function on $t \in [0, T]$, we have

$$\|(B^k f)(t)\|_{L_2(0,t)}^2 \leq C^k \|f\|_{L_2(0,t)}^2 \cdot I_{0,t}^{k\alpha_{\min}} 1 = \frac{C^k t^{k\alpha_{\min}}}{\Gamma(k\alpha_{\min} + 1)} \|f\|_{L_2(0,t)}^2.$$

Accordingly, we have

$$\|(\mathcal{I} - B)^{-1}f\|_{L_2(0,T)} \leq \sum_{k=0}^{+\infty} \frac{(\sqrt{CT^{\alpha_{\min}}})^k}{\sqrt{\Gamma(k\alpha_{\min} + 1)}} \|f\|_{L_2(0,t)}.$$

So, it follows that the resolvent operator $(\mathcal{I} - B)^{-1} : L_2(0, T) \rightarrow L_2(0, T)$ is bounded and continuous mapping and

$$f(t) = (\mathcal{I} - B)^{-1} \begin{bmatrix} E_t(t) \\ g^*(t) \end{bmatrix}.$$

6. Conclusion

In our research, we concentrated on investigating the direct and inverse source problems related to the subdiffusion equation on a metric graph with an edge-dependent order of time-fractional derivative. We achieved this by transforming the problem into the task of solving an operator equation. We were able to prove the existence and uniqueness of a generalized solution in the direct problem. Additionally, we showed that the resolvent operator is appropriately defined in the inverse source problem, as evidenced by the overdetermination condition. We are particularly excited about the potential applications of our research in modeling subdiffusion processes in branched nanostructures. The subdiffusion equation on a metric graph with an edge-dependent order of the time-fractional derivative provides a robust mathematical framework for simulating and understanding subdiffusion phenomena in these complex nanostructures.

References

- [1] Kottos T., Smilansky U. Periodic orbit theory and spectral statistics for quantum graphs. *Ann. Phys.*, 1999, **274**, P. 76–124.
- [2] Gnuzmann S., Smilansky U. Quantum graphs: Applications to quantum chaos and universal spectral statistics. *Adv. Phys.*, 2006, **55**, P. 527–625.
- [3] Exner P., Post O. Approximation of quantum graph vertex couplings by scaled Schrödinger operators on thin branched manifolds. *J. Phys. A: Math. Theor.*, 2009, **42**, P. 415305.
- [4] Kurasov P., Suhr R. Schrödinger operators on graphs and geometry. III. General vertex conditions and counterexamples. *J. Math. Phys.*, 2018, **59**, P. 102104.
- [5] Chivilikhin S.A., Gusarov V.V., Popov I.Y. Charge pumping in nanotube filled with electrolyte. *Chinese Journal of Physics*, 2018, **56**(5), P. 2531–2537.
- [6] Smolkina M.O., Popov I.Y., Blinova I.V., Milakis E. On the metric graph model for flows in tubular nanostructures. *Nanosystems: Physics, Chemistry, Mathematics*, 2019, **10** (1), P. 6–11.
- [7] Yusupov J.R., Sabirov K. K., Ehrhardt M., Matrasulov D.U. Transparent nonlinear networks. *Physical Review E*, 2019, **100** (3), P. 1–6.
- [8] Yusupov J.R., Sabirov K.K., Asadov Q.U., Ehrhardt M. and Matrasulov D.U. Dirac Particles in Transparent Quantum Graphs: Tunable transport of relativistic quasiparticles in branched structures. *Physical Review E*, 2020, **101** (6), P. 1–7.
- [9] Lavrukhina A.A., Popov A.I., Popov I.Y. On transparent vertex boundary conditions for quantum graphs. *Indian Journal of Physics*, 2023, **97**(7), P. 2095-2102.
- [10] Sobirov Z.A., Akhmedov M.I., Karpova O.V., Jabbarova B. Linearized KdV equation on a metric graph. *Nanosystems: Physics, Chemistry, Mathematics*, 2015, **6**, P. 757–761.
- [11] Sobirov Z.A., Khujakulov J.R., Turemuratova A.A. Unique solvability of IBVP for pseudo-subdiffusion equation with Hilfer fractional derivative on a metric graph. *Chelyabinsk Physical and Mathematical Journal*, 2023, **8**(3), P. 351–370.
- [12] Nikiforov D.S., Blinova I.V., Popov I.Y. Schrödinger and Dirac dynamics on time-dependent quantum graph. *Indian Journal of Physics*, 2018, **93**(7), P. 913–920.
- [13] Sobirov Z.A., Eshimbetov M.R. *Fokas method for the heat equation on metric graphs*. *Journal of Mathematical Sciences*, 2024, **278**(4), P. 1-16.
- [14] Sobirov Z.A., Rakhimov K.U., Ergashov R.E. Green's function method for time-fractional diffusion equation on the star graph with equal bonds. *Nanosystems: physics, chemistry, mathematics*, 2021, **12**(3), P. 271–278.
- [15] Kurasov P. On magnetic boundary control for metric graphs. *Acta Physica Polonica Series A*, 2023, **144**(6), P. 456–461.
- [16] Luchko Y. Initial-boundary-value problems for the one-dimensional time-fractional diffusion equation. *Fractional Calculus and Applied Analysis*, 2012, **15**(1), P. 141-160.
- [17] Metzler R., Klafter J. The random walk's guide to anomalous diffusion: A fractional dynamics approach. *Physics Reports*, 2000, **339** (1).
- [18] Sakamoto K., Yamamoto M. Initial value/boundary value problems for fractional diffusion-wave equations and applications to some inverse problems. *Journal of Mathematical Analysis and Applications*, 2011, **382**, P. 426–447.
- [19] Kubica A., Yamamoto M. Initial-boundary Value Problems for Fractional Diffusion Equations with Time-Dependent Coefficients. *Fractional Calculus and Applied Analysis*, 2017, **21**(2).
- [20] Gorenflo R., Luchko Y., Yamamoto M. Time-fractional diffusion equation in the fractional Sobolev spaces. *Fract. Calc. Appl. Anal.*, 2015, **18**, P. 799–820.
- [21] Kubica A., Ryszewska K., Yamamoto M. *Time-Fractional Differential Equations: A Theoretical Introduction*. Springer, Singapore, 2020.
- [22] Alimov Sh., Ashurov R. Inverse problem of determining an order of the Caputo time-fractional derivative for a subdiffusion equation. *Journal of Inverse and Ill-posed Problems*, 2020, **28**, P. 651–658.
- [23] Ashurov R., Umarov S. An inverse problem of determining orders of systems of fractional pseudo-differential equations. *Fractional Calculus and Applied Analysis*, 2022, **25**, P. 109–127.
- [24] Kamynin V.L. On the inverse problem of determining the right-hand side of a parabolic equation under an integral overdetermination condition. *Mathematical Notes*, 2005, **77**, (4), P. 482–493.
- [25] Kamynin V.L. On the solvability of the inverse problem for determining the right-hand side of a degenerate parabolic equation with integral observation. *Mathematical Notes*, 2015, **98**(5), P. 765–777.
- [26] Sobirov Z.A., Turemuratova A.A. Inverse source problem for the heat equation on a metric star graph with integral over-determination condition. *Bulletin of National University of Uzbekistan Mathematics and Natural Sciences*, 2023, **6**(1), P. 1-15.
- [27] Kilbas A.A., Srivastava H.M., Trujillo J.J. *Theory and Applications of Fractional Differential Equations*. North-Holland Mathematics Studies, 2006, **204**, Amsterdam, etc., Elsevier.

- [28] Berkolaiko G., Kuchment P. Introduction to Quantum Graphs. Mathematical surveys and monographs. AMS, 2013, **186**.
- [29] Mainardi F., Mura A., Pagnini G., Gorenflo R. Sub-diffusion equations of fractional order and their fundamental solutions. *Mathematical Methods in Engineering*. Springer, Dordrecht. 2007.
- [30] Mehandiratta V., Mehra M., Leugering G. Existence and uniqueness of time-fractional diffusion equation on a metric star graph. *Communications in Computer and Information Science book series*, 2021, **1345**, P. 25-41.
- [31] Sobirov Z.A. Cauchy problem for subdiffusion equation on metric star graph with edge dependent order of time-fractional derivative. *Lobachevskii Journal of Mathematics*, 2023, **43**(11), P. 3282–3291.
- [32] Ladyzhenskaya O.A. Boundary Problems of Mathematical Physics. Nauka, Moscow, 1973.
- [33] Alikhanov A.A. A priori estimate for solutions of boundary value problems for fractional-order equations. *Differential Equations*, 2010, **46**(5), P. 660–666.
- [34] Mehandiratta V., Mehra M., Leugering G. Distributed optimal control problems driven by space-time fractional parabolic equations. *Control and Cybernetics*, 2022, **51**(2), P. 191–226.
- [35] Pskhu A.V. On solution representation of generalized Abel integral equation. *J.Math.*, 2013, ID 106251, P. 1–5.

Submitted 8 August 2024; revised 22 September 2024; accepted 23 September 2024

Information about the authors:

Zarifboy A. Sobirov – National University of Uzbekistan, Universitet str., 4, 100174, Tashkent, Uzbekistan; V.I. Romanovskiy Institute of Mathematics, Uzbekistan Academy of Science, 100174, Tashkent, Uzbekistan; ORCID 0000-0002-6019-907X; z.sobirov@nuu.uz

Ariukhan A. Turemuratova – National University of Uzbekistan, Universitet str., 4, 100174, Tashkent, Uzbekistan; Branch of Russian Economic University named after G. V. Plekhanov in Tashkent, 100164, Tashkent, Uzbekistan; ORCID 0009-0003-5428-3958; ariuxanturemuratova@gmail.com

Conflict of interest: the authors declare no conflict of interest.

Skyrmionium – semicircular magnetic defect interaction on a racetrack

S. Navarro-Vilca^{1,a}, S. Urcia-Romero^{2,b}, H. Vigo-Cotrina^{3,c}

¹Universidad Nacional Jorge Basadre Grohmann, Tacna, Perú

²University of Puerto Rico, Mayaguez Campus, Puerto Rico, USA

³Universidad Privada del Norte, Trujillo, Perú

^asrnavarro@unjbg.edu.pe, ^bsilvana.urcia@upr.edu, ^chelmunt.vigo@upn.edu.pe

Corresponding author: H. Vigo-Cotrina, helmunt.vigo@upn.edu.pe

ABSTRACT Different types of skyrmionics magnetic configurations can be created and manipulated on different types of nanostructures. In this research, we use micromagnetic simulations to study the dynamics of a skyrmionium on a racetrack in the presence of a semicircular magnetic defect. We considered a defect with physical parameters different from those of the racetrack itself. Our results show that, depending on the size of the defect, the width of the racetrack, and the intensity of the spin current density, it is possible to manipulate the trajectory of a skyrmionium. Also, we obtain the interaction energies between the skyrmionium and the magnetic defect and derive phase diagrams showing the different dynamic states that can be obtained during the movement of the skyrmionium.

KEYWORDS skyrmionium, micromagnetic simulation, target skyrmion

FOR CITATION Navarro-Vilca S., Urcia-Romero S., Vigo-Cotrina H. Skyrmionium – semicircular magnetic defect interaction on a racetrack. *Nanosystems: Phys. Chem. Math.*, 2024, **15** (5), 597–620.

1. Introduction

Skyrmions are considered exotic magnetic configurations characterized by a topological charge $Q = \pm 1$ [1–5]. They can be created in different types of nanostructures [6–9]. Skyrmions have a central region (skyrmion core) where the magnetization can point along the $+z$ axis ($Q = +1$) or along the $-z$ -axis ($Q = -1$) [2, 8, 10–12].

Due to their topological charge, skyrmions are affected by the skyrmion Hall effect (SkHE) when they are moving along the length of a racetrack, which causes the skyrmion not to maintain its original path and to be annihilated at the edges of the racetrack.

Another possible problem for potential applications is the presence of defects and/or impurities within the nanostructure due to inherent manufacturing processes. Therefore, some investigations show how a skyrmion interacts in the presence of a magnetic defect [8, 13–18]. Combining a skyrmion with $Q = +1$ and a skyrmion with $Q = -1$ gives the magnetic configuration of a 2π skyrmion with topological charge $Q = 0$ [3, 8, 19]. This configuration, also known as target skyrmion [20] or skyrmionium is not affected by the SkHE, which allows the skyrmionium to move in a straight line without suffering any deviation, thus avoiding the possibility of being destroyed at the edges of a racetrack [3, 8, 19].

Skyrmioniums can be created in nanostructures using external agents, such as spin-polarized currents [3, 8, 21, 22] or magnetic fields [20, 23–25]. These external agents can also induce skyrmionium movement, as shown in various works [3, 4, 19, 21, 22, 26]. It is also possible to move a skyrmionium using an anisotropy gradient [27]. The translational speed of a skyrmionium can be much higher than that of a skyrmion, making it more desirable for potential applications in the field of spintronics [3, 19, 25].

Skyrmioniums can collapse into a skyrmion due to random thermal fluctuations following a core annihilation process as shown by Jiang et al. [28]. Furthermore, other more complex magnetic configurations, such as the heliknoton, may also be sensitive to thermal fluctuations and collapse [29]. Such transitions are of importance and still open for future research.

In our previous work [30], we studied the dynamics of a skyrmionium on a racetrack in the presence of a magnetic defect with its physical parameter $D_{\text{int}}^{\text{def}}$. However, in an actual situation, the defect may have other physical parameters different from those of the racetrack, such as exchange constant ($A_{\text{ex}}^{\text{def}}$), saturation magnetization (M_s^{def}), and perpendicular uniaxial anisotropy constant (K_z^{def}). As has been shown by Can Önel et al. [21], even the racetrack's width can influence the skyrmionium's dynamics. In that sense, we expanded our recently published work, considering that the magnetic defect can have different physical parameters with respect to the racetrack. Lastly, we studied the influence of defect size and racetrack width on the skyrmionium dynamics.

2. Method

All simulations were carried out using the open-source program MuMax3, which numerically solves the Landau–Lifshitz–Gilbert (LLG) equation [31]:

$$\dot{m} = -\gamma_e m \times B_{\text{eff}} + \alpha m \times \dot{m} + \gamma_e \epsilon \beta [(m \times s) \times m],$$

where m is the reduced magnetization, B_{eff} is the effective field, $\gamma_e = 1.76 \times 10^{11} \text{ T}^{-1} \text{ s}^{-1}$ is the electron gyromagnetic ratio, the last term of the equation is related to the torque exerted by the current on magnetization. The constants are detailed and defined in references [3, 16].

We simulated a ferromagnetic cobalt racetrack with a width of $W = 512, 256, \text{ and } 128 \text{ nm}$, and a thickness of 1 nm coupled to a heavy metal material (HM) (see Fig. 1). The racetrack was discretized into $2 \times 2 \times 1 \text{ nm}^3$ cells, using the following typical parameters for cobalt [3, 8, 13]: saturation magnetization $M_s = 580 \text{ kA/m}$, exchange constant $A_{\text{ex}} = 15 \text{ pJ/m}$, DMI constant $D_{\text{int}} = 3.4 \text{ mJ/m}^2$, perpendicular uniaxial anisotropy constant $K_z = 0.8 \text{ MJ/m}^3$ and damping constant $\alpha = 0.3$.

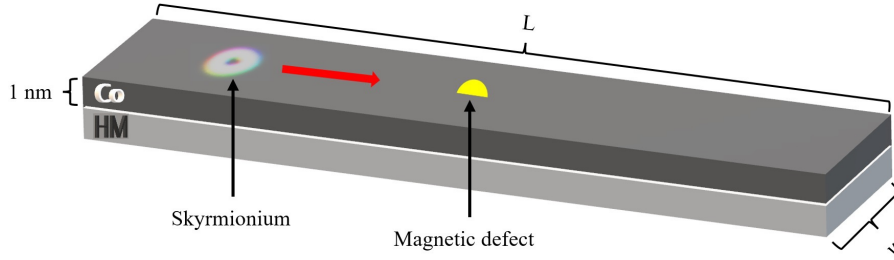


FIG. 1. Schematic representation of the cobalt racetrack coupled to a heavy metal material. The red arrow indicates the direction of movement of the skyrmionium

For these values, the racetrack supports three magnetic configurations: a perpendicular domain, a skyrmion, or a skyrmionium. The perpendicular domain state is the ground state. However, a skyrmionium can be created in the racetrack using any of the methods used in the literature [3, 8, 20–23, 25]. The inner and outer diameters have values of approximately 8 and 75 nm, respectively. The widths of the inner and outer domain walls have values of approximately 6 and 12 nm. Both the values of the diameters and the widths of the domain walls remain approximately constant for all widths W .

A semicircular magnetic defect was located in the center of the racetrack. We considered defects with diameters $\rho = 20, 30, \text{ and } 40 \text{ nm}$ and the following physical values: DMI constant $D_{\text{int}}^{\text{def}}$ varying between 3.0 and 3.8 mJ/m^2 in increments of 0.1 mJ/m^2 , saturation magnetization M_s^{def} varying between 540 and 620 kA/m in increments of 10 kA/m , exchange constant $A_{\text{ex}}^{\text{def}}$ varying between 11 and 19 pJ/m with increments of 1 pJ/m , and uniaxial anisotropy constant K_z^{def} varying between 0.4 and 1.2 MJ/m^3 in increments of 0.1 MJ/m^3 .

3. Results and discussions

The interaction energy $E_{\text{int}}(x)$, where x is the position of the defect along the length of the racetrack between the magnetic defect and the skyrmionium, was calculated using the expression [16]:

$$E_{\text{int}}(x) = E(x) - E(x \rightarrow \infty). \quad (1)$$

Figure 2 shows the interaction energy values for different physical parameters of the defect with a diameter of $\rho = 40 \text{ nm}$ and width of $W = 512 \text{ nm}$. The figure shows that the interaction energy is repulsive (see Fig. 2(a) and Fig. 2(g)) when the values of the physical parameters $D_{\text{int}}^{\text{def}}$ and M_s^{def} of the defect are less than the values of D_{int} and M_s of the racetrack and attractive (see Fig. 2(b) and Fig. 2(h)) when these parameters are greater than those of the racetrack. On the other hand, the interaction energy is attractive (see Fig. 2(c) and Fig. 2(e)) when the physical parameters $A_{\text{ex}}^{\text{def}}$ and K_z^{def} are lower than the values of A_{ex} and K_z of the racetrack and repulsive (see Fig. 2(d) and Fig. 2(f)) when they are larger than those of the racetrack. The same behavior is observed for all defect diameters and widths W considered in this work (see Figs. A1–A9 in Appendix). Also these figures show that the absolute value of the interaction energy decreases with decreasing defect size and increases with increasing diameter. Defects with minimal diameters will have a negligible effect on the dynamics of the skyrmionium.

In some cases, small oscillations in the interaction energy values are observed near the position $x = 0$. These oscillations may occur due to the defect having an asymmetric shape. Additionally, when a skyrmionium comes into contact with the defect (with its own specific physical parameters) it can deform, causing oscillations.

Interestingly, for all M_s^{def} values used in this research, the interaction energy is an order of magnitude lower than for the other cases. This fact suggests that modifying this parameter will have a negligible effect on the dynamics of the skyrmionium, which will be evidenced in the next section.

In Appendix, we have added figures (Fig. A20–A22) showing the interaction energy for the case of a skyrmion, using $W = 512$ nm. These figures show that the same physical principles that apply for the skyrmionium also apply to the skyrmion, i.e., the same repulsive and attractive potentials appear for the same physical parameters of the defect. On the other hand, we can see that the intensity of the interaction energy, in some cases, is almost the same.

Next, to study the dynamics of the skyrmionium in the presence of the magnetic defect, a skyrmionium is created to the left of the defect (see Fig. 1). The movement of the skyrmionium is induced via the Spin Orbit Torque effect (SOT). That is, a current density flowing in the HM material along the x -axis generates a current density in the racetrack with spin polarization in the $-y$ direction. We consider J values between 1 and 9 MA/cm² in increments of 0.5 MA/cm².

3.1. Magnetic defect with different $D_{\text{int}}^{\text{def}}$

Figure 3 shows phase diagrams with three possible states: (i) the skirting state, in which the skyrmionium manages to avoid the defect by skirting it (see Fig. A13 in Appendix); (ii) the passing state, where the skyrmionium crosses the defect while maintaining approximately its original trajectory (see Fig. A14 in Appendix); and (iii) the pinning state, trapping the skyrmionium inside the defect (see Fig. A15 in Appendix). The maximum deviation in the passing state, obtained for the parameters used in this work, was less than 10 nm below its original trajectory, which is negligible compared to the size of the racetrack.

When $D_{\text{int}}^{\text{def}} < D_{\text{int}}$, there are two possible states: skirting and passing. The number of skirting states increases with increasing defect diameter size. The maximum number of skirting states for each diameter occurs when the difference between D_{int} and $D_{\text{int}}^{\text{def}}$ is largest ($D_{\text{int}}^{\text{def}} = 3$ mJ/m²). When $D_{\text{int}}^{\text{def}} = 3$ mJ/m², the minimum value of the current density J_{min} is necessary to overcome the repulsion by the defect is 2.5 MA/cm² for a diameter of 20 nm. When the diameter size increases to 30 and 40 nm, the value of J_{min} also increases to 4 and 5.5 MA/cm², respectively. This behavior is explained by the repulsive interaction energy becomes more intense with increasing defect diameter (see Figs. A1–A3 in Appendix); therefore, a higher value of current J is needed to overcome the interaction.

When the value of $D_{\text{int}}^{\text{def}}$ is reduced to 3.3 mJ/m², the repulsive interaction energy becomes smaller; therefore, the value of J_{min} necessary to overcome it also decreases. In our case, the skyrmionium crosses the magnetic defect for all current density values considered in this work for $\rho = 20$ and 30 nm. For $\rho = 40$ nm, there is a J_{min} value of 1.5 MA/cm².

When $D_{\text{int}}^{\text{def}} > D_{\text{int}}$, there are two possible states: passing and pinning. In this case, the interaction energy is attractive; therefore, the defect tends to attract the skyrmionium towards it, thus acting as a trap. This energy becomes higher with the defect's increasing diameter. Therefore, the current values necessary to counteract the pinning effect must also increase. For example, when $D_{\text{int}}^{\text{def}} = 3.8$ mJ/m², J_{min} has a value of 3 MA/cm² when $\rho = 20$ nm, while it has a value of 3.5 MA/cm² when $\rho = 40$ nm.

3.2. Magnetic defect with different $A_{\text{ex}}^{\text{def}}$

Figure 3 also shows two new states in addition to the three states mentioned above. We dub the two new states TA and TB. In TA (see Fig. A16 in Appendix), the skyrmionium collapses into the defect, transforming into a skyrmion and becoming trapped within the defect. The TB state (see Fig. A17 in Appendix) is similar to the TA state, with the difference that the created skyrmion continues to advance deviating towards the edges of the racetrack due to the SkHE effect. The transformation from skyrmionium to skyrmion is also possible because the racetrack parameters allow the existence of a skyrmion, as mentioned above.

For $\rho = 20$ nm, $A_{\text{ex}}^{\text{def}} = 11$ pJ/m, and $J < 3.5$ MA/cm², the skyrmionium will be trapped due to the robust and attractive interaction of the defect and the low influence of the drag force produced by the current. As the current increases ($J \geq 3.5$ MA/cm²), the driving force on the skyrmionium also increases, causing it to collapse and become a skyrmion. Furthermore, due to the balance between the defect's driving force and attractive force, the skyrmion will be trapped inside the defect (TA state). This behavior can be seen in Fig. 3. For values of $A_{\text{ex}}^{\text{def}} > 11$ and < 14 pJ/m, the dynamic states of the skyrmionium are similar to $A_{\text{ex}}^{\text{def}} = 11$ pJ/m, but depending on the value of J , the skyrmion will manage to overcome the well of the attractive potential, crossing the defect (TB state). The movement of the skyrmion is affected by the (SKHE) ($\theta_{sk} \sim 63.43^\circ$), causing it to move near the edges of the racetrack, as shown in Fig. A17 in Appendix. When the diameter of the defect increases, the attractive interaction becomes more intense; therefore, the number of pinning states also increases (see Fig. 3).

For values of $A_{\text{ex}}^{\text{def}} > 15$ pJ/m, depending on the competition between the force exerted by the current and the repulsive force exerted by the defect, the skyrmionium will avoid the defect by passing around it or will pass through it. When the diameter of the defect increases, the repulsive interaction energy also increases, favoring the appearance of skirting states (see Fig. 3)

For a value of $A_{\text{ex}}^{\text{def}} = 17$ pJ/m, a minimum value of $J = 2.5$ MA/cm² is necessary for the skyrmionium to overcome the repulsion generated by the defect when the diameter of the defect is 20 nm. When the diameter increases to 40 nm, the value of J also increases to 4 MA/cm².

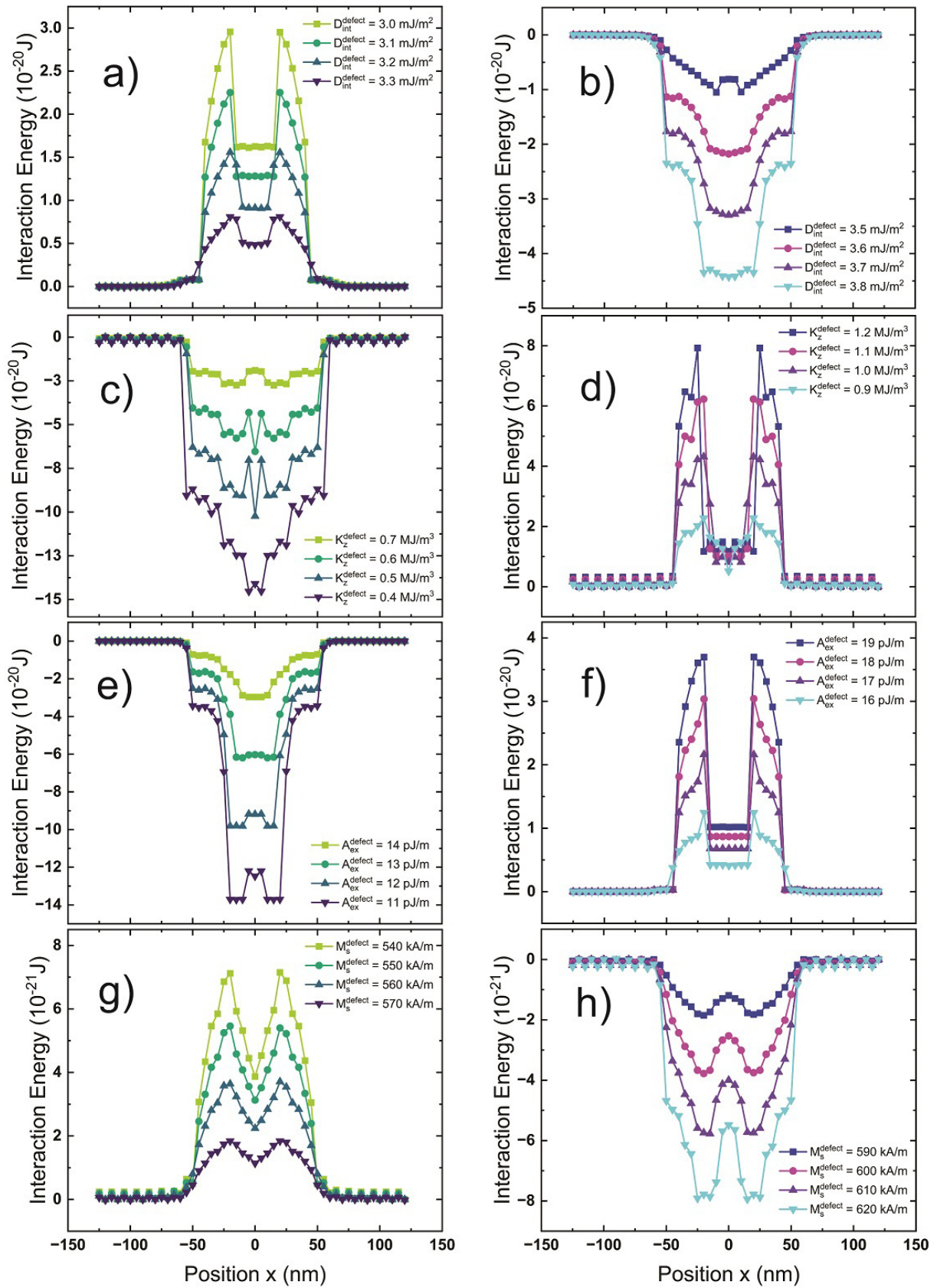


FIG. 2. Interaction energy between the skyrmionium and the defect ($\rho = 40$ nm) obtained by micro-magnetic simulation using eq. (1) considering different parameters with a width of $W = 512$ nm

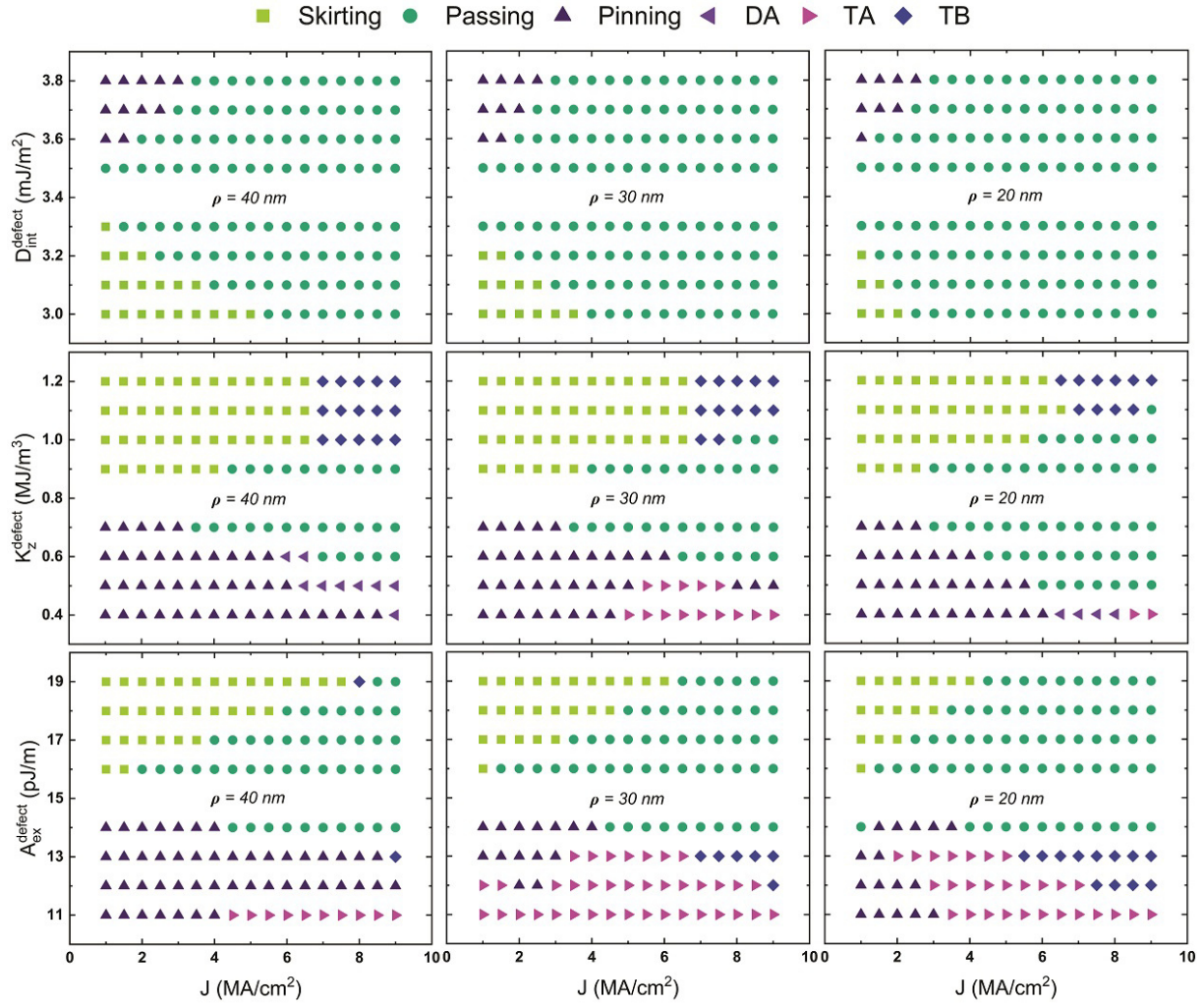


FIG. 3. The phase diagrams of possible states for the skyrmionium dynamics in the presence of a magnetic defect depict a wide range of physical parameters and diameters, offering a comprehensive view of the system's behavior for a width $W = 512$ nm

3.3. Magnetic defect with different K_z^{def}

In this case, a new state we dub as DA (see Fig. A18 in Appendix) appears where the skyrmionium is trapped by the defect; however, due to the current's effect, it deforms, increasing its size along the racetrack.

The interaction is attractive for values of $K_z^{\text{def}} < K_z$, promoting the pinning states until the current can overcome the attraction. For example, when $\rho = 20$ nm and $K_z^{\text{def}} = 0.7$ MJ/m³, the skyrmionium crosses the defect (passing state) from a minimum value $J_{\text{min}} = 3$ MA/cm². However, when the value of ρ increases to 40 nm, the value of J_{min} also increases to 3.5 MA/cm². This effect is even more pronounced for a value of $\rho = 20$ nm and $K_z^{\text{def}} = 0.6$ MJ/m³. The skyrmionium crosses the defect (passing state) from a minimum value of $J_{\text{min}} = 4.5$ MA/cm², but for $\rho = 40$ nm, J_{min} increases to 7 MA/cm².

For values of $K_z^{\text{def}} > K_z$, the interaction between the defect and the skyrmionium becomes repulsive, favoring the appearance of skirting and passing states depending on the value of the current density. In some cases, depending on the competition between the repulsive interaction and the driving force exerted by the current, there are states where the skyrmionium collapses to a skyrmion but continues to move along the racetrack.

3.4. Magnetic defect with different M_s^{def}

Figure A12 in Appendix shows the phase diagrams M_s^{def} vs. J , where we can notice that the passing states are predominant. For $\rho = 40$ nm, there are two different states, skirting and pinning, both for small current densities and where the interaction force with the defect is maximum. The absence of other dynamical states can be attributed to the low influence of this magnetic parameter on the skyrmionium-defect interaction (Fig. 2 (g–h)). The interaction energy corresponding to M_s^{def} is an order of magnitude lower than the interaction energies of the other physical parameters of the defect.

Finally, in Fig. 4, we show how a sequence of magnetic defects can be used to modify the trajectory of the skyrmionium throughout its movement.



FIG. 4. Diagram of the trajectory followed by a skyrmionium along the racetrack in the presence of a sequence of magnetic defects (yellow semicircles)

4. Conclusions

We have shown how modifying the magnetic properties of a defect makes it possible to manipulate a skyrmionium along a racetrack. We calculated the interaction energies between the skyrmionium and the defect, considering different physical parameters of the defect and obtaining attractive and repulsive potentials depending on the physical parameters of the defect. Furthermore, we studied how these magnetic defects influence the dynamics of the skyrmionium. The magnetic defects that produce attractive potentials can be used as pinning centers to stop the movement of the skyrmionium. In contrast, magnetic defects with repulsive potentials can be used as skyrmionium dispersal centers. Our work may be of interest in using magnetic defects to modify the trajectory of a skyrmionium, which could find applications in creating logic gates in potential applications in the area of spintronics.

A. Appendix

A.1. Skyrmionium-magnetic defect interaction energy

Interaction energies were obtained using eq. (1) as given in the main article. Each term of the equation was obtained using the MuMax [31] built-in function relax, which calculates the system ground state. The origin of the coordinates is located in the center of the racetrack.

A.1.1. Skyrmionium–semicircular magnetic defect interaction energy with a width of $W = 512$ nm.

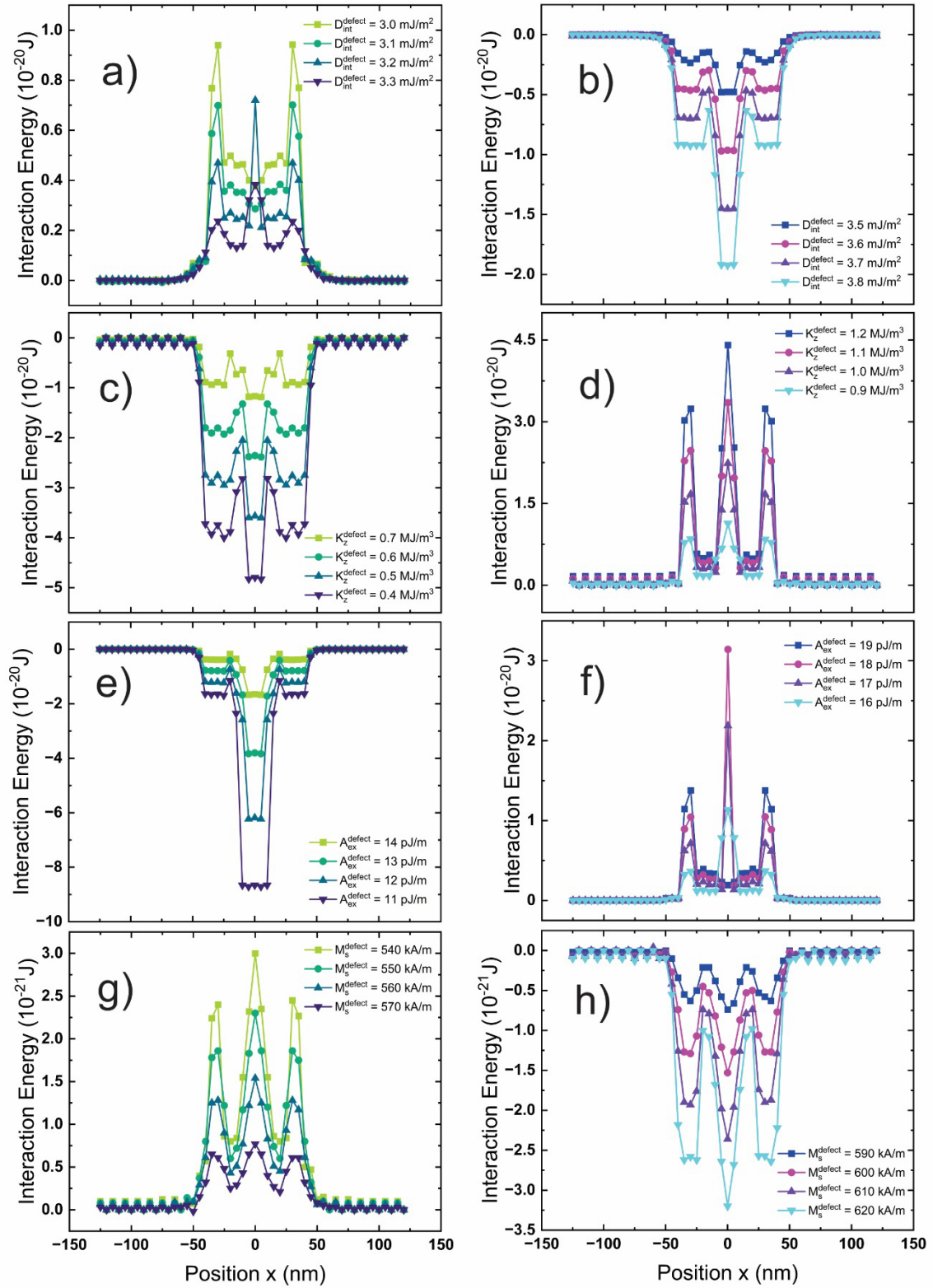


FIG. A1. Interaction energy between the skyrmionium and the defect ($\rho = 20$ nm) obtained by micro-magnetic simulation using eq. (1) considering different defect parameters with a width of $W = 512$ nm

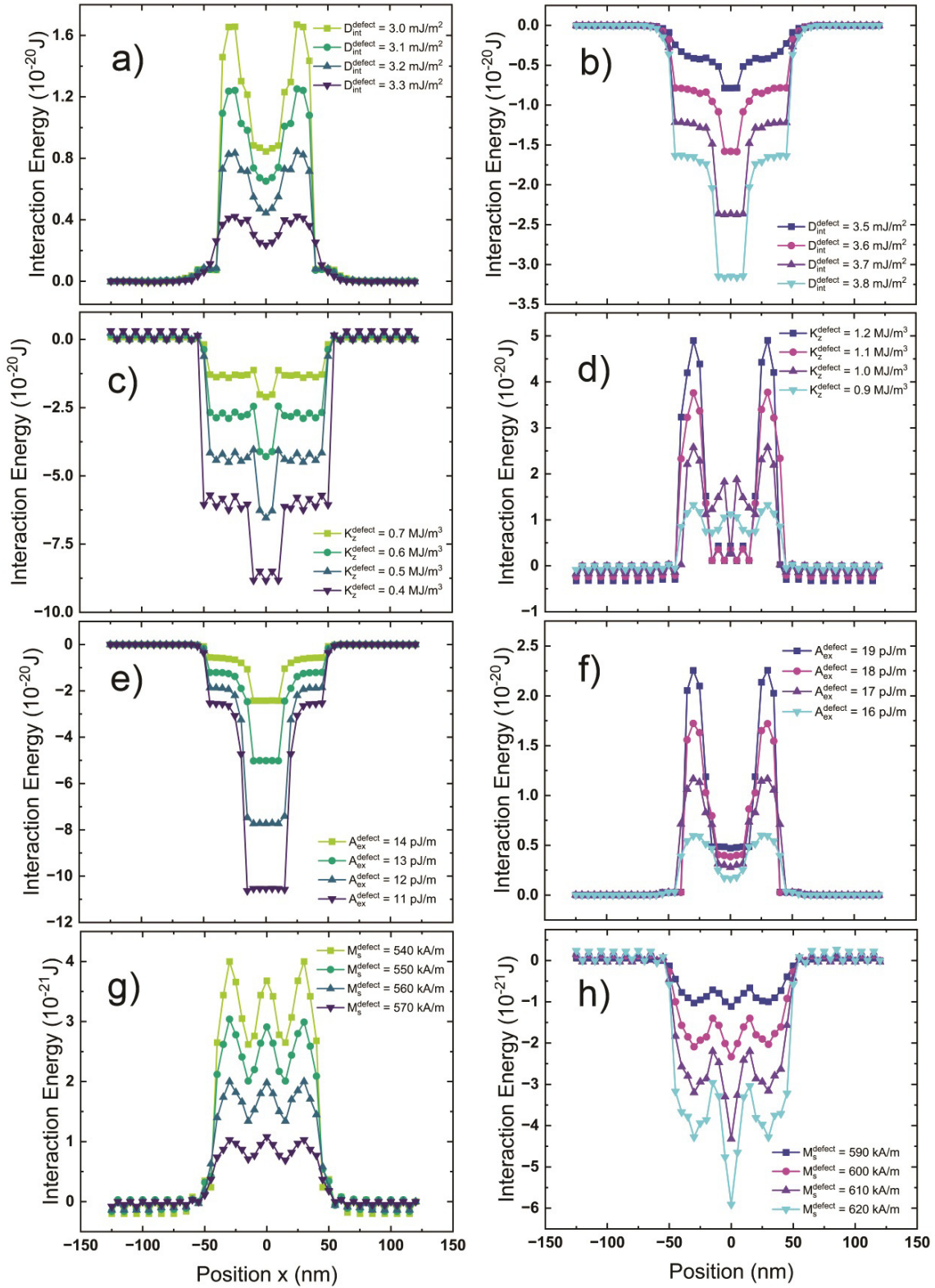


FIG. A2. Interaction energy between the skyrmionium and the defect ($\rho = 30$ nm) obtained by micro-magnetic simulation using eq. (1) considering different defect parameters with a width of $W = 512$ nm

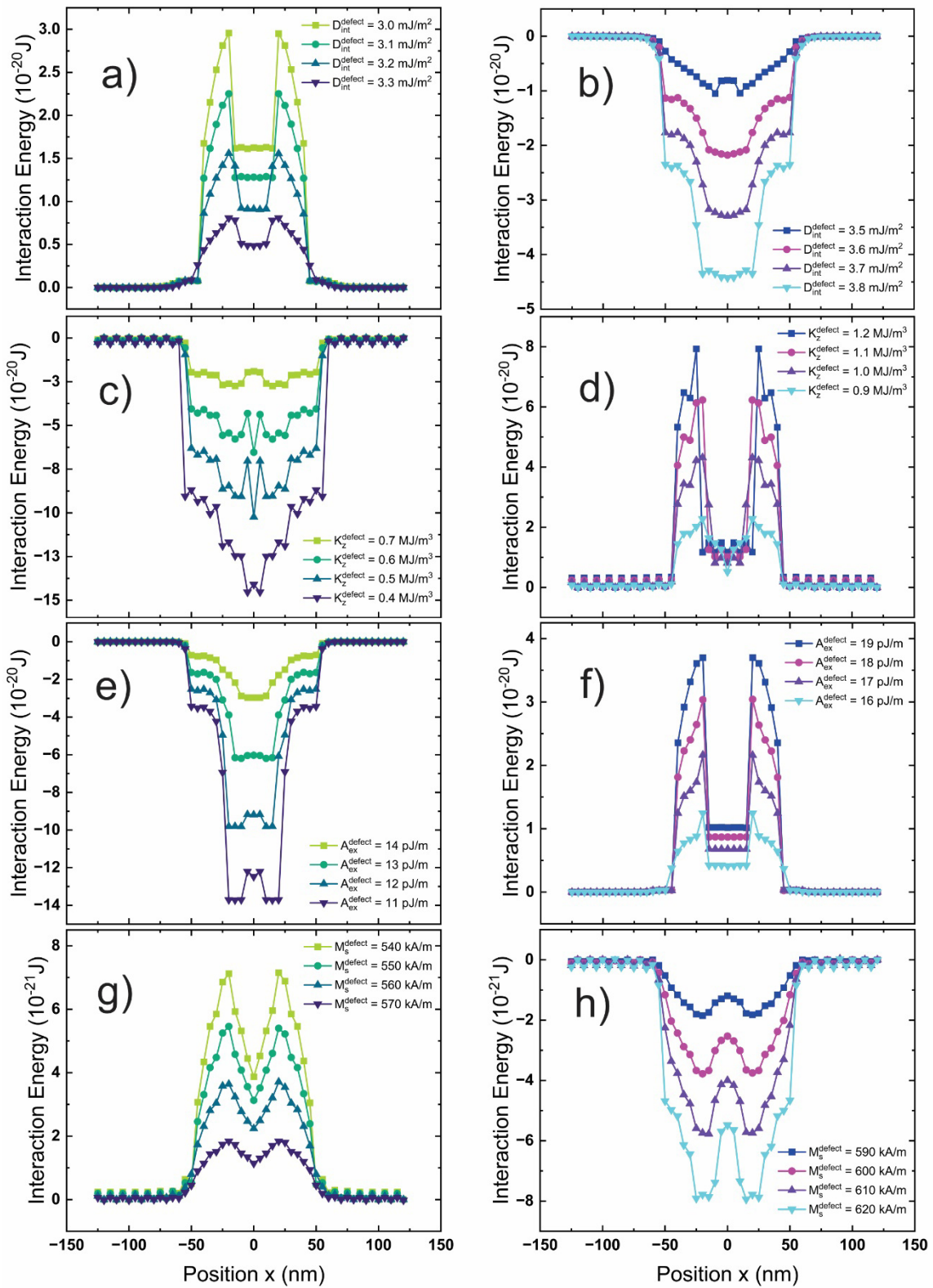


FIG. A3. Interaction energy between the skyrmionium and the defect ($\rho = 40$ nm) obtained by micro-magnetic simulation using eq. (1), considering different defect parameters with a width of $W = 512$ nm

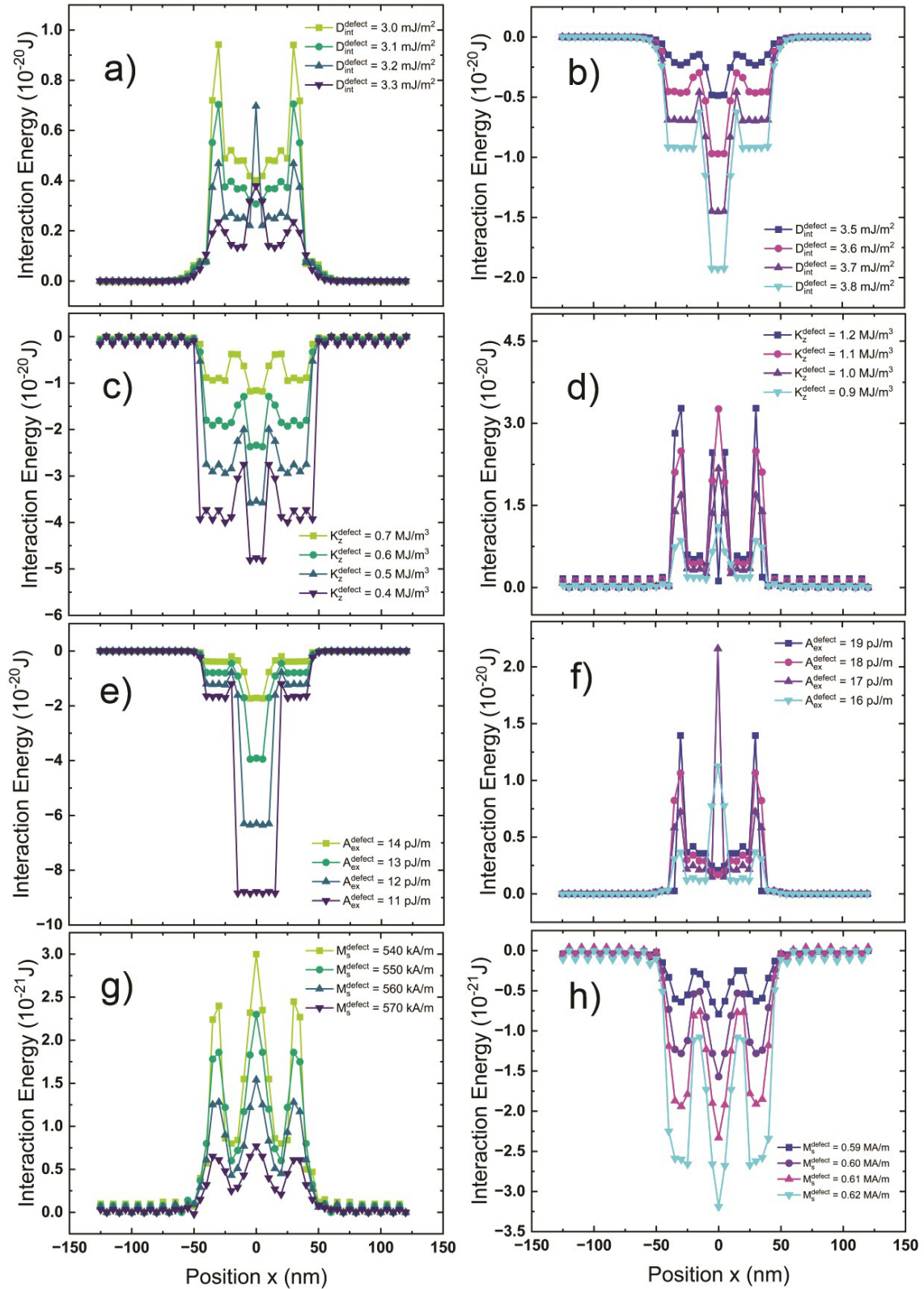
A.1.2. Skymionium-semicircular magnetic defect interaction energy with a width of $W = 256$ nm.

FIG. A4. Interaction energy between the skyrmionium and the defect ($\rho = 20$ nm) obtained by micro-magnetic simulation using eq. (1) considering different defect parameters with a width of $W = 256$ nm

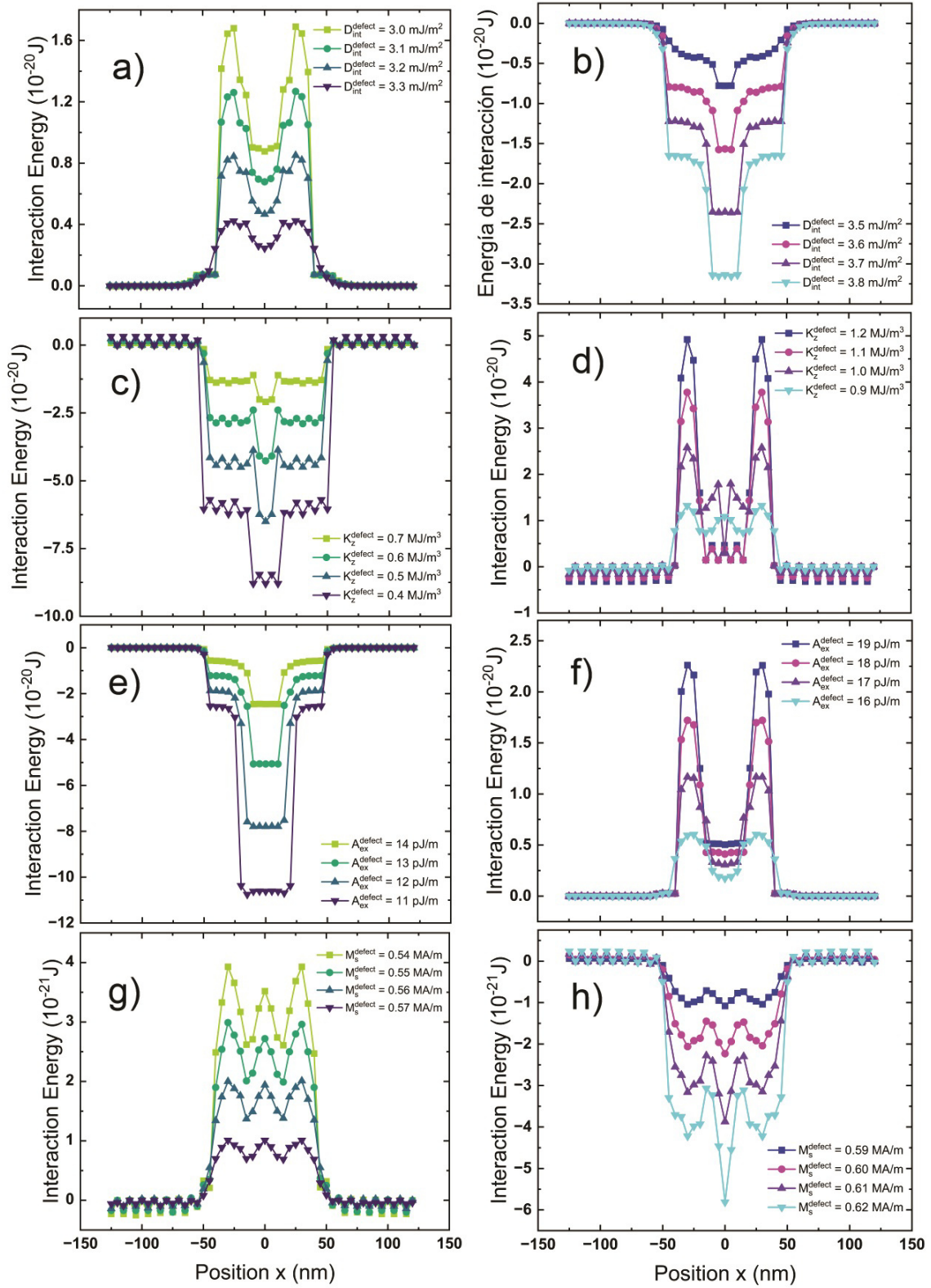


FIG. A5. Interaction energy between the skyrmionium and the defect ($\rho = 30$ nm) obtained by micromagnetic simulation using eq. (1) considering different defect parameters with a width of $W = 256$ nm

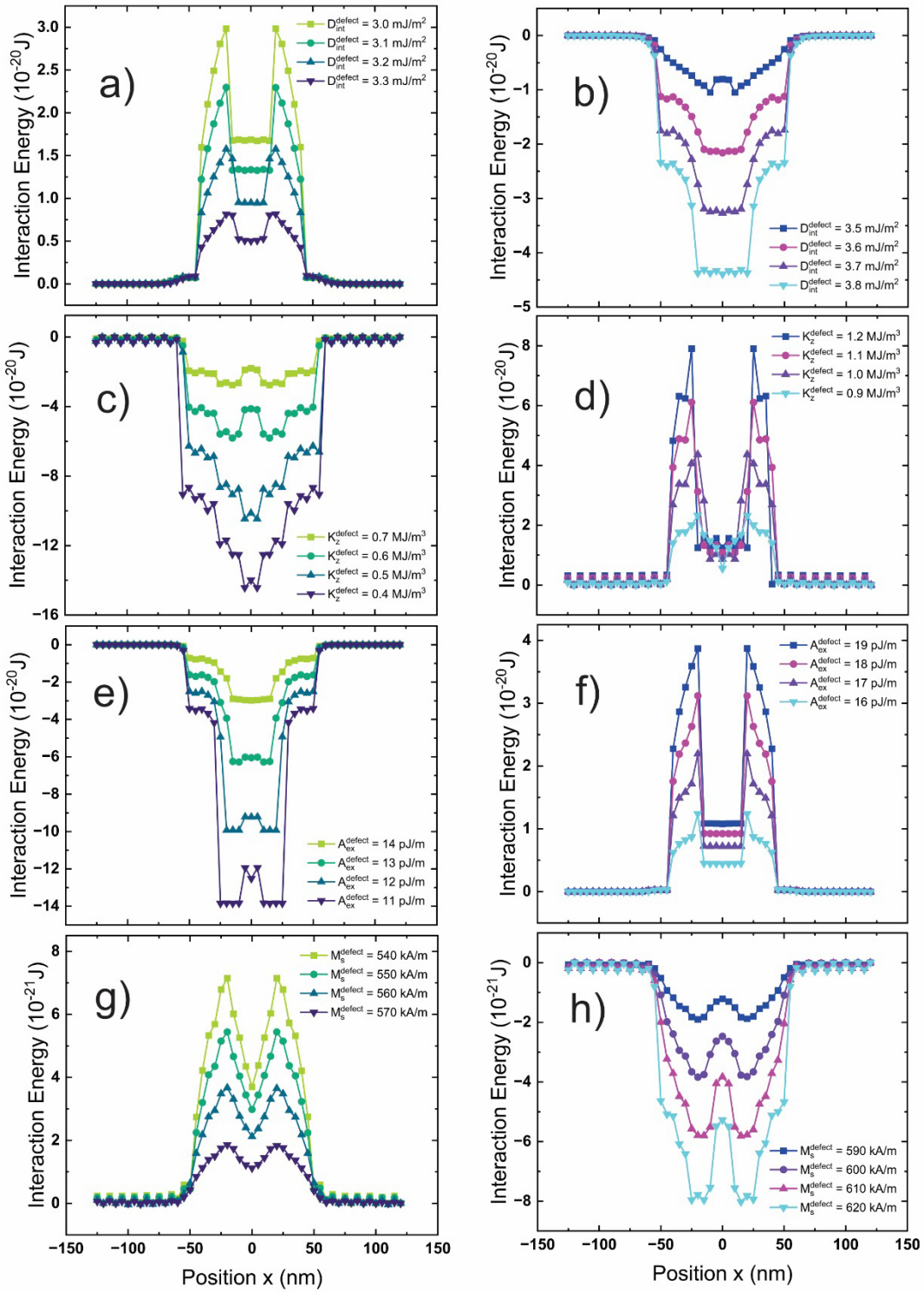
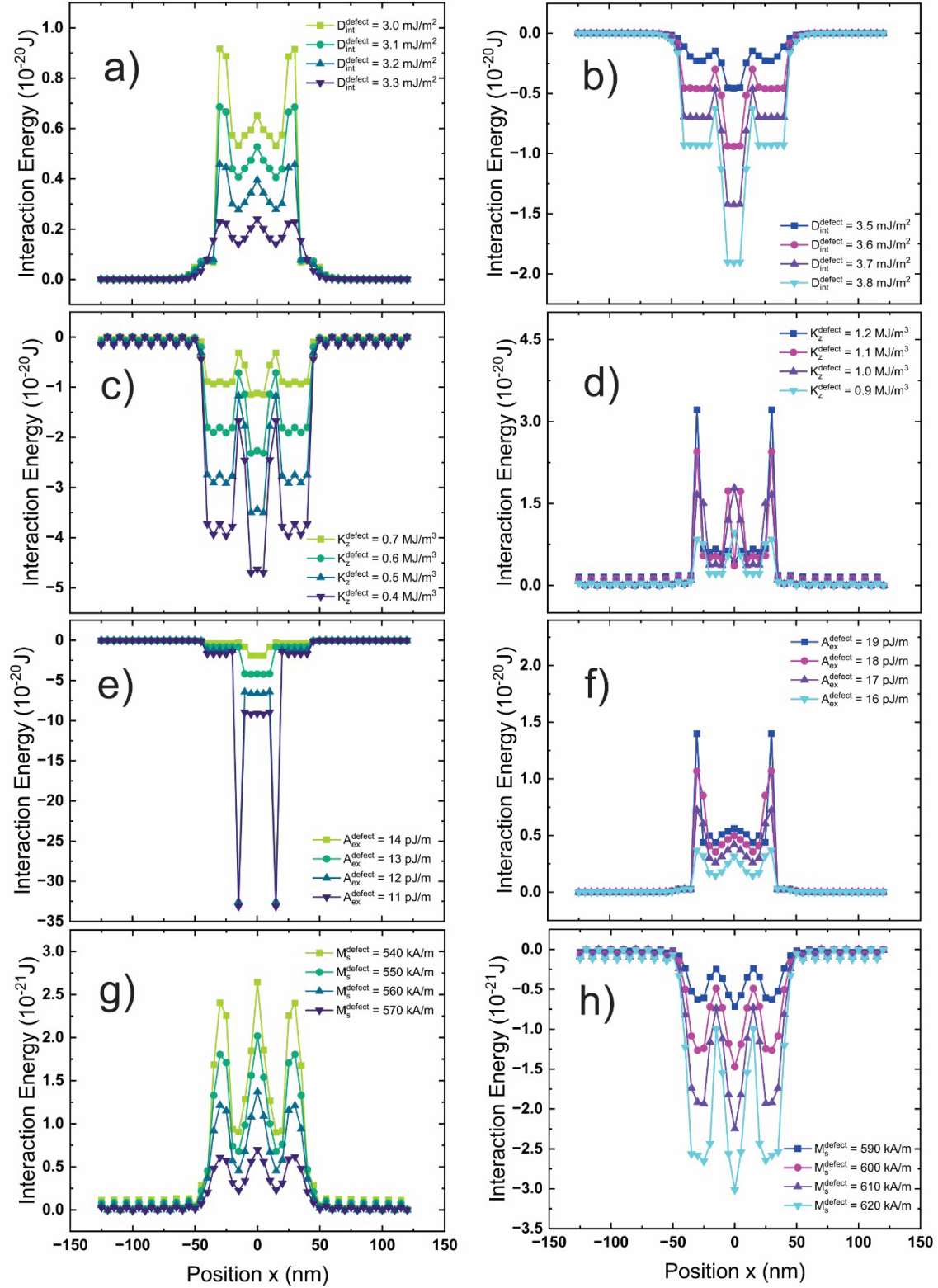


FIG. A6. Interaction energy between the skyrmionium and the defect ($\rho = 40$ nm) obtained by micro-magnetic simulation using eq. (1) considering different defect parameters with a width of $W = 256$ nm

A.1.3. Skymionium–semicircular magnetic defect interaction energy with a width of $W = 128$ nm.

 FIG. A7. Interaction energy between the skymionium and the defect ($\rho = 20$ nm) obtained by micro-magnetic simulation using eq. (1) considering different defect parameters with a width of $W = 128$ nm

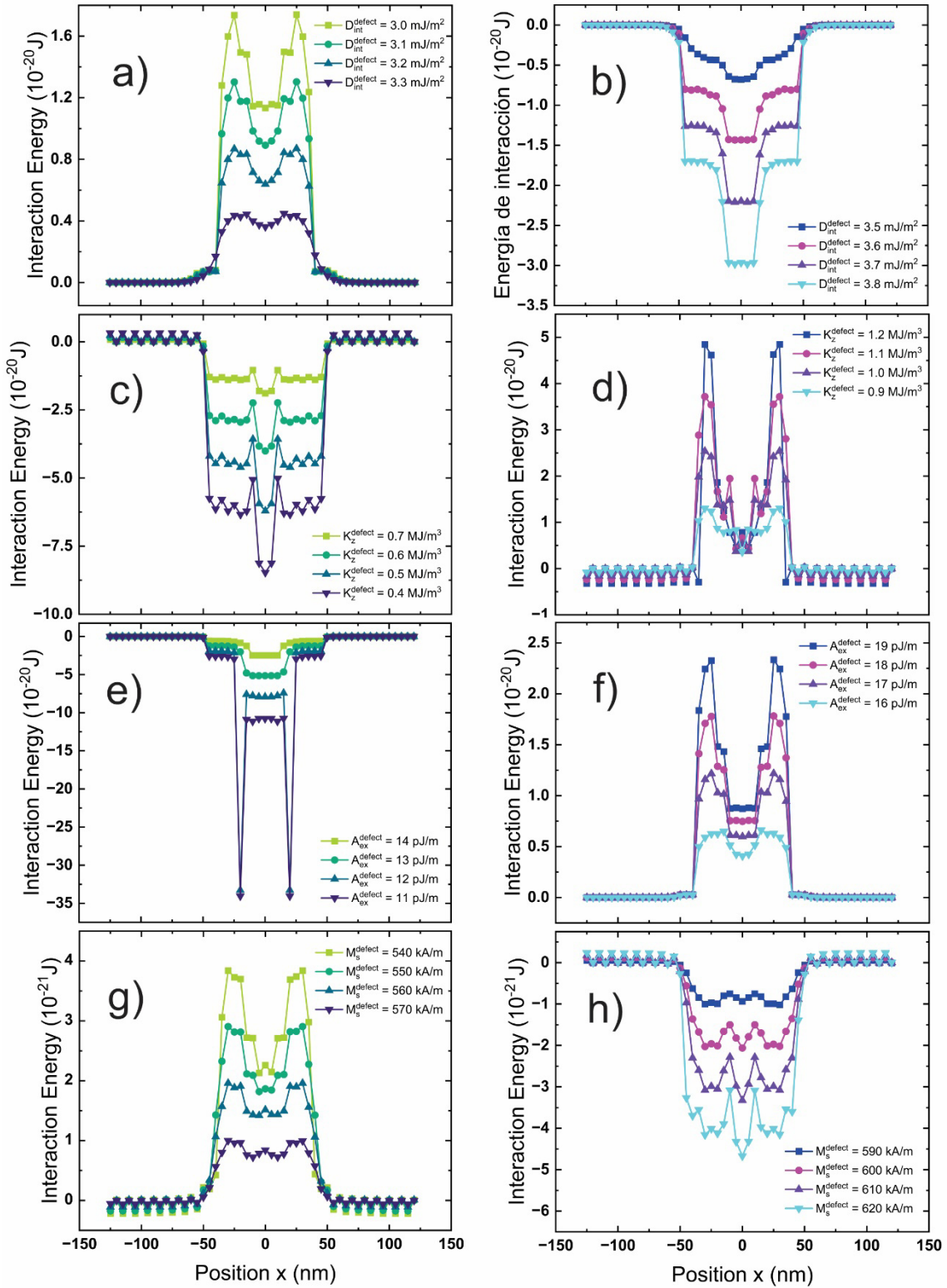


FIG. A8. Interaction energy between the skyrmionium and the defect ($\rho = 30$ nm) obtained by micro-magnetic simulation using eq. (1) considering different defect parameters with a width of $W = 128$ nm

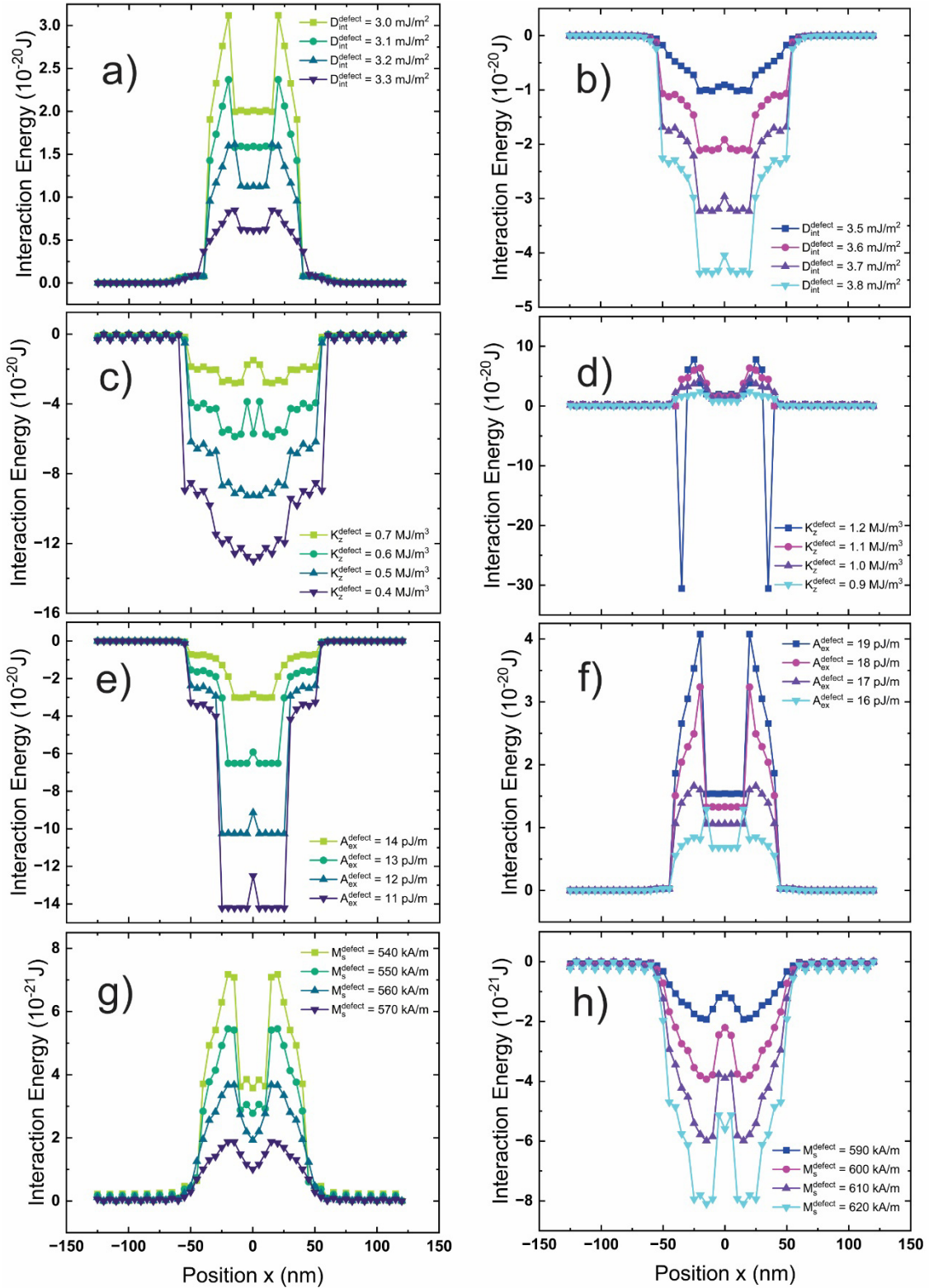


FIG. A9. Interaction energy between the skyrmionium and the defect ($\rho = 40$ nm) obtained by micromagnetic simulation using eq. (1) considering different defect parameters with a width of $W = 128$ nm

A.2. Phase diagrams for different values for the width W

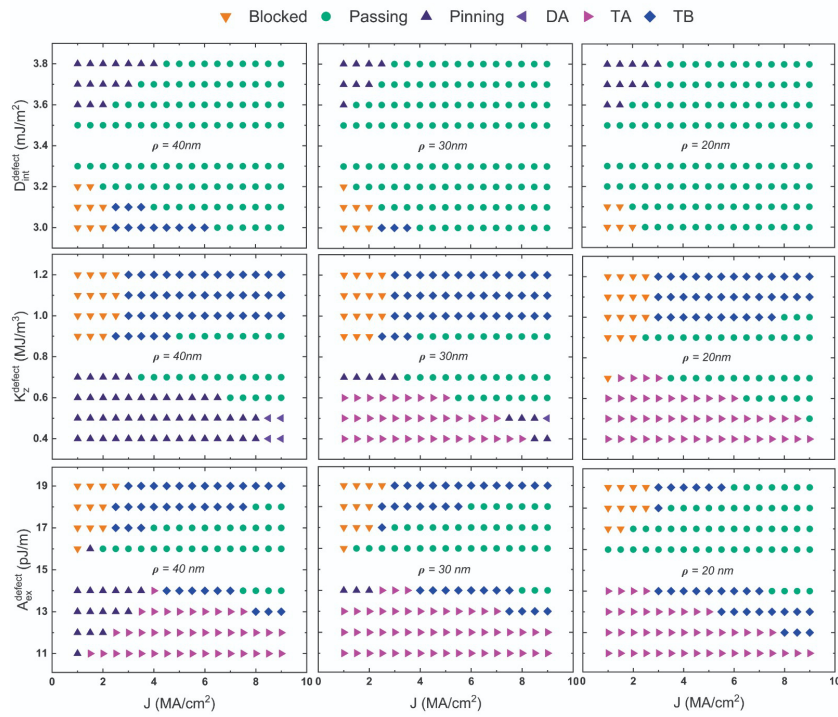


FIG. A10. The phase diagrams of possible states for the skyrmionium dynamics in the presence of a magnetic defect depict a wide range of physical parameters and diameters, offering a comprehensive view of the system's behavior for a width $W = 128$ nm

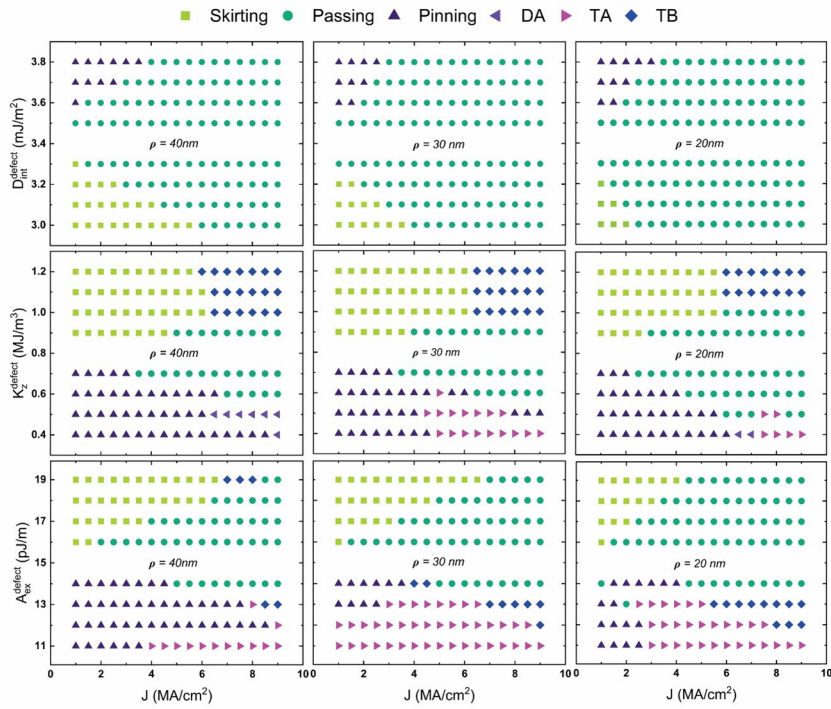


FIG. A11. The phase diagrams of possible states for the skyrmionium dynamics in the presence of a magnetic defect depict a wide range of physical parameters and diameters, offering a comprehensive view of the system's behavior for a width $W = 256$ nm

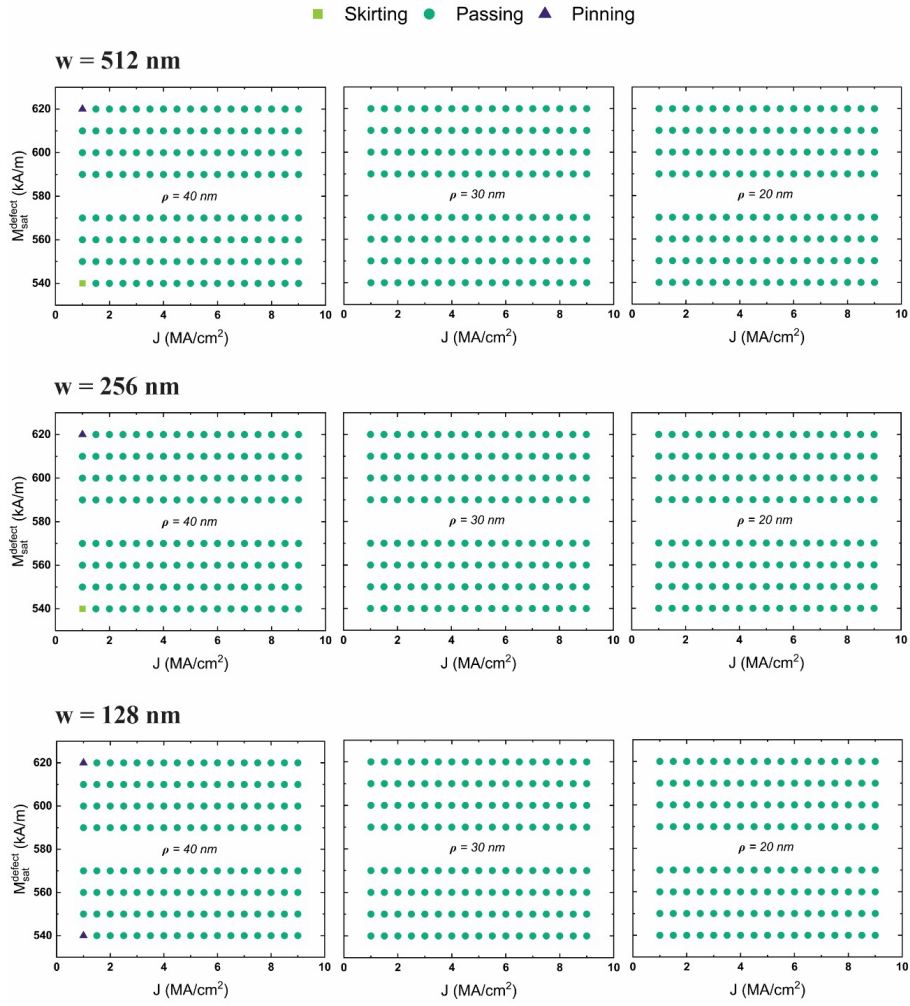


FIG. A12. Phase diagrams showing all possible skyrmionium dynamics states in the presence of a defect, with its saturation magnetization value $M_{\text{sat}}^{\text{defect}}$, for different widths (W) and diameters (ρ)

A.3. Schematic representation of different skyrmionium dynamics states

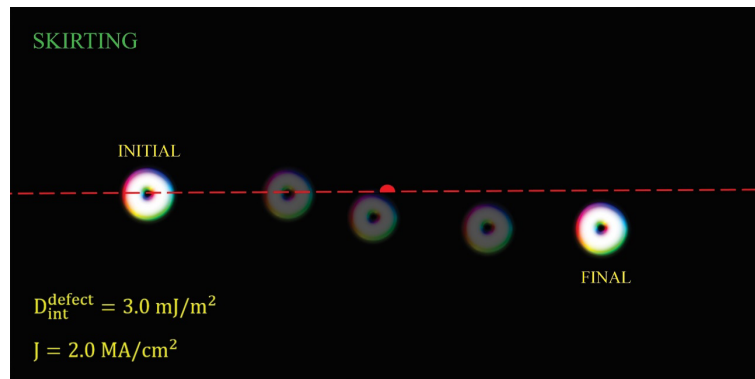


FIG. A13. Representation of the skirting state in which the skyrmionium avoids the magnetic defect to continue its movement along the racetrack

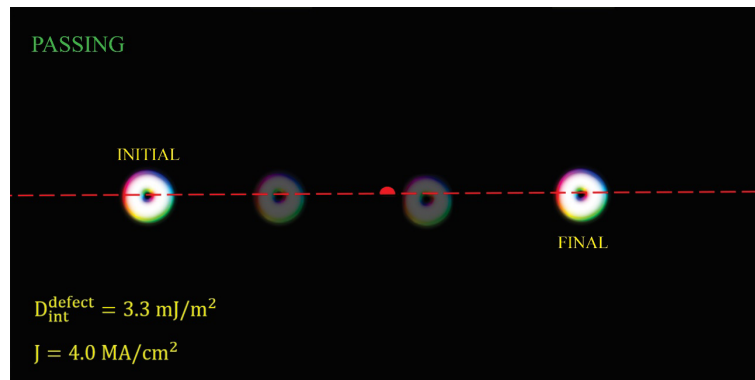


FIG. A14. Representation of the passing state in which the skyrmionium manages to cross the magnetic defect to continue its path along the racetrack

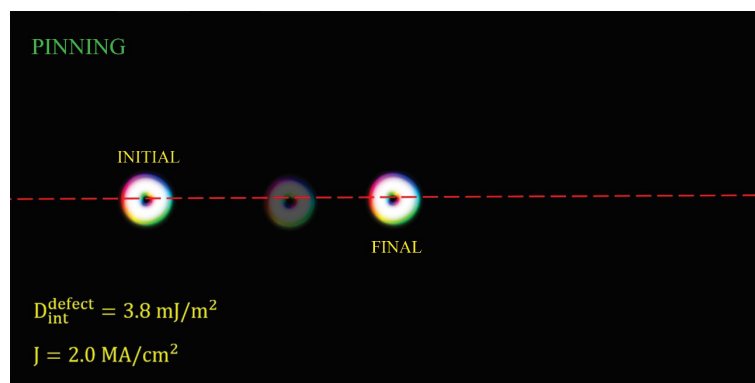


FIG. A15. Representation of the pinning state in which the skyrmionium is trapped inside the magnetic defect

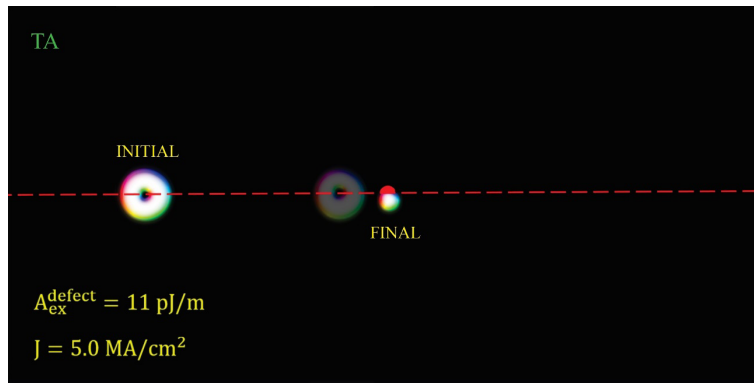


FIG. A16. Representation of the TA state in which a skyrmionium collapses into the defect, transforming into a skyrmion and becoming trapped within the defect

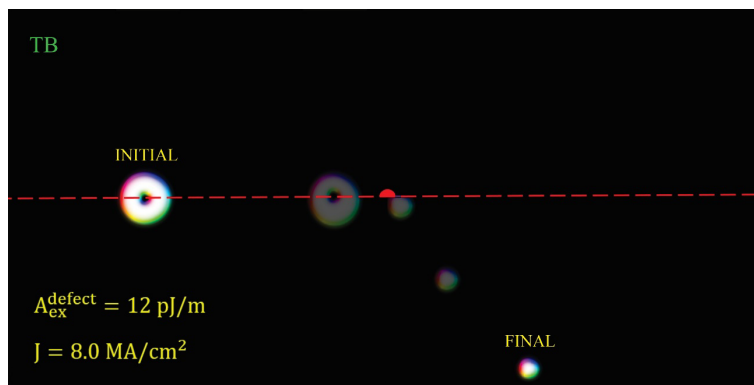


FIG. A17. Schematic representation of a skyrmionium collapsing into a defect, transforming to a skyrmion, and changing path from its original trajectory

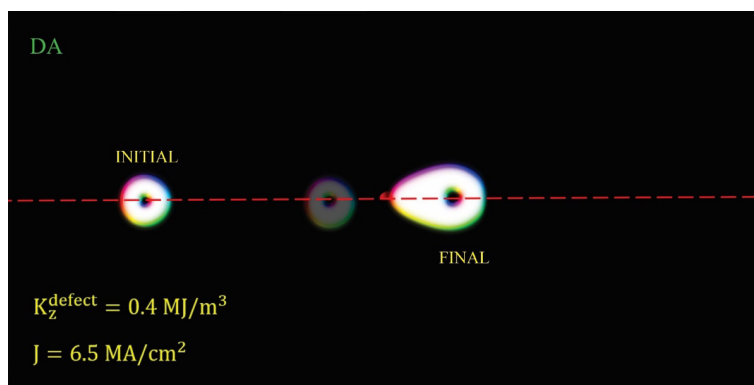


FIG. A18. A schematic representation shows a skyrmionium trapped by a defect. However, due to the current's effect, it deforms and increases in size along the racetrack

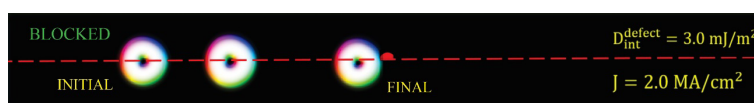


FIG. A19. Schematic representation of the blocked state; the skyrmionium stops before colliding with the defect

A.4. Skyrmion–magnetic defect interaction energy

$W = 512\text{nm} ; D = 20\text{nm}$

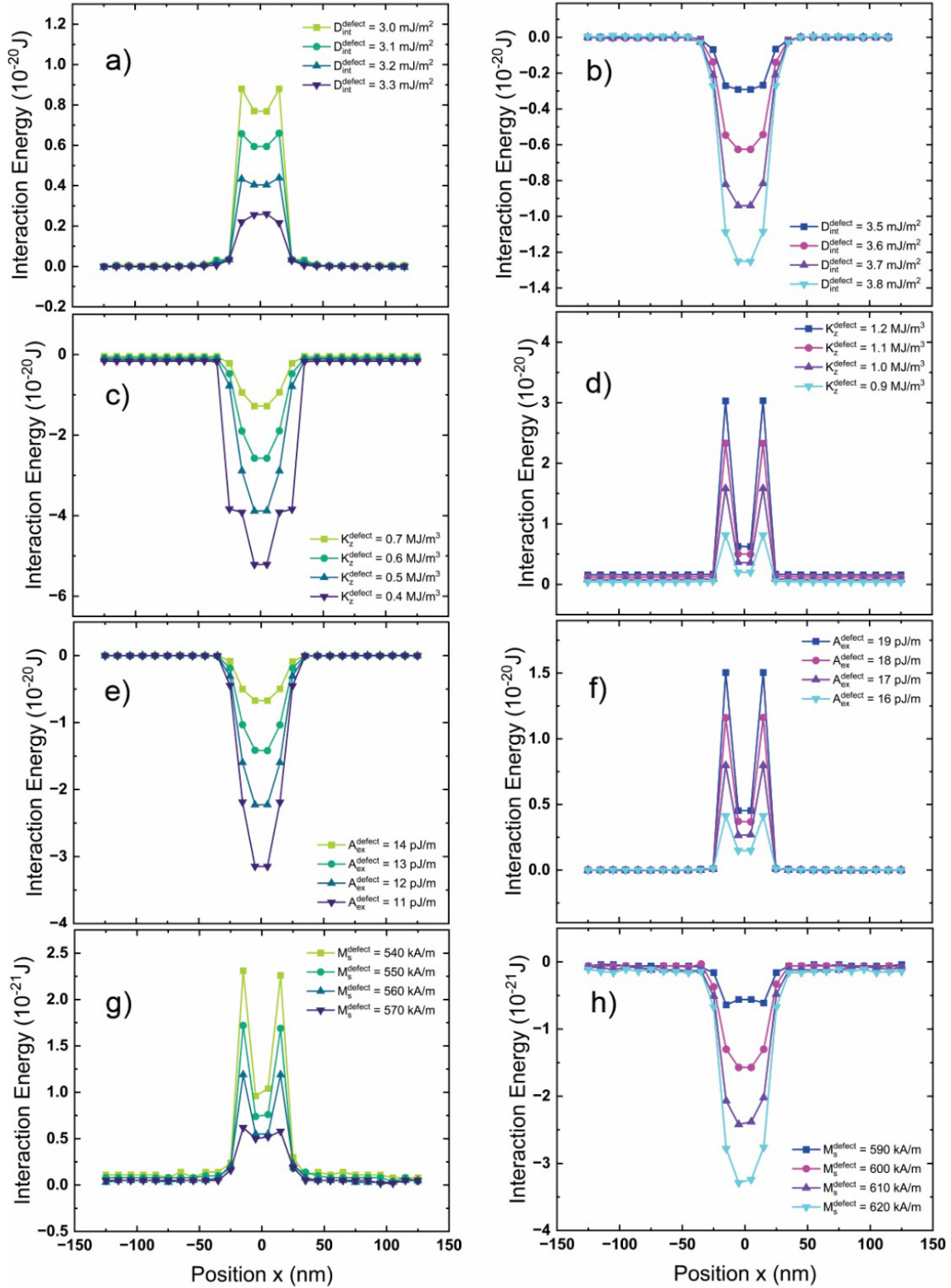


FIG. A20. Interaction energy between the skyrmion and the defect ($\rho = 20\text{ nm}$) obtained by micro-magnetic simulation using eq. (1) considering different defect parameters with a width of $W = 512\text{ nm}$

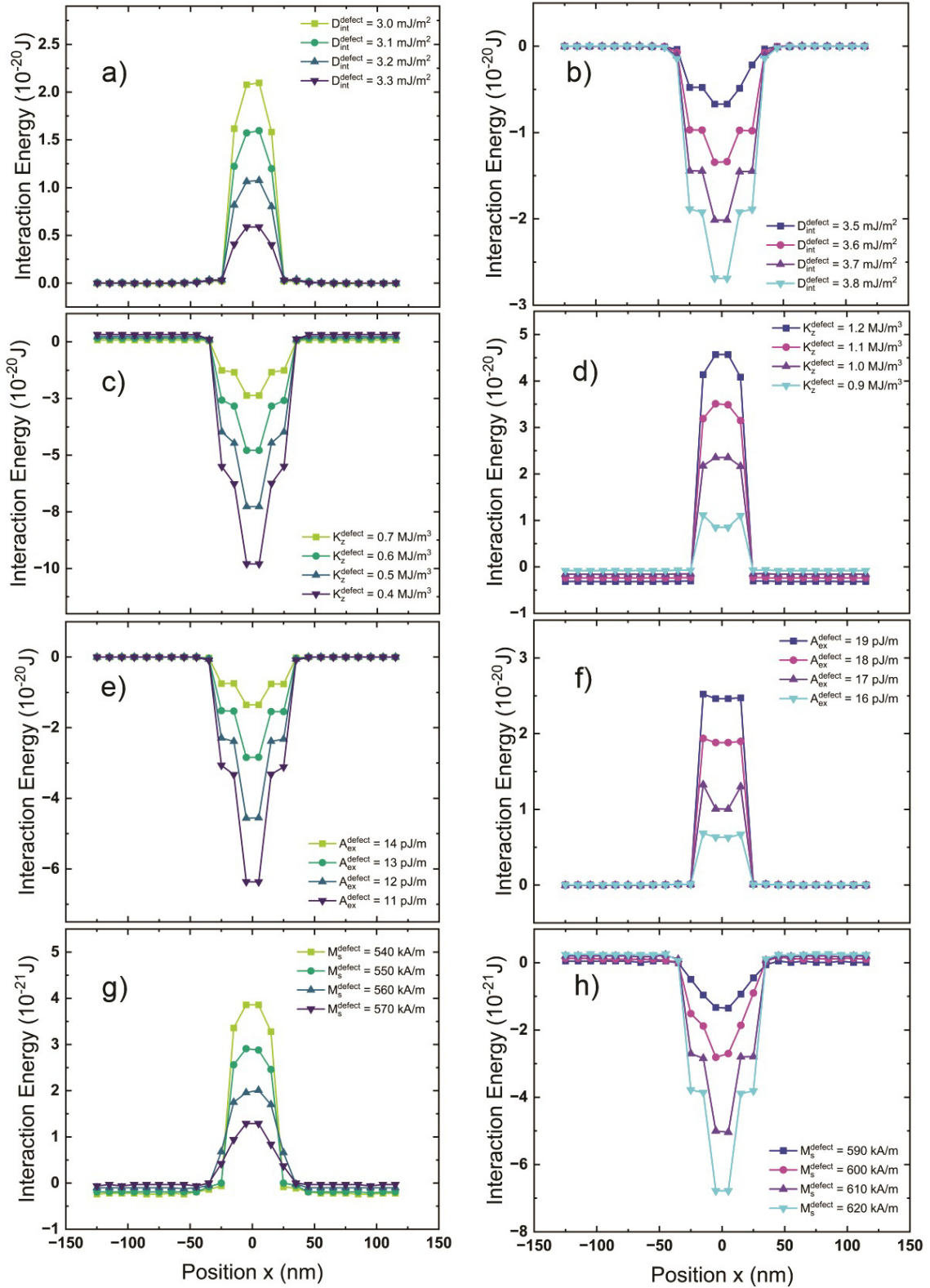
$W = 512\text{nm} ; D = 30\text{nm}$


FIG. A21. Interaction energy between the skyrmion and the defect ($\rho = 30\text{ nm}$) obtained by micro-magnetic simulation using eq. (1) considering different defect parameters with a width of $W = 512\text{ nm}$

$W = 512\text{nm}$; $D = 40\text{nm}$

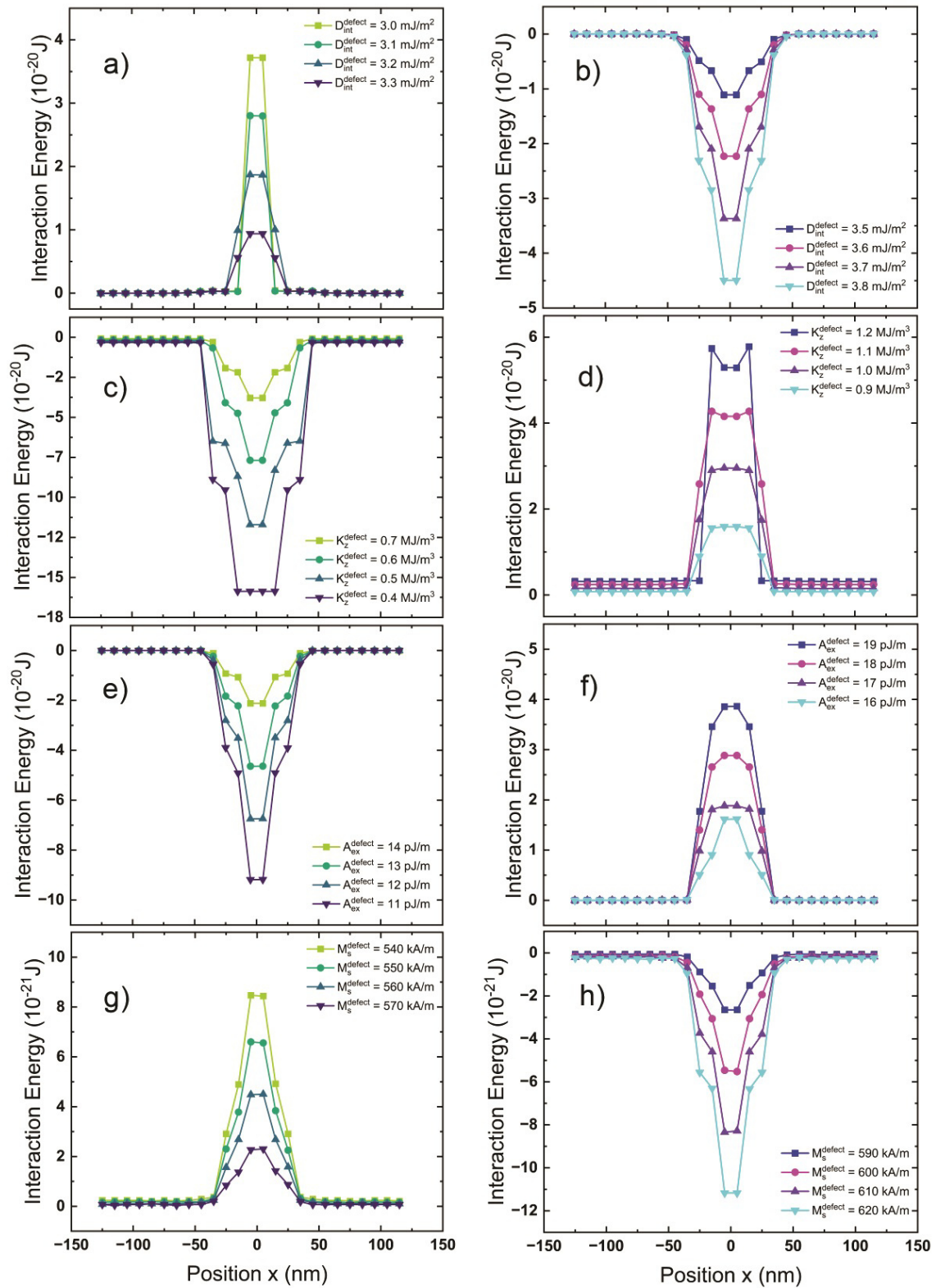


FIG. A22. Interaction energy between the skyrmion and the defect ($\rho = 40\text{ nm}$) obtained by micromagnetic simulation using eq. (1) considering different defect parameters with a width of $W = 512\text{ nm}$

References

- [1] Göbel B., Mertig I., Tretiakov O.A. Beyond skyrmions: Review and perspectives of alternative magnetic quasiparticles. *Physics Reports*, 2021, **895**, P. 1–28.
- [2] Jin C., Song C., Wang J., Liu Q. Dynamics of antiferromagnetic skyrmion driven by the spin Hall effect. *Applied Physics Letters*, 2016, **109** (18), 182404.
- [3] Göbel B., Schäffer A.F., Berakdar J., Mertig I., Parkin S.S. Electrical writing, deleting, reading, and moving of magnetic skyrmioniums in a racetrack device. *Scientific reports*, 2019, **9** (1), 12119.
- [4] Li S., Xia J., Zhang X., Ezawa M., Kang W., Liu X., Zhou Y., Zhao, W. Dynamics of a magnetic skyrmionium driven by spin waves. *Applied Physics Letters*, 2018, **112** (14), 142404.
- [5] Novak R.L., Garcia F., Novais E.R.P., Sinnecker J.P., Guimaraes A.P. Micromagnetic study of skyrmion stability in confined magnetic structures with perpendicular anisotropy. *J. of Magnetism and Magnetic Materials*, 2018, **451**, P. 749–760.
- [6] Beg M., Carey R., Wang W., Cortés-Ortuño D., Vousden M., Bisotti M. A., Albert M., Chernyshenko D., Hovorka O., Stamps R.L., Fangohr H. Ground state search, hysteretic behaviour, and reversal mechanism of skyrmionic textures in confined helimagnetic nanostructures. *Scientific Reports*, 2015, **5** (1), 17137.
- [7] Ponsudana M., Amuda R., Madhumathi R., Brinda A., Kanimozhi N. Confinement of stable skyrmionium and skyrmion state in ultrathin nanoring. *Physica B*, 2021, **618**, 413144.
- [8] Zhang X., Xia, J., Zhou Y., Wang, D., Liu X., Zhao, W., Ezawa M. Control and manipulation of a magnetic skyrmionium in nanostructures. *Physical Review B*, 2016, **94** (9), 094420.
- [9] Tejo F., Riveros A., Escrig J., Guslienko K.Y., Chubykalo-Fesenko O. Distinct magnetic field dependence of Néel skyrmion sizes in ultrathin nanodots. *Scientific Reports*, 2018, **8** (1), 6280.
- [10] Jiang W., Zhang X., Yu G., Zhang W., Wang X., Benjamin Jungfleisch M., Pearson J.E., Heinonen O., Wang K.L., Zhou Y., Hoffmann A., Te Velthuis S.G. Direct observation of the skyrmion Hall effect. *Nature Physics*, 2017, **13**, P. 162–169.
- [11] Yanes R., Garcia-Sanchez F., Luis R.F., Martinez E., Raposo V., Torres L., Lopez-Diaz L. Skyrmion motion induced by voltage-controlled in-plane strain gradients. *Applied Physics*, 2019, **115** (13), 132401.
- [12] Zhu H., Xiang G., Feng Y., Zhang X. Dynamics of elliptical magnetic skyrmion in defective racetrack. *Nanomaterials*, 2024, **14** (3), 312.
- [13] Sampaio J., Cros V., Rohart S., Thiaville A., Fert A. Nucleation, stability and current-induced motion of isolated magnetic skyrmions in nanostructures. *Nature Nanotechnology*, 2013, **8** (11), P. 839–844.
- [14] Fert A., Cros V., Sampaio J. Skyrmions on the track. *Nature Nanotech.*, 2013, **8** (3), P. 152–156.
- [15] Lima Fernandes I., Bouaziz J., Blügel S., Lounis S. Universality of defect-skyrmion interaction profiles. *Nature Communication*, 2018, **9** (1), 4395.
- [16] Toscano D., Leonel S.A., Coura P.Z., Sato F. Building traps for skyrmions by the incorporation of magnetic defects into nanomagnets: Pinning and scattering traps by magnetic properties engineering. *J. of Magnetism and Magnetic Materials*, 2019, **480**, P. 171–185.
- [17] Lin J.Q., Chen J.P., Tan Z.Y., Chen Y., Chen Z.F., Li W.A., Gao X.S., Liu J.M. Manipulation of Skyrmion Motion Dynamics for Logical Device Application Mediated by Inhomogeneous Magnetic Anisotropy. *Nanomaterials*, 2022, **12** (2), 278.
- [18] Toscano D., Mendonça J.P.A., Miranda A.L.S., de Araujo C.I.L., Sato F., Coura P.Z., Leonel S.A. Suppression of the skyrmion Hall effect in planar nanomagnets by the magnetic properties engineering: Skyrmion transport on nanotracks with magnetic strips. *J. of Magnetism and Magnetic Materials*, 2020, **504**, 166655.
- [19] Kolesnikov A.G., Stebliy M.E., Samardak A.S., Ognev A.V. Skyrmionium–high velocity without the skyrmion Hall effect. *Scientific Reports*, 2018, **8** (1), 16966.
- [20] Zheng F., Li H., Wang S., Song D., Jin C., Wei W., Kovács A., Zang J., Tian M., Zhang Y., Du H., Dunin-Borkowski R.E. Direct Imaging of a Zero-Field Target Skyrmion and Its Polarity Switch in a Chiral Magnetic Nanodisk. *Physical Review Letters*, 2017, **119** (9), 197205.
- [21] Can Önel A., Çimen M., Yarımbiyik A.E., Arikan M., Rameev B. Interaction of a magnetic skyrmionium with an engineered defect. *J. of Superconductivity and Novel Magnetism*, 2023, **36** (6), P. 1533–1539.
- [22] Chen R., Li Y., Pavlidis V.F., Moutafis C. Skyrmionic interconnect device. *Physical Review Research*, 2020, **2** (4), 043312.
- [23] Song C., Ma Y., Jin C., Wang J., Xia H., Wang J., Liu Q. Field-tuned spin excitation spectrum of $k\pi$ skyrmion. *New J. of Physics*, 2019, **21** (8), 083006.
- [24] Vigo-Cotrina H., Guimarães A.P. Creating skyrmions and skyrmioniums using oscillating perpendicular magnetic fields. *J. of Magnetism and Magnetic Materials*, 2020, **507**, 166848.
- [25] Ishida Y., Kondo K. Theoretical comparison between skyrmion and skyrmionium motions for spintronics applications. *Japanese J. of Applied Physics*, 2020, **59**, SGGI04.
- [26] Komineas S., Papanicolaou N. Skyrmion dynamics in chiral ferromagnets. *Physical Review B*, 2015, **92** (6), 064412.
- [27] Song C., Jin C., Wang J., Ma Y., Xia H., Wang J., Xia H., Wang J., Liu Q. Dynamics of a magnetic skyrmionium in an anisotropy gradient. *Applied Physics Express*, 2019, **12** (8), 083003.
- [28] Jiang A., Zhou Y., Zhang X., Mochizuki M. Transformation of a skyrmionium to a skyrmion through the thermal annihilation of the inner skyrmion. *Physical Review Research*, 2024, **6** (1), 013229.
- [29] Kuchkin V.M., Kiselev N.S., Rybakov F.N., Lobanov I.S., Blügel S., Uzdin V.M. Heliknoton in a film of cubic chiral magnet. *Frontiers in Physics*, 2023, **11**, 1201018.
- [30] Vigo-Cotrina H., Navarro-Vilca S., Urcia-Romero S. Skyrmionium dynamics on a racetrack in the presence of a magnetic defect. *J. of Applied Physics*, 2024, **135** (16), 163903.
- [31] Vansteenkiste A., Leliaert J., Dvornik M., Helsen M., Garcia-Sanchez F., Van Waeyenberge B. The design and verification of MuMax3. *AIP Advances*, 2014, **4** (10), 107133.

Information about the authors:

Sebastian Rodrigo Navarro Vilca – Departamento de Física Aplicada, Universidad Nacional Jorge Basadre Grohmann, Avenida Miraflores, S/N, Ciudad Universitaria, Tacna 23003, Perú; ORCID 0009-0000-8508-0406; srnavarro@unjbgu.edu.pe

Silvana Rocio Urcia Romero – Department of Physics, University of Puerto Rico, Mayagüez, Puerto Rico 00681, USA; ORCID 0000-0002-0730-9081; silvana.urcia@upr.edu

Helmunt Eduardo Vigo Cotrina – Grupo de Investigación en Ciencias Aplicadas y Nuevas Tecnologías, Universidad Privada del Norte, Trujillo, Perú; ORCID 0000-0003-4335-8777; helmunt.vigo@upn.edu.pe

Conflict of interest: the authors declare no conflict of interest.

Magnesium based tin-silicon alloys under pressure: first-principles evolution search results

Yuri V. Luniakov

Institute of Automation and Control Processes of the Far Eastern Branch of the Russian Academy of Sciences, Vladivostok, Russia

luniakov@mail.ru

PACS 61.50-f, 61.50.Ks, 71.15.Mb

ABSTRACT The search of minimal enthalpy structures of ternary magnesium alloys of different stoichiometry $Mg_xSi_ySn_z$ under pressure $P \leq 6$ GPa has been performed using the software suite USPEX implementing the evolution algorithm combined with the density functional theory (DFT) approach. The evolutionary search has yielded new possible ternary compounds of the stoichiometries $Mg_{12}Si_3Sn$, Mg_4SiSn and Mg_6Si_3Sn , which have negative enthalpy of formation at pressures in the range of 0 to 10 GPa and which are not substitution solutions. These compounds have metallic properties and formation energies comparable to those of binary silicides Mg_xSi_y .

KEYWORDS $Mg_xSi_ySn_z$, crystal structure, phase transitions, hydrostatic pressure, evolutionary search, Density Functional Theory

ACKNOWLEDGEMENTS The results were obtained using the equipment of Shared Resource Center “Far Eastern Computing Resource” IACP FEB RAS (<https://www.cc.dvo.ru>). The research was carried out within the state assignment of IACP FEB RAS (Theme FFW-2021-0001).

FOR CITATION Luniakov Yu.V. Magnesium based tin-silicon alloys under pressure: first-principles evolution search results. *Nanosystems: Phys. Chem. Math.*, 2024, **15** (5), 621–631.

1. Introduction

Due to their promising properties such as high melting point [1], small size of the forbidden zone, environmental safety and sufficient cheapness compared to thermoelectrics based on bismuth, tellurium and lead, e.g. Bi_2Te_3 [2], $PbTe$ and $PbSn$ [3], semiconductor magnesium silicides and stannides are very interesting materials. They are very effective for infrared detection due to their high electrical conductivity and ability to absorb light in the infrared region of the spectrum. All of these properties allow these materials to be widely used as thermal elements in industrial production [4–8], as infrared detectors in optical fibers [9], and for use in hydrogen energy technologies [10].

Regarding the research on magnesium silicides, only the pressure-stabilized Si-rich phases, like $MgSi_2$, Mg_5Si_6 , $MgSi$ and Mg_9Si_5 can form near the interface Mg_2Si/Si [11, 12]. Two relatives of Mg_2Si , namely Mg_9Si_5 and Mg_5Si_6 , have been experimentally observed in the supersaturated solid solution of Al–Mg–Si [13]. Two phases of this solution, i.e., the β' and β'' phases, have been resolved and are considered to correspond to the hexagonal $P6_3/m$ phase of Mg_9Si_5 [14, 15] and the monoclinic $C2/m$ phase of Mg_5Si_6 [16, 17], respectively. Huan et al. [11, 12] discovered that Mg_2Si is nearly equivalent to Mg_9Si_5 from 6 to 24 GPa based on the first principles investigation of high-pressure phases of Mg_2Si . Stable compounds of magnesium with tin and germanium are much more difficult to make, so the only known structures are Mg_2X , where X is Sn and Ge. It is even more complicated to obtain stable compounds for the ternary systems of different stoichiometry than $Mg_2Si_{1-x}Sn_x$ and $Mg_2Si_{1-x}Ge_x$. At present, there are only experimental data on solid solutions of the composition $Mg_2Si_{1-x}Sn_x$ and $Mg_2Si_{1-x}Ge_x$.

Besides binary stannides and magnesium silicides, their mixed compounds Mg_2XY (where X, Y = Si, Sn, Ge) are also of interest, as they have rather unique thermoelectric properties compared to the corresponding binary compounds. Some experimental results suggest [18] that solid solutions of $Mg_2Si_{1-x}Sn_x$ show better thermoelectric performance when n-type doping is used. For example, three-component alloys of composition $Mg_2Si_{0.35}Sn_{0.65}$ and $Mg_2Ge_{0.25}Sn_{0.75}$ are characterized by lower thermal conductivity and higher figure of merit due to mixing of different components and high carrier mobility [19–21]. Solid solutions of the composition $Mg_2Si_{0.4}Sn_{0.6}$ have promising thermodynamic properties [22, 23] due to the overlap and degeneracy of the valence bands of Si and Sn, which leads to an increase in the effective mass of electrons [24, 25]. These properties make mixed compositions of Mg_2X potentially interesting materials for thermoelectric applications.

Changes in the thermal conductivity of $Mg_2Si_{1-x}Sn_x$ silicon-tin alloys can also occur when their stoichiometry is altered due to the presence of various defects and impurities in them. This is due to the lack of complete solubility in the $Mg_2Si_{1-x}Sn_x$ and $Mg_2Ge_{1-x}Sn_x$ systems [1]. Several attempts to improve the thermal conductivity have been made by

modifying the structure of alloys by doping. To study the thermoelectric properties of $\text{Mg}_2\text{Si}_{1-x}\text{Sn}_x$, many theoretical and experimental investigations have been carried out [26–28] in order to determine the most effective alloying elements and to evaluate the influence of internal and external defects.

However, the properties of the three-component alloys $\text{Mg}_x\text{Si}_y\text{Sn}_z$ for all possible stoichiometries have not yet been investigated [29]. At present, only data on solid solutions of the compositions $\text{Mg}_2\text{Si}_{1-x}\text{Sn}_x$ and $\text{Mg}_2\text{Si}_{1-x}\text{Ge}_x$ are available. This implies that only the structure of antiferroite with symmetry $\text{Fm}\bar{3}\text{m}$ is considered in the calculation of the structures of stannidosilicides, since the silicide and magnesium stannide Mg_2Si and Mg_2Sn have this structure. In besides the silicides, application of evolutionary search methods to the calculations of Mg_2Si , Mg_2Sn and Mg_2Ge allowed us to reproduce the known phase transitions from antiferroite to anticottunite and Ni_2In -type structures and to predict unknown structures of the silicide Mg_2Si [30], Mg_2Sn [31] and Mg_2Ge [32] at high pressures. This gives hope for new results for $\text{Mg}_x\text{Si}_y\text{Sn}_z$ alloys of arbitrary stoichiometry. The aim of this work is to search for optimal structures of the three-component system $\text{Mg}_x\text{Si}_y\text{Sn}_z$ using modern evolutionary methods [33] and to study the stability of these structures under normal pressure conditions and zero temperature as well as under pressures from 0 to 10 GPa.

2. Methodology of calculation

For evolutionary modeling of the three-component Mg–Si–Sn system, Universal Structure Predictor: Evolutionary Xtallography (USPEX) algorithms were applied in the variable composition mode [33–37]. Details of the evolutionary search algorithms can be found in the reviews [37, 38]. During the evolutionary search, from 40 to 60 generations of structures were produced depending on the convergence, which was considered to be achieved when the most energetically favorable structure remained unchanged for 20 consecutive generations. Each generation contained 20 structures and the first generation contained more than 120 structures, with 4 to 32 atoms per every structure. The convex hull obtained from the calculations contained structures of 6 – 10 atoms each with very few exceptions as shown below in the next section (see Table 1). The structures of the first generation were randomly selected from the list of 230 space groups. In the following generations, 50 % of the lowest-energy structures were inherited from the previous generation, 10 % of the structures were produced by lattice mutation, 10 % of the structures were obtained by atom transmutation, and the remaining 30 % of the structures were generated randomly.

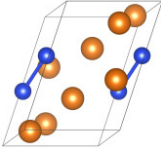
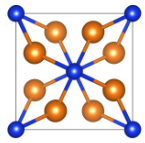
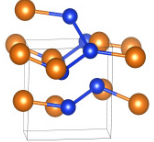
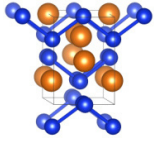
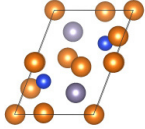
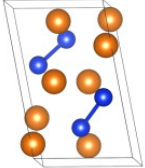
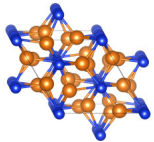
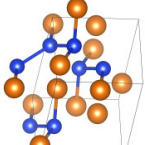
All USPEX generated structures were then relaxed using the conjugate gradient method implemented in the VASP software [39] with an energy precision of up to 0.1 meV per cell. The one-electron wave functions were expanded using a plane-wave basis with a kinetic energy cutoff of $E_{cut} = 500$ eV; the exchange-correlation potential in the Perdew–Burke–Ernzerhof parameterization [40] was used in the generalized gradient approximation. The valence electron states of the Mg, Si and Sn atoms are $2p^63s^2$, $3s^23p^2$ and $3s^23p^22d^{10}$, respectively. The Brillouin zones were sampled using a Monkhorst–Pack mesh with k-points resolution of $\pi \times 0.1 \text{ \AA}^{-1}$. Atomic positions were optimized until the convergence was achieved in the force of $\sim 10^{-3} \text{ eV/\AA}$ and in the energy of $\sim 10^{-6} \text{ eV}$. The dependence of the relative energies of the studied structures on a kinetic energy cutoff and the density of the k-point mesh was investigated and found to have no significant influence on entropy difference.

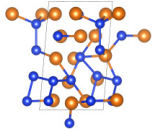
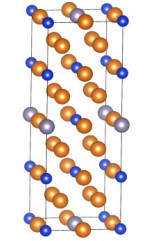
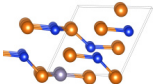
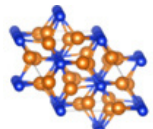
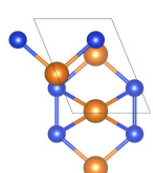
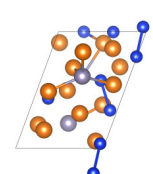
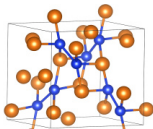
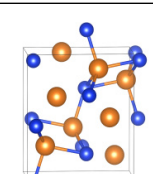
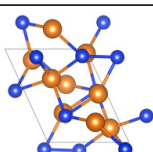
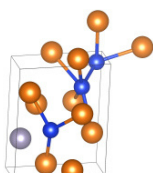
3. Results and discussion

More than ten thousand negative enthalpy magnesium based tin-silicon alloys $\text{Mg}_A\text{Si}_B\text{Sn}_C$ at pressures from 1 to 6 GPa were obtained by evolutionary searching. The projections of $\text{Mg}_A\text{Sn}_B\text{Si}_C$ structure formation enthalpies to the ternary Mg_2Si –Si–Sn plot is shown in Fig. 1, the color of each symbol on which is determined by the value of the distance in eV/atom to the ternary convex hull. The warmer the color, the more the structure deviates from the convex hull, which is the most stable configuration, colored deep blue. This increased distance from the most stable arrangement corresponds to a reduction in the overall structural stability of the crystal lattice. The unstable crystal structures with positive enthalpies are shown in gray.

Enthalpy of formation for the three-component system $\text{Mg}_A\text{Si}_B\text{Sn}_C$ can be defined as $E_F = [E(\text{Mg}_A\text{Si}_B\text{Sn}_C) - (AE_{\text{Mg}} + BE_{\text{Si}} + CE_{\text{Sn}})] / (A + B + C)$, where A , B , C are the number of magnesium, silicon, and tin atoms; E_{Mg} , E_{Si} , are E_{Sn} their formation energies in the normal (crystalline) states, respectively. For each pressure, USPEX calculations automatically determine the optimal structure of silicon, diamond, and magnesium silicide, that can be used in formation enthalpy calculations of multicomponent structures. For silicon and tin, only a third of all calculations yielded the correct diamond-like structure, while the rest of calculations yielded structures with higher enthalpy and wrong symmetry, such as P6_422 (181 space group) for silicon and $\text{P6}_3/\text{mmm}$ (194 space group) for tin. The energy difference between the structure obtained in this way and the structure in the ground state does not exceed 0.001 eV/atom for silicon and 0.04 eV/atom for tin. The structure of magnesium was not determined during the evolutionary search, only the structure of its silicide Mg_2Si has been obtained. To calculate the enthalpy of all structures obtained in this work, the enthalpies of the known ground-state structures of Mg [41–43], Si [41] and Sn [44, 45] at investigated pressures were used as a reference for the formation enthalpy calculations. The reference crystalline structures at the ambient pressure conditions were taken from the on-line databases [34, 46, 47]. For magnesium, this structure is a hexagonal close packed structure of 194 space group symmetry $\text{P6}_3/\text{mmc}$, while for silicon and tin it is a diamond-like cubic structure b-tin $\text{Fd}\bar{3}\text{m}$ of 227 symmetry group.

Table 1: Structures, corresponding to the vertices of the convex hull at pressures of 6, 4, 2, 1 and 0.025 GPa. The brackets in the first column of the table indicate the total number of atoms in the unit cell. On the unit cell shown in the last column Si atoms are represented by small blue spheres, Mg atoms by large yellow spheres, and Sn atoms by large gray spheres.

Pressure/ composition	Lattice parameters						Symmetry	$E_{\text{formation}}$, eV/atom	Unit cell
	a , Å	b , Å	c , Å	α , °	β , °	γ , °			
6 GPa, Mg ₄ Si (10 atoms)	5.28	7.42	5.32	76.86	76.98	71.65	P-1 (2)	-0.042	
6 GPa, Mg ₂ Si (6 atoms)	6.49		5.09	90	90	90	I4/mcm (140)	-0.098	
6 GPa, MgSi (8 atoms)	5.19	5.39	5.25	68.67	89.25	100.15	P-1 (2)	-0.113	
6 GPa, Mg ₃ Si ₄ (14 atoms)	13.75	3.57	5.07	90	90	90	Imm2(44)	-0.080	
6 GPa, Mg ₄ SiSn (12 atoms)	5.03	7.14	7.58	71.67	76.64	106.78	P-1 (2)	-0.137	
4 GPa, Mg ₂ Si (12 atoms)	5.30	8.28	5.12	90	90	100.95	P21(4)	-0.073	
4 GPa, Mg ₃ Si ₂ (10 atoms)	7.720	7.235	6.643	90	90	104.5	C2/c (15)	-0.108	
4 GPa, MgSi (8 atoms)	5.736	5.330	5.362	84.53	111.57	112.68	P-1 (2)	-0.075	

4 GPa, Mg ₇ Si ₅ (24 atoms)	10.5	7.08	7.05	60.19	79.08	77.05	P1 (1)	−0.087	
4 GPa, Mg ₁₂ Sn ₃ Si (16 atoms)	6.12	6.12	17.24	90	90	90	I4/mmm (139)	−0.144	
4 GPa, Mg ₆ Si ₃ Sn (10 atoms)	7.06	4.18	7.279	90	114.3	90	Pm(6)	−0.095	
2 GPa, Mg ₃ Si ₂ (10 atoms)	7.41	7.41	12.16	90	90	120	R-3C(167)	−0.087	
2 GPa, Mg ₂ Si (6 atoms)	5.67	10.14	4.07	90	90	90	I(mmm) (71)	−0.046	
2 GPa, Mg ₇ Si ₂ Sn (20 atoms)	9.49	7.50	7.88	75.12	111.12	118.41	P1 (1)	−0.063	
1 GPa, Mg ₃ Si ₂ (20 atoms)	8.21	8.66	5.94	90	110.40	90	P21/c(14)	−0.040	
1 GPa, Mg ₂ Si (12 atoms)	6.99	4.17	8.01	90	90	90	Pnma(62)	−0.115	
0.025 GPa, Mg ₂ Si (12 atoms)	5.68	7.42	7.20	70.72	73.87	107.88	P-1 (2)	−0.024	
0.025 GPa, Mg ₆ Si ₃ Sn (10 atoms)	5.41	6.52	6.29	75.63	98.64	97.77	P1 (1)	−0.060	

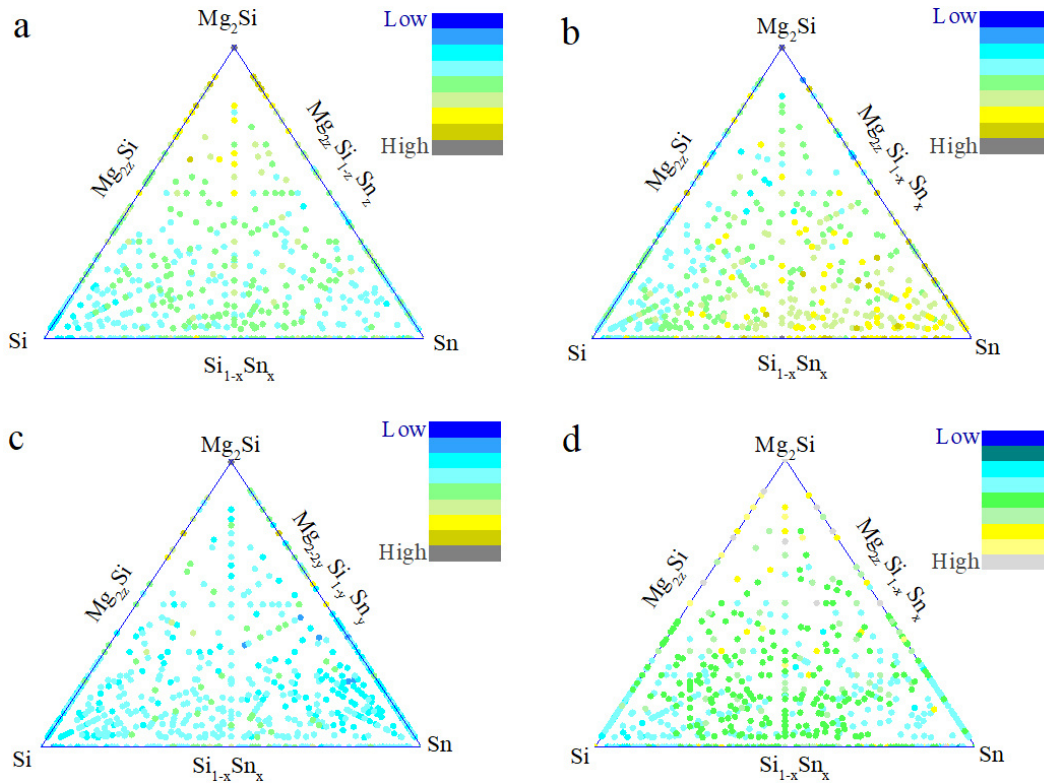


FIG. 1. The ternary composition-formation enthalpy phase diagram of the $Mg_A Si_B Sn_C$ at pressures: 1 GPa (a), 2 GPa (b), 4 GPa (c), and 6 GPa (d). Each structure is colored according to the distance from the convex hull in eV/atom, which varies from blue minimum to dark gray (maximum) see the legend bar on the left. As the color of a crystal structure becomes more dark, the crystal structure is the less stable and further away from the convex hull

As can be seen in Fig. 1, the number of stable compounds of magnesium, tin and silicon is strongly dependent on both the pressure and the enthalpy of formation of these structures. Thus, if at 6 GPa we have more than a hundred structures with negative enthalpy of formation, at 4 GPa there are less than thirty, at 2 GPa there are twelve, and at 1 GPa there are only three. There are too few three-component systems that are stable at ambient pressure conditions, most of them are two-component ones.

Table 1 shows the lattice parameters and enthalpies of formation of the most stable compounds of magnesium, silicon and tin obtained by evolutionary methods at external hydrostatic pressures of 1, 2, 4 and 6 GPa. The largest number of stable structures is found at pressure $P = 6$ GPa. The convex hull at this pressure is formed by four binary silicides Mg_4Si , Mg_2Si , $MgSi$, Mg_3Si_4 and one ternary compound, which has the composition Mg_4SiSn and the symmetry P-1. The corresponding unit cells are shown in the last column of Table 1. The tin-silicon alloy Mg_4SiSn (2 symmetry group) is a solid solution with a triclinic unit cell in which Ge and Si atoms are uniformly distributed throughout the volume. Binary silicides at pressure $P = 6$ GPa are characterized by a wide range of stoichiometry, symmetry and composition from 80 % of Mg and 20 % of Si (Mg_4Si), to 43 % of Mg and 57 % of Si (Mg_3Si_4). If we compare the enthalpy of formation of ternary alloy Mg_4SiSn and binary silicides Mg_xSi_y , it turns out that at a pressure of 6 GPa, the ternary alloy Mg_4SiSn is about 0.02 eV more stable than the monosilicide $MgSi$ 2 symmetry group P-1 and 0.04 eV more stable than the disilicide Mg_2Si 140 symmetry group I4/mcm.

At pressure $P = 4$ GPa, the convex hull is formed by four binary silicides $MgSi$, Mg_2Si , Mg_3Si_2 , Mg_7Si_5 and two three-component alloys Mg_6Si_3Sn and $Mg_{12}Si_3Sn$. Binary silicides exhibit different symmetry and structure, which can be compared to corresponding silicides in open access databases [41, 46, 47] as will be shown later. The ternary alloy Mg_6Si_3Sn at pressure $P = 4$ GPa has an enthalpy of formation $E \sim -0.1$ eV and it forms crystal structure of group 6 symmetry (Pm). As shown in the last column of Table 1, the ternary compound Mg_6Si_3Sn comprises alternating Mg-Sn-Mg-Si and Mg-Si layers. In each mixed Mg-Sn-Mg-Si type layer one Sn or Si atom is bonded to two Mg atoms, with the bond length of Mg-Sn approximately 2.9 Å and the bond length of Mg-Si ranging from 2.6 to 2.8 Å. Similarly, in each Mg-Si type layer, one atom of Si is bonded to two atoms of Mg, with the bond length of the Mg-Si varying from 2.6 to 2.8 Å. The $Mg_{12}Si_3Sn$ compound has an enthalpy of formation $E = -0.144$ eV and consists of alternating layers of binary compounds Mg_2Si and Mg_2Sn . First, there is a layer of alternating MgSi and MgSn in this structure. Then there is a continuous layer of Mg atoms at 16 m Wyckoff position in the unit cell. Then there is a layer of MgSi silicide followed by a layer of Mg atoms. That is followed by a layer of alternating MgSi and MgSn and all repeats. The distance

between neighboring layers is equal to 2.155 Å. The alloy with stoichiometry $\text{Mg}_{12}\text{Si}_3\text{Sn}$ surprisingly turns out to be the most energetically favorable in the entire range of given pressures from 0 to 10 GPa.

At pressure $P = 2$ GPa, the convex hull is formed by two binary silicides Mg_2Si , Mg_3Si_2 and one ternary compound $\text{Mg}_7\text{Si}_2\text{Sn}$. The binary silicides Mg_2Si , Mg_3Si_2 have 71 and 167 space groups symmetry (Immm and $R\bar{3}c$), respectively. The three-component alloy $\text{Mg}_7\text{Si}_2\text{Sn}$ has the lowest possible symmetry P1 and consists of Mg, Si and Ge atoms randomly distributed throughout the unit cell. The sustainability of this low symmetry structure remains questionable and requires further investigations. At pressure $P = 1$ GPa, the convex hull is formed only by two binary silicides Mg_2Si , Mg_3Si_2 of symmetry group 14 and 62 ($P2_1/c$ and Pnma), respectively. At ambient pressure conditions, USPEX evolutionary searches found it difficult to identify stable three-component systems because most calculations tend to converge on two-component ones. There is only one ternary structure $\text{Mg}_6\text{Si}_3\text{Sn}$ of 2 symmetry group P-1 at pressure $P = 0.25$ GPa, as shown at the end of Table 1.

For a more detailed study of the stability of the most energetically favorable structures in different pressures, all results presented in Table 1 were recalculated in the pressure range from 0 to 10 GPa with full geometry re-optimization. Fig. 2 shows the most stable structures with negative formation enthalpy, obtained by optimizing the results of the evolutionary search at each pressure in steps of 1 GPa. The most energetically favorable three-component alloy structure is three-component alloy $\text{Mg}_{12}\text{Si}_3\text{Sn}$ of 139 space group symmetry I4/mmm. This structure is the most stable of all obtained three-component ones. At pressures above 10 GPa, it loses enthalpy to a binary silicide Mg_3Si_2 of space group 15 symmetry, which has the lowest enthalpy of all binary silicides Mg_xSi_y obtained. The other two three-component structures $\text{Mg}_6\text{Si}_3\text{Sn}$ and Mg_4SiSn are sufficiently higher in enthalpy than the $\text{Mg}_{12}\text{Si}_3\text{Sn}$ one. As shown in Fig. 2, it is also more stable than the trigonal structure of Mg_3Si_2 of symmetry group 167 ($R\bar{3}c$) in the entire pressure range below 10 GPa. Next on the Enthalpy-axis is the three-component structure $\text{Mg}_6\text{Si}_3\text{Sn}$, which is energetically more favorable than the binary silicide structure Mg_3Si_2 167 symmetry group only at pressures $P < 2$ GPa. At $P > 2$ GPa it loses to other structures, such as non-symmetric three-component alloy $\text{Mg}_6\text{Si}_3\text{Sn}$ and binary silicide Mg_7Si_5 . The Mg_7Si_5 structure looks defective and its stability remains questionable, as well as the stability of the non-symmetrical $\text{Mg}_6\text{Si}_3\text{Sn}$ one.

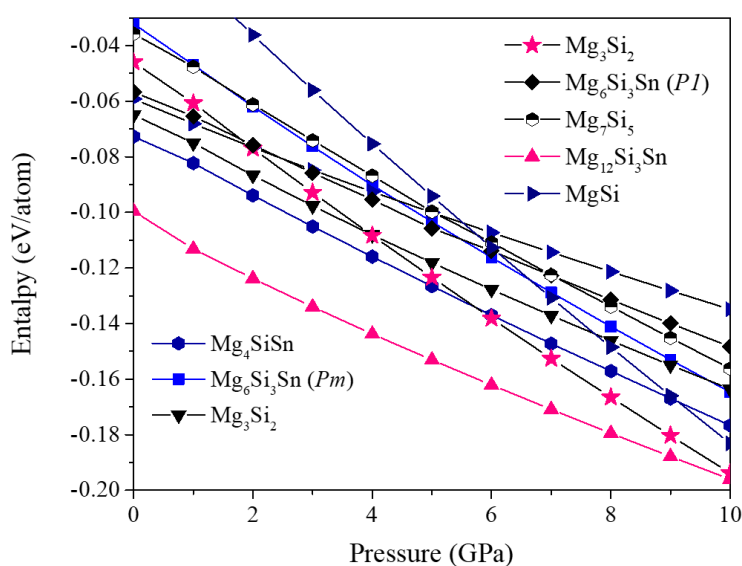


FIG. 2. Enthalpy-pressure dependence for the most energetically favorable crystal structures obtained by optimizing the results of the evolutionary search

Although this work is aimed at investigating ternary compounds, it is also useful to compare the obtained binary Mg_xSi_y compounds with the known results available in Material Project [41] and the Open Quantum Materials [46, 47] databases. Most were shared by our Vietnamese colleagues Huan et al., they are described in [11, 12].

The graph in Fig. 3 compares the enthalpy-pressure dependencies for known binary structures [41, 46, 47] with those obtained in the current study. The top two curves correspond to the most energetically favorable Mg_3Si_4 structures from the database [41] obtained by Huan et al. [11, 12]. We can see that their formation enthalpy is negative only for large non-zero pressures $P > 2$ GPa. Below, these two curves in Fig. 3 are the dark blue curve corresponding to the more energetically favorable Mg_3Si_4 structure obtained in the current study. This structure has the negative enthalpy of formation at any pressure $P \geq 0$. The binary silicide Mg_3Si_4 has 44 group symmetry Imm2 and the following lattice parameters: $a = 13.75$ Å, $b = 3.57$ Å, $c = 5.07$ Å, $\alpha = \beta = \gamma = 90^\circ$.

Below, the curves discussed above are green curves with triangular symbols pointing upwards, corresponding to the structure of the monosilicide MgSi. The enthalpy values of this curve practically coincide with those of the curve obtained in the calculation of the most favorable MgSi structure from the database [41] in the whole pressure range

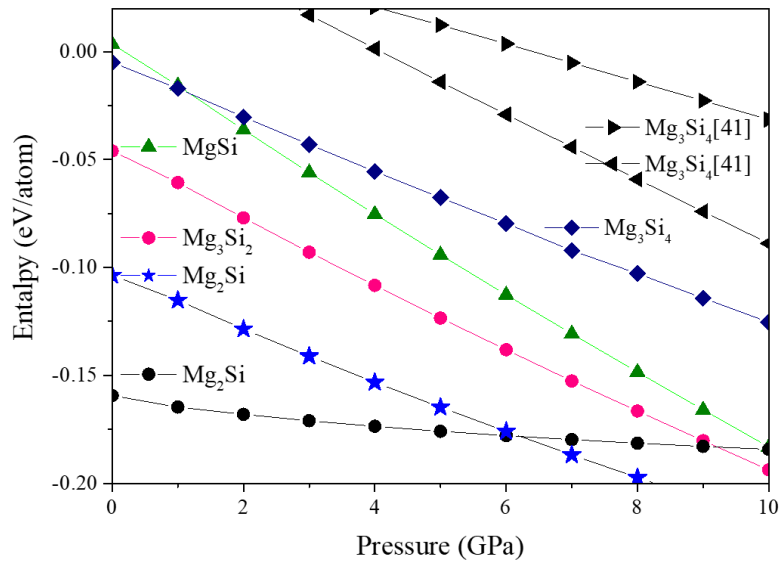


FIG. 3. Enthalpy-pressure dependence for the most stable binary magnesium silicides, obtained by evolutionary search, in comparison with the calculated enthalpy pressure-dependence of known structures

studied. If we plot the enthalpy-pressure dependence for the MgSi structure from the database [41] and then compare it with the dependence obtained for the triclinic MgSi structure in this work, their difference does not exceed 0.03 eV in the entire pressure $0 < P \leq 10$ GPa. The binary monosilicide MgSi has 2 group symmetry P-1 and the following lattice parameters: $a = 5.44 \text{ \AA}$, $b = 5.42 \text{ \AA}$, $c = 6.06 \text{ \AA}$, $\alpha = 110.7^\circ$, $\beta = 113.8^\circ$, $\gamma = 83.6^\circ$. In this structure, there are three non-equivalent Mg atoms bonded to six Si atoms (see Table 1, last column).

The red curve with triangular symbols pointing down corresponds to the structure of Mg₃Si₂. As in the case of MgSi monosilicide, the curve practically coincides with the curve obtained in these calculations for the most energetically favorable Mg₃Si₂ structure. The possible difference is not more than 0.03 eV, which can be considered an acceptable error, making the curves for these structures practically indistinguishable. The Mg₃Si₂ structure with the lowest energy from [41] has 15 group symmetry C2/c and lattice parameters: $a = 7.82 \text{ \AA}$, $b = 7.30 \text{ \AA}$, $c = 6.87 \text{ \AA}$, with angles $\alpha = 90^\circ$, $\beta = 104.26^\circ$, $\gamma = 90^\circ$ (see Table 1, last column). In the ambient pressure conditions, the Mg₃Si₂ structure, obtained in this work and shown in Fig. 3, has 15 group symmetry and lattice parameters $a = 8.09 \text{ \AA}$, $b = 7.38 \text{ \AA}$ and $c = 6.63 \text{ \AA}$, and angle $\beta = 104^\circ$, leading to an increase in unit cell volume of about 1 % compared to the data from [41]. Both of these structures are characterized by parallel-oriented silicon dimers with Si–Si bond lengths of approximately 2.4 Å. The enthalpy-pressure dependence for the structure in this work is practically identical to that obtained from the database structure [41] (see Fig. 2). The difference between them does not exceed 0.025 eV per atom in the pressure range from 0 to 10 GPa.

The Mg₂Si anticottunite-type structure obtained in this study (star-marked curve in Fig. 1) differs from the known antiferrotype structure of Mg₂Si of symmetry group 225 (bullet-marked curve in Fig. 1). In the absence of external pressure, the energy difference between the structure obtained in this work and the known antiferrotype structure is 0.056 eV and decreases to 0 at pressure around 6 GPa. Obviously, in this study a suboptimal anticottunite-type Mg₂Si structure has been obtained, which is more energetically favorable at high pressures $P > 6$ GPa [30]. It has 62 group symmetry Pnma and cell parameters $a = 7.04 \text{ \AA}$, $b = 4.20 \text{ \AA}$ and $c = 8.05 \text{ \AA}$, which are close to the Material Project Pnma cell parameters $a = 6.99 \text{ \AA}$, $b = 4.14 \text{ \AA}$ and $c = 7.99 \text{ \AA}$ [41]. This difference in results might be caused by the use of the variable composition mode in the USPEX code [33–37], where for each fixed ratio of Mg, Si, Sn components a smaller number of structures is generated, which does not always allow finding the minimum energy structure.

Nevertheless, the results for ternary structures with other stoichiometries of Mg₄SiSn, Mg₆Si₃Sn, and Mg₁₂Sn₃Sn demonstrate rather good stability with respect to their enthalpies. As shown in Fig. 2, besides two curves corresponding to the ternary compounds Mg₄SiSn and Mg₁₂Sn₃Sn, there are two curves corresponding to two different types of structures of the ternary compound Mg₆Si₃Sn. The first one is triclinic with 1 group symmetry P1 and the second one is monoclinic with 6 group symmetry Pm. The triclinic structure of Mg₆Si₃Sn (Table 1, last row) has an asymmetric cell with lattice parameters $a = 5.41 \text{ \AA}$, $b = 6.52 \text{ \AA}$, $c = 6.29 \text{ \AA}$, $\alpha = 75.63^\circ$, $\beta = 98.64^\circ$, $\gamma = 97.77^\circ$, while the monoclinic structure of Mg₆Si₃Sn (Table 1 10 row) has two right angles $\alpha = \gamma = 90^\circ$, one obtuse angle $\beta = 114.5^\circ$ and lattice parameters $a = 7.29 \text{ \AA}$, $b = 4.26 \text{ \AA}$, $c = 7.42 \text{ \AA}$. The enthalpy difference for these two Mg₆Si₃Sn structures is no more than 0.01 eV at pressures $P \leq 1$ GPa and increases to ~ 0.02 meV with increasing pressure up to $P = 10$ GPa. At pressures $P \leq 2$ GPa, the triclinic structure is more stable, and at pressures $P > 2$ GPa, the monoclinic structure becomes more

enthalpy favorable. However, in order to draw conclusions about the stability of the obtained structures, it is also necessary to study their phonon spectra, which was done in this work.

To confirm the dynamical stability of three-component alloys, phonon dispersion curves at ambient pressure conditions have been calculated for Mg_4SiSn , $\text{Mg}_{12}\text{Sn}_3\text{Si}$ and two $\text{Mg}_6\text{Si}_3\text{Sn}$ structures. The method of obtaining force constants from forces and atomic displacements using the $2 \times 2 \times 2$ supercells, developed by Togo A. and implemented in the PHONOPY code [48, 49], was used. As shown in Fig. 4, the phonon dispersion curves do not show any imaginary frequencies, which prove the stability of the corresponding compounds. Imaginary frequencies appear near the gamma points in the two graphs of the figure, imaginary frequencies appear only at the gamma points in the graphs of Fig. 4 (c and d), which is simply related to the size of the supercell used in the calculations. If it is too small, this leads to inaccurate force constants, which is the reason for the appearance of imaginary phonon frequencies [50]. To check the influence of size effects, additional calculations were performed with an enlarged $3 \times 3 \times 3$ supercell for $\text{Mg}_6\text{Si}_3\text{Sn}$, both triclinic and monoclinic. The results show that for monoclinic structure the imaginary frequencies disappear near the gamma point when the supercell size is increased, and the rest of the dispersion curves remain almost unchanged (see Fig. 4(e,f)). On the contrary, for triclinic structure, the negative dip near gamma point becomes deeper than for the $2 \times 2 \times 2$ supercell calculations which evidence the instability of the monoclinic structure in contrast to the triclinic one.

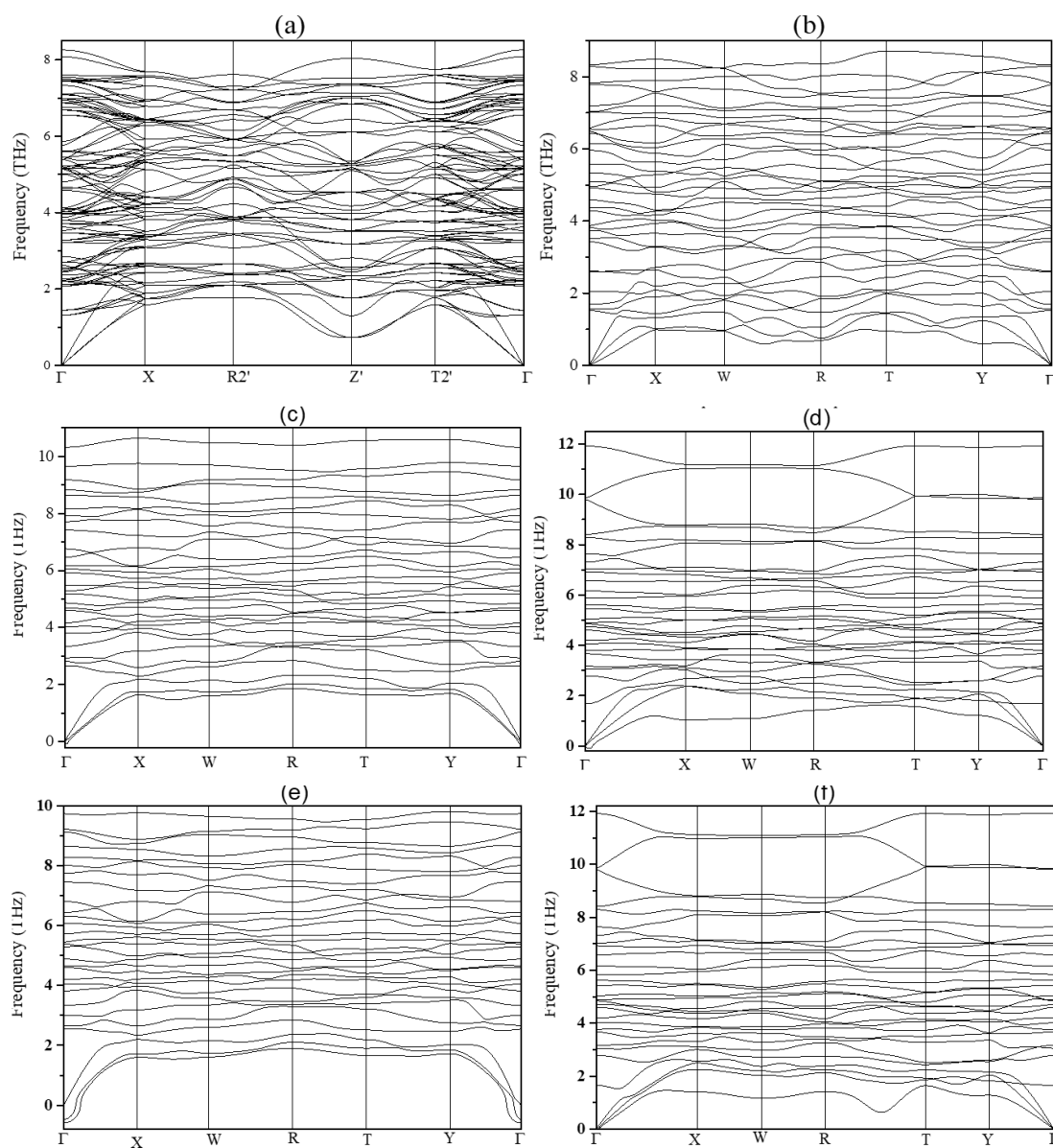


FIG. 4. Phonon dispersion curves of (a) $\text{Mg}_{12}\text{Sn}_3\text{Si}$; (b) Mg_4SiSn ; (c) triclinic $\text{Mg}_6\text{Si}_3\text{Sn}$; (d) monoclinic $\text{Mg}_6\text{Si}_3\text{Sn}$; (e) triclinic $\text{Mg}_6\text{Si}_3\text{Sn}$ obtained using the enlarged $3 \times 3 \times 3$ supercell; (f) monoclinic $\text{Mg}_6\text{Si}_3\text{Sn}$ obtained using the enlarged $3 \times 3 \times 3$ supercell

Phonon structure calculations allow a simple estimation of the phonon contribution to the free energy

$$F_{\text{phonon}} = \frac{1}{2} \sum_{q,\nu} \hbar\omega_{q,\nu} + k_B T \sum_{q,\nu} \ln \left(1 - e^{-\frac{\hbar\omega_{q,\nu}}{k_B T}} \right),$$

where q denotes the wave vector, ν is the phonon band index, ω is the corresponding phonon frequency, T is the temperature, and k_B is the Boltzmann constant. The estimate shows that at temperatures $T \leq 350$ K, this contribution does not exceed 0.05 eV per atom in absolute value, and for different structures, this contribution is approximately the same value, their difference being less than 0.02 eV.

In order to investigate the conductive properties of three-component systems at ambient pressure conditions, densities of states were calculated for the most energetically favorable compounds $\text{Mg}_x\text{Si}_y\text{Sn}_z$. Fig. 5 displays the electronic state densities of the three-component alloys with the lowest formation energy $\text{Mg}_{12}\text{Si}_3\text{Sn}$, Mg_4SiSn and $\text{Mg}_6\text{Si}_3\text{Sn}$. This information can be used to evaluate the conductive properties of the materials. All of the alloys considered above have states at Fermi levels indicating that they all exhibit metallic properties in one way or another unlike the binary silicide Mg_2Si and stannide Mg_2Sn , which are semiconductors under normal conditions [30–32]. However, from the magnitude of the density of states in Fig. 5, the best metallic properties are likely to be exhibited by the solid solutions of Mg_4SiSn (Fig. 5(a)) and $\text{Mg}_{12}\text{Si}_3\text{Sn}$ (Fig. 5(b)) stoichiometries, which has significantly more of them at the Fermi level.

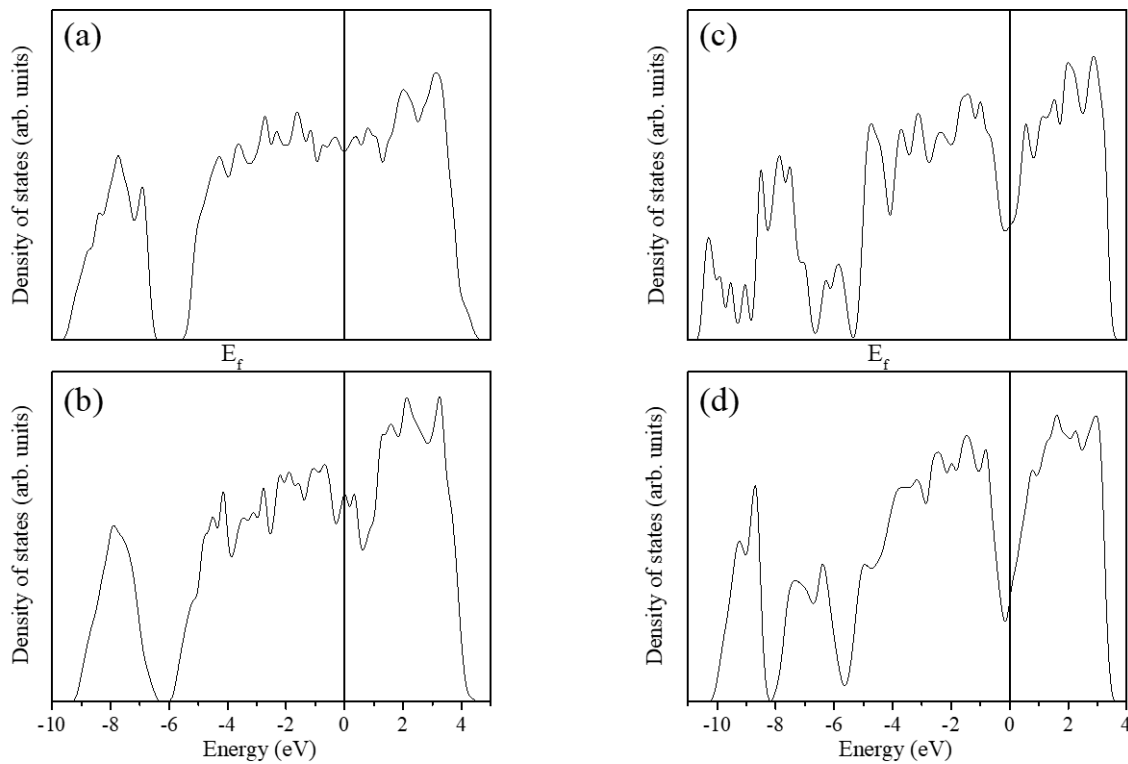


FIG. 5. Density of electronic states of the most energetically favorable ternary compounds (a) Mg_4SiSn ; (b) $\text{Mg}_{12}\text{Si}_3\text{Sn}$; (c) triclinic $\text{Mg}_6\text{Si}_3\text{Sn}$; (d) monoclinic $\text{Mg}_6\text{Si}_3\text{Sn}$. The Fermi level is chosen as the energy reference point

4. Conclusion

The results of the evolutionary modeling of three-component systems allowed to reproduce binary structures of the known stoichiometries MgSi and Mg_3Si_2 , as well as to obtain new structures of the stoichiometries Mg_4SiSn , $\text{Mg}_6\text{Si}_3\text{Sn}$, $\text{Mg}_{12}\text{Si}_3\text{Sn}$, and $\text{Mg}_7\text{Si}_2\text{Sn}$ with the ternary alloy $\text{Mg}_{12}\text{Si}_3\text{Sn}$ being the most stable one. All of them have a negative enthalpy of formation, comparable to the enthalpy of formation of binary structures in the studied pressure range $0 < P \leq 10$ GPa. Phonon dispersion and density of states calculations confirmed the dynamical stability and metallic properties of the newly identified ternary alloys besides the triclinic structure. Density of states calculations indicate that the ternary alloys exhibit metallic properties, unlike the binary silicides and stannides.

References

- [1] Nayeb-Hashemi A.A., Clark J.B. The Mg-Sn (Magnesium-Tin) system. *Bulletin of Alloy Phase Diagrams*, 1984, **5** (5), P. 466–476.
- [2] Yamashita O., Tomiyoshi S. Effect of annealing on thermoelectric properties of bismuth telluride compounds. *Jpn J. Appl. Phys.*, 2003, **42** (2R), 492.
- [3] Marfoua B., Lagoun B., Lidjici H., Benghia A., Gueddouh A. Theoretical investigation of structural, electronic and thermoelectric properties of p-n type $\text{Mg}_2\text{Si}_{1-x}\text{Sn}_x$ system. *Pramana J. Phys.*, 2020, **94** (1), 6.
- [4] Liu W., Tan X., Yin K., Liu H., Tang X., Shi J., Zhang Q. Convergence of conduction bands as a means of enhancing thermoelectric performance of n-type $\text{Mg}_2\text{Si}_{1-x}\text{Sn}_x$ solid solutions. *Phys. Rev. Lett.*, 2012, **108** (16), 166601.
- [5] Sankhla A., Patil A., Kamila H., Yasserli M., Farahi N., Mueller E. and de Boor J. Mechanical alloying of optimized $\text{Mg}_2(\text{Si},\text{Sn})$ solid solutions: understanding phase evolution and tuning synthesis parameters for thermoelectric applications. *ACS Appl. Energy Mater.*, 2018, **1** (2), P. 531–542.
- [6] LeBlanc S., Yee S.K., Scullin M.L., Dames C., Goodson K.E. Material and manufacturing cost considerations for thermoelectrics. *Renew. Sustain. Energy Rev.*, 2014, **32**, P. 313–327.
- [7] Gaultois M.W., Sparks T.D., Borg C.K.H., Seshadri R.K., Bonificio W.D., Clarke D.R. Data-driven review of thermoelectric materials: performance and resource considerations. *Chemistry of Materials*, 2013, **25** (15), P. 2911–2920.
- [8] de Boor J., Dasgupta T., Mueller E. Thermoelectric properties of magnesium silicide-based solid solutions and higher manganese silicides. In *Materials Aspect of Thermoelectricity*, CRC press, Boca Ration, USA, 2016, 160 p.
- [9] Vantomme A., Mahan J.E., James G.L., Margriet P.B., Bael V., Temst K., Haesendonck C.V. Thin film growth of semiconducting Mg_2Si by codeposition. *Appl. Phys. Lett.*, 1997, **70** (9), P. 1086–1088.
- [10] Zhu Y., Han Zh., Jiang F., Dong E., Zhang B.-P., Zhang W., Liu W. Thermodynamic criterions of the thermoelectric performance enhancement in Mg_2Sn through the self-compensation vacancy. *Mater. Today Physics*, 2021, **16** (1), 100327.
- [11] Huan T.D. Pressure-stabilized binary compounds of magnesium and silicon. *Phys. Rev. Mater.*, 2018, **2** (2), 023803.
- [12] Huan T.D., Tuoc V.N., Le N.B., Minh N.V., Woods L.M. High-pressure phases of Mg_2Si from first principles. *Phys. Rev. B*, 2016, **93** (9), 094109.
- [13] Huan T.D., Tuoc V.N., Le N.B., Minh N.V., Woods L.M. Characterizing magnesium-silicon binaries in Al-Mg-Si supersaturated solid solution by first-principles calculations. *J. Sci.-Adv. Mater. Dev.*, 2016, **1** (4), P. 527–530.
- [14] Vissers R., Huis M.A., Jansen J., Zandbergen H.W., Marioara C.D., Andersen S.J. The crystal structure of the β' phase in Al–Mg–Si alloys. *Acta Mater.*, 2007, **55** (11), P. 3815–3823.
- [15] Ravi C., Wolverson C. First-principles study of crystal structure and stability of Al–Mg–Si–(Cu) precipitates. *Acta Mater.*, 2004, **52** (14), P. 4213–4227.
- [16] Zandbergen H.W., Andersen S.J., Jansen J. Structure determination of Mg_5Si_6 particles in Al by dynamic electron diffraction studies. *Science*, 1997, **277** (5330), P. 1221–1225.
- [17] Andersen S.J., Zandbergen H.W., Jansen J., Traeholt C., Tundal U., Reiso O. The crystal structure of the β -phase in Al–Mg–Si alloys. *Acta Mater.*, 1998, **46** (9), P. 3283–3298.
- [18] Gao H., Zhu T., Liu X., Chen L., Zhao X. Flux synthesis and thermoelectric properties of eco-friendly Sb doped $\text{Mg}_2\text{Si}_{0.5}\text{Sn}_{0.5}$ solid solutions for energy harvesting. *J. Mater. Chem.*, 2011, **21** (16), P. 5933–5937.
- [19] Zaitsev V.K., Fedorov M.I., Gurieva E.A., Eremin I.S., Konstantinov P.P., Samunin A.Y., Vedernikov M.V. Highly effective $\text{Mg}_2\text{Si}_{1-x}\text{Sn}_x$ thermoelectrics. *Phys. Rev. B*, 2006, **74** (4), 045207.
- [20] Liu W., Tan X.J., Yin K., Liu H.J., Tang X.F., Shi J., Zhang Q.J., Uher C. Convergence of conduction bands as a means of enhancing thermoelectric performance of n-type $\text{Mg}_2\text{Si}_{1-x}\text{Sn}_x$ solid solutions. *Phys. Rev. Lett.*, 2012, **108** (16), 166601.
- [21] Liu W., Kim H.S., Chen S., Jie Q., Lv B., Yao M., Ren Z., Opeil C.P., Wilson S., Chu Ch.-W., Ren Z. N-type thermoelectric material $\text{Mg}_2\text{Sn}_{0.75}\text{Ge}_{0.25}$ for high power generation. *Proc. Natl. Acad. Sci.*, 2015, **112** (11), P. 3269–3274.
- [22] Zaitsev V.K., Fedorov M.I., Gurieva E.A., Eremin I.S., Konstantinov P.P., Samunin A., Vedernikov M.V. Thermoelectrics of n-type with $\text{ZT}_d > 1$ based on $\text{Mg}_2\text{Si-Mg}_2\text{Sn}$ solid solutions. In: *ICP, 24th International Conference on Thermoelectrics*, Clemson, SC, USA, 2005, P. 204–210.
- [23] Gao P., Berkun I., Schmidt R.D., Luzenski M.F., Lu X., Bordon Sarac P., Case E.D., Hogan T.P. Transport and mechanical properties of high-ZT $\text{Mg}_{2.08}\text{Si}_{0.4-x}\text{Sn}_{0.6}\text{Sb}_x$ thermoelectric materials. *J. Electron. Mater.*, 2014, **43**, P. 1790–1803.
- [24] Tan J., Liu W., Liu H.J., Shi J., Tang X.F., Yin X.K., Zhang Q.J., Uher C. Multiscale calculations of thermoelectric properties of n-type $\text{Mg}_2\text{Si}_{1-x}\text{Sn}_x$ solid solutions. *Phys. Rev. B*, 2012, **85** (20), 205212.
- [25] Dasgupta T., Stiewe C., de Boor J., Müller E. Influence of power factor enhancement on the thermoelectric figure of merit in $\text{Mg}_2\text{Si}_{0.4}\text{Sn}_{0.6}$ based materials. *Phys. Stat. Sol. A*, 2014, **211** (6), P. 1250–1254.
- [26] Tobola J., Kaprzyk S., Scherrer H. Mg-vacancy-induced semiconducting properties in $\text{Mg}_2\text{Si}_{1-x}\text{Sb}_x$ from Electronic Structure Calculations. *J. Electron. Mater.*, 2010, **39**, P. 2064–2069.
- [27] Kim S., Wiendlocha B., Jin H., Tobola J., Heremans J.P. Kim S., Wiendlocha B., Jin H., Tobola J., Heremans J.P. Electronic structure and thermoelectric properties of p-type Ag-doped Mg_2Sn and $\text{Mg}_2\text{Sn}_{1-x}\text{Si}_x$ ($x = 0.05, 0.1$). *J. Appl. Phys.*, 2014, **116** (15), 153706.
- [28] Zhang L., Xiao P., Shi L., Henkelman G., Goodenough J.B., Zhou J. Suppressing the bipolar contribution to the thermoelectric properties of $\text{Mg}_2\text{Si}_{0.4}\text{Sn}_{0.6}$ by Ge substitution. *J. Appl. Phys.*, 2015, **117** (15), 155103.
- [29] Kamila H., Sahu P., Sankhla A., Yasserli M., Pham H.N., Dasgupta T., Mueller E., de Boor J. Analyzing transport properties of p-type $\text{Mg}_2\text{Si-Mg}_2\text{Sn}$ solid solutions: optimization of thermoelectric performance and insight into the electronic band structure. *J. Mater. Chem. A*, 2019, **7** (3), P. 1045–1054.
- [30] Luniakov Yu.V. Mg_2Si silicide under pressure: first-principles evolution search results. *Physics of the Solid State*, 2020, **62** (5), P. 880–884.
- [31] Luniakov Yu.V. Mg_2Sn stannide under pressure: first-principles evolutionary search results. *Physics of the Solid State*, 2021, **63** (4), P. 590–594.
- [32] Luniakov Yu.V. Mg_2Ge germanide under pressure: first principle evolutionary search results. *Physics of the Solid State*, 2022, **64** (10), P. 1414–1419.
- [33] Oganov A.R., Pickard C.J., Zhu Q., Needs R.J. Structure prediction drives materials discovery. *Nat. Rev. Mater.*, 2019, **4** (5), P. 331–348.
- [34] Oganov A.R., Lyakhov O.A., Valle M. How evolutionary crystal structure prediction works – and why. *Acc. Chem. Res.*, 2011, **44** (3), P. 227–237.
- [35] Lyakhov A.O., Oganov A.R., Stokes H.T., Zhu Q. New developments in evolutionary structure prediction algorithm USPEX. *Comp. Phys. Comm.*, 2013, **184** (4), P. 1172–1182.
- [36] Oganov A.R., Ma Y., Lyakhov A.O., Valle M., Gatti C. Evolutionary crystal structure prediction as a method for the discovery of minerals and materials. *Rev. Mineral. Geochem.*, 2010, **71** (1), P. 271–298.
- [37] Oganov A.R. *Modern methods of crystal structure prediction*. John Wiley & Sons, USA, New York, 2011, 274 p.
- [38] Oganov A.R., Glass C.W. Crystal structure prediction using ab initio evolutionary techniques: Principles and applications. *J. Chem. Phys.*, 2006, **124** (24), 244704.

- [39] Kresse G., Furthmüller J.E. Efficient iterative schemes for ab initio total-energy calculations using a plane-wave basis set. *Phys. Rev. B*, 1996, **54** (16), P. 11169–11186.
- [40] Perdew J.P., Burke K., Ernzerhof M. Generalized gradient approximation made simple. *Phys. Rev. Lett.*, 1996, **77** (18), P. 3865–3868.
- [41] Jain A., Ong S.P., Hautier G., Wei Ch., Richards W.D., Dacek S., Cholia S., Gunter D., Skinner D., Ceder G., Persson K.A. The materials project: a materials genome approach to accelerating materials innovation. *APL materials*, 2013, **1** (011), 011002.
- [42] Olijnyk H., Holzapfel W.B. High-pressure structural phase transition in Mg. *Phys. Rev. B*, 1985, **31** (7), 4682.
- [43] Errandonea D., Meng Y., Husermann D., Uchida T. Study of the phase transformations and equation of state of magnesium by synchrotron x-ray diffraction. *J. Phys.: Condens. Matter*, 1989, **15** (8), 1277.
- [44] Desgreniers S., Vohra Y.K., Ruoff A.L. Tin at high pressure: An energy-dispersive X-ray-diffraction study to 120 GPa. *Phys. Rev. B*, 2012, **39** (14), P. 10359–10361.
- [45] Salamat, Ashkan, et al. High-pressure structural transformations of Sn up to 138 GPa: Angle-dispersive synchrotron X-ray diffraction study. *Phys. Rev. B*, 2013, **88** (10), 104104.
- [46] Saal J.E., Kirklin S., Aykol M., Meredig B., Wolverton C. Materials design and discovery with high-throughput density functional theory: The Open Quantum Materials Database (OQMD). *JOM*, 2013, **65**, P. 1501–1509.
- [47] Kirklin S., Saal J.E., Meredig B., Thompson A., Doak J.W., Aykol M., Ruhl S., Wolverton Ch. The Open Quantum Materials Database (OQMD): assessing the accuracy of DFT formation energies. *NPJ Comput. Mat.*, 2015, **1**, 15010.
- [48] Togo A., Chaput L., Tadano T., Tanaka I. Implementation strategies in Phonopy and Phono3py. *J. Phys. Condens. Matter*, 2023, **35**, 353001-1-22.
- [49] Togo A. First-principles phonon calculations with Phonopy and Phono3py. *J. Phys. Soc. Jpn.*, 2023, **92**, 012001-1-21.
- [50] Lloyd-Williams J.H., Monserrat B. Lattice dynamics and electron-phonon coupling calculations using nondiagonal supercells. *Phys. Rev. B*, 2015, **92** (18), 184301.

Submitted 18 July 2024; revised 24 September 2024; accepted 26 September 2024

Information about the authors:

Yuri V. Luniakov – Institute of Automation and Control Processes of the Far Eastern Branch of the Russian Academy of Sciences, Radio Str. 5, 690041, Vladivostok, Russia; luniakov@mail.ru

Tuning the nonlinear optical properties of a 1D excitonic GaAs quantum dot system under a semi-parabolic potential with a detailed comparison with the experimental results: interplay of hydrostatic pressure and temperature

Suman Dahiya¹, Siddhartha Lahon^{2,a}, Rinku Sharma^{1,b}

¹Department of Applied Physics, Delhi Technological University, Delhi 110042, India

²Physics Department, KMC, University of Delhi, Delhi 110007, India

^asid.lahon@gmail.com, ^brinkusharma@dtu.ac.in

Corresponding author: Siddhartha Lahon, sid.lahon@gmail.com

ABSTRACT The present study is dedicated to study the effect of Temperature and Hydrostatic Pressure on the absorption coefficient and refractive index of one-dimensional semi-parabolic excitonic GaAs QD's by applying the compact density matrix formalism. Calculations are performed to obtain the excitonic state wave functions and energies in the strong confinement regime using the effective mass approximation. A significant dependence of nonlinear optical refractive index and absorption coefficient on hydrostatic pressure and temperature can be observed for excitonic and without excitonic case. Our investigations show that the peaks blue/red shifts are substantial when the excitonic interactions are taken into account. The opposite effects caused by temperature and pressure have substantial practical importance as they extend an alternative approach to tune and control the optical frequencies resulting from the transitions. The comparative analysis of the analytical optical properties of excitonic system facilitates the experimental identification of these transitions which are often close. We have attempted a comparison of the absorption coefficient obtained in the present work with experimental data at $T \cong 10$ and 100 K and found that the theoretical prediction is in agreement for $T \cong 10$ K and it is in slight deviation from the experimental data for higher temperatures. The whole of these conclusions may have broad implications in future designing of Optoelectronic devices.

KEYWORDS nanostructures, quantum dot, exciton, nonlinear effects, hydrostatic pressure, temperature

ACKNOWLEDGEMENTS We acknowledge sincere gratitude to Delhi Technological University to appreciate their help and enhance our services and facilities.

FOR CITATION Dahiya S., Lahon S., Sharma R. Tuning the nonlinear optical properties of a 1D excitonic GaAs quantum dot system under a semi-parabolic potential with a detailed comparison with the experimental results: interplay of hydrostatic pressure and temperature. *Nanosystems: Phys. Chem. Math.*, 2024, **15** (5), 632–642.

1. Introduction

The semiconductor nanomaterials such as quantum dots (QD), quantum wires and quantum wells have many applications in the generation of optoelectronic devices such as lasers, infrared and THz photodetectors, solar cells, biological imaging devices, photovoltaics, LEDs, etc., owing to their enchanting physical properties due to the quantum confinement effects in all spatial directions [1–5]. Out of all these nanostructures, quantum dots of various shapes, sizes and strong confinement of electron and holes have been given special attention as they possess interesting physics in terms of the unique electronic and optical properties. Quasi-zero-dimensional quantum dots can be considered as nano crystalline structures that can provide limitless utility in the implementation of many semiconductors' optoelectronic devices such as quantum dot solar cells, spintronics and ultrafast quantum computers. Accordingly, unprecedented attention has been given to the semiconductor nanomaterials in the last few decades [6–13].

The parabolic and semi parabolic confinement potential can allow various resonances, due to the constant spacing of the discrete energy levels which accounts for the enormous enhancement of the nonlinear optical susceptibilities, optical transitions within the valence and conduction band, and absorption properties [14–17]. Furthermore, the parabolic and semi parabolic potential confinement is more relevant when the zero-dimensional quantum dots are fabricated by using an etching process, ion implantation or electrostatic gates. We have found considerable investigations on the nonlinear optical and electronic properties such as Refractive Index (RI), Absorption Coefficient (AC) and Rectification Coefficient (RC) with photon energy and external factors such as temperature, hydrostatic pressure and dot size [18–20]. For photons having energies equal to that of inter-subband transition energies, host material finds a significant change in dielectric constant, thereby inducing changes in the nonlinear excitonic optical properties [21–24].

Numerous investigations and interesting studies are done on the nonlinear optical properties of nanostructures especially Quantum dots under the influence of external factors such as electric field, magnetic field etc. [21–30]. Many

authors studied the effect of excitons in one dimensional semi parabolic quantum dots [31–34]. Duque et al. studied the effect of external factors such as electric field, magnetic field, hydrostatic pressure, laser field and temperature on nonlinear properties in excitonic system [35–38]. Bejan et al. demonstrated the effect of electric field on the optical properties of a semi parabolic quantum dot in an excitonic system [39]. Kumar et al. further investigated the effect of hydrostatic pressure, temperature and spin on the optical and electronic properties of nanostructures [40,41]. To summarize, the interesting results of the ramifications of external factors such as hydrostatic pressure, temperature, electric field and magnetic field on the nanostructures bring out plethora of novel and exciting physical properties.

The main objective of the present work is to investigate the effect of external factors such as temperature and hydrostatic pressure on the RI and AC of excitonic system in 1D semi parabolic quantum dot. An excitonic system is a bound electron-hole pair with more closely matched effective masses that is formed by the electrostatic interaction between the electron and hole. Theoretically, this system can be related to the hydrogenic system and it possess discrete energies. A 1D QD is principally a nanostructure which can be assumed as a small portion of a 1D QW which is bordered by a two-wall potential. The charge carriers are free to move along the wire in 1-D QW, whereas they are restricted to move along the spatial length in 1D QD [27,42–45]. The core study undertaken in this research paper focuses on a one-dimensional semi parabolic quantum dot, which is strongly confined in the x and y direction and electrons and holes are confined by a semi parabolic potential along the z direction. We know that the hydrostatic pressure and temperature can alter the nonlinear properties such as the refractive index and absorption coefficient for excitonic effects (EE) as well as without excitonic effect (WEE). In order to keep the study concise and in line with the experimentally available results, we have restricted our studies to the two extreme limits of a temperature range 10 – 100 K where it is observed that the sharpest absorption peaks or transmittance dips are observed at low temperatures in the mentioned range or even lower than that. Furthermore, it is observed that as temperature increases above 100K, the value of the thermal excitation energy of the charge carriers, namely $kT/2$, attains significant values.

In our recent work, we have reported the effect of temperature and hydrostatic pressure on the optical rectification associated with the excitonic system in a semi-parabolic quantum dot [46]. It is highlighted that most available literature reports are primarily based on the nonlinear optical properties due to impurities or due to different shape of quantum structures. To our sincere understanding, there are no studies available where the hydrostatic pressure and temperature effects on the nonlinear optical properties of excitonic system in one dimensional semi parabolic quantum dots have been studied and explained. The present paper is structured as follows: In the next section, theoretical analytical framework is presented to calculate the eigen energies, eigen functions and optical properties for the excitonic system. In the Results and Discussion section, we have presented our numerical results and discussion. In the last section of conclusion, we have summarized our results.

2. Theory and model

A theoretical model of the system taken is presented in Fig. 1. Here, the gate voltage in the model is used to control Rashba spin-orbit interaction (SOI) where the effects of SOI are studied. In our case, we have kept the gate voltage to be Zero. The x -direction is kept to be very small i.e., about 2nm so that the charge carriers behave as a 2D charge carrier gas. The y -length of the wire is in μm -range, so the charge carrier exhibit e^{-ky} wave function. The z -directions breadth is determined by the potential strength and in our case, the effective z -length turns out to be 5 nm. Now, moving towards the mathematical calculations related to the system.

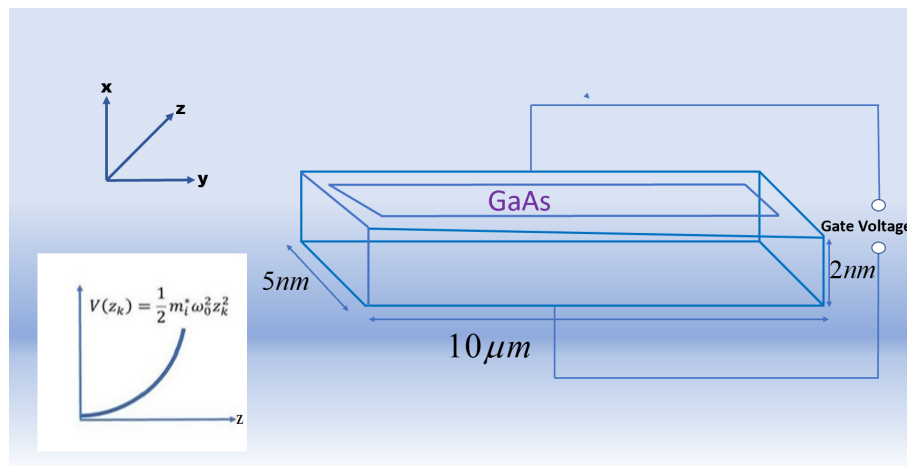


FIG. 1. Schematic diagram of GaAs Quantum Dot

Hamiltonian for a 1D excitonic QD having semi-parabolic confining potential within the framework of effective mass approximation can be written as [25, 27, 31, 42]:

$$H_e = \frac{p_h^2}{2m_h^*(P, T)} + \frac{p_e^2}{2m_e^*(P, T)} + V(z_e) + V(z_h) - \frac{e^2}{\varepsilon |z_e - z_h|}, \quad (1)$$

where $z_e, z_h > 0$.

Here m_h^* and m_e^* represents the effective mass of hole and electron, respectively, ε represents the background dielectric constant and the last term represents the electrostatic Coulomb interaction term between the electron and the hole. The semi-parabolic confinement potential $V(z_k)$ is written as:

$$V(z_k) = \begin{cases} \frac{1}{2} m_i^* \omega_0^2 z_k^2, & z_k \geq 0; \\ \infty, & z_k \leq 0 \quad (k = e, h). \end{cases} \quad (2)$$

The temperature and hydrostatic pressure dependent effective mass of the electron for GaAs is given as [38, 40, 41]:

$$m_e^*(P, T) = m_o \left[1 + \frac{7510}{E_g(P, T) + 341} + \frac{15020}{E_g(P, T)} \right]^{-1}, \quad (3a)$$

$$m_h^*(P, T) = (0.09 - 0.20 \cdot 10^{-3}P - 3.55 \cdot 10^{-5}T) m_o, \quad (3b)$$

with

$$E_g(P, T) = \left[1519 - \frac{0.5405T^2}{T + 204} + 10.7P \right]. \quad (4)$$

Here temperature and hydrostatic pressure dependent energy gap GaAs, E_g is in meV, P is in ‘‘kbar’’ and T is in ‘‘Kelvin’’. The pressure dependent oscillator frequency is expressed as

$$\omega(P) = \omega_0 / [1 - 2P(1.16 \cdot 10^{-3} - 7.4 \cdot 10^{-4})]. \quad (5)$$

The Hamiltonian is segmented into two terms taking the relative motion and the center of mass into consideration and is given by:

$$H_{e1} = H_{r1} + H_{c1}, \quad (6)$$

$$H_{r1} = \frac{p^2}{2\mu} + \frac{1}{2} \mu \omega_0^2 z_{r1}^2 - \frac{e^2}{\varepsilon(P, T) |z_{r1}|}, \quad (7)$$

$$H_{c1} = \frac{P^2}{2M_{T1}} + \frac{1}{2} M_{T1} \omega_0^2 Z_{T1}^2. \quad (8)$$

For $T < 200$, the dielectric constant of GaAs is [38–40]:

$$\varepsilon(P, T) = 12.74e^{(9.4 \cdot 10^{-5})(T-75.6)+1.73 \cdot 10^{-3}P}. \quad (9)$$

The coordinate of the centre of mass is written as:

$$Z_{T1} = \frac{m_h^*(P, T)z_h + m_e^*(P, T)z_e}{M_{T1}}. \quad (10)$$

Here, total mass is $M_{T1}(P, T) = m_h^*(P, T) + m_e^*(P, T)$; the relative coordinate is $z_{r1} = z_e - z_h$, the momentum operator is $p_{Z_{T1}} = \frac{\hbar}{i} \nabla_{Z_{T1}}$, and the reduced mass is

$$\mu_{r1} = m_h^*(P, T)m_e^*(P, T)/M_{T1}(P, T). \quad (11)$$

The excitonic wave function and energy levels are written as

$$\psi_{f1}(z_h, z_e) = \phi(z_{r1})\varphi(Z_{T1}), \quad (12)$$

$$E_{T1} = E_{z_{r1}} + E_{Z_{T1}}. \quad (13)$$

The term signifying the center of mass part is considered as the problem for 1D semi-parabolic oscillator where the Hamiltonian is H_{c1} and eigenfunction and eigenenergies are [42]:

$$\varphi_{k1}(Z_{T1}) = N_{k1} \exp\left(-\frac{1}{2}\alpha^2 Z_{T1}^2\right) H_{2k1+1}(\alpha Z_{T1}), \quad (14)$$

$$E_{k1} = \left(2k1 + \frac{3}{2}\right) \hbar\omega_0, \quad k1 = (0, 1, 2, \dots), \quad (15)$$

where H_{2k1+1} is the Hermite polynomial

$$N_{k1} = \left[\frac{1}{\alpha} \sqrt{\pi} 2^{2k1} (2k1 + 1)! \right]^{-1/2}, \quad (16)$$

$$\alpha = \sqrt{M_{T1}\omega(P)/\hbar_k}. \quad (17)$$

We analytically obtained the eigenvalues and wave function of the relative motion part in the strong and weak confinement regime. For the strong regime, H_{r1} reduces to:

$$H_{r1s} = \frac{p^2}{2\mu} + \frac{1}{2}\mu\omega_0^2 z_{r1}^2. \quad (18)$$

Neglecting the coulomb term as per the strong confinement regime, $\varphi(z_{r1})$ is determined as:

$$\phi(z_{r1}) = N_n \exp\left[-\frac{1}{2}\beta^2 z_{r1}^2\right] H_{2n+1}(\beta z_{r1}), \quad (19)$$

$$E_{y1} = \left(2n + \frac{3}{2}\right) \hbar\omega_0, \quad (y1 = 0, 1, 2, \dots), \quad (20)$$

$$N_n = \left[\frac{1}{\beta}\sqrt{\pi}2^{2n+1}(2n+1)!\right]^{-1/2}, \quad (21)$$

$$\beta = \sqrt{\mu\omega(P)/\hbar}. \quad (22)$$

Our quantum dot interacts with the electromagnetic field $E(t)$ having a frequency ω , such that [47–49]:

$$E(t) = Ee^{i\omega t} + E^*e^{-i\omega t}. \quad (23)$$

Upon such interactions, the time evolution equation for the matrix elements of one-electron density operator, ρ , is given by

$$\frac{\partial\rho}{\partial t} = \frac{1}{i\hbar} [H_0 - qx E(t)\rho] - \Gamma(\rho - \rho^{(0)}), \quad (24)$$

where H_0 represents the Hamiltonian of this system in the absence of the electromagnetic field $E(t)$, and electronic charge is given by q , unperturbed density matrix operator is ρ^0 , and Γ is the phenomenological operator responsible for the damping due to the electron-phonon interaction, collisions among electrons, etc. It is assumed that Γ is a diagonal matrix and its elements are equal to the inverse of relaxation time τ_0 .

For solving Eq. (19), standard iterative method is being used and hence ρ has been expanded as $\rho(t) = \sum_n \rho^{(n)}(t)$.

Now, using this expansion in Eq. (19), the density matrix elements can be obtained as shown below:

$$\frac{\partial\rho_{ij}^{(n+1)}}{\partial t} = \left[\frac{1}{i\hbar}[H_0, \rho^{(n+1)}]_{ij} - \Gamma_{ij}\rho_{ij}^{(n+1)} - \frac{1}{i\hbar}[qx, \rho^{(n)}]_{ij}E(t)\right]. \quad (25)$$

As the density matrix ρ has been obtained, the electronic polarization $P(t)$ and susceptibility $\chi(t)$ can be calculated as:

$$P(t) = \varepsilon_0\chi(\omega)Ee^{-i\omega t} + \varepsilon_0\chi(-\omega)Ee^{-i\omega t} = \frac{1}{V} \text{Tr}(\rho M), \quad (26)$$

where ρ is the density matrix for one electron and V is the volume of the system, ε_0 represents permittivity of free space, and the symbol Tr (trace) denotes the summation over the diagonal elements of the matrix.

Now, using the real part of the susceptibility, refractive index changes can be determined as:

$$\frac{\Delta n(\omega)}{n_r} = \text{Re} \left[\frac{\chi(\omega)}{2n_r^2} \right]. \quad (27)$$

Within a two-level system approach, the linear and the third order nonlinear optical absorption coefficient are obtained from the imaginary part of the susceptibility [25, 34, 45–51] as:

$$\alpha^{(1)}(\omega) = \omega \sqrt{\frac{\mu}{\varepsilon_r}} \frac{|M_{01}|^2 N \hbar \Gamma_0}{[(E_{10} - \hbar\omega)^2 + (\hbar\Gamma_0)^2]}, \quad (28)$$

$$\alpha^{(3,I)}(\omega) = -2\omega \sqrt{\frac{\mu}{\varepsilon_r}} \left(\frac{I}{\varepsilon_0 \eta_r c} \right) \frac{|M_{01}|^4 N \hbar \Gamma_0}{[(E_{10} - \hbar\omega)^2 + (\hbar\Gamma_0)^2]^2} \times \left(1 - \frac{|M_{11} - M_{00}|^2}{4|M_{01}|^2} \left\{ \frac{(E_{10} - \hbar\omega)^2 - (\hbar\Gamma_0)^2 + 2E_{10}(E_{10} - \hbar\omega)}{(E_{10})^2 + (\hbar\Gamma_0)^2} \right\} \right). \quad (29)$$

Total absorption coefficient $\alpha(\omega, I)$ is given as:

$$\alpha(\omega, I) = \alpha^{(1)}(\omega) + \alpha^{(3,I)}(\omega). \quad (30)$$

The linear and nonlinear changes in the refractive index are written as [25, 30, 46–54]:

$$\frac{\Delta\eta^{(1)}(\omega)}{\eta_r} = \frac{1}{2\eta_r^2 \varepsilon_{\partial 0}} |M_{01}|^2 \left[\frac{E_{10} - \hbar\omega}{(E_{10} - \hbar\omega)^2 + (\hbar\Gamma_0)^2} \right], \quad (31)$$

$$\frac{\Delta\eta^{(3,I)}(\omega, I)}{\eta_r} = -\frac{\mu c}{4\eta_r^3 \varepsilon_{\partial 0}} |M_{01}|^2 \left[\frac{NI}{[(E_{10} - \hbar\omega)^2 + (\hbar\Gamma_0)^2]^2} \right] \times \left[4(E_{10} - \hbar\omega) |M_{01}|^2 - \frac{|M_{11} - M_{00}|^2}{(E_{10})^2 + (\hbar\Gamma_0)^2} \{E_{10}(E_{10} - \hbar\omega) \times -(\hbar\Gamma_0)^2(2E_{10} - \hbar\omega)\} \right]. \quad (32)$$

The total refractive index change is

$$\frac{\Delta\eta(\omega, I)}{\eta_r} = \frac{\Delta\eta^{(1)}(\omega)}{\eta_r} + \frac{\Delta\eta^{(3,I)}(\omega, I)}{\eta_r}, \quad (33)$$

where $\mu_{ij} = |\langle \psi_i | z_{T1} | \psi_j \rangle|$, ($i, j = 0, 1$) are the matrix elements of the dipole moment, $\psi_i(\psi_j)$ are the eigenfunctions, $\omega_{01} = \frac{E_1 - E_0}{\hbar}$ is the difference between two energy levels, is the frequency of the electromagnetic field, τ_0 is the relaxation time.

3. Results and discussions

We have considered the GaAs semiconductor material constants for our numerical results. We used the numerical parameters such as [38, 40–44] $m_e^* = 0.067m_0$, $m_h^* = 0.09m_0$ (m_0 is the mass of a free electron), $N = 3 \cdot 10^{22} \text{ m}^{-3}$, $\varepsilon = 12.53$, $\tau_0 = 0.2 \text{ ps}^{-1}$, $I = 2000 \text{ MW/m}^2$.

To understand the effect of change in hydrostatic pressure and temperature on the Linear Absorption Coefficient (LAC) and third order (Nonlinear) Absorption coefficient (NAC), we present the same in Fig. 2(a) and 2(b). Here we also have shown the effects of inclusion of Excitonic Effects (EE) on the LAC and NAC. One can observe that for the cases where (2(a) and 2(b)) the EE is not included, the NAC and LAC peaks occurred at photon energies much lower than the cases of inclusion of EE in the study. This is attributed to the energy associated with the excitonic interactions between the electron and holes. Moreover, the peak heights, for both LAC and Total Absorption Coefficient (TAC), increased when excitonic effects are taken into account. This is a consequence of enhancement of the dipole moment due to the positive-negative charge separation of the electron-hole pair, which otherwise is not there in the case of Without Excitonic Effects (WEE). In Fig. 2(a), shift from 60.28 to 56.70 meV when pressure is increased from 10 to 100 kbar in case of WEE. Whereas for identical change in pressure, the LAC and NAC peaks are shifted from 91.78 to 88.58 meV for the case of EE. This shifting is accompanied by decrease in absorption LAC peak height from $0.35 \cdot 10^5$ to $0.32 \cdot 10^5 \text{ m}^{-1}$ in case of WEE and from $0.80 \cdot 10^5$ to $0.72 \cdot 10^5 \text{ m}^{-1}$ for the EE case. Similar effects are also observed for the NAC. The LAC and NAC shift towards the lower energy end of the spectrum as the pressure increases. This shifting is accompanied by a diminishing absorption peak height for both EE and WEE case. These effects are due to the counter affecting action of pressure on the confinement potential and energy band gap. The pressure increases the confinement strength but it also strongly alters the energy band gap. For GaAs, in the pressure range of 10 kbar to 100 bar, these two opposing effects results in a net red shift of the peaks as the pressure increases. Whereas, in Fig. 2(b), one can see that the absorption peaks, LAC and NAC, moves from 60.28 to 62.40 meV and peak heights of LAC increase from $0.35 \cdot 10^5$ to $0.39 \cdot 10^5 \text{ m}^{-1}$ and NAC changes from $-0.062 \cdot 10^5$ to $-0.066 \cdot 10^5 \text{ m}^{-1}$ when the temperature increases from 10 to 100 K, keeping $P = 10$ kbar. For the case of EE, the blue shift in peaks happen from 91.7 to 94.39 meV and the LAC peak heights change from $0.80 \cdot 10^5$ to $0.85 \cdot 10^5 \text{ m}^{-1}$ and the NAC peak enhances from $-0.13 \cdot 10^5$ to $-0.17 \cdot 10^5 \text{ m}^{-1}$ as the temperature increases from 10 to 100 K. These effects, similar in nature for both EE and WEE, result from the interplay complex second term of Eq. (5) and the direct dependence of on the temperature. Physically, the change in the entropy of the charge carriers induces a change in the energy of the states. In Fig. 3(a,b), we present the TAC as a function of incoming photon energy. Here, we observe similar effects of change in pressure and temperature on the TAC peaks as in the case of LAC and NAC. However, in TAC, the effects of LAC dominate the NAC for the light intensity of 2000 MW/m^2 . Furthermore, owing to the diametrically opposed behavior of the first and the third-order nonlinear ACs, a decrease in the total ACs is observed due to the reduction in the effective mass of the electron with the intensification of the temperature. A close relationship between the peak values of the total ACs, the transition dipole element and the difference between energy levels E_{10} can be disclosed from the figure. Total ACs is influenced in opposite by the dipole matrix element $|M_{10}|^2$ to that of the energy difference E_{10} . Hence, a blue shift is observed as a result of increase in the temperature and the red shift is observed when the pressure increases. This happens due to increase/decrease in the transition energy E_{10} on a significant increase in temperature/pressure. Upon increasing temperature/pressure, a drop/enhancement in the electron effective mass with an expansion/compression of the transition energy is observed due to the dependence of the electron-photon interaction of the temperature/pressure. Hence, the blue/red shift is observed. Same can be observed from Fig. 2(c,d) that how matrix elements get vary with pressure and temperature.

To compare our results in Fig. 3(b), we plotted the total absorption coefficient and compared with experimental data [55, 56] at $T \cong 10$ and 100 K. As it can be observed from the graph, a similar pattern is observed in both the experimental results as well as theoretical results but deviation can be observed in the theoretical prediction from the experimental data [55, 56]. At $T = 10$ K, the quantitative value is similar to the experimental value but this is not the same for the $T = 100$ K. Although, it can be observed from both experimental values as well as theoretical values that a

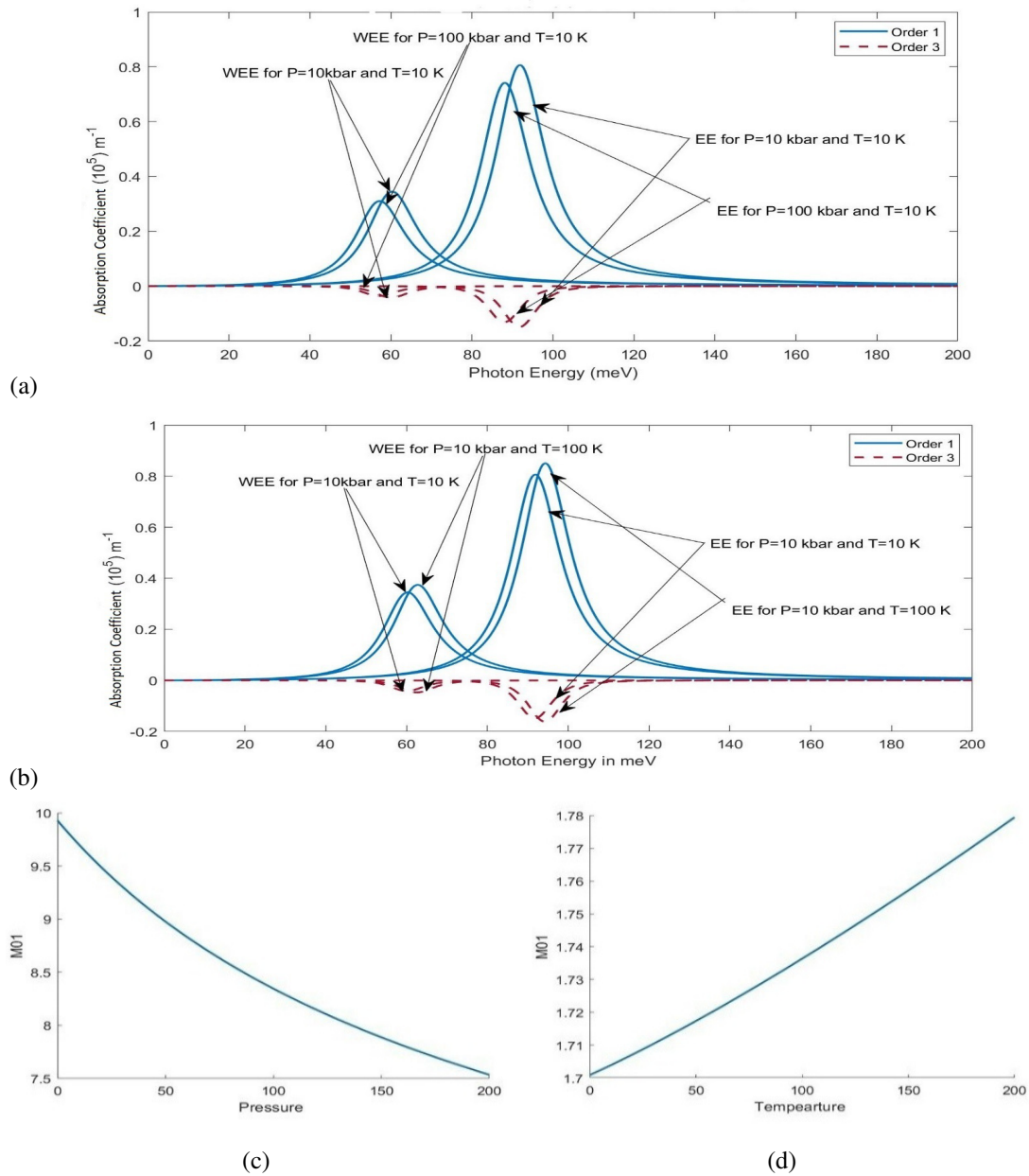


FIG. 2. (a,b) – the linear and nonlinear absorption coefficients with and without considering excitonic (EE and WEE) effects for $T = 10$ and 100 K and $P = 10 \text{ kbar}$ and $P = 100 \text{ kbar}$ and $I = 2000 \text{ MWm}^2$; (c,d) – behavior of matrix element with pressure and temperature

blue shift is happening in the absorption coefficient on increasing the temperature. For example, for temperature between $0 - 20$ and $40 - 100 \text{ K}$ peaks shift towards higher energy values for the both cases, i.e., theoretical and experimental. But as there was no significant difference between the peaks ranging from $21 - 90 \text{ K}$, hence, only values for 20 and 100 K have been presented in the theoretical graphs. Several points can be thought of as a cause for this deviation in the quantitative value. Some of these points are: (i) electronic transitions are not perfectly exact for the two-level system, (ii) several parameters such as dot size, intensity, σ , v are temperature dependent but are here considered as temperature independent, (iii) calculations have been performed theoretically using numerical methods and these methods have some limitations, (iv) approximation have been taken into account for solving the Eqs. (23–27).

As the interacting light changes the physical nature of the quantum dot material, it, therefore induces drastic changes in the refractive index of the QDs near the resonance energy. The same can be observed from the dispersion curves presented in Fig. 4(a,b) and 4(c,d). In 4(a), for WEE and hydrostatic pressure of 10 kbar , the dispersion curve of Linear Refractive Index change (LRI) rises to a maximum value 0.062 at photon energy 60.28 meV and crosses over to the negative polarity region to reach -0.063 at photon energy 74.40 meV . When the pressure increases to 100 kbar , this dispersion area shifts to 56.70 meV (maxima of 0.059) and 64.86 meV (minima of -0.059). Further, in 4(a), for pressure of 10 kbar , when EE is taken into account the area of polarity change of the LRI shifts to higher photon energy, viz. reaches

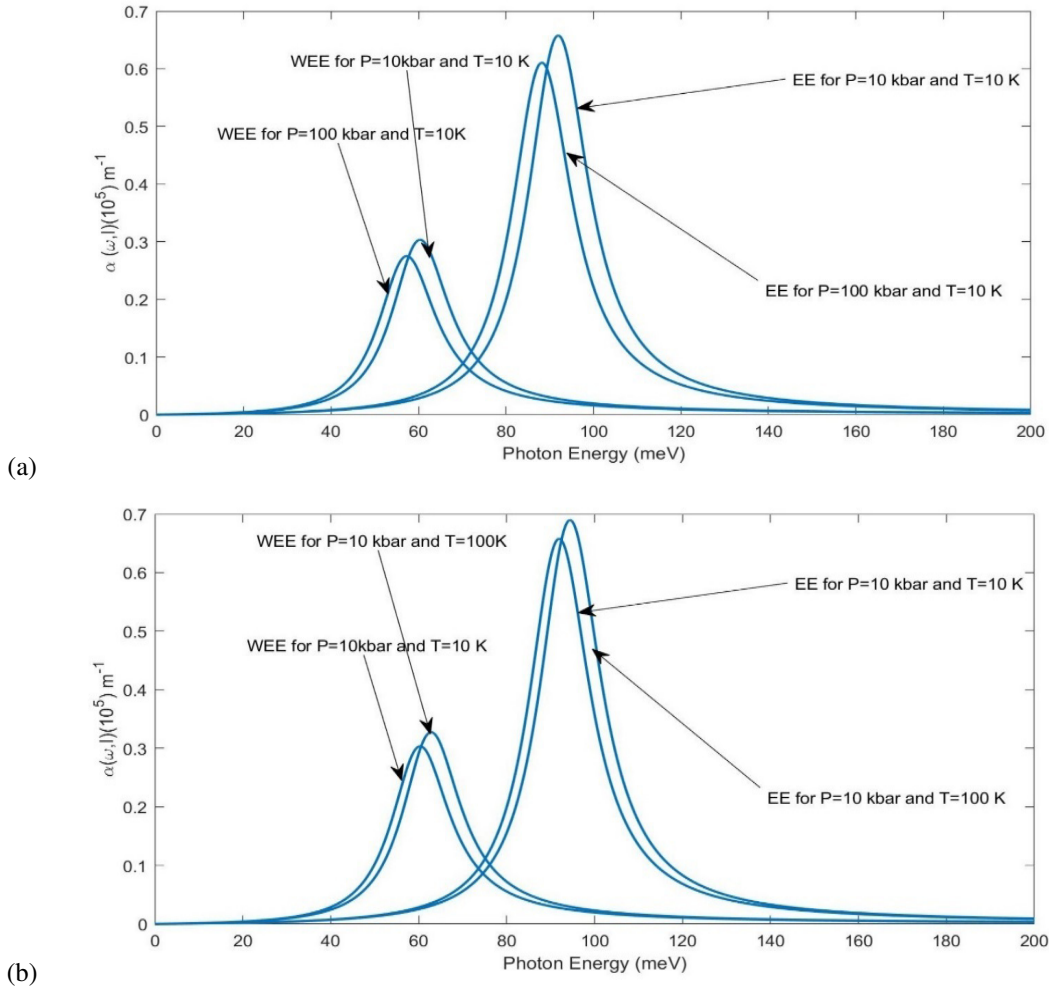


FIG. 3. Total absorption coefficients with and without considering excitonic (EE & WEE) effects for $T = 10 \text{ \& } 100 \text{ K}$ and $P = 10 \text{ \& } P = 100 \text{ kbar}$ and $I = 2000 \text{ MWm}^{-2}$

maximum at photon energy 91.7 meV (maxima of 0.088) and crosses over to the negative values to reach the minimum value at 106.33 meV (minima of -0.088). Again, for EE case, when pressure increases to 100 kbar, the dispersion area red shifts to 88.58 meV (maxima 0.085) and 103.48 meV (minima -0.086). Similar effects are observed (Fig. 4(b)) for Nonlinear Refractive Index change (NRI) at the identical photon energies as in the case of LRI. However, in case of NRI, the polarity of the refractive index change first reaches a negative valued minima and then crosses over to a positive valued maximum. Opposite nature of shifting of the dispersion is observed when the temperature is changed from 10 to 100 K keeping $P = 10 \text{ kbar}$ (Fig. 4(c,d)). In Fig. 4(c), it is obtained that the maximum value of the LRI (minimum value of NRI in Fig. 4(d)) occurs at photon energy 60.28 meV (maxima of 0.062) when the temperature is kept at 10 K for the case of WEE. When the temperature increases to 100 K, in case of WEE, the maximum value of the LRI (minimum of NRI, Fig. 4(d)) shifts to a higher photon energy value of 62.40 meV. Whereas for the case of EE, the LRI (and NRI) maximum value (minima for NRI) shifts from 91.7 to 94.39 meV when the temperature increases to 100 from 10 K. These two-opposite natures of influences on the RI change of hydrostatic pressure and temperature are attributed to the fact that the increase in pressure strengthens the confinement whereas the temperature acts the other way.

In Fig. 5(a,b), the total refractive index change is presented at two values of applied hydrostatic pressure (5a) keeping $T = 10 \text{ K}$ and in (5b), the temperature is varied from 10 to 100 K keeping $P = 10 \text{ kbar}$. It can be observed that the magnitude of the change in refractive index with variation in hydrostatic pressure and temperature are different on the two scenarios, i.e., one with the excitonic effect and the other without excitonic effects. This is the consequence of the fact that in case of WEE, the properties are determined by the effective mass of the electron whereas in case of EE, the properties are manifested from the reduced mass of the electron-hole pair. This is one of the major factors for variation in the optical properties in between EE and WEE, in addition to the fact of opposite polarity charges being involved in the case of EE.

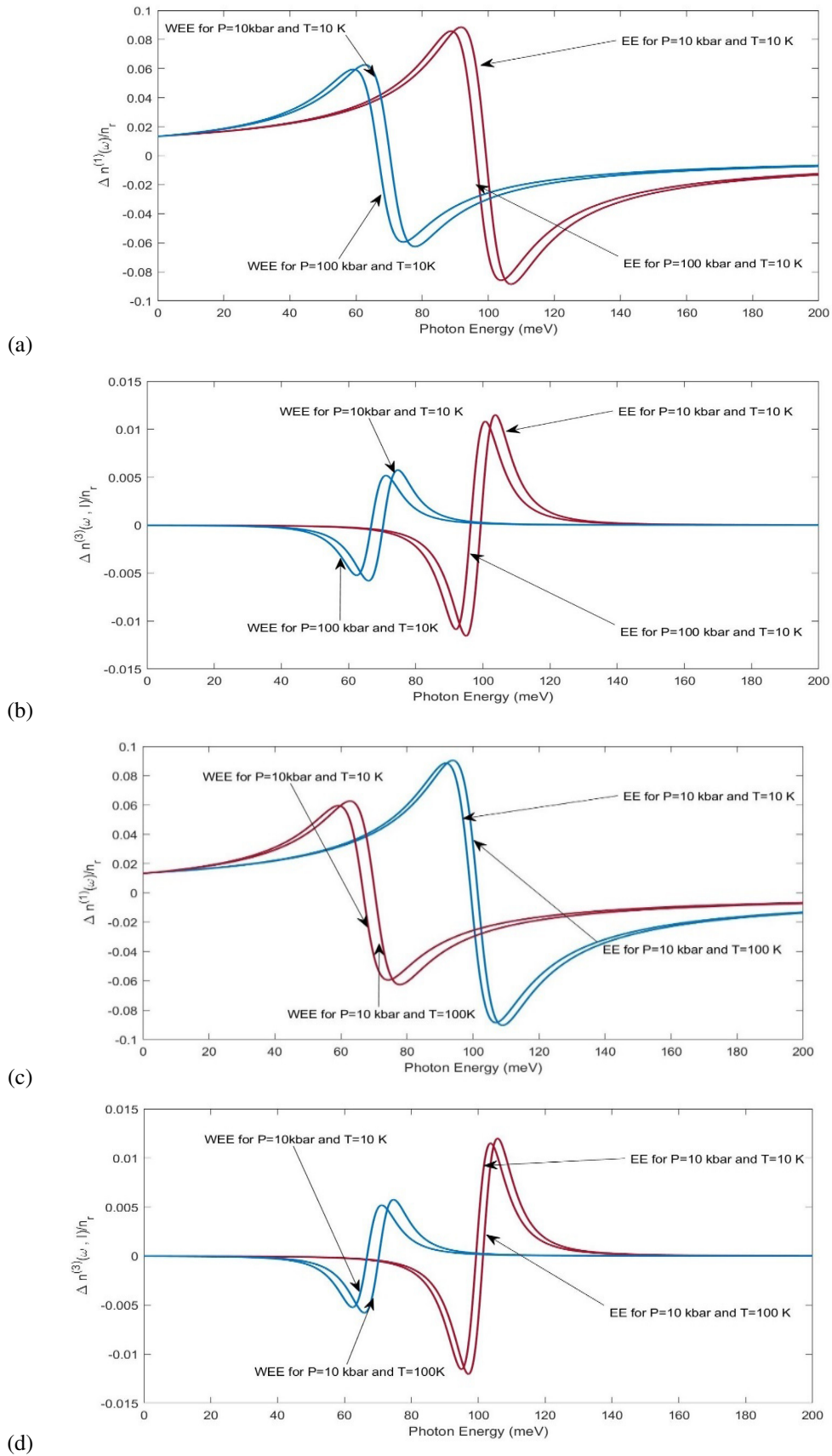


FIG. 4. Schematic diagram of GaAs Quantum Dot. The linear and nonlinear refractive index for with and without considering excitonic (EE & WEE) effects for $T = 10$ and 100 K and $P = 10$ kbar and $P = 100$ kbar and $I = 2000 \text{ MWm}^{-2}$

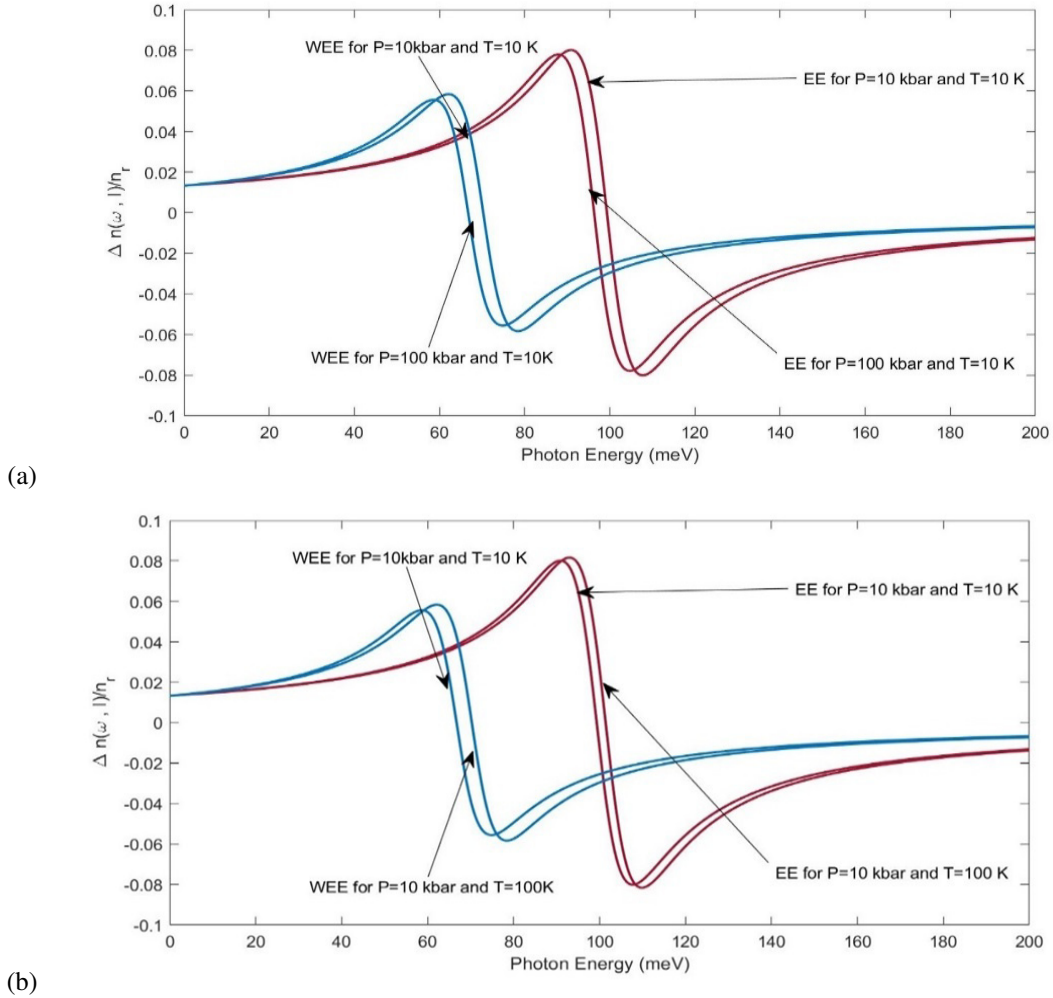


FIG. 5. The total refractive index for with and without considering excitonic (EE and WEE) effects for $T = 10$ and 100 K and $P = 10$ kbar and $P = 100$ kbar and $I = 2000 \text{ MWm}^{-2}$

4. Conclusion

We have reported the linear and nonlinear optical properties, viz. absorption coefficient and refractive index of a GaAs semi-parabolic QD by employing the compact density matrix formalism. We have demonstrated that the absorption coefficient peaks and refractive index dispersion variation is blue shifted with the inclusion of excitonic effects. The increase in the pressure alters the optical properties of the QD by controlling the effective mass of electron, energy band gap and the dielectric constant. This intricate counter-balancing act results in a red shift in the nonlinear optical properties' resonance position when the applied hydrostatic pressure is incremented, while augmenting the ambient temperature results in blue shifts of the LAC, NAC and TAC and refractive index change. Further, it is observed that the enhancing the pressure lowers the peak height of the absorption coefficient and the refractive index dispersions curves. This is due to the diminishing of dipole moments of the QD by the reinforcing the confinement by the hydrostatic pressure which results in shrinking of the orbital wave functions. To our best knowledge no such research work illustrating the effects of Hydrostatic Pressure and Temperature on the RI and AC (Linear and third order) of GaAs QD for a semi-parabolic system (excitonic as well as non-excitonic cases) has been carried out earlier. According to our consideration, the obtained results can have important practical applications in fabricating optoelectronic devices and hence have a sound share in progressive product technology. The shifting of absorption peaks can specially be used in devices where optical switches can be turned on and off depending on absorption of incident radiation. Hydrostatic pressure and temperature can act as external parameters. Further, the same property may also be used to detect changes in temperature and pressure by observing the refractive index change and absorption of photons at particular wavelength. Analysis of the experimental results [55, 56] and comparing with the theoretical results obtained, some disagreement is observed in the absorption coefficients. This variation with the experimental results is explained in the previous section.

References

- [1] Jamieson T., Bakhshi R., Petrova D., Pocock R., Imani M., Seifalian A.M. Biological applications of quantum dots. *Biomaterials*, 2007, **28** (31), P. 4717–4732.
- [2] Salata O. Applications of nanoparticles in biology and medicine. *J. Nanobiotechnol.*, 2004 **2** (1), 3.
- [3] Mocatta D., Cohen G., Schattner J., Millo O., Rabani E., Banin U. Heavily doped semiconductor nanocrystal quantum dots. *Science*, 2011, **332** (6025), P. 77–81.
- [4] Koenraad P.M., Flatté M.E. Single dopants in semiconductors. *Nat. Mater.*, 2011, **10**, P. 91–100.
- [5] Aghoutane N., Pérez L.M., Tiutiunnyk A., Laroze D., Baskoutas S., Dujardin F., Fatimy A.E., El-Yadri M., Feddi E.M. Adjustment of Terahertz Properties Assigned to the First Lowest Transition of (D+, X) Excitonic Complex in a Single Spherical Quantum Dot Using Temperature and Pressure. *Applied Sciences*, 2021, **11** (13), 5969.
- [6] Schneider H., Fuchs F., Dischler B., Ralston J.D., Koidl P. Intersubband absorption and infrared photodetection at 3.5 and 4.2 μm in GaAs quantum wells. *Appl. Phys. Lett.*, 1991, **58**, P. 2234–2236.
- [7] Ferry D.K., Goodnick S.M. *Transport in Nanostructures*. Cambridge University Press, Cambridge, 1997.
- [8] Sarkisyan H.A. Direct optical absorption in cylindrical quantum dot. *Mod. Phys. Lett. B*, 2004, **18** (10), P. 443–452.
- [9] Saravanamoorthy S.N., John Peter A., Lee C.W. Optical peak gain in a PbSe/CdSe core-shell quantum dot in the presence of magnetic field for mid-infrared laser applications. *Chem. Phys.*, 2017, **483–484**, P. 1–6.
- [10] Bera A., Ghosh M. Dipole moment and polarizability of impurity doped quantum dots driven by noise: Influence of hydrostatic pressure and temperature. *Physica B*, 2017, **515**, P. 18–22.
- [11] Schaller R.D., Klimov V.I. High Efficiency Carrier Multiplication in PbSe Nanocrystals: Implications for Solar Energy Conversion. *Phys. Rev. Lett.*, 2004, **92** (18), 186601.
- [12] Huynh W.U., Dittmer J.J., Alivisatos A.P. Hybrid nanorod-polymer solar cells. *Science*, 2002, **295** (5564), P. 2425–2427.
- [13] Zhong X., Xie R., Basche Y., Zhang T., Knoll W. High-Quality Violet- to Red-Emitting ZnSe/CdSe Core/Shell Nanocrystals. *Chem. Mater., Chem. Mater.*, 2005, **17** (16), P. 4038–4042.
- [14] Ungan F., Mart'inez-Orozco J.C., Restrepo R.L., Mora-Ramos M.E., Kasapoglu E., Duque C.A. Nonlinear optical rectification and second-harmonic generation in a semi-parabolic quantum well under intense laser field: Effects of electric and magnetic fields. *Superlattice Microstruct.*, 2015, **81**, 26.
- [15] Karimi M.J., Rezaei G. Effects of external electric and magnetic fields on the linear and nonlinear intersubband optical properties of finite semi-parabolic quantum dots. *Physica B*, 2011, **406**, 4423.
- [16] Fl'orez J., Camacho A. Excitonic effects on the second-order nonlinear optical properties of semi-spherical quantum dots. *Nanoscale Res. Lett.*, 2011, **6**, 268.
- [17] Cristea M. Comparative study of the exciton states in CdSe/ZnS core-shell quantum dots under applied electric fields with and without permanent electric dipole moment. *Eur. Phys. J. Plus*, 2016, **131**, 86.
- [18] Chaurasiya R., Dahiya S., Sharma R. A study of confined Stark effect, hydrostatic pressure and temperature on nonlinear optical properties in 1D Ga_xAl_{1-x}As/GaAs/Ga_xAl_{1-x}As quantum dots under a finite square well potential. *Nanosystems: Phys. Chem. Math.*, 2023, **14** (1), P. 44–53.
- [19] Eseau N. Simultaneous effects of laser field and hydrostatic pressure on the intersubband transitions in square and parabolic quantum wells. *Phys. Lett. A*, 2010, **374**, 1278.
- [20] Rezaei G., Karimi M.J., Keshavarz A. Excitonic effects on the nonlinear intersubband optical properties of a semi-parabolic one-dimensional quantum dot. *Physica E*, 2010, **43**, 475.
- [21] Yuan H.J., Zhang Y., Mo H., Chen N., Zhang Z.-H. Electric field effect on the second-order nonlinear optical properties in semiparabolic quantum wells. *Physica E*, 2016, **77**, 102.
- [22] Karabulut I., Safak H., Tomak M. Nonlinear optical rectification in asymmetrical semiparabolic quantum wells. *Solid State Commun.*, 2005, **135**, 735.
- [23] Bautista J.E., Lyra M.L., Lima R.P.A. Screening effect on the exciton mediated nonlinear optical susceptibility of semiconductor quantum dots. *Photon. Nanostruct.*, 2013, **11**, 8.
- [24] Paspalakis E., Boviatsis J., Baskoutas S. Effects of probe field intensity in nonlinear optical processes in asymmetric semiconductor quantum dots. *J. Appl. Phys.*, 2013, **114**, 153107.
- [25] Karabulut I., Safak H., Tomak M. Excitonic effects on the nonlinear optical properties of small quantum dots. *J. Phys. D: Appl. Phys.*, 2008, **41**, 155104.
- [26] Baghramy H.M., Barseghyan M.G., Kirakosyan A.A., Restrepo R.L., Duque C.A. Linear and nonlinear optical absorption coefficients in GaAs/Ga_{1-x}Al_xAs concentric double quantum rings: Effects of hydrostatic pressure and aluminum concentration. *J. Lumin.*, 2013, **134**, P. 594–599.
- [27] Gambhir M., Varsha, Prasad V. Pressure- and temperature-dependent EIT studies in a parabolic quantum dot coupled with excitonic effects in a static magnetic field. *Pramana – J. Phys.*, 2022, **96**, 81.
- [28] Gambhir M., Kumar P., Kumar T. Investigation of linear and third-order nonlinear optical properties in a laser-dressed parabolic quantum dot with a hydrogenic donor impurity in the presence of a static electric field. *Indian J. Phys.*, 2023, **97**, P. 2169–2178.
- [29] Zhang L., Li X., Zhao Z. The influence of optical absorption under the external electric field and magnetic field of parabolic quantum dots. *Indian J. Phys.*, 2022, **96**, P. 3645–3650.
- [30] Duan Y., Li X., Chang C. Effects of Magnetic Field on Nonlinear Optical Absorption in Quantum Dots Under Parabolic-Inverse Squared Plus Modified Gaussian Potential. *Braz. J. Phys.*, 2022, **52**, 123.
- [31] Yu Y.-B., Zhu S.-N., Guo K.-X. Exciton effects on the nonlinear optical rectification in one-dimensional quantum dots. *Phys. Lett. A*, 2005, **175**, 335.
- [32] Karabulut İ., Şafak H. Nonlinear optical rectification in semiparabolic quantum wells with an applied electric field. *Physica B*, 2005, **82**, 368.
- [33] Duque C.M., Mora-Ramos M.E., Duque C.A. Simultaneous effects of electron-hole correlation, hydrostatic pressure, and temperature on the third harmonic generation in parabolic GaAs quantum dots. *J. Nanopart. Res.*, 2013, **13**, P. 6103–6112.
- [34] Baskoutas S., Paspalakis E., Terzis A.F. Effects of excitons in nonlinear optical rectification in semiparabolic quantum dots. *Phys. Rev. B*, 2006, **74**, 153306.
- [35] Duque C.A., Porras-Montenegro N., Barticevic Z., Pacheco M., Oliveira L.E. Effects of applied magnetic fields and hydrostatic pressure on the optical transitions in self-assembled InAs/GaAs quantum dots. *J. Phys.: Condens. Matter*, 2006, **18**, P. 1877–1884.
- [36] Duque C.M., Morales A.L., Mora-Ramos M.E., Duque C.A. Optical nonlinearities associated to applied electric fields in parabolic two-dimensional quantum rings. *J. of Luminescence*, 2013, **143**, P. 81–88.

- [37] Mughnetsyan V.N., Manaselyan Kh.A., Barseghyan M.G., Kirakosyan A.A. Simultaneous effects of hydrostatic pressure and spin-orbit coupling on linear and nonlinear intraband optical absorption coefficients in a GaAs quantum ring. *J. Lumin.*, 2013, **134**, P. 24–27.
- [38] Duque C.M., Mora-Ramos M.E., Duque C.A. Hydrostatic pressure and electric field effects and nonlinear optical rectification of confined excitons in spherical quantum dots. *Superlattices and Microstructures*, 2011, **49**, P. 264–268.
- [39] Bejan D. Exciton effects on the nonlinear optical properties of semiparabolic quantum dot under electric field. *Eur. Phys. J. Plus*, 2017, **132**, 102.
- [40] Antil S., Kumar M., Lahon S., Dahiya S., Ohlan A., Punia R., Maan A.S. Influence of hydrostatic pressure and spin orbit interaction on optical properties in quantum wire. *Physica B: Condensed Matter*, 2019, **552**, P. 202–208.
- [41] Antil S., Kumar M., Lahon S., Maan A.S. Pressure dependent optical properties of quantum dot with spin orbit interaction and magnetic field. *Optik – Int. J. for Light and Electron Optics*, 2019, **176**, P. 278–286.
- [42] Dahiya S., Lahon S., Sharma R. Effects of temperature and hydrostatic pressure on the optical rectification associated with the excitonic system in a semi-parabolic quantum dot. *Physica E*, 2020, **118**, 113918.
- [43] Braggio A., Grifoni M., Sassetti M., Napoli F. Plasmon and charge quantization effects in a double-barrier quantum wire. *Europhys. Lett.*, 2000, **50**, 236.
- [44] Unlu S., Karabulut I., Safak H. Linear and nonlinear intersubband optical absorption coefficients and refractive index changes in a quantum box with finite confining potential. *Physica E*, 2006, **33**, 319.
- [45] Fickenscher M., Shi T., Jackson Howard E., Smith Leigh M., Yarrison-Rice Jan M., Zheng C., Miller P., Etheridge J., Wong Bryan M., Gao Q., Deshpande S., Hoe Tan H., Jagadish C. Optical, Structural, and Numerical Investigations of GaAs/AlGaAs Core-Multishell Nanowire Quantum Well Tubes. *Nano Letters*, 2013, **13** (3), P. 1016–1022.
- [46] Raigoza N., Morales A., Montes A., Porras-Montenegro N., C.A. Duque. Optical nonlinearities associated to applied electric fields in parabolic two-dimensional quantum rings. *Phys. Rev. B*, 2004, **69**, 045323.
- [47] Oyoko H., Parras-Montenegro N., Lopez S., Duque C.A. Comparative study of the hydrostatic pressure and temperature effects on the impurity-related optical properties in single and double GaAs–Ga_{1-x}Al_xAs quantum wells. *Phys. Status Solidi C*, 2007, **4**, 298.
- [48] Herbert Li E. Material parameters of InGaAsP and InAlGaAs systems for use in quantum well structures at low and room temperatures. *Physica E*, 2000, **5**, 215.
- [49] Haldane F.D.M. ‘Luttinger liquid theory’ of one-dimensional quantum fluids. I. Properties of the Luttinger model and their extension to the general 1D interacting spinless Fermi gas. *J. Phys. C*, 1981, **14**, 2585.
- [50] Boyd R.W. *Nonlinear Optics*, Elsevier Science, 2020.
- [51] Naghmaish Aishah AL., Dakhlaoui H., Ghrib T. Effects of magnetic, electric, and intense laser fields on the optical properties of AlGaAs/GaAs quantum wells for terahertz photodetectors. *Physica B: Condensed Matter*, 2022, **635**, 413838.
- [52] Dahiya S., Lahon S., Sharma R. Study of third harmonic generation in In_xGa_{1-x}As semi-parabolic 2-D quantum dot under the influence of Rashba spin-orbit interactions (SOI): Role of magnetic field, confining potential, temperature & hydrostatic pressure. *Physica E: Low-dimensional Systems and Nanostructures*, 2023, **147**, 115620.
- [53] Kuhn K.J., Lyengar G.U., Yee S. Free carrier induced changes in the absorption and refractive index for interurban optical transitions in Al_xGa_{1-x}As/GaAs/Al_xGa_{1-x}As quantum wells. *J. Appl. Phys.*, 1991, **70**, 5010.
- [54] Kopf R.F., Herman M.H., Lamont Schnoes M., Perley A.P., Livescu G., Ohring M. Band offset determination in analog graded parabolic and triangular quantum wells of GaAs/AlGaAs and GaInAs/AlInAs. *J. Appl. Phys.*, 1992, **71** (10), P. 5004–5011.
- [55] Gurmessa A., Melese G., Choudary V.L., Shewamare S. Photoluminescence from GaAs nanostructures. *Int. J. of Physical Sciences*, 2015, **10** (3), P. 106–111.
- [56] Lourenc S.A., Dias I.F.L., Duarte J.L., Laureto E., Aquino V.M., Harmand J.C. Temperature-Dependent Photoluminescence Spectra of GaAsSb/AlGaAs and GaAsSbN/GaAs Single Quantum Wells under Different Excitation Intensities. *Brazilian J. of Physics*, 2007, **37** (4), P. 1212–1217.

Submitted 29 July 2024; revised 26 August 2024; accepted 1 September 2024

Information about the authors:

Suman Dahiya – Department of Applied Physics, Delhi Technological University, Delhi 110042, India; ORCID 0000-0003-4815-5354

Siddhartha Lahon – Physics Department, KMC, University of Delhi, Delhi 110007, India; sid.lahon@gmail.com

Rinku Sharma – Department of Applied Physics, Delhi Technological University, Delhi 110042, India; ORCID 0000-0003-6812-4358; rinkusharma@dtu.ac.in

Conflict of interest: the authors declare no conflict of interest.

Inertial nanostep piezoelectric drive: modeling and experiment

Olga M. Gorbenko^{1,a}, Stanislav Y. Lukashenko^{1,b}, Stepan V. Pichakhchi^{1,2,c},
Ivan D. Sapozhnikov^{1,d}, Mikhail L. Felshtyn^{1,e}, Alexander O. Golubok^{1,2,f}

¹Institute for Analytical Instrumentation of RAS, St. Petersburg, Russia

²St. Petersburg Academic University, St. Petersburg, Russia

^agorolga64@gmail.com, ^blukashenko13@mail.ru, ^cpichakhchi.s@yandex.ru,

^dsapozhnikov@gmail.com, ^emfelsztyn@yandex.ru, ^faogolubok@mail.ru

Corresponding author: O.M. Gorbenko gorolga64@gmail.com

ABSTRACT A vertical inertial nanostep piezoelectric drive is considered. A virtual model was created, and the operating modes of a real drive were studied by numerical experiment. Piezo electromechanical resonance was discovered and a method to eliminate resonant vibrations by increasing electrical losses in the discharge circuit of the piezo actuator capacitance was proposed. A satisfactory agreement between the calculated and experimental data for the drive steps in the nanometer displacement range was obtained.

KEYWORDS inertial piezoelectric drive, nano positioning system, piezo actuator, piezoelectric effect

FOR CITATION Gorbenko O.M., Lukashenko S.Y., Pichakhchi S.V., Sapozhnikov I.D., Felshtyn M.L., Golubok A.O. Inertial nanostep piezoelectric drive: modeling and experiment. *Nanosystems: Phys. Chem. Math.*, 2024, **15** (5), 643–653.

1. Introduction

Due to the development of nanotechnology, precision mechanical scanning, positioning and manipulating systems with nanometer accuracy are of great interest. There are various approaches to the implementation of nano movements based on the use of purely mechanical systems, such as a lever, differential screw or a “soft spring-rigid membrane” type gearbox, as well as systems based on electromagnetic and piezoelectric nano drives. The nanometer step value imposes special requirements on their protection of such systems from thermal drifts, acoustic, mechanical and electromagnetic noise. In some cases, there are also restrictions for the size of nano movement systems and special requirements for their operating conditions (low temperatures, ultrahigh vacuum). In this regard, piezoelectric drives are of particular interest [1–4]. Indeed, since piezoelectric actuators (PA) generate small mechanical displacements in the range of 1 – 100 microns, positioning and manipulation systems based on them have high accuracy of $\sim 1 - 10$ nm, and due to the fact that in PA the energy of the electric field is directly converted into mechanical displacement, they are simple, compact and relatively high rigidity and, as a result, they have good protection against thermal drift and external mechanical vibrations. Piezoelectric drives are usually divided into three groups: resonant drives in which vibrations in the ultrasonic frequency range are transmitted through a friction coupling to a moving element [5–10], stepper drives operating in a quasi-static mode when the drive supports are alternately pressed against a fixed base during compression/stretching of the PA [1, 11] and, finally piezo-inertial drives, the movement of which is determined by the ratio between the friction force and the inertia force [12–15]. Inertial stepper piezoelectric drives, which will be called below as inertial drives (ID) for simplicity, are based on the electromechanical system consisting, as a rule, of a PA and a slider sliding along the rod. There are ID in which the PA is connected to a fixed base or moves along with the slider [16]. In this paper, the first option is considered. A qualitative explanation of the effect of moving the slider along the rod is based on the fact that the slider with a mass of M located on the rod moves with it during the smooth movement of the rod and slips due to inertia with a sharp acceleration of the rod. Thus, by applying asymmetric voltage control pulses with slow and fast fronts to the PA, leading to a slow elongation (compression) of the PA and subsequent rapid compression (elongation) to its original size, it is possible to move the slider step by step along the rod. There are known ID with both horizontal and vertical rod arrangement, having the same operating principles and differing in the fact that in the vertical ID, there is an additional clamping of slider to the rod. The stage of movement, when the slider moves along with the rod, and their relative velocity is zero, has a stable term in the literature – Stick (sticking). The stage when the relative velocity of the rod and slider is different from zero and slippage occurs has the term Slip. The paper considers an ID with a vertical rod arrangement. The reason is as follows. When moving up and down along the axis of the rod, only gravity and friction force F_{fr} act on the slider, its acceleration in the up direction a_{up} and in the down direction a_{down} in the inertial coordinate system (ICS) relative to the fixed base is determined by expressions (2) and (2), respectively:

$$a_{\text{up}} = \frac{F_{\text{fr}}}{m_{\text{slider}}} - g = \frac{\mu F_{\text{clamp}}}{m_{\text{slider}}} - g, \quad (1)$$

$$a_{\text{down}} = \frac{F_{\text{fr}}}{m_{\text{slider}}} + g = \frac{\mu F_{\text{clamp}}}{m_{\text{slider}}} + g, \quad (2)$$

$$F_{\text{fr}} = \mu N = \mu F_{\text{clamp}}, \quad (3)$$

where m_{slider} is the slider mass, N is the reaction force of the support, μ is the coefficient of friction, g is the acceleration of gravity, F_{clamp} is the clamping force.

As follows from these expressions, the amount of slider acceleration in the ISC is limited. Thus, the slider can move up or down with the rod (Stick phase) only if the acceleration value of the rod does not exceed the threshold values of the air, or down, and, as follows from the expressions (1, 2), $a_{\text{up}} < a_{\text{down}}$. If the absolute value of the rod acceleration exceeds the threshold value, then the slider will slip along the rod (Slip phase) [17, 18]. When slipping, the slider has a velocity in a non-inertial coordinate system (NICS) relative to the rod, directed opposite to the acceleration of the rod in the ICS. At all times when the rod is moving, the frictional force acting on the slider is a thrust force for it. This fact is important for understanding the nature of the slider movement. Of course, the quantitative ID model must take into account the detailed shape of the control pulses, the mechanical resonant frequency of the structure, the friction force in the rod-slider pair, and energy losses in the ‘‘PA-rod-slider’’ oscillatory electromechanical system. In [15], a study of the operation of the ID was conducted and it was shown that the trajectory of the slider depends on a combination of various factors. In [19, 20], the influence of the shape of the pulse on the movement of the slider was investigated. In [18, 21], the attention is paid to trajectories containing sections where the slider moves in the direction opposite to the direction of movement of the rod and the results of modeling of such trajectories are presented. It was shown in [22] that the ID can work even under the control of symmetric control pulses. Note that in some cases, for example, when moving over long distances, it is important to have a relatively high speed of the slider moving under the action of a sequence of pulses. To increase the ID speed, it is necessary to minimize the intervals between the control voltage pulses. However, with an increase in the frequency of repetition of control pulses, it is necessary to take into account the finiteness of the relaxation time of vibrations arising in the electromechanical system in response to a sharp excitation from a short front of the control pulse. The presence of vibrations was already noted in one of the first works on ID [23]. Vibrations caused by strong high-frequency harmonics of sawtooth and cycloidal control signals were noted in [24]. These vibrations affect the movement of the slider under the control of a sequence of pulses, but they can be ignored if the vibrations fade out in the time intervals between pulses [25]. Therefore, for the stable operation of the precision displacement system, it is necessary to coordinate the frequency of the control pulses with the attenuation time of vibrations occurring in the ID. Thus, despite the simplicity of the design and ease of operation, the trajectory of the slider in the ID can have a rather complex appearance, since it depends on many factors. It is clear that in order to carry out movements in increments of several tens of nanometers, which, generally speaking, corresponds to a distance separating only about a hundred atoms in a solid, a special ‘‘smart setting’’ of the ID is required. At the same time, it is useful to have preliminary calculated data obtained on the basis of an adequate model of a real ID [13, 26].

In this paper, we build the model, and use it for investigation the trajectories of movement of the rod and slider in the ICS (relative to a fixed base) and the trajectory of movement of the slider in the NICS (relative to a fixed rod). We also calculate the step value of the real ID depending on the amplitude and shape of the sawtooth control pulse and the clamping force of the slider to the rod. Also, the step value of the real ID is measured experimentally, depending on the shape of the control pulse and the calculated data are compared with experiment.

2. The design of the inertial stepper piezoelectric drives and the scheme of the experiment

The appearance and layout of the vertical ID are shown in Fig. 1(a,b,c), respectively.

A titanium rod (2) is fixed on the PA (1), to which a slider (3) is pressed. In cross-section, the rod has the shape of a triangle (Fig. 1(c)). The slider surface, which has the shape of a two-sided angle, is pressed against two flat surfaces of the corresponding dihedral angle on the rod using an elastic clamp (4) mounted on the slider. A fluoroplastic washer is installed in the contact area of the elastic element with the rod to reduce friction, so that the main friction acts between the surfaces of the rod and the slider. The slider design consists of several parts. The part of the slider in contact with the rod is made of titanium. Due to the triangular shape of the rod, the slider has one degree of freedom and can only move along the axis of the rod. A multilayer piezoelectric package (PP) (Pst150/5×5/7H) was used as a surfactant. The rod is connected to the PP through a thin layer of epoxy glue.

The general scheme for measuring the steps of the ID is shown in Fig. 2. To control the PP, a simple scheme for forming sawtooth control pulses based on an electronic key in the form of a field-effect transistor is used, the input of which is supplied with a sequence of rectangular pulses (Fig. 3). In the initial state, for the voltage at the input of the circuit $V = 0$, the transistor is closed, the capacitance of the PP is charged to a voltage $V_0 = 50$ V, and the PP is stretched by $3.5 \cdot 10^{-6}$ m. Under the action of an initial rectangular pulse with a voltage of $V = 12$ V and a duration of t_0 , the transistor opens, and the PP is discharged to zero, passing into the initial equilibrium state. Here t_1, t_2 are

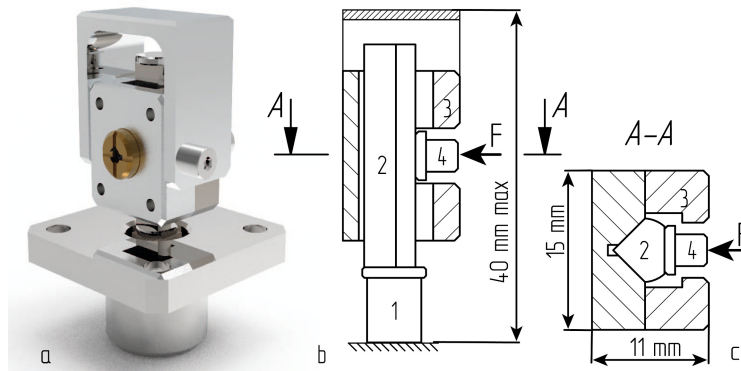


FIG. 1. Appearance (a) and the scheme of the inertial nano step piezoelectric drive (b – front view, c – top view) 1 – piezo package, 2 – rod, 3 – slider, 4 – clamp

the times set for the formation of a control sawtooth pulse with long leading and short trailing edges. Under the action of the leading edge, the PP slowly lengthens, and under the action of the trailing edge, it quickly contracts, returning to an equilibrium position. To reverse the direction of movement of the slider, switching is provided (not shown in the diagram) of the contacts at the input of the PP, leading to slow compression and rapid return of the PP to an equilibrium state. When the transistor is closed, the PP with its own capacity of $\sim 0.7 \cdot 10^{-6}$ F is charged through the resistance $R_1 = 2000$ ohms, and when the transistor is open, the PP is discharged through the resistance R_2 . Using such a simple scheme, it is possible to control the step of the ID by changing the charging time of the PP t_1 , or changing the time of its discharge by changing the resistance R_2 . In our experiment, the resistance of R_2 varied from 1 ohm to 30 ohms. With a sharp voltage jump from 50 V to zero and a corresponding sharp compression of the PP in the PP-rod oscillatory system, damped resonant vibrations occur, depending on the quality factor of the system, and, thanks to the piezoelectric effect, there will be mutual influence of mechanical and electrical vibrations. The time t_0 required for relaxation of resonant vibrations and the transition of PP to an equilibrium state was determined experimentally and was ~ 2 ms. After the PP is transferred to an equilibrium state, the piezoelectric package is charged during time t_1 . In our experiment, the time t_1 was 0.4 ms and 0.14 ms, which corresponded to the amplitude of 14 V and 5 V for the control sawtooth voltage pulse. Since the charging time constant is as follows: $\tau_1 = R_1 C \gg t_1$, the leading edge of the voltage pulse on the PP has a close to linear dependence on time, which leads to a corresponding smooth movement of the rod. The trailing edge is formed when the capacitance of the PP is discharged through the resistance R_2 when the transistor is opened for the time t_2 . If the capacitance of the PP had a purely electrical nature, then its charging or discharging would not be accompanied by mechanical compression or stretching, and the trailing edge of the pulse would decay exponentially with a time constant $\tau_2 = R_2 C = (1 \div 30) \cdot 10^{-6}$ s. However, as mentioned above, it is necessary to take into account the emerging resonant vibrations, the attenuation of which will depend on the Q-factor of the oscillatory piezo electromechanical system. Using simulation, it will be shown below how the shape of the trailing edge depends on the resistance R_2 , which affects both the discharge time of the PP and the Q-factor of the “PA-rod” oscillatory system.

Measurements of the ID step were carried out using the scanning probe microscopy (SPM) method. For this purpose, the ID was included in the “home-made” SPM as a system for approaching the probe with the sample. The sample had a smooth surface (roughness less than 1 nm) and was fixed on a slider. To measure the step value, the interaction between

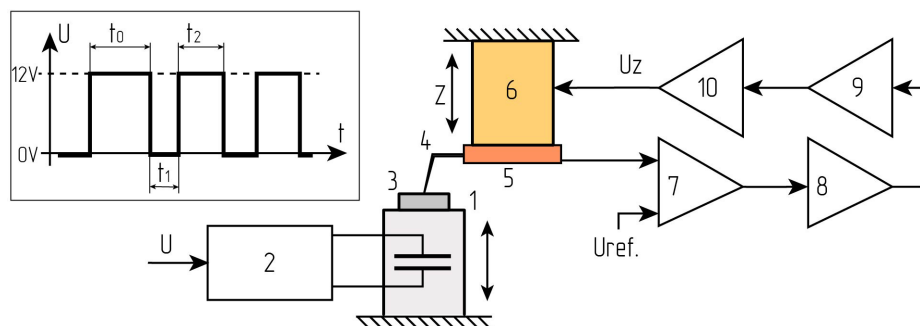


FIG. 2. Diagram of the experiment on measuring the value of the ID step. 1 – inertial piezo drive, 2 – sawtooth pulse control circuit, 3 – sample, 4 – probe, 5 – probe sensor, 6 — SPM scanner, 7 – differential amplifier, 8 – integrator, 9 – amplifier, 10 – high voltage amplifier

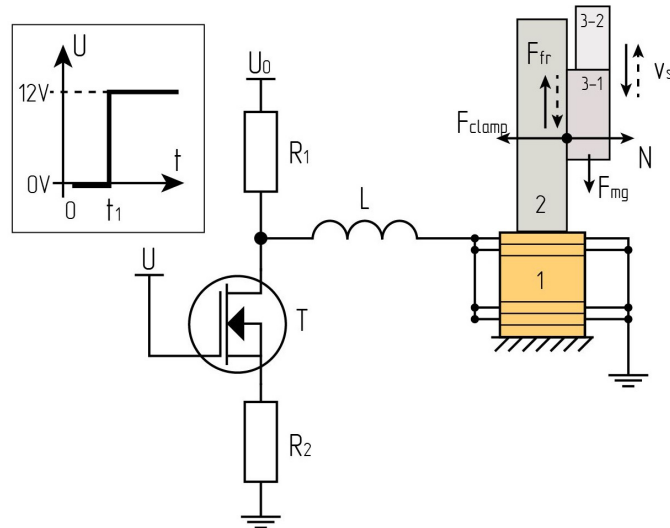


FIG. 3. Scheme of the ID calculation model 1 – piezo package, 2 – rod, 3-1 – slider (part in contact with the rod), 3-2 – slider (part without contact with the rod)

the probe and the sample was captured, after which the feedback in the SPM tracking system was broken, and the probe was withdrawn from the sample surface. Then the ID took a step, the tracking system turned on again, and the interaction was re-captured. The step length h was measured at the same interaction signal between the probe and the sample as the difference in positions of the SPM scanner before and after moving the ID under the action of a single control pulse [14]

$$h = \alpha |U_{Z_{n+1}} - U_{Z_n}|, \quad (4)$$

where α is the sensitivity of the SPM scanner, U_{Z_n} is the voltage on the SPM scanner after the (n) -th step of the slider, $U_{Z_{n+1}}$ is the voltage on the SPM scanner after the $(n + 1)$ -th step. To measure the average value of a single step, multiple one-step movements were performed under the action of a sequence of control pulses and a histogram of the size distribution of steps was constructed. At the same time, the time t_2 was set so that the ID had time to relax after executing the next step.

3. Description of the model

Figure 3 shows the ID model investigated by the finite element method using the COMSOL software package. Since the slider moves only along one (vertical) spatial Z axis, a two-dimensional simplification of the three-dimensional problem is considered. The model includes a multilayer PP Pst150/5×5/7H and a sawtooth control pulse generation circuit based on an n-type MOSFET field-effect transistor. The parameters of the transistor were chosen so that the calculated shape of the control sawtooth pulse most closely corresponded to the shape of the real pulse, which was observed in the experiment when charging and discharging a conventional electrical capacitance equal in value to the capacitance of the used PP ($C = 0.7 \mu\text{F}$). At the same time, the values of the main parameters corresponded to the default parameters set in COMSOL, and the values of the parameters “Gate Length” and “Transconductance Parameter” were selected to be $1 \cdot 10^{-7}$ m and $2 \cdot 10^{-3}$ A/B², respectively. The package consists of 40 layers of piezoceramic material PZT 5H with a thickness of 0.17 mm, connected in parallel. The physical parameters of the PZT 5H were selected in the COMSOL library. In this case, the value of the piezoelectric module $e_{33} = 72$ KJ/m² was set based on the data specified by the manufacturer in the PP passport. The inductance $L = 2 \cdot 10^{-6}$ H is also included in the electrical circuit. The inductance $L \sim 1 \cdot 10^{-6}$ H is also included in the model, due to the conductive electrodes between the PP layers and the conductive wires in the electrical circuit. The value of this constructive inductance was estimated from an experimentally measured frequency $f \sim 200$ kHz in an electromagnetic oscillatory circuit with a known capacitance $C = 0.7 \cdot 10^{-6}$ F.

For a two-dimensional simulation of a three-dimensional slider, in the construction of which different materials (titanium and steel) are used, the slider is made up of two parts rigidly connected to each other. The material of the part in contact with the rod has all the properties of titanium, as does the rod. The density of the second part of the slider is set so that the total weight of the slider is 10 g, which corresponds to its real weight. The titanium rod is rigidly connected to the PP. The size of the rod and its weight embedded in the model correspond to the actual design of the ID. The slider is pressed against the rod by an elastic element with the force of F_{clamp} . Dry friction contact interaction is enabled between the surface of the rod and the slider. The friction at the point of contact of the elastic element with the surface of the rod is neglected, since it is much less than the friction in contact of the slider with the rod. The rod and slider are modeled as linear elastic materials, the calculations take into account the density, Young’s modulus and Poisson’s ratio for each material.

The ID model (Fig. 3) consists of a composition of several physical Comsol modules. The PP model is built using the modules “Solid Meshes” and “Electrostatics” using a multiphysical combination of these modules “Piezoelectric Effect”. The finite element method was used to calculate both the deformation field at each point of the model grid and the electric field in the PP. The model of an electric circuit built with the help of the “Electrical Circuit” module using the “Terminal” mechanism fully reproduces the electrical circuit shown in Fig. 3. The step pulse with a height of 12 V is supplied at the input of circuit, and the time interval t_1 ($t_1 \ll R_1 C$) before the start of the voltage surge corresponds to the time of the open state of the transistor, when the PP is charging, and sets the amplitude of the control sawtooth pulse. The models of the rod, slider and contact interaction between them are made using the “Multibody Dynamics” module. At the same time, a rigid connection of the rod and the PP is implemented using the “Fixed Joint” element. For the rightmost border of the rod and the leftmost border of the slider, a “Prescribed displacement” offset constraint is set along the horizontal axis. The introduction of this restriction is due to the rigidity of the actual ID design. The contact interaction between the rod and the slider is modeled based on the condition that the movement of the touching bodies occurs along one spatial axis (vertical). Due to the limited information on contact interaction, the most generalized method of describing contact was chosen using a lumped connection of the prismatic type “Prismatic Joint”, in which the movement of contacting bodies is allowed only along one direction and any turns are prohibited.

The following equations were solved jointly:

1. The equation of motion in a form that takes into account mechanical vibrations in the system

$$\rho \frac{d^2 x}{dt^2} - \rho \omega^2 x = \nabla \cdot S, \quad (5)$$

where S is the stress tensor, $\omega = 2\pi f_0$, where f_0 is the mechanical resonance frequency.

2. Linear elasticity equation (linear relationship between mechanical stress and strain)

$$S = c : \varepsilon, \quad (6)$$

where c is the stiffness matrix, ε is the strain tensor. Deformations are considered as engineering, which is an acceptable approximation when linear changes in the size of objects are relatively small.

3. The electric field is additionally calculated for PP

$$\mathbf{E} = -\nabla V, \quad (7)$$

$$\nabla \cdot (\varepsilon_0 \varepsilon_r \mathbf{E}) = \rho_v, \quad (8)$$

where \mathbf{E} is the vector of the electric field, V is the electric potential, ε_r is the dielectric constant of material, ε_0 is the dielectric constant of vacuum, ρ_v is the spatial charge density.

4. Equation for the dry friction force

$$F_{\text{fr}} = -\mu N \frac{v}{|v|} \left(1 - \exp\left(-\frac{|v|}{v_0}\right) \right), \quad (9)$$

where v is the velocity of the slider relative to the rod, μ is the coefficient of friction, N is the normal reaction force of the support, v_0 is the velocity, the value of which is small compared to the velocities in the system. The minimum velocity v_0 is introduced to ensure the continuity of the function by which the friction force is calculated. This eliminates the mathematical problem associated with the discontinuity of the slider speed during the transition from the sticking phase to the sliding phase. Considering that the minimum slider speed in our case is $\sim 10^{-4}$ m/sec, the value for v_0 was $\sim 5 \cdot 10^{-5}$ m/sec. The above formulation is the law of continuous friction and describes both slip and stick, and thus completely replaces Coulomb’s law. Sticking is replaced by sliding between touching bodies with a small relative velocity. This explains the slight slope of the slider trajectory $X(t)$, which always takes place under the influence of gravity. Therefore, within the framework of this model, the resulting step is calculated at the moment when the slider speed relative to the rod becomes less than v_0 .

5. Equations describing the piezo effect in the “Stress-Share” formulation

$$T = c^E S - e_t \mathbf{E}, \quad (10)$$

$$\mathbf{D} = e_t S + \varepsilon_0 \varepsilon^S \mathbf{E}, \quad (11)$$

where T is the mechanical stress tensor, S is the strain tensor, \mathbf{D} is the electric displacement field (induction), e_t is the relationship matrix (piezomodule), c^E is the stiffness matrix, ε^S is the relative permittivity matrix. The values of the main parameters of the ID model are presented in Table 1.

TABLE 1. The main parameters of the ID model

Name	Value	Units of measurement
PP dimensions	$9 \times 5 \times 5$	mm
Rod dimensions	$25 \times 5 \times 5$	mm
Slider mass	10	g
Clamp force	1.2	N
Friction coefficient	0.25	
Charge resistance R_1	2000	Ω
Discharge resistance R_2	1 – 30	Ω
Young's modulus of PP (c_{33}^E)	117	GPa
Piezo module of PP (e_{33})	72	C/m ²
Density of PP	7500	kg/m ³
Young's modulus of titanium	112	GPa
Poisson's ratio of titanium	0.32	
Density of titanium	4505	kg/m ³
Young's modulus of steel	200	GPa
Poisson's ratio of steel	0.3	
Density of steel	7850	kg/m ³
Voltage V_0	50	V
PP charging time (t_1)	0.4, 0.14	ms

4. Simulation results, comparison with experiment

Let's analyze the dependence of the slider trajectory and the step size on the shape of the control pulse in the case of slider steps direction upward. Fig. 4(a,b) shows the shape of the control voltage pulse at the input of the PP for various resistance values R_2 . Fig. 5(a,b) show the trajectories of the rod and slider, respectively, in the ICS relative to the fixed base. As mentioned above, a small slope in the dependence of the slider offset on time, which occurs after the end of the control pulse in the ICS (Fig. 5(b)), should not be taken into account, since it is an artifact of the model. Figs. 6(a,b) show the speed of the slider and the movement of the slider, respectively, in NICS (with relation to a rod). Under the action of a linearly increasing leading edge (Fig. 4(a)), the PP linearly expands, which leads to a smooth linear movement of the rod upwards in the ICS by ~ 800 nm (Fig. 5(a)) with acceleration and deceleration at the beginning and at the end of the linear movement, causing a slip phase. Slippage leads to the fact that the slider lags behind the rod and has a nonlinear dependence of movement on time (Fig. 5(a)). As can be seen from Fig. 6(b), the slider descends downwards relative to the fixed rod by ~ 600 nm. As a result, under the action of the slow leading edge of the sawtooth voltage, the slider rises only by ~ 200 nm in the direction of the fixed base (Fig. 5(b)).

Changing the resistance of R_2 changes the constant τ_2 and affects the shape of the trailing edge of the control pulse. At small resistances R_2 (1 and 5 ohm), there is a rapid discharge of the PP capacitance, which leads to its sharp contraction, causing the excitation of electromechanical resonance oscillations with exponentially decaying amplitude in the system "PP-rod". Fig. 5(a) observes the resonant oscillations of the rod at 30 kHz, while Fig. 4(b) shows the corresponding voltage oscillations on the PP. The resonant oscillation of the rod produces slip, which is confirmed by the appearance of the slider's velocity relative to the stationary rod in the NICS (Fig. 6(a)). The change in sign of velocity observed in Fig. 6(a) means that the slider slips both up the rod (positive sign of velocity) and down the rod (negative sign). For example, with $R_2 = 1$ ohm, when the rod is first sharply lowered downward maximally, the slider moves upward maximally by ~ 1400 nm relative to the stationary rod due to slip. Then, as a result of several oscillations of the rod with damped amplitude, the slider periodically slips up and down the rod, dropping to ~ 650 nm (Fig. 6(b)), and stops at ~ 110 nm above the fixed base in the ICS, i.e., the resulting step of slider movement is ~ 110 nm. Note that in the case of fast discharge of the PP and low losses in the discharge circuit ($R_2 = 1$ and 5 ohm), the voltage on the PP changes sign, (Fig. 4(b)) and the rod passes through the equilibrium position in the ICS during oscillation (Fig. 5(a)).

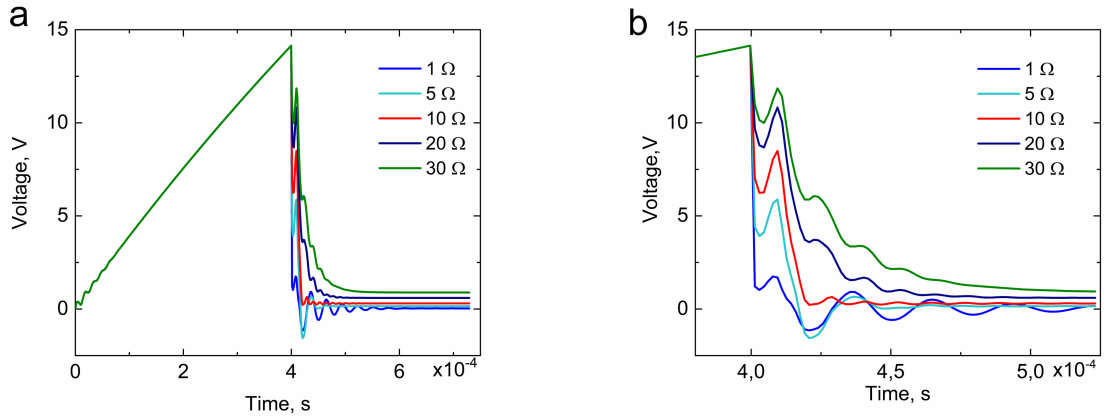


FIG. 4. The shape of the control voltage pulse at various resistances R_2 . a – is the entire pulse, b – is the time-stretched trailing edge of the pulse

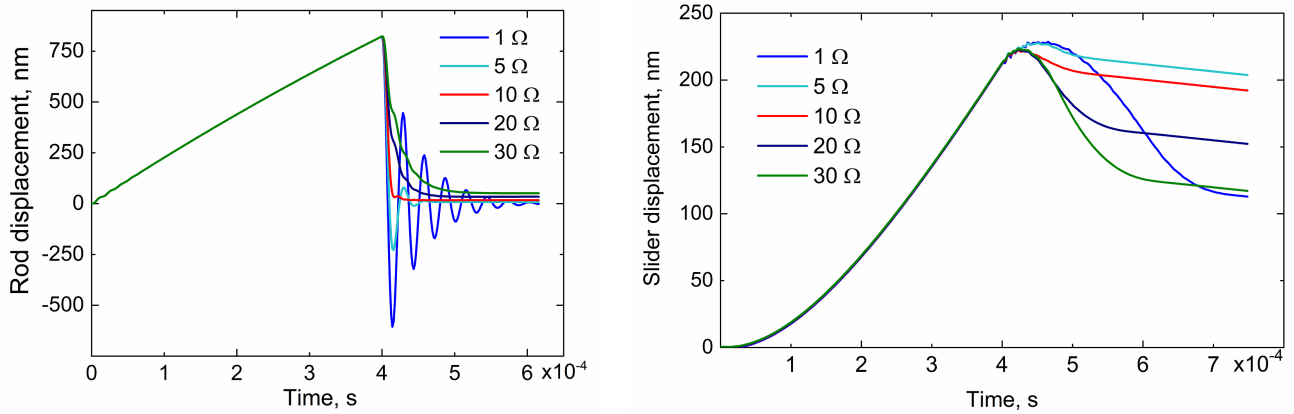


FIG. 5. Movement of the rod (a) and slider (b) in the ICS relative to the fixed base at different resistances R_2

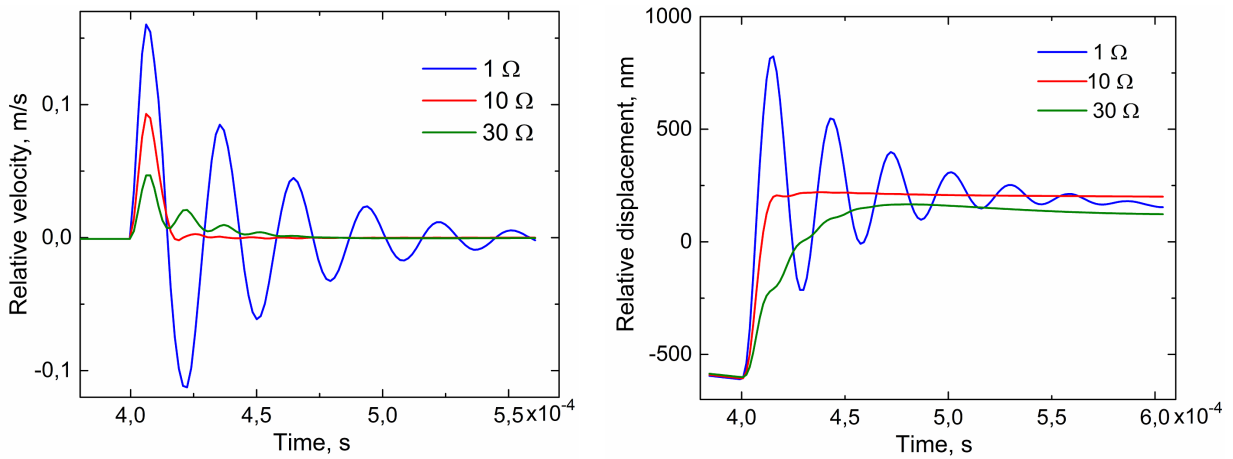


FIG. 6. The speed (a) and movement (b) of the slider in ICS relative to a fixed rod at various resistances R_2

When R_2 is increased (10, 20, 30) ohms, the character of the change in the voltage across the PCB and the rod displacement changes. Now there are no oscillations and there is an exponential in time decrease of the voltage on the PCB and corresponding exponential in time displacement of the rod to the equilibrium position (Figs. 4(b), 5(a)). The exponential decline is explained, firstly, by the fact that as the resistance increases, the Joule losses in the PP discharge circuit also increase and, consequently, the goodness of the piezo electromechanical oscillating system decreases. Second, as R_2 increases, the discharge time constant τ_2 increases, and the PP contracts more smoothly, so that resonant oscillations with appreciable amplitude are not excited, or are quickly damped. We attribute the observed steps on the exponential tails to the manifestation of the piezo effect. As can be seen from Fig. 6(a), in this case the slider velocity does not change sign and the slip is only one way up the rod without oscillation. At resistance $R_2 = 30$ ohm, under the action of the trailing edge of the control pulse, the slider acquires a velocity in NICS relative to the stationary rod, which, however, does not change sign, and slippage occurs only one way up the rod without oscillation. As a result, under the action of a fairly smooth trailing edge ($R_2 = 30$ ohm) when the rod is lowered, the slider slips ~ 700 nm up the rod (Fig. 6(b)) and stops ~ 120 nm above the fixed base in the NICS (Fig. 5(b)). Thus, despite the different nature of slider movement along the rod at $R_2 = 1$ ohm and $R_2 = 30$ ohm, the resulting slider pitch appears to be approximately the same and equal to 110 and 120 nm, respectively. In the case of $R_2 = 10$ ohm, due to a rather sharp voltage drop on the PP (Fig. 4(b)) and a sharp downward movement of the rod without oscillations in the ICS (Fig. 5(a)), there is a strong slip of the slider up the rod by ~ 800 nm (Fig. 6(b)) practically without rolling down, so that the resulting slider step has a value equal to ~ 200 nm (Fig. 5(b)).

We consider the optimal trajectory of the slider to be one where there is no oscillation of the slider relative to the rod and the time for the rod to return to the equilibrium state is minimized. Indeed, the absence of oscillations reduces the length of the trajectory of the slider movement along the rod and, consequently, reduces wear and heating of the surface, and the reduction of the relaxation time allows to reduce the intervals between steps, which is important for increasing the movement speed. In our case, as can be seen from Figs. 5,6, the optimum trajectory takes place when the resistance is as follows: $R_2 = 10$ ohm. Fig. 7 shows the histogram of the distribution of the value of ID steps obtained at the optimal trajectory of the slider.

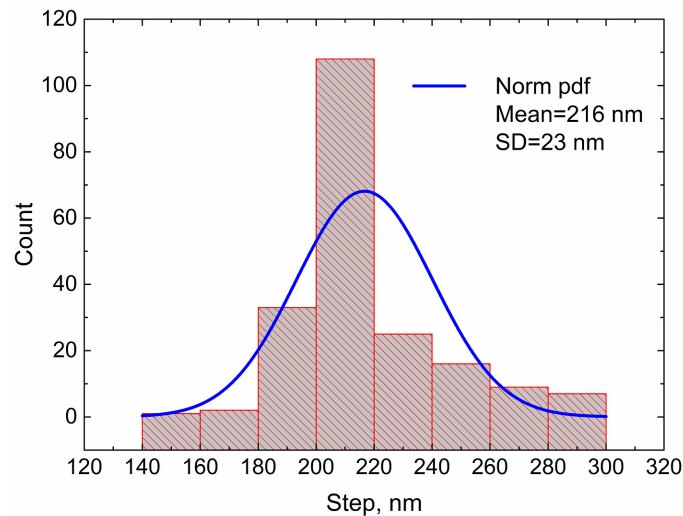


FIG. 7. Histogram of the distribution of ID steps at $R_2 = 10$ Ohm

Figure 8 shows the calculated and experimental curves obtained for the slider pitch value as a function of resistance R_2 . It can be seen that the calculated and experimental curves have close maximum values, $h = 220$ nm at $R_2 = 7$ ohm and $h = 205$ nm at $R_2 = 10$ ohm, respectively, which confirms the adequacy of the constructed model.

Figure 9 demonstrates the trajectory of the slider in the ICS relative to the fixed base as a function of the clamping force. It can be seen that when the clamping force increases, the slip of the slider on the slow edge of the sawtooth control pulse decreases and the slider practically does not lag behind the displacement of the rod in the ICS. Indeed, at a clamping force of 120 g, the slider moves ~ 200 nm in the ICS relative to the fixed base (Fig. 9), while the rod moves ~ 800 nm (Fig. 5(a)), indicating that the slider lags significantly behind the rod as a result of slippage. However, at a clamping force of 400 g, the slider practically moves with the rod as its displacement is ~ 800 nm (Fig. 9), indicating negligible slippage. At the same time, the displacement step also increases from ~ 200 to ~ 800 nm. Thus, we can see that by increasing the clamping, it is possible to reduce the slip under the action of the slow edge of the control pulse and to increase the length of the ID step. Of course, it should be remembered that increasing the pressure increases the wear of the rubbing surfaces, which can impair the reproducibility of the ID steps. In addition, increasing the pressure will reduce the slippage under

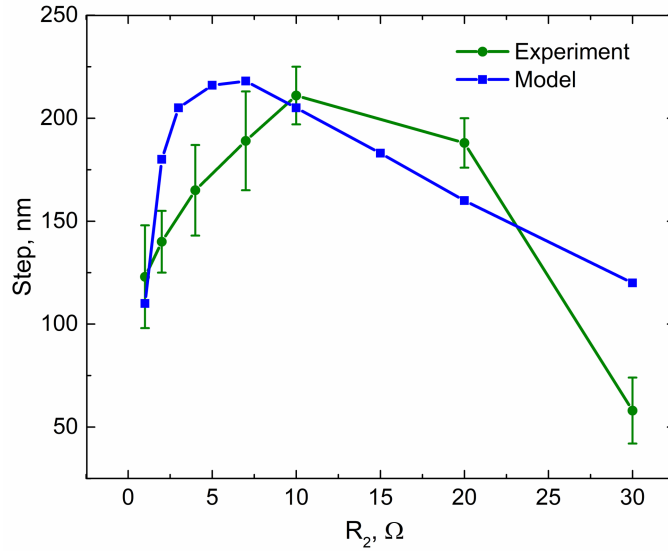


FIG. 8. Model and experimental plots of the dependence of the slider step size on the resistance R_2 in the PA discharge circuit

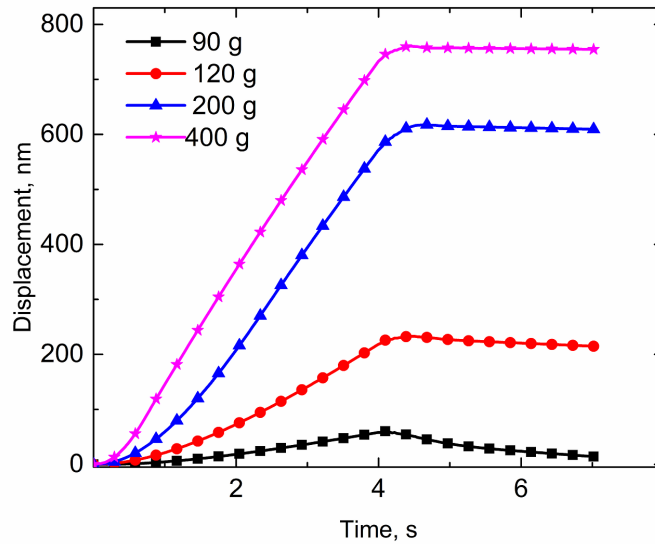


FIG. 9. Trajectories of the slider in the ICS relative to the stationary base at different pressing force

the action of the fast trailing edge, which will reduce the value of the ID step, and if the pressure is too high, it will stop the operation of the ID altogether.

The slider displacement step can also be controlled by changing the amplitude of the sawtooth voltage of the control pulse. Fig. 10 shows the results of calculating the rod, slider and slider displacement step size in the ICS with resistance $R_2 = 10$ ohm, but under the action of a sawtooth control pulse with a smaller amplitude, formed by decreasing the time t_1 from 0.4 to 0.14 ms. It can be seen that reducing the amplitude of the control sawtooth pulse from 14 to 5 V results in a decrease in the step size from ~ 200 to ~ 30 nm.

5. Results and conclusions

The design and numerical model of a vertical ID controlled by sawtooth voltage pulses with slow leading and fast trailing edges are proposed. The control pulses are generated by a simple circuit based on an electronic key by charging/discharging the electrical capacitance of the PA at a large charge time constant and a small discharge time constant. Using the finite element method, the trajectories of the rod and slider movement and the step size of the vertical ID depending on the amplitude and shape of the sawtooth-shaped control pulse and the force of the slider pressure on the rod are investigated. It is found that inertial slippage in the friction pair “slider-rod” occurs both at the fast and slow fronts of the control pulse. A piezo electromechanical resonance in the system “PA-rod-slider”, which is excited by a sharp discharge of PA capacitance and causes harmful oscillations of the slider, is detected. It is shown that it is possible to eliminate

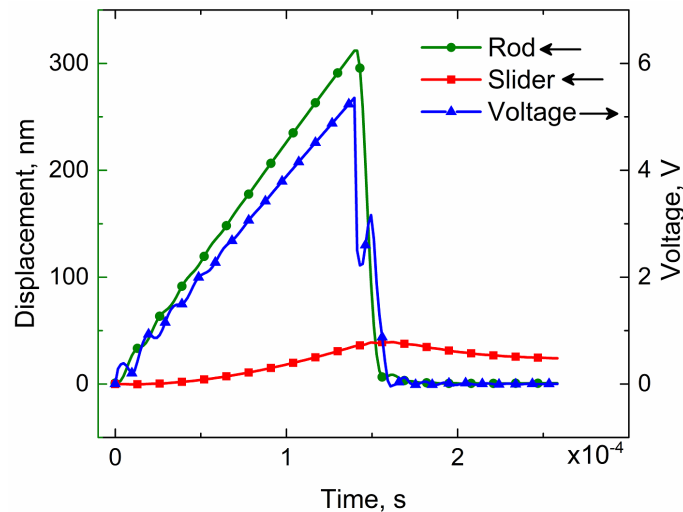


FIG. 10. Trajectories of rod and slider motion in the ICS relative to the fixed base under the action of the control sawtooth voltage pulse with amplitude ~ 5 V

resonance oscillations by selecting the optimum value for the resistance in the PA discharge circuit, which affects both the discharge rate and the goodness of the piezo electromechanical resonator. It is shown that, with the optimal resistance in the PA discharge circuit, it is possible, by changing the charge time and the pressure force, to control the slider movement step during its progressive upward movement along the guide rod without rolling back. The magnitude of the actuator step as a function of the resistance in the PA discharge circuit is experimentally measured. A satisfactory agreement between the calculated and experimental data in the nanometer range of the ID displacements was obtained, which confirms the adequacy of the proposed model. The obtained results can be used in the development and tuning of ID.

References

- [1] Spanner K., Koc B. Piezoelectric Motors, an Overview. *Actuators*, 2016, **5**, 6.
- [2] Bobtsov A.A., Boykov V.I., Bystrov S.V., Grigoriev V.V., Karev P.V. *Actuators and systems for micromovements: textbook*. ITMO University, SPb, 2017, 134 p.
- [3] Mohith S., Upadhyaya A.R., Navin K.P., Kulkarni S.M., Rao M. Recent trends in piezoelectric actuators for precision motion and their applications: a review. *Smart Materials and Structures*, 2021, **30** (1), 3002.
- [4] Wang L., Chen W., Liu J., Deng J., Liu Y. A review of recent studies on non-resonant piezoelectric actuators. *Mechanical Systems and Signal Processing*, 2019, **133** (1), 106254.
- [5] Bansevicius R., Ragulskis K. *Vibromotors*. MOKSLAS Publishing House, Vilnius, Lithuania, 1981, 170 p. (In Russian)
- [6] Ragulskis K., Bansevicius R., Barauskas R., Kulvietis G. *Vibromotors for Precision Microrobots (Application of Vibration Series)*, Hemisphere Publishing Co., Detroit, 1988, 310 p.
- [7] Ueha U., Tomikawa Y. *Ultrasonic Motors: Theory and Applications*. Clarendon: Oxford, UK, 1993, 297 p.
- [8] Sashida T., Kenjo T. *An Introduction to Ultrasonic Motors*. Clarendon: Oxford, UK, 1993, 254 p.
- [9] Uchino K. *Piezoelectric Actuators and Ultrasonic Motors*. Boston, MA: Kluwer Academic Publisher, USA, 1997, 347 p.
- [10] Zhao C. *Ultrasonic Motors: Technologies and Applications*. Science Press: Beijing, China; Springer Verlag: Berlin, Germany, 2011, 494 p.
- [11] Müller K.D., Marth H., Pertsch P., Gloess R., Zhao X. Piezo-Based, Long-Travel Actuators for Special Environmental Conditions. *Proceedings of the 10th Int. Conference on New Actuators*, Bremen, Germany, 14 – 16 June 2006, P. 149 – 153.
- [12] Golubok A.O., Timofeev V.A. STM Combined with SEM without SEM Capability Limitations. *Ultramicroscopy*, 1992, **42–44** (2), P. 1558–1563.
- [13] Koc B., Delibas B. Impact Force Analysis in Inertia-Type Piezoelectric Motors. *Actuators*, 2023, **12**, 52.
- [14] Gorbenko O.M., Zhukov M.V., Pichakhchi S.V., Sapozhnikov I.D., Felshtyn M.L., Golubok A.O. Compact Scanning Probe Microscope Head Based on Inertial Trusters Using Piezopakets. *Nauchnoe Priborostroenie*, 2021, **31** (2), P. 3–22.
- [15] Hunstig M. Piezoelectric Inertia Motors – A Critical Review of History, Concepts, Design, Applications, and Perspectives. *Actuators*, 2017, **6**, 7.
- [16] Liu P., Wen Z., Sun L. An In-Pipe Micro Robot Actuated by Piezoelectric Bimorphs. *Chin. Sci. Bull.*, 2009, **54**, P. 2134–2142.
- [17] Okamoto Y., Yoshida Y. Development of linear actuators using piezoelectric elements. *Electron. Comm. Jpn.*, 1998, **81**, P. 11–17.
- [18] Drevniok B., Paul W.M., Hairsine K.R., McLean A.B. Methods and instrumentation for piezoelectric motors. *Rev. Sci. Instrum.*, 2012, **83**, 033706.
- [19] Wang J., Lu Q. How are the behaviors of piezoelectric inertial sliders interpreted? *Rev. Sci. Instrum.*, 2012, **83**, 093701.
- [20] Gao Q., He M., Lu X., Zhang C., Cheng T. Simple and high-performance stick-slip piezoelectric actuator based on an a symmetrical flexure hinge driving mechanism. *J. of Intelligent Material Systems and Structures*, 2019, **30** (14), P. 2125–2134.
- [21] Sun P., Xu Z., Jin L., Zhu X. A Novel Piezo Inertia Actuator Utilizing the Transverse Motion of Two Parallel Leaf-Springs. *Micromachines (Basel)*, 2023, **14** (5), 954.
- [22] Renner C., Niedermann P. A vertical piezoelectric inertial slider. *The Review of scientific instruments*, 1990, **61** (3), P. 965–967.
- [23] Pohl D.W. Dynamic Piezoelectric Translation Devices. *Rev. Sci. Instrum.*, 1987, **58**, P. 54–57.
- [24] Dubois F., Belly C., Saulot A., Berthier Y. Stick-slip in stepping piezoelectric Inertia Drive Motors – Mechanism impact on a rubbing contact. *Tribology International*, 2016, **100**, P. 371–379.

- [25] Zhang H., Zeng P., Hua S., Cheng G., Yang Z. Impact Drive Rotary Precision Actuator with Piezoelectric Bimorphs. *Front. Mech. Eng. China*, 2008, **3**, P. 71–75.
- [26] Ceponis A., Jurenas V., Mažeika D., Bakanauskas V., Deltuviene D. Rod-Shaped Linear Inertial Type Piezoelectric Actuator. *Actuators*, 2023, **12**, 379.

Submitted 14 August 2024; revised 2 September 2024; accepted 3 September 2024

Information about the authors:

Olga M. Gorbenko – Institute for Analytical Instrumentation of RAS, St. Petersburg, Russia; ORCID 0000-0002-7054-6602; gorolga64@gmail.com

Stanislav Y. Lukashenko – Institute for Analytical Instrumentation of RAS, St. Petersburg, Russia; ORCID 0000-0002-5356-1261; lukashenko13@mail.ru

Stepan V. Pichakhchi – Institute for Analytical Instrumentation of RAS, St. Petersburg, Russia; St. Petersburg Academic University, St. Petersburg, Russia; ORCID 0000-0002-8578-5200; pichakhchi.s@yandex.ru

Ivan D. Sapozhnikov – Institute for Analytical Instrumentation of RAS, St. Petersburg, Russia; ORCID 0000-0003-2575-5015; sapojnikov@gmail.com

Mikhail L. Felshtyn – Institute for Analytical Instrumentation of RAS, St. Petersburg, Russia; ORCID 0000-0001-8677-061X; mfelsztyn@yandex.ru

Alexander O. Golubok – Institute for Analytical Instrumentation of RAS, St. Petersburg, Russia; St. Petersburg Academic University, St. Petersburg, Russia; ORCID 0000-0001-9970-9172; aogolubok@mail.ru

Conflict of interest: the authors declare no conflict of interest.

Hybrid quantum communication protocol for fiber and atmosphere channel

Ilnur Z. Latypov^{1,a}, Vladimir V. Chistyakov^{2,3,b}, Maxim A. Fadeev^{2,4,c}, Danil V. Sulimov^{2,d}, Alexey K. Khalturinsky^{3,e}, Sergey M. Kynev^{2,3,f}, Vladimir I. Egorov^{2,3,g}

¹FRC Kazan Scientific Center of the Russian Academy of Sciences, Kazan, 420111, Russia

²ITMO University, Kronverkskiy, 197101, Russia

³Quanttelecom LLC., St. Petersburg, 199178, Russia

⁴Russian Quantum Center, Skolkovo, Moscow 121205, Russia

^abibidey@mail.ru, ^bv_chistyakov@itmo.ru, ^cwertsam@itmo.ru, ^ddvsulimov@itmo.ru,

^ea.halturinsky@quanttelecom.ru, ^fsergey.kynev@itmo.ru, ^gviegorov@itmo.ru

Corresponding author: I. Z. Latypov, bibidey@mail.ru

PACS 03.67.-a, 42.50.-p

ABSTRACT In this paper, we explore a hybrid quantum communication protocol that operates concurrently over fiber optic and atmospheric channels. This new protocol addresses challenges in urban settings where laying optical fiber may be impractical or costly. By integrating the subcarrier wave (SCW) quantum key distribution (QKD) with phase coding, our approach enhances the flexibility and reliability of quantum communication systems. We have developed and tested an atmospheric optical module equipped with an auto-tuning system to ensure precise optical axis alignment, crucial for minimizing signal loss in turbulent environments. Experimental results demonstrate stable sifted key rates and low quantum bit error rate (QBER) across various channel lengths, confirming the efficacy of our hybrid protocol in securing communication over diverse transmission environments.

KEYWORDS free-space optics, quantum communication, quantum key distribution, atmosphere channel.

ACKNOWLEDGEMENTS Atmospheric channel experiments were done by IZL, MAF, DVS, and AKK with the support of the government assignment for the FRC Kazan Scientific Center of RAS. The analytical work of VVC, SMK is supported by a grant from the Russian Science Foundation (project No. 24-29-00786).

FOR CITATION Latypov I.Z., Chistyakov V.V., Fadeev M.A., Sulimov D.V., Khalturinsky A.K., Kynev S.M., Egorov V.I. Hybrid quantum communication protocol for fiber and atmosphere channel. *Nanosystems: Phys. Chem. Math.*, 2024, **15** (5), 654–657.

1. Introduction

Protocols for quantum key distribution (QKD) are being developed for both fiber optic networks [1,2] and atmospheric links [3–5]. However, integrating fiber optic and atmospheric links to overcome challenges requiring the flexibility and reliability of both transmission media remains a key need. Atmospheric links are actively being developed for both traditional communication tasks within Internet networking and quantum cryptography. Atmospheric laser communication lines are effectively used at short and medium distances (up to 1 km), where laying fiber lines or radio frequency channels is technically or economically impractical. Modern atmospheric quantum communication systems are usually designed for long distances (ranging from 50 to 150 km) using ground-to-satellite or ground-satellite-ground configurations.

This paper presents a quantum communication system utilizing a universal “hybrid” protocol that generates a quantum key simultaneously in both the fiber and atmospheric channels. This scheme’s relevance stems from the specific requirements of constructing quantum telecommunication networks in urban environments, where areas often exist where laying fiber lines is impossible or economically unfeasible. This issue is known as the “last mile” problem [6,7]. A hybrid scheme is feasible when the sites are within the line of sight of each other. Subcarrier wave (SCW) quantum communication systems adopt a different approach to coding quantum states, avoiding issues prevalent in polarization coding systems.

2. Quantum key distribution in a hybrid communication channel

The scheme of the SCW QKD protocol with phase coding in free space is shown in Fig. 1 [8]. According to the scheme, the source of coherent radiation emits monochromatic light with frequency ω . After phase modulation with an electrical signal with low modulating frequency Ω and phase ϕ_A , the modulated signal passes through an attenuator and enters the quantum channel (atmosphere), where it undergoes attenuation.

After passing through the second electro-optic modulator with the same modulating frequency Ω and phase ϕ_B , the amplitudes of the sidebands increase (taking part of the energy from the carrier mode in the case $\phi_A = \phi_B$) or decrease (energy flows to the carrier mode). The narrowband spectral filter passes only the sidebands, and then the signal is detected by a single photon detector.

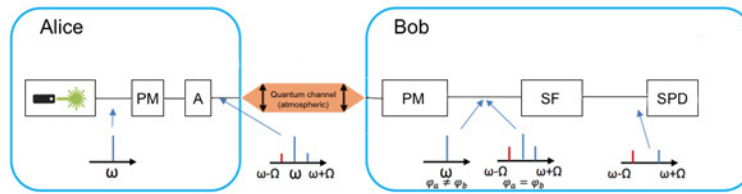


FIG. 1. Experimental setup of free-space subcarrier wave quantum communication system. PM is the phase modulator, A is the optical attenuator, SF is the spectral filter, and SPD is the single photon detector

TABLE 1. Statistics of optical line operation under typical turbulence conditions

Optical line	optical losses, average value, dB	optical loss, average deviation, dB	optical losses, minimum value, dB	optical losses, maximum value, dB	time
20 m	9,78	2,54	7,65	15,43	134 min

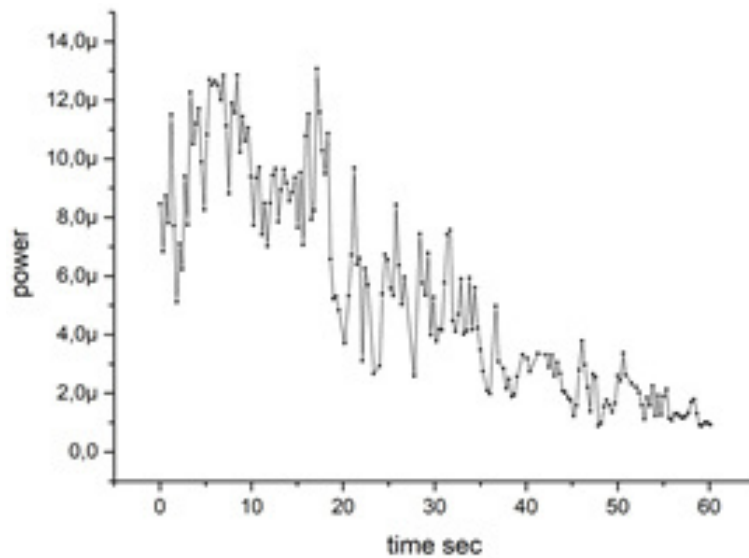


FIG. 2. The power of the laser radiation transmitted through the atmospheric line without auto-tuning system

To create a stable atmospheric channel, we developed transmitting and receiving optical modules equipped with an auto-tuning system. For the optical line to operate reliably, it is crucial to keep the optical axes of the receiver and the transmitter aligned with the accuracy of just a few microradians. When the length of the optical line increases from 5 to 100 meters, the losses in the optical signal remain relatively stable and range from 6 to 10 dB. The main part of the losses is associated with the deformation of the energy profile of the beam in a turbulent atmosphere. The automatic tuning system is based on the use of reference radiation of an optical diode at a wavelength of 900 nm, which is coaxially aligned with the optical axis of the quantum channel. The coordinates of the reference radiation are determined by a CCD matrix that generates a signal for a mirror controlled by four electromagnets. Thus, the auto-tuning system always maintains the alignment of the transmitter and receiver.

In the absence of an auto-tuning system, misalignment of the optical axes can occur within one minute. Fig. 2 shows an example of the dependence of the power of laser radiation at a wavelength of 1550 nm transmitted through an atmospheric line without an auto-tuning system.

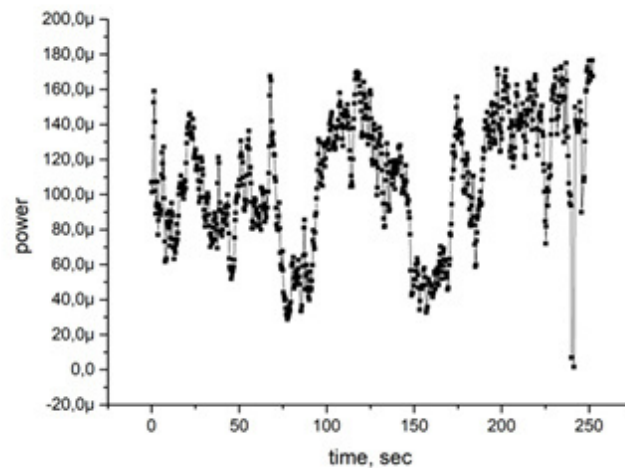


FIG. 3. The power of the laser radiation transmitted through the atmospheric line. Deviation from the maximum value is associated with the influence of turbulence

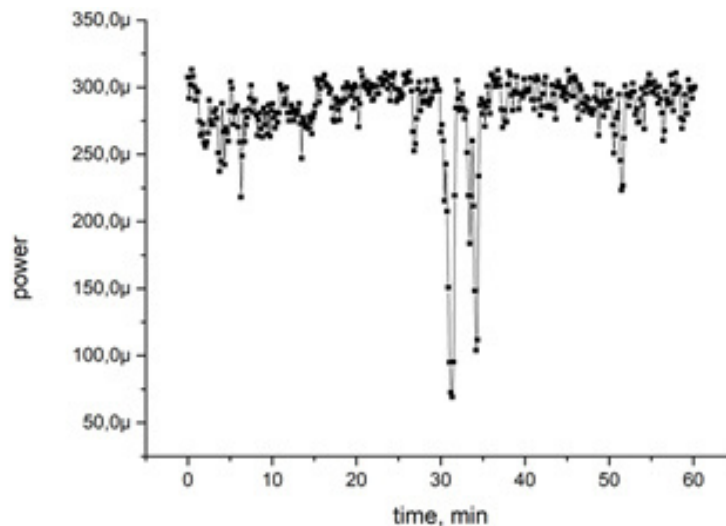


FIG. 4. The power dependence of the signal transmitted through the optical line on time. The operation of the auto-tracking system for a long time is demonstrated

Fig. 3 shows an example of the effect of turbulence on losses in the optical channel. The magnitude and nature of turbulence depend on the location of the optical line, the speed of movement of air masses, and the temperature gradient. Fig. 4 shows the effectiveness of the auto-tracking system over a long time. The accuracy of our track system was 7 microradian, which made it possible to keep the optical signal at the level of 1 dB.

After setting up the optical and QKD systems, we measured the performance of the systems over different channel lengths: 25 meters, 40 meters, and 50 meters. For all optical channels, the optical loss was 6.5 dB, and the sifted key generation rate was 1.45 KB/s, with a quantum bit error rate (QBER) of 6%. Losses at the output and input into the optical fiber determined losses in the optical line. An optical beam with an aperture of 80 mm has a low diffraction divergence, thus at a distance of 15, 25, and 40 meters, we get the same key generation rate.

3. Conclusion

Measurements of the key rate in a hybrid communication protocol including fiber optic and atmospheric sections have been carried out. The atmospheric link was implemented using the developed transceivers equipped with an auto-tuning system. The results show that the SCW QKD protocol functions effectively in the atmospheric link, and the key generation rate depends solely on the optical loss. In the future, it is planned to improve the persistence of the protocol by detailed theoretical analysis of the possibility of using turbulence to obtain information accessible by an intruder (Eve).

References

- [1] Honjo T., Nam S.W., Takesue H., Zhang Y., Hadfield R.H., Dardy H.H., and Yamamoto Y. Long-distance entanglement-based quantum key distribution over optical fiber. *Optics Express*, 2008, **16**(23), P. 19118–19126.
- [2] Rosenberg D., Harrington J.W., Rice P.R., Hiskett P.A., Peterson C.G., Hughes R.J., Lita A.E., Nam S.W., and Nordholt J.E. Long-distance decoy-state quantum key distribution in optical fiber. *Physical Review Letters*, 2007, **98**(1), P. 010503.
- [3] Cao Y., Li Z., Zhang W., You Z., Zhang X., Wang Z., Huang C., Li H.W., and Guo G.C. Long-distance free-space measurement-device-independent quantum key distribution. *Physical Review Letters*, 2020, **125**(26), P. 260503.
- [4] Pirandola S. Limits and security of free-space quantum communications. *Physical Review Research*, 2021, **3**(1), P. 013279.
- [5] Schmitt-Manderbach T., Weier H., Furst M., Ursin R., Tiefenbacher F., Scheidl T., Perdigues J., Sodnik Z., Kurtsiefer C., and Weinfurter H. Experimental demonstration of free-space decoy-state quantum key distribution over 144 km. *Physical Review Letters*, 2007, **98**(1), P. 010504.
- [6] Cao Y., Zhang Z., Xu B., You L., Wang Z., and Li H. W. The evolution of quantum key distribution networks: On the road to the qinternet. *IEEE Communications Surveys & Tutorials*, 2022, **24**(2), P. 839–894.
- [7] Techateerawat P. Simulating Network Management System for Quantum Key Distribution based on rural and remote broadband in Thailand. *PBRU Science Journal*, 2023, **20**(1), P. 97–110.
- [8] Kynev S.M., Chistyakov V.V., Fadeev M.A., and Latypov I.Z. Free-space subcarrier wave quantum communication. *Journal of Physics: Conference Series*. IOP Publishing, 2017, **917**(5), P. 052003.

Submitted 9 September 2024; revised 22 September 2024; accepted 23 September 2024

Information about the authors:

Ilnur Z. Latypov – FRC Kazan Scientific Center of the Russian Academy of Sciences, ul. Lobachevskogo, 2/31, POB 261, Kazan, 420111, Russia; ORCID 0000-0003-2990-249X; bibidey@mail.ru

Vladimir V. Chistyakov – ITMO University, Kronverkskiy, 49, St. Petersburg, 197101, Russia; Quanttelecom LLC., 6 Line, 59, St. Petersburg, 199178, Russia; ORCID 0000-0002-2414-3490; v.chistyakov@itmo.ru

Maxim A. Fadeev – ITMO University, Kronverkskiy, 49, St. Petersburg, 197101, Russia; Russian Quantum Center, Skolkovo, Moscow 121205, Russia; ORCID 0000-0003-4290-4852; wertsam@itmo.ru

Danil V. Sulimov – ITMO University, Kronverkskiy, 49, St. Petersburg, 197101, Russia; ORCID 0000-0002-7964-0697; dvsulimov@itmo.ru

Alexey K. Khalturinsky – Quanttelecom LLC., 6 Line, 59, St. Petersburg, 199178, Russia; a.khalturinsky@quanttelecom.ru

Sergey M. Kynev – ITMO University, Kronverkskiy, 49, St. Petersburg, 197101, Russia; Quanttelecom LLC., 6 Line, 59, St. Petersburg, 199178, Russia; ORCID 0000-0001-8698-1804; sergey.kynev@itmo.ru

Vladimir I. Egorov – ITMO University, Kronverkskiy, 49, St. Petersburg, 197101, Russia; Quanttelecom LLC., 6 Line, 59, St. Petersburg, 199178, Russia; ORCID 0000-0003-0767-0261; viegorov@itmo.ru

Conflict of interest: the authors declare no conflict of interest.

Effect of structural parameters, and spin-orbit interaction on the electronic properties of double quantum wire systems in the presence of external magnetic field

Mahmoud Ali, Mohammad Elsaid

Physics Department, An-Najah National University, Palestine

Corresponding author: Mohammad Elsaid, mkelsaid@najah.edu

ABSTRACT This study explores the effect of the structural parameters of the confining potential and external magnetic field on the electronic properties of a double quantum wire (DQW) system. Using theoretical analysis and graphical representations, we investigate the effects of varying parameters such as structural parameters (μ and λ) on the confinement potential profiles, probability density distributions and energy spectra of DQWs. Furthermore, we investigate the effect of variation of the confinement potential, the Rashba spin-orbit coupling and the external magnetic field on the energy spectra and the local density of states of the system. The changes in the energy spectra and the local density of states of the system due to Rashba spin-orbit coupling, and the external magnetic field were highlighted. The shifts and variations in energy and in the local density of states were discussed in detail. Our research results provide valuable insights into possibility of using the structural parameters and the external magnetic fields for control the electronic properties of the double quantum wire system.

KEYWORDS double quantum wire, spin-orbit interaction, local density of states

FOR CITATION Ali M., Elsaid M. Effect of structural parameters, and spin-orbit interaction on the electronic properties of double quantum wire systems in the presence of external magnetic field. *Nanosystems: Phys. Chem. Math.*, 2024, **15** (5), 658–669.

1. Introduction

The physical properties of semiconductors form the basis of the latest and current technological revolution, the development of ever smaller and more powerful devices, which affect not only the prospects of modern science but also practically all aspects of our daily life. This development is based on the ability to engineer the physical properties of semiconductors to make smaller devices with promising applications in high-performance devices [1–4]. Modern crystal growth techniques make it possible to grow layers of semiconductor material, which are so small that their physical properties are different from those of bulk materials. In these low-dimensional semiconductor structures, the carriers can be confined spatially, in quantum wires the electron is confined in two directions and can move freely only in the remaining direction. Quantum wires (QW) have been investigated widely and the number of published articles in this field increases because of their exciting applications, such as quantum wires laser, transistor, light-emitting diode, sensors, solar cells, optical filters, and displays [5–10]. Quantum wires have been made experimentally in different ways through various techniques, such as the vapor-liquid-solid (VLS) method, electron-beam lithography (EBL), nano sphere lithography, etching of quantum wells and ion implantation [11–15]. Two identical quasi-one-dimensional systems can be coupled by additional lateral confinement to produce a double quantum wire (DQW) structure. One-dimensional double quartic-well potential can be used to make double quantum wire heterostructures with controllable tunneling barrier thickness [16].

Both theoretical [17–23] and experimental studies [24, 25] have delved into the impact of the external magnetic field on the electronic and transport characteristics of the double quantum wire structure, formed by introducing a potential barrier that separates two identical narrow quantum wires. Huang and his research collaborators have examined the conductivity, thermoelectric power, and magnetization in ballistic coupled double quantum wires when exposed to an external magnetic field [26]. Additionally, Yenal Karaaslan et al. have investigated the conductivity and optical response of double quantum wires under the external magnetic and electric fields, considering Rashba and Dresselhaus spin-orbit couplings [27]. The change in the energy dispersion curve and ballistic conductance of a double quantum wire under the influence of the external magnetic field, electric field, and Rashba spin-orbit interaction are studied theoretically in [28]. The electronic transport properties of double QWs made of GaAs by considering impurity and external magnetic field were investigated by Korepov [29].

Sharma et al. have explored the influence of the temperature, hydrostatic pressure, and impurity on the energy spectrum, and ballistic conductivity of the $\text{In}_x\text{Ga}_{1-x}\text{As}$ double QWR [30].

The investigation of the local density of states (LDOS) spectra has captivated the attention of numerous researchers, they have been motivated to explore the LDOS spectra due to their fundamental role in explaining the electronic structure and behavior of materials at the quantum level. By analyzing the LDOS, scientists gain valuable insights into the

distribution of electronic states within a given system, allowing for comprehension of its unique characteristics and functionalities. Consequently, researchers have conducted extensive investigations focusing on the comparison between LDOS results obtained through experimental work [31–33] and their associated theoretical counterparts [34–36]. Cristina Bena and Steven A. Kivelson calculated the local density of states in graphite theoretically in the presence of impurity [37]. The authors in reference [38] obtained the local density of states in graphene numerically by using the tight-binding model.

This paper is organized as follows: The Hamiltonian theory and computation procedures of double quantum wires are shown in the second section taking into consideration the Rashba spin-orbit coupling, the external magnetic field and the structural parameters. The computed results for eigenenergies, probability density, local density of states, and their dependence on the Rashba spin-orbit coupling, the external magnetic field and the structural parameters were presented in the third section. Section 4 is devoted to the conclusion.

2. Theory

The total Hamiltonian of an electron in the DQW which is subjected to an external magnetic field along the z -direction with Rashba spin-orbit coupling can be written as:

$$\hat{H} = \frac{(\vec{p} - e\vec{A})^2}{2m^*} + V_{\text{conf}}(x) + V_{\text{var}}(x) + H_R + H_{\text{Zeeman}}, \quad (1)$$

where $(\vec{p} - e\vec{A})$ is the canonical momentum, \vec{p} is the momentum operator, \vec{A} is the vector potential corresponding to the magnetic field along the z -direction, m^* is the effective mass of the electron in InSb-medium and e is the electron charge.

The double nanowires along the y -direction are characterized by a double-well confinement written as [39]:

$$V_{\text{conf}}(x) = \frac{1}{4}\lambda\left(x^2 - \frac{\mu^2}{\lambda}\right)^2, \quad (2)$$

where λ and μ are positive adjustable parameters for adjusting the width of the wires and the height of the barrier between the two-coupled wires, respectively [40]. The addition,

$$V_{\text{var}}(x) = V_0 \exp\left(-\frac{(x - x_1)^2}{d^2}\right), \quad (3)$$

has been taken as a variation of the confinement potential in the x -direction, where x_1 denotes the perturbation position and V_0 is the strength of the variation where d is a tunable parameter to impact variation stretch, this variation potential adds an extra potential to break the symmetry between the two wires in the double quantum wires (i.e a line of localized impurities at x_1 along the growth direction).

The Zeeman effect caused by the interaction between the electron spin and external magnetic field is given by:

$$\hat{H}_{\text{Zeeman}} = \frac{1}{2}g^*\mu_B B\sigma_z, \quad (4)$$

where g^* is the effective Lande g -factor, μ_B is the Bohr magneton and σ_z is the z -component of Pauli matrices.

The effects of Rashba spin-orbit coupling is taken into account by adding the following term [27]:

$$\hat{H}_R = \frac{\alpha_R}{\hbar} [\sigma_x(p_y + eBx) - \sigma_y p_x]. \quad (5)$$

Here α_R is the Rashba spin-orbit coupling parameters, σ_x , σ_y are the x - and y -component of the Pauli matrices, and p_x , p_y are the components of the electron momentum.

The local density of states can give information about the tunneling current and the tunneling conductance in the STM spectroscopy:

$$LDOS(r, E) = \sum_{n=1}^N |\psi_n|^2 \delta(E - E_n). \quad (6)$$

The delta function that appears in the LDOS can be replaced by a more practical expression in the computational process [41]:

$$LDOS(E) = \frac{1}{\sqrt{2\pi}\Gamma^2} \sum_n |\psi_n|^2 \exp\left(-\frac{(E - E_n)^2}{2\Gamma^2}\right), \quad (7)$$

where Γ is the broadening factor and E_n is the energy value for the n -th eigenstate.

The continuous spectrum eigenfunctions of the Hamiltonian can be expressed in terms of plane waves due to the translational invariance along the y -direction as:

$$\psi(x, y) = \varphi(x) \exp(ik_y y), \quad (8)$$

where k_y represents the wave numbers of the plane wave along the y -direction. The Schrödinger equation becomes separable in x and y and, accordingly, the Hamiltonian ($H = H_1 + H_2 + H_R + V_{\text{imp}}$) can be rewritten as follows:

$$H_1 = \left[-\frac{\hbar^2}{2m^*} \frac{d^2}{dx^2} + \frac{1}{2} m^* \omega^2 (x - x_0)^2 + \frac{\omega_0^2 \hbar^2 k_y^2}{\omega^2 2m^*} \right] \sigma_0 + \frac{1}{2} g^* \mu_B B \sigma_z, \quad (9)$$

$$H_2 = \left[-\frac{1}{2} (m^* \omega_0^2 + \mu^2) x^2 + \frac{1}{4} \lambda x^4 + \frac{1}{4} \frac{\mu^4}{\lambda} \right] \sigma_0, \quad (10)$$

$$H_R = \alpha_R \left[\sigma_x \left(k_y + \frac{eB}{\hbar} x \right) + i \sigma_y \frac{d}{dx} \right], \quad (11)$$

$$V_{\text{var}}(x) = V_0 \exp \left[-\frac{(x - x_1)^2}{d^2} \right]. \quad (12)$$

Here ω_0 is the harmonic oscillator frequency, $\omega = \sqrt{\omega_0^2 + \omega_c^2}$ is the effective oscillator frequency and $\omega_c = eB/m^*$ is the cyclotron frequency, $l_0 = \sqrt{\hbar/m^* \omega_0}$ is the characteristic length of the harmonic oscillator and $x_0 = -\frac{l_0^2 \tilde{\omega}_c k_y}{\tilde{\omega}_c^2 + 1}$ is the guiding center coordinate where $\tilde{\omega}_c = \frac{\omega_c}{\omega_0}$ and $\tilde{\omega} = \frac{\omega}{\omega_0} = \sqrt{\tilde{\omega}_c^2 + 1}$.

The set of eigenfunctions of H_1 is given as:

$$\phi_{n\sigma}(x) = \frac{1}{\sqrt{l_0} \sqrt{\frac{\pi}{\sqrt{\tilde{\omega}_c^2 + 1}}} 2^n n!} H_n \left(\frac{x - x_0}{\frac{l_0}{\sqrt{\tilde{\omega}_c^2 + 1}}} \right) \exp \left(-\frac{1}{2} \left(\frac{x - x_0}{\frac{l_0}{\sqrt{\tilde{\omega}_c^2 + 1}}} \right)^2 \right) \chi_\sigma. \quad (13)$$

Here $H_n(x)$ are the Hermite polynomials of integer order n , χ_σ are the spinor functions with $\chi_+ = \begin{pmatrix} 1 \\ 0 \end{pmatrix}$ for spin-up and $\chi_- = \begin{pmatrix} 0 \\ 1 \end{pmatrix}$ for spin-down in the z -direction.

By using the set of eigenfunctions of H_1 , the matrix elements of the full Hamiltonian can be written as:

$$\langle \phi_{n\sigma} | H | \phi_{m\sigma'} \rangle = \langle \phi_{n\sigma} | H_1 | \phi_{m\sigma'} \rangle + \langle \phi_{n\sigma} | H_2 | \phi_{m\sigma'} \rangle + \langle \phi_{n\sigma} | H_R | \phi_{m\sigma'} \rangle + \langle \phi_{n\sigma} | V_{\text{var}} | \phi_{m\sigma'} \rangle. \quad (14)$$

The energy eigenvalues corresponding to H_1 are as follows:

$$\frac{E_1}{\hbar\omega_0} = \sqrt{\tilde{\omega}_c^2 + 1} \left(n + \frac{1}{2} \right) + \frac{l_0^2 k_y^2}{2(\tilde{\omega}_c^2 + 1)} \pm \frac{g^* \mu_B B}{2\hbar\omega_0} \quad (15)$$

and the matrix elements corresponding to H_2 are:

$$\left\langle \phi_{n\sigma} \left| \frac{H_2}{\hbar\omega_0} \right| \phi_{m\sigma'} \right\rangle = A_{-4} \delta_{n,m-4} + A_{-3} \delta_{n,m-3} + A_{-2} \delta_{n,m-2} + A_{-1} \delta_{n,m-1} + A_0 \delta_{n,m} + A_{+1} \delta_{n,m+1} + A_{+2} \delta_{n,m+2} + A_{+3} \delta_{n,m+3} + A_{+4} \delta_{n,m+4}, \quad (16)$$

where:

$$\begin{aligned}
A_{-4} &= \frac{1}{16} \frac{\tilde{\lambda}}{\tilde{\omega}_c^2 + 1} \sqrt{(n+4)(n+3)(n+2)(n+1)}, \\
A_{-3} &= \frac{1}{4} \frac{x_0}{l_0 \sqrt{\tilde{\omega}_c^2 + 1}} \tilde{\lambda} \sqrt{\frac{2}{\sqrt{\tilde{\omega}_c^2 + 1}}} (n+3)(n+2)(n+1), \\
A_{-2} &= \frac{1}{4 \sqrt{\tilde{\omega}_c^2 + 1}} \sqrt{(n+2)(n+1)} \left[\tilde{\lambda} \left(3 \frac{x_0^2}{l_0^2} + \frac{1}{\sqrt{\tilde{\omega}_c^2 + 1}} \left(n + \frac{3}{2} \right) \right) - (1 + \tilde{\mu}^2) \right], \\
A_{-1} &= \frac{1}{2} \frac{x_0}{l_0} \sqrt{\frac{2}{\sqrt{\tilde{\omega}_c^2 + 1}}} (n+1) \left[\tilde{\lambda} \left(\frac{x_0^2}{l_0^2} + \frac{3}{2 \sqrt{\tilde{\omega}_c^2 + 1}} (n+1) \right) - (1 + \tilde{\mu}^2) \right], \\
A_0 &= \frac{1}{4} \tilde{\lambda} \left[\frac{x_0^4}{l_0^4} + \frac{3}{\sqrt{\tilde{\omega}_c^2 + 1}} \frac{x_0^2}{l_0^2} (2n+1) + \frac{\tilde{\mu}^4}{\tilde{\lambda}^2} \right] + \frac{1}{4} \tilde{\lambda} \left[\frac{3}{2(\tilde{\omega}_c^2 + 1)} \left(n^2 + n + \frac{1}{2} \right) \right] - \\
&\quad \frac{1}{2} (1 + \tilde{\mu}^2) \left[\frac{x_0^2}{l_0^2} + \frac{1}{\sqrt{\tilde{\omega}_c^2 + 1}} \left(n + \frac{1}{2} \right) \right], \\
A_{+1} &= \frac{1}{2} \frac{x_0}{l_0} \sqrt{\frac{2}{\sqrt{\tilde{\omega}_c^2 + 1}}} n \left[\tilde{\lambda} \left(\frac{x_0^2}{l_0^2} + \frac{3}{2 \sqrt{\tilde{\omega}_c^2 + 1}} n \right) - (1 + \tilde{\mu}^2) \right], \\
A_{+2} &= \frac{1}{4 \sqrt{\tilde{\omega}_c^2 + 1}} \sqrt{n(n-1)} \left[\tilde{\lambda} \left(3 \frac{x_0^2}{l_0^2} + \frac{1}{\sqrt{\tilde{\omega}_c^2 + 1}} \left(n - \frac{1}{2} \right) \right) - (1 + \tilde{\mu}^2) \right], \\
A_{+3} &= \frac{1}{4} \tilde{\lambda} \frac{x_0}{l_0 \sqrt{\tilde{\omega}_c^2 + 1}} \sqrt{\frac{2}{\sqrt{\tilde{\omega}_c^2 + 1}}} n(n-1)(n-2), \\
A_{+4} &= \frac{1}{16(\tilde{\omega}_c^2 + 1)} \tilde{\lambda} \sqrt{n(n-1)(n-2)(n-3)},
\end{aligned}$$

with $\tilde{\lambda} = \frac{\lambda \hbar \omega_0}{(m^* \omega_0^2)^2}$ and $\tilde{\mu} = \frac{\mu}{\sqrt{m^* \omega_0}}$.

The matrix elements of Rashba Hamiltonian H_R are given by the expression:

$$\begin{aligned}
\left\langle \phi_{n\sigma} \left| \frac{H_R}{\hbar \omega_0} \right| \phi_{m\sigma'} \right\rangle &= \sqrt{2} \frac{\Delta_R}{\hbar \omega_0} \left[l_0 k_y \left(1 - \frac{\tilde{\omega}_c^2}{\tilde{\omega}_c^2 + 1} \right) \right] \delta_{n,m} + \\
&\quad \sqrt{2} \frac{\Delta_R}{\hbar \omega_0} \sqrt{\tilde{\omega}_c^2 + 1} \left[\left(\frac{\tilde{\omega}_c}{\sqrt{\tilde{\omega}_c^2 + 1}} \pm 1 \right) \sqrt{\frac{(n+1)}{2}} \delta_{n,m-1} + \left(\frac{\tilde{\omega}_c}{\sqrt{\tilde{\omega}_c^2 + 1}} \mp 1 \right) \sqrt{\frac{n}{2}} \delta_{n,m+1} \right], \quad (17)
\end{aligned}$$

where: $\Delta_R = \frac{\alpha_R^2 m^*}{2 \hbar^2}$.

The matrix elements of the variation Hamiltonian are presented by the expression:

$$\left\langle \phi_{n\sigma} \left| \frac{V_{\text{var}}(x)}{\hbar \omega_0} \right| \phi_{m\sigma'} \right\rangle = \left\langle \phi_{n\sigma} \left| \frac{V_0}{\hbar \omega_0} \exp \left(-\frac{(x-x_1)^2}{d^2} \right) \right| \phi_{m\sigma'} \right\rangle, \quad (18)$$

which can be simplified by using the standard integral [42]:

$$\int_{-\infty}^{\infty} e^{-(x-y)^2} H_m(\alpha x) H_n(\alpha x) dx = \pi^{1/2} \sum_{k=0}^{\min(m,n)} 2^k k! \binom{m}{k} \binom{n}{k} (1 - \alpha^2)^{\frac{m+n}{2} - k} H_{m+n-2k} \left[\frac{\alpha y}{(1 - \alpha^2)^{1/2}} \right]. \quad (19)$$

The matrix elements of $V_{\text{var}}(x)$ can be written as:

$$\begin{aligned}
\left\langle \phi_{n\sigma} \left| \frac{V_{\text{var}}(x)}{\hbar \omega_0} \right| \phi_{m\sigma'} \right\rangle &= \frac{V_0}{\sqrt{2^{n+m} n! m!}} \times \sqrt{\frac{\sqrt{\tilde{\omega}_c^2 + 1}}{\sqrt{\tilde{\omega}_c^2 + 1} + \frac{1}{d^2}} \exp \left[\frac{-(x_0 - x_1)^2 (1 - \frac{1}{d^2})}{\frac{\sqrt{\tilde{\omega}_c^2 + 1}}{\sqrt{\tilde{\omega}_c^2 + 1} + \frac{1}{d^2}} d^2} \right]} \times \\
&\quad \sum_{k=0}^{\min(m,n)} 2^k k! \binom{m}{k} \binom{n}{k} \times \left(\frac{\sqrt{\tilde{\omega}_c^2 + 1}}{\sqrt{\tilde{\omega}_c^2 + 1} + \frac{1}{d^2}} \right)^{\frac{m+n}{2} - k} H_{m+n-2k} \left[\frac{\frac{-(x_0 - x_1)}{d^2} \sqrt{\tilde{\omega}_c^2 + 1} / (\sqrt{\tilde{\omega}_c^2 + 1} + \frac{1}{d^2})}{\sqrt{(1 - \sqrt{\tilde{\omega}_c^2 + 1}) / \sqrt{\tilde{\omega}_c^2 + 1} + \frac{1}{d^2}}} \right]. \quad (20)
\end{aligned}$$

In the calculations the characteristic length l_0 corresponding to the confinement potential is chosen as the length scale and, consequently, the energy scale becomes to be $\hbar\omega_0$. The parameters used in the numerical calculations are the effective mass of Indium Antimonide (InSb) ($m^* = 0.015m_e$) and the effective Lande-g factor ($g^* = 51$) [43].

The changes in the confinement potential shape, influenced by structural parameters and varying across the x -coordinates, are illustrated in Fig. 1, while keeping the parameter $\tilde{\lambda}$ constant. In Fig. 1(a), it is evident that for $\tilde{\mu} = 0$, the confinement exhibits a SQW (single quantum wire) structure. However, for $\tilde{\mu} \neq 0$, the potential confines the carriers within two narrower wires, resulting in a DQW (double quantum wire) confinement. To investigate the influence of the adjustable parameter μ , the confinement potential has been graphically represented for various $\tilde{\mu}$ values in Fig. 1(b). As μ increases, the barrier between the two wires becomes higher. Consequently, the probability of carriers tunneling between the wires decreases. Therefore, the increase in $\tilde{\mu}$ acts as a controlling factor, influencing the confinement potential and, in turn, limiting the probability of quantum tunneling events between the two distinct wires.

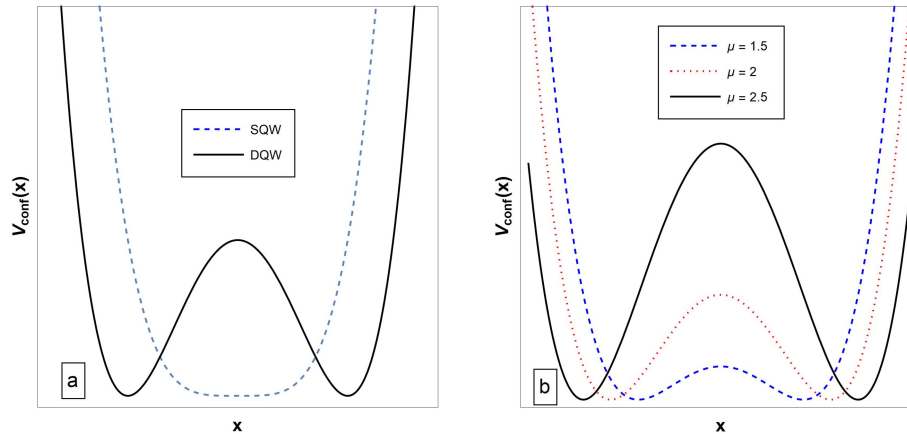


FIG. 1. Confinement potential profile versus the growth direction coordinate a) SQW and DQW; b) DQW for different $\tilde{\mu}$ at fixed $\tilde{\lambda}$ value

In Fig. 2, the influence of the adjustable parameter $\tilde{\mu}$ on probability density is apparent. When $\tilde{\mu}$ is set to zero, As illustrated in Fig. 2(a), choosing $\tilde{\mu} = 0$ leads to the formation of a single quantum wire (SQW) shape. Fig. 2(a) presents a clear representation of the probability density distribution for the first few energy levels. However, in Figs. 2(b) ($\tilde{\mu} = 2$) and 2(c) ($\tilde{\mu} = 2.5$), the introduction of a barrier results in a double quantum wires (DQW) configuration, causing a noticeable change in the distribution of the probability density. The effect of the barrier on the probability density is evident, as it decreases the probability density in its location of effect, especially for states with initially higher probability density at the barrier position. The redistributed probability density is equally distributed in two wires, and the energy value for each state increases. This increase is greater for the levels that had a higher probability at the location of the barrier's effect. For example, the barrier's impact on the first level is greater than its impact on the second level because the wave function for the first level has an antinode at the barrier's location. Consequently, the barrier divides the probability into two equal parts in each wire, and the energy increase for this level is significant. As for the second level, it originally had a node in its wave function in the barrier's location, which resulted in a smaller energy increase compared to the first level. Therefore, the first and second levels become degenerate within each wire. Furthermore, as $\tilde{\mu}$ increases, the barrier height also increases, affecting higher energy states. Therefore, $\tilde{\mu}$ causes a degenerate state in each wire and also causes symmetry degeneracy in probability density across the two wires, as it is clear from the comparison between Figs. 2(a and b). The symmetry degeneracy becomes more pronounced at higher energy levels as the value of $\tilde{\mu}$ increases, as illustrated in Fig. 2(c).

Figure 2.

Figure 3 provides insight into the effect of potential variation on the probability density within a double quantum wire system. The variation was placed in the center of one of the wires ($x_1/l_0 = 1.2$) as shown in Fig. 3(a), the variation in the confinement potential significantly influenced the probability density of the energy levels. A comparative analysis between Fig. 3(a) and Fig. 3(b) reveals a significant change in the probability density due to variation in the potential which results in the elevation of the energy levels within the wire where they are situated ($V_0 \exp(-(x - x_0)^2/d^2)$) where d (which represents the standard deviation of the Gaussian function) is chosen to be small ($d/l_0 = 0.5$) to get more localized potential. This effect leads to large redistribution of the probability density resulting in the elimination of the symmetry degeneracy which is clearly evident in the Fig. 3(a). From the comparison, it becomes evident that the probability density has undergone a marked redistribution. For example, the first peak in the left wire now corresponds to the ground energy level, while the first peak in the right wire represents the first excited energy level. So the energy levels have been extensively redistributed, and the symmetry degeneracy has been removed.

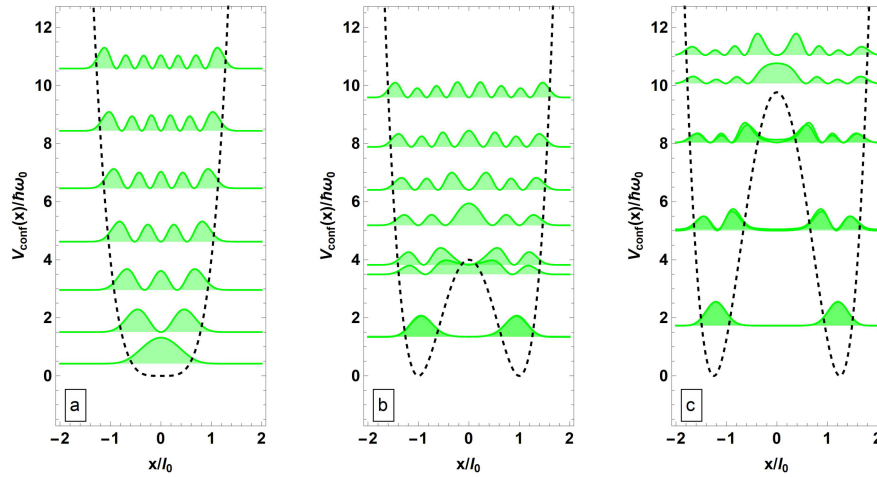


FIG. 2. The confinement potential and square wave functions corresponding to the first few energy levels: a) for SQW; b) DQW at $\tilde{\mu} = 2$ and $\tilde{\lambda} = 1$; c) DQW at $\mu = 2.5$ and $\tilde{\lambda} = 1$

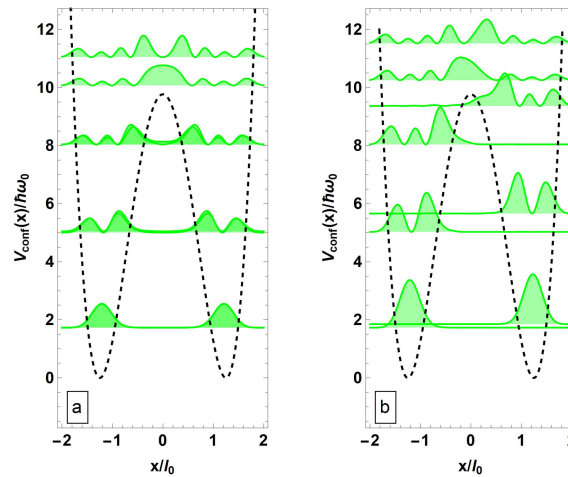


FIG. 3. The confinement potential and square wave functions corresponding to the first few energy levels: a) DQW at $\tilde{\mu} = 2.5$ and $\tilde{\lambda} = 1$ without variation; b) DQW at $\tilde{\mu} = 2.5$ and $\tilde{\lambda} = 1$, $V_0/(\hbar\omega_0) = 3$, $x_1/l_0 = 1.2$ and $d/l_0 = 0.5$

The influence of the parameter $\tilde{\mu}$ on merging energy levels is distinctly evident in Fig. 4(a). It is apparent that at higher values of $\tilde{\mu}$, the merging is exhibiting at higher energy levels. Additionally, the energy levels associated with the system have a degeneracy related to the spin of the electron, namely, each line in the figure represents two degenerate energy levels due to the spin of the electron. The external magnetic field has a significant effect, as shown in Fig. 4(b). The external magnetic field plays a dual role by removing the spin degeneracy and causing the separation of energy levels that were previously merged due to the confinement potential in each wire. This leads to a noticeable change in the levels of the energy and provides a clear illustration of the magnetic field's influence on the quantum characteristics of the system. The external magnetic field results in a shift up in the energy levels of the system. This shift is dependent on the magnetic field strength, and each energy level in the system will split into two sublevels due to the interaction with the external magnetic field, i.e. this leads to the remove of the degeneracy in the energy levels. In conclusion, the external magnetic field has an essential effect on the double quantum wire system, causing the splitting of energy levels and giving rise to changes in the electronic structure. The ability to adjust the strength of the external magnetic field provides a technique to organize energy levels and control the electronic properties of the double quantum wire system.

For a more focused analysis of the magnetic field and Rashba spin-orbit coupling effect on the DQW system, Fig. 5 has been introduced. Fig. 5(a) illustrates the effect of the magnetic field on certain energy levels within the system. It is observed in the figure that the energy levels are merged due to the influence of the barrier potential created by the confinement potential. Lower energy levels experience a more significant impact from the barrier since they are situated where its effect is stronger. In the higher energy levels, the influence of the barrier diminishes. Thus, in lower energy

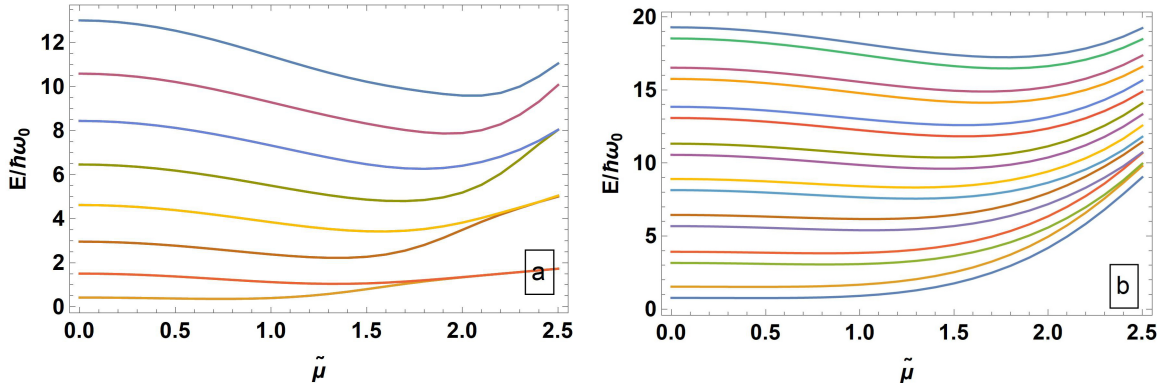


FIG. 4. The energy versus $\tilde{\mu}$: a) at $\tilde{\omega}_c = 0$; b) at $\tilde{\omega}_c = 2$, at $\tilde{\lambda} = 1$

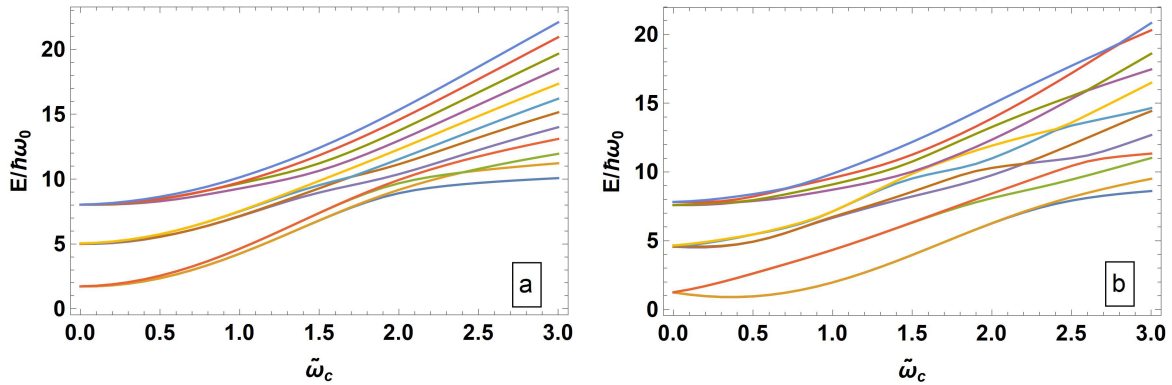


FIG. 5. The energy dispersion at $k_y l_0 = 0$ as a function of $\tilde{\omega}_c$ for $\tilde{\mu} = 2.5$, $\tilde{\lambda} = 1$; a) $\Delta_R/(\hbar\omega_0) = 0$; b) $\Delta_R/(\hbar\omega_0) = 0.5$

levels where the influence of the barrier is significant, the magnetic field needs more strength to separate the merged energy levels, while higher energy levels require a smaller magnetic field strength. As illustrated in the figure, the magnetic field eliminates the spin degeneracy and separates the merged energy levels, raising the energy for all levels. This emphasizes the role of the magnetic field in redistributing and controlling the energy levels, thereby influencing and controlling the physical properties of the DQW system.

The interaction between the magnetic field and the Rashba spin-orbit coupling plays a crucial role in creating a significant separation in spin-up and spin-down branches of the energy levels. When higher magnetic field values are applied, the behavior of the energy spectrum becomes complicated compared to the case where no Rashba spin-orbit coupling is present. The interaction between the magnetic field and the Rashba spin-orbit coupling results in anti-crossings between the various sub-bands of the energy states leading to a more complex and rich structure in the overall energy spectrum of the system. These anti-crossings represent points where the energy levels of different spin states intersect, providing a unique insight into the dynamics of the system under the influence of both magnetic field and Rashba spin-orbit coupling as demonstrated in Fig. 5(b).

Figure 6 illustrates the effect of the variation positions and strength, as well as the external magnetic field on the energy levels in two cases: when $\tilde{\mu} = 0$ (no barrier, SQW) and when $\tilde{\mu} = 2.5$ (barrier, DQW). Through a detailed examination of Fig. 6(a and b) which represents the first case, the effect of the variation on the energy levels at each position in the SQW system becomes evident. This effect occurs at the positions where there is a probability density of the energy level. Consequently, the extra potential will raise the energy levels at these positions. This also clarifies the probability density distribution in this case which we have previously discussed in Fig. 2. The magnetic field eliminates the spin degeneracy. It separates the spin-up and spin-down branches of the energy levels. In Figure 6 (c and d), the effect of the variation's position and the external magnetic field for the second case ($\tilde{\mu} = 2.5$) is explained. Initially, the presence of the barrier re-distributes the energy levels, resulting in the merging of the first level with the second and the third level with the fourth. This phenomenon was previously illustrated in the second figure. Consequently, each spectral line corresponding to the energy levels represents a combination of four distinct levels: two merged due to the barrier and two merged due to spin degeneracy. The introduction of asymmetric variation separates the merged levels caused by the barrier. Additionally, the application of an external magnetic field breaks the degeneracy associated with the spins.

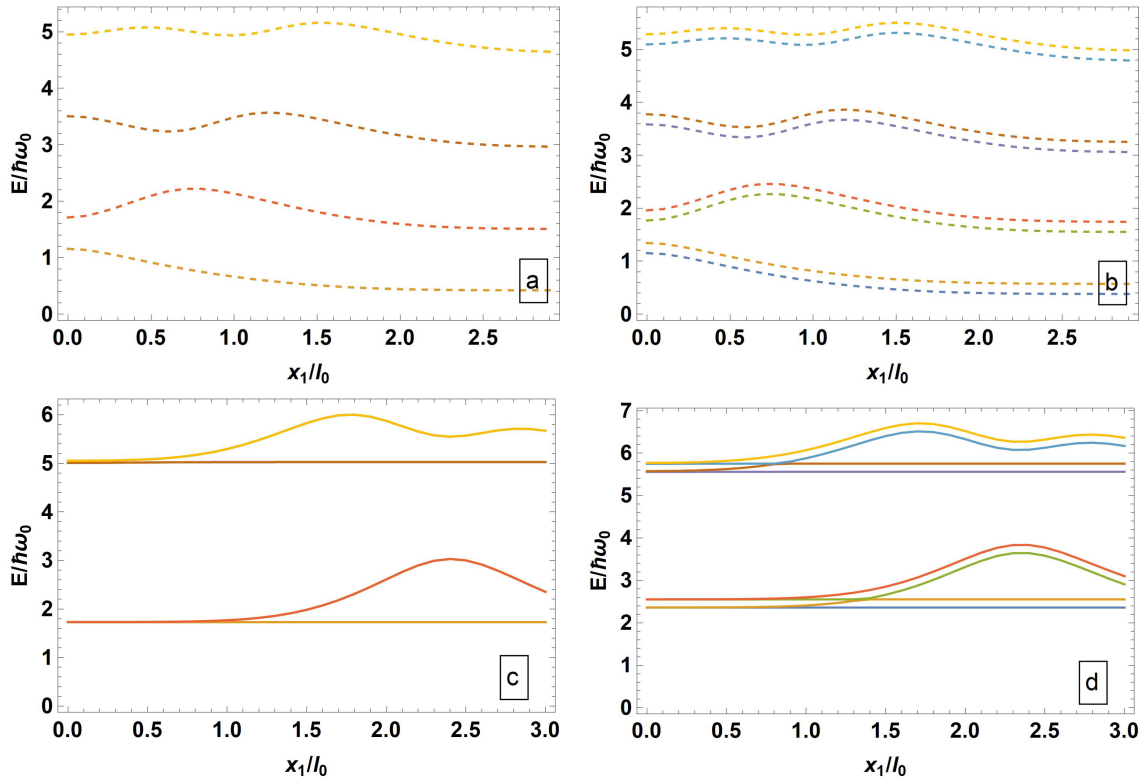


FIG. 6. The energy dispersion at $k_y l_0 = 0$ versus x_1/l_0 for $(V_0/(\hbar\omega_0)) = 5$, $d/l_0 = 0.5$; a) $\tilde{\mu} = 0$, $\tilde{\lambda} = 1$, $\tilde{\omega}_c = 0$; b) $\tilde{\mu} = 0$, $\tilde{\lambda} = 1$, $\tilde{\omega}_c = 0.5$; c) $\tilde{\mu} = 2.5$, $\tilde{\lambda} = 1$, $\tilde{\omega}_c = 0$; d) $\tilde{\mu} = 2.5$, $\tilde{\lambda} = 1$, $\tilde{\omega}_c = 0.5$

In Fig. 7, the local density of states has been plotted at $(x/l_0 = 0)$ as a function of energy for $(\tilde{\mu}=0)$ dashed line and for $(\tilde{\mu}=2.5)$ solid line at a fixed value of $\tilde{\lambda}$ ($\tilde{\lambda}=1$). The vertical lines in the LDOS figure reflect the quantized nature of the energy levels and the presence of localized quantum states, and it gives one an idea about the spatial distribution of electronic wavefunctions in the confined system. These features offer valuable insights into the electronic properties of the quantum system at a local scale. The vertical dashed lines in Fig. 7 result from specific energy levels at $(x/l_0 = 0)$ position for a single quantum wire ($\tilde{\mu} = 0$), these lines represent energy levels with probability density at the center of the wire. This is evident when referring back to Fig. 2, where these vertical dashed lines in the figure correspond to the odd-numbered energy levels, such as the first and the third levels. These levels exhibit peaks in probability density at the center of the wire. The solid line represents the local density of states at $(x/l_0 = 0)$ position for a double quantum wire separated by a barrier ($\tilde{\mu} = 2.5$) (see Fig. 2). The presence of the barrier rearranges the probability density distribution as shown in Fig. 2. It is clear that the lowest energy levels, are significantly affected by the barrier and they lose the probability density at $(x/l_0 = 0)$ position compared with $(\tilde{\mu} = 0)$ case. Consequently, the local density of states at $(x/l_0 = 0)$ position will not have vertical lines for these lower energy levels. On the other hand, higher energy levels that are not significantly affected by the barrier exhibit vertical lines in the local density of states at $(x/l_0 = 0)$ position. These lines represent levels that have a probability density at this position, as they are not affected by the presence of the barrier potential.

Figure 8 illustrates the effect of an external magnetic field and the Rashba spin-orbit coupling on the local density of states, where the figure displays the local density of states as a function of energy at $(x/l_0 = 1.7)$ for a double quantum wire. Fig. 8(a) shows the local density of states in the absence of an external magnetic field. The first three vertical lines, each of them actually consists of four identical lines, meaning four degenerate energy levels, two because of the spin degenerate states and two due to the barrier. As for the remaining lines after the first three, each one represents two degenerate energy levels due to the spin because the barrier's effect vanished and did not work to merge the energy levels while Fig. 8(b) illustrates the local density of states under the presence of an external magnetic field ($\tilde{\omega}_c = 1$). The effect of the external magnetic field becomes evident from this figure as it works to shift up energy levels, removes the spin degeneracy for all energy levels, and separates the merged energy levels caused by the barrier potential if they become higher than the barrier potential effective range. By raising the energy levels, the magnetic field effectively separates previously merged states that are pushed up higher than the barrier potential effective range. Consequently, states previously merged due to the barrier potential separate once more as evidenced by the four converging vertical lines in Fig. 8(b). The four converging vertical lines in the figure represent a single energy level before the magnetic field's influence, with the presence of the magnetic field, it separated into two levels, which were initially merged due

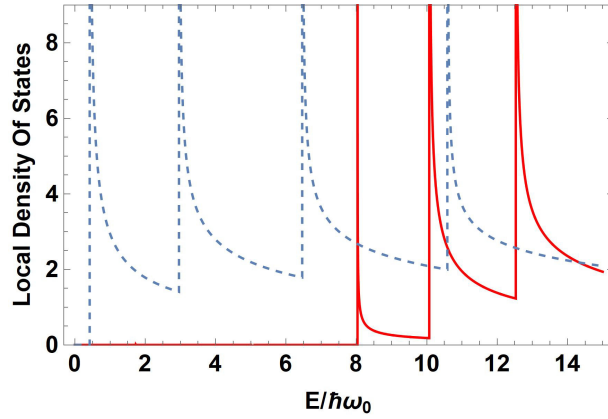


FIG. 7. Local density of states at $x/l_0 = 0$ for $\tilde{\omega}_c = 0$, dashed lines for $\tilde{\mu} = 0, \tilde{\lambda} = 1$, solid lines for $\tilde{\mu} = 2.5, \tilde{\lambda} = 1$

to the barrier potential, and each level of these two levels split into two due to the removal of the spin degeneracy. The higher energy levels, which were not originally affected by the barrier potential, separate into two distinct levels upon the removal of spin degeneracy. The lower energy levels, such as the ground state, persist in their merged state due to the external magnetic field's insufficient strength to push it beyond the influence of the barrier potential, and the magnetic field only removed the spin degeneracy and separated it into two distinct levels. The Rashba spin-orbit coupling generates a significant separation in spin-up and spin-down states in the energy spectra levels. This is clearly evident when comparing Fig. 8(b), where ($\tilde{\omega}_c = 1$) and ($\Delta_R/(\hbar\omega_0) = 0$), with Fig. 8(c), where ($\tilde{\omega}_c = 1$) and ($\Delta_R/(\hbar\omega_0) = 0.1$). It is now evident how the Rashba spin-orbit coupling increases the separation between the spin-up and spin-down states.

Figure 9 illustrates the Local Density of States (LDOS) as a function of energy for the double quantum wire. Fig. 9(a) shows the LDOS at the position ($x/l_0 = 1.25$) corresponding to parameters $\tilde{\mu} = 2.5, \tilde{\lambda} = 1$, and in the absence of variation potential. Likewise, Fig. 9(b) exhibits the LDOS at position ($x/l_0 = -1.25$), maintaining the same parameter settings. A notable observation lies in the remarkable congruence between the LDOS profiles presented in Figs. 9(a) and 9(b) plots,

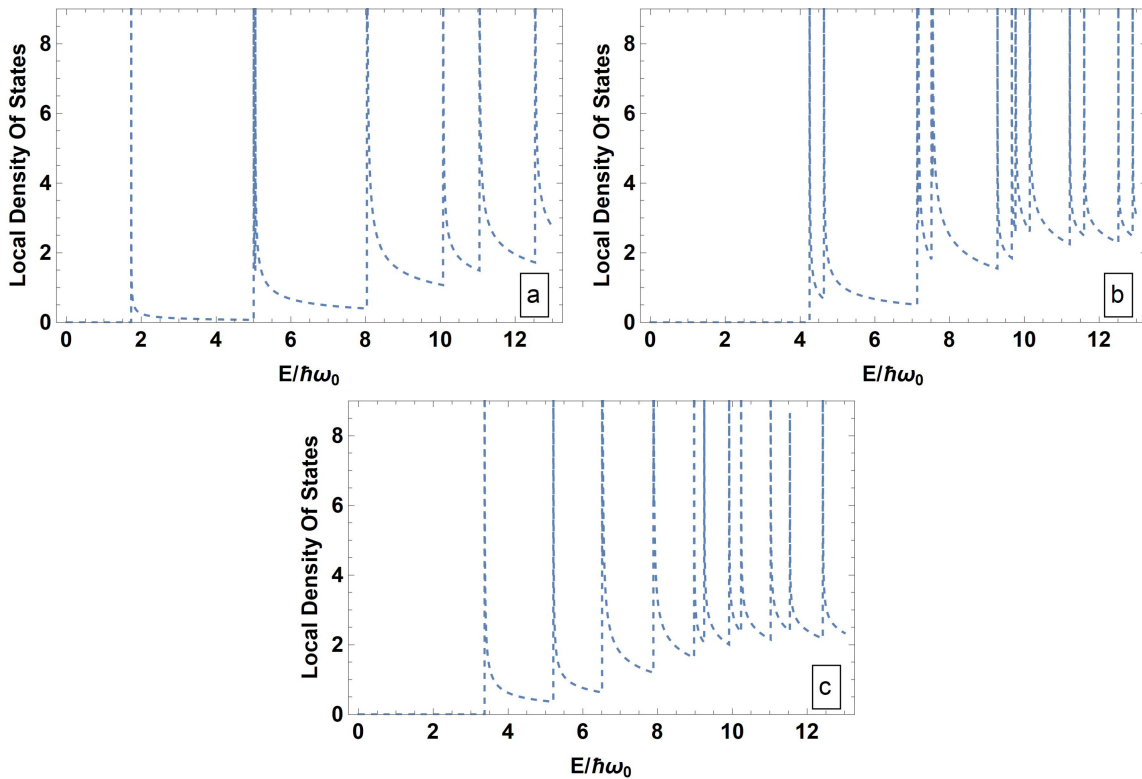


FIG. 8. Local density of states at $x/l_0 = 1.7, \tilde{\mu} = 2.5, \tilde{\lambda} = 1$; a) for $\tilde{\omega}_c = 0$ and $\Delta_R/(\hbar\omega_0) = 0$; b) for $\tilde{\omega}_c = 1$ and $\Delta_R/(\hbar\omega_0) = 0$; c) for $\tilde{\omega}_c = 1$ and $\Delta_R/(\hbar\omega_0) = 0.1$

indicating a profound degeneracy in the energy levels between the two quantum wires. This observation supports the conclusions previously depicted in Fig. 2. Upon closer examination in Fig. 9(c) which represents the LODS for the same parameter settings in Fig. 9(a and b) but in the presence of variation potential ($V_0/(\hbar\omega_0) = 3$, $x_1/l_0 = 1.15$, $d/l_0 = 0.5$) where the dashed lines represent the LDOS plotted at the position ($x/l_0 = 1.25$) and the solid lines represent the LDOS plotted at the position ($x/l_0 = -1.25$). It becomes evident how the extra variation exerts a discernible influence on the energy spectra. Indeed, the introduction of the variation potential brings about a noticeable increase in the energy levels near its location (standard deviation of the Gaussian function chosen to be small ($d/l_0 = 0.5$) to get more localized potential). This observation implies that the adding variation exerts a significant influence on the local electronic structure, resulting in changes to the energy levels within the quantum wire system. This observation aligns with the results discussed in Fig. 3. Furthermore, when examining the dashed and solid lines in Fig. 9(c), it becomes apparent that the two quantum wires exhibit different behaviors in respect to the variation potential. While one wire experiences notable shifts in its energy spectrum as a result of variation potential, the other wire remains relatively unaffected. This selective effect can be attributed to the deliberate choice of a Gaussian distribution, which confines the variation potential influence to specific regions within the quantum wire. Consequently, the difference in the energy profiles between the two wires confirms the localized nature of the variation potential distribution and their effect on the energy levels of the double quantum wire system.

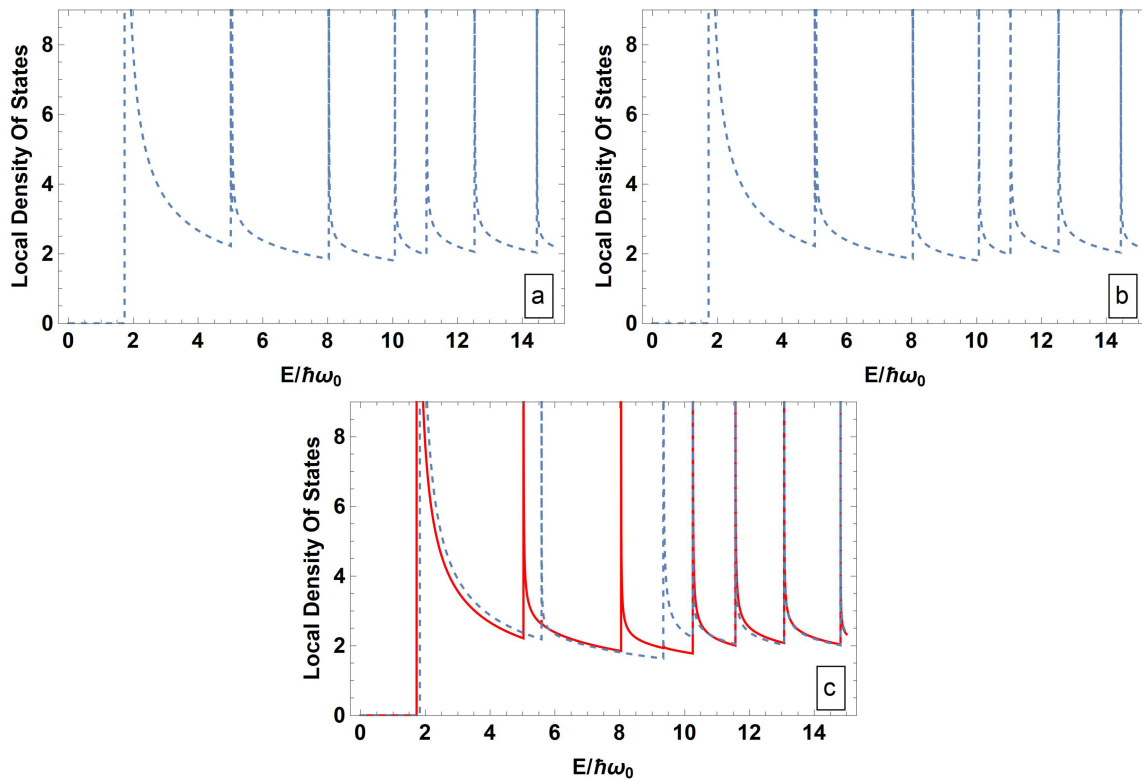


FIG. 9. Local density of states for $\tilde{\mu} = 2.5$, $\tilde{\lambda} = 1$ and $\tilde{\omega}_c = 0$; a) $x/l_0 = 1.25$, without variation potential; b) $x/l_0 = -1.25$, without variation; c) dashed lines for $x/l_0 = 1.25$, $V_0/(\hbar\omega_0) = 3$, $x_1/l_0 = 1.15$, $d/l_0 = 0.5$, solid lines for $x/l_0 = -1.25$, $V_0/(\hbar\omega_0) = 3$, $x_1/l_0 = 1.15$, $d/l_0 = 0.5$

3. Conclusion

In conclusion, our study has provided a comprehensive understanding of the behaviors exhibited by double quantum wire (DQW) systems under varying structural parameters, variation potential, external magnetic field, and the Rashba spin-orbit coupling. Through detailed theoretical analyses and graphical representations, we have explained the effects of the confinement potential structural parameters μ and λ on the confinement potential profiles, probability density distributions, energy spectra, and local density of states in DQWs. Moreover, the introduction of variation potential within the DQW system has been discussed, makes significant alterations in the energy levels and the local density of states. Additionally, the influence of the external magnetic field and the Rashba spin-orbit coupling on the energy levels and the local density of states in the DQW system has been explored and discussed in detail. Overall, our findings contribute to advancing the understanding of quantum phenomena in DQW systems and offer valuable insights for the development of novel electronic devices and quantum technologies. Further experimental investigations are warranted to validate the theoretical predictions and explore practical applications of the observed phenomena in the real-world.

References

- [1] Baghranyan H.M., Barseghyan M.G., Kirakosyan A.A., Restrepo R.L., Mora-Ramos M.E., Duque C.A. Donor impurity-related linear and nonlinear optical absorption coefficients in GaAs/Ga_{1-x}Al_xAs concentric double quantum rings: Effects of geometry, hydrostatic pressure, and aluminum concentration. *J. of Luminescence*, 2014, **145**, P. 676-683.
- [2] Dakhlouli H. Linear and nonlinear optical absorption coefficients and refractive index changes in GaN/Al_xGa_(1-x)N double quantum wells operating at 1.55 μm. *J. of Applied Physics*, 2015, **117** (13), 135705.
- [3] Kolokolov K.I., Beneslavski S.D., Minina N.Y., Savin A.M. Far-infrared intersubband absorption in p-type GaAs/Al_xGa_{1-x}As single heterojunctions under uniaxial compression. *Physical Review B*, 2001, **63** (19), 195308.
- [4] Panda M., Das T., Panda B.K. Nonlinear optical properties in the laser-dressed two-level Al_xGa_{1-x}N/GaN single quantum well. *Int. J. of Modern Physics B*, 2018, **32** (4), 1850032.
- [5] Liao Q.L., Jiang H., Zhang X.W., Qiu Q.F., Tang Y., Yang X.K., Liu Y.L., Huang W.H. A single nanowire sensor for intracellular glucose detection. *Nanoscale*, 2019, **11** (22), P. 10702–10708.
- [6] Chen W., Cabarrocas P.R. Rational design of nanowire solar cells: from single nanowire to nanowire arrays. *Nanotechnology*, 2019, **30** (19), 194002.
- [7] Robertson K.W., LaPierre R.R., Krich J.J. Efficient wave optics modeling of nanowire solar cells using rigorous coupled-wave analysis. *Optics Express*, 2019, **27** (4), A133–147.
- [8] Espinet-Gonzalez P., Barrigón E., Otnes G., Vescovi G., Mann C., France R.M., Welch A.J., Hunt M.S., Walker D., Kelzenberg M.D., Åberg I. Radiation tolerant nanowire array solar cells. *ACS Nano*, 2019, **13** (11), P. 12860–12869.
- [9] Hsu C.L., Wang Y.C., Chang S.P., Chang S.J. Ultraviolet/visible photodetectors based on p–n NiO/ZnO nanowires decorated with Pd nanoparticles. *ACS Applied Nano Materials*, 2019, **2** (10), P. 6343–6351.
- [10] Chen Y., Hrachowina L., Barrigon E., Beech J.P., Alcer D., Lyttleton R., Jam R.J., Samuelson L., Linke H., Borgström M. Semiconductor nanowire array for transparent photovoltaic applications. *Applied Physics Letters*, 2021, **118** (19).
- [11] Wu Y., Yang P. Direct observation of vapor- liquid- solid nanowire growth. *J. of the American Chemical Society*, 2001, **123** (13), P. 3165–3166.
- [12] Pevzner A., Engel Y., Elnathan R., Ducobni T., Ben-Ishai M., Reddy K., Shpaisman N., Tsukernik A., Oksman M., Patolsky F. Knocking down highly-ordered large-scale nanowire arrays. *Nano letters*, 2010, **10** (4), P. 1202–1208.
- [13] Madaria A.R., Yao M., Chi C., Huang N., Lin C., Li R., Povinelli M.L., Dapkus P.D., Zhou C. Toward optimized light utilization in nanowire arrays using scalable nanosphere lithography and selected area growth. *Nano Letters*, 2012, **12** (6), P. 2839–2845.
- [14] No Y.S., Gao R., Mankin M.N., Day R.W., Park H.G., Lieber C.M. Encoding active device elements at nanowire tips. *Nano Letters*, 2016, **16** (7), P. 4713–4719.
- [15] Chaure S., Chaure N.B., Pandey R.K. Self-assembled nanocrystalline CdSe thin films. *Physica E: Low-dimensional Systems and Nanostructures*, 2005, **28** (4), P. 439–446.
- [16] Fischer S.F., Apetrii G., Kunze U., Schuh D., Abstreiter G. Tunnel-coupled one-dimensional electron systems with large subband separations. *Physical Review B*, 2006, **74** (11), 115324.
- [17] Wang D.W., Mishchenko E.G., Demler E. Pseudospin ferromagnetism in double-quantum-wire systems. *Physical Review Letters*, 2005, **95** (8), 086802.
- [18] Karaaslan Y., Gisi B., Sakiroglu S.E., Kasapoglu E.S., Sari H.Ü., Sokmen I. Rashba spin-orbit coupling effects on the optical properties of double quantum wire under magnetic field. *Superlattices and Microstructures*, 2016, **93**, P. 32–39.
- [19] Gudmundsson V., Tang C.S. Magnetotransport in a double quantum wire: Modeling using a scattering formalism built on the Lippmann-Schwinger equation. *Physical Review B-Condensed Matter and Materials Physics*, 2006, **74** (12), 125302.
- [20] Abdullah N.R., Tang C.S., Gudmundsson V. Time-dependent magnetotransport in an interacting double quantum wire with window coupling. *Physical Review B – Condensed Matter and Materials Physics*, 2010, **82** (19), 195325.
- [21] Liu G., Liu R., Chen G., Zhang Z., Guo K., Lu L. Nonlinear optical rectification and electronic structure in asymmetric coupled quantum wires. *Results in Physics*, 2020, **17**, 103027.
- [22] Su Y., Guo K., Liu G., Yang T., Yu Q., Hu M., Yang Y. Nonlinear optical properties of semiconductor double quantum wires coupled to a quantum-sized metal nanoparticle. *Optics Letters*, 2020, **45** (2), P. 379–382.
- [23] Gisi B., Karaaslan Y., Sakiroglu S.E., Kasapoglu E.S., Sari H.Ü., Sokmen I. Effects of an in-plane magnetic field on the energy dispersion, spin texturing and conductance of double quantum wires. *Superlattices and Microstructures*, 2016, **91**, P. 391–400.
- [24] Moon J.S., Blount M.A., Simmons J.A., Wendt J.R., Lyo S.K., Reno J.L. Magnetoresistance of one-dimensional subbands in tunnel-coupled double quantum wires. *Physical Review B*, 1999, **60** (16), 11530.
- [25] Bielejec E., Reno J.L., Lyo S.K., Lilly M.P. Tunneling spectroscopy in vertically coupled quantum wires. *Solid State Communications*, 2008, **147** (3–4), P. 79–82.
- [26] Huang D., Lyo S.K., Thomas K.J., Pepper M. Field-induced modulation of the conductance, thermoelectric power, and magnetization in ballistic coupled double quantum wires under a tilted magnetic field. *Physical Review B*, 2008, **77** (8), 085320.
- [27] Karaaslan Y., Gisi B., Sakiroglu S.E., Kasapoglu E.S., Sari H.Ü., Sokmen I. Electric and magnetic field modulated energy dispersion, conductivity and optical response in double quantum wire with spin-orbit interactions. *Physics Letters A*, 2018, **382** (7), P. 507–515.
- [28] Kumar S., Kumar M., Kumar A. Combined effect of rashba spin-orbit interaction, hydrostatic pressure and temperature on energy dispersion based ballistic conductance of InAs tunnel-coupled (double) quantum wire under exterior magnetic and electric field. *Physica B: Condensed Matter*, 2024, **677**, 415715.
- [29] Korepov S.V., Liberman M.A. Tunnel-coupled double quantum wires in a magnetic field: electron scattering on impurities and boundary roughness. *Physica B: Condensed Matter*, 2002, **322** (1–2), P. 92–109.
- [30] Sharma R. Impurity-modulated physical and transport properties in a In_xGa_{1-x}As double quantum wire. *Physica B: Condensed Matter*, 2023, **659**, 414845.
- [31] Naydenov B., Boland J.J. Variable-height scanning tunneling spectroscopy for local density of states recovery based on the one-dimensional WKB approximation. *Physical Review B*, 2010, **82** (24), 245411.
- [32] Widmer R., Gröning P., Feuerbacher M., Gröning O. Experimental signatures of spiky local density of states in quasicrystals. *Physical Review B*, 2009, **79** (10), 104202.
- [33] Martín-Jiménez A., Fernández-Domínguez A.I., Lauwaet K., Granados D., Miranda R., García-Vidal F.J., Otero R. Unveiling the radiative local density of optical states of a plasmonic nanocavity by STM. *Nature Communications*, 2020, **11** (1), P. 1–8.
- [34] Ivanov D.A., Ostrovsky P.M., Skvortsov M.A. Correlations of the local density of states in quasi-one-dimensional wires. *Physical Review B – Condensed Matter and Materials Physics*, 2009, **79** (20), 205108.

- [35] Ignatchenko V.A., Tsikalov D.S. Local density of states in one-dimensional photonic crystals and sinusoidal superlattices. *Physics Procedia*, 2017, **86**, P. 113–116.
- [36] Segovia-Chaves F., Vinck-Posada H., Navarro-Barón E.P. Local density of states in a one-dimensional photonic crystal with a semiconducting cavity. *Results in Physics*, 2022, **33**, 105129.
- [37] Bena C., Kivelson S.A. Quasiparticle scattering and local density of states in graphite. *Physical Review B*, 2005, **72** (12), 125432.
- [38] Shimomura Y., Takane Y., Wakabayashi K. Electronic states and local density of states in graphene with a corner edge structure. *J. of the Physical Society of Japan*, 2011, **80** (5), 054710.
- [39] Karaaslan Y., Gisi B., Sakiroglu S., Kasapoglu E.S., Sari H.Ü., Sokmen I. Spin–orbit interaction and magnetic field effects on the energy dispersion of double quantum wire. *Superlattices and Microstructures*, 2015, **85**, P. 401–409.
- [40] Hosseinpour P. Effect of Gaussian impurity parameters on the valence and conduction subbands and thermodynamic quantities in a doped quantum wire. *Solid State Communications*, 2020, **322**, 114061.
- [41] Chen Q., Li L.L., Peeters F.M. Magnetic field dependence of electronic properties of MoS₂ quantum dots with different edges. *Physical Review B*, 2018, **97** (8), 085437.
- [42] Gradshteyn I.S., Ryzhik I.M., Romer R.H. *Tables of Integrals, Series, and Products*. American Association of Physics Teachers: College Park, MD, USA, 1988.
- [43] Nilsson H.A., Samuelsson P., Caroff P., Xu H.Q. Supercurrent and multiple Andreev reflections in an InSb nanowire Josephson junction. *Nano Letters*, 2012, **12** (1), P. 228–233.

Submitted 11 September 2024; revised 5 October 2024; accepted 8 October 2024

Information about the authors:

Mahmoud Ali – Physics Department, An-Najah National University, Palestine; ORCID 0000-0002-3738-5851; mahmoud.Ali@najah.edu

Mohammad Elsaid – Physics Department, An-Najah National University, Palestine; ORCID 0000-0002-1392-3192; mkelsaid@najah.edu

Conflict of interest: the authors declare no conflict of interest.

Simulation of Bessel plasmon polariton field formation in a dielectric-metal structure

Nguyen Pham Quynh Anh^{1,a}

¹Faculty of Electronics and Telecommunications, SaiGon University, 273 An Duong Vuong, Dist. 5, Ho Chi Minh City, Viet Nam

^anpqanh@sgu.edu.vn

Corresponding author: Nguyen Pham Quynh Anh, npqanh@sgu.edu.vn

ABSTRACT We study the conditions for the formation and transformation of the Bessel plasmon-polariton field in a dielectric-metal structure excited by a Bessel light beam with arbitrary polarization. The effect of the metal layer thickness on the resulting plasmon field structure is investigated. The formation of Bessel plasmon-polaritons in a scheme consisting of a conical axicon with its base in contact with a silver layer of defined thickness is simulated.

KEYWORDS surface plasmons, Bessel light beam, surface Bessel plasmon-polariton, dielectric-metal structure.

FOR CITATION Nguyen Pham Quynh Anh Simulation of Bessel plasmon polariton field formation in a dielectric-metal structure. *Nanosystems: Phys. Chem. Math.*, 2024, **15** (5), 670–674.

1. Introduction

Plasmonics, the study of surface plasmon polaritons (SPPs) generated at the interface between a dielectric and a metal, has seen remarkable interest in recent years [1–3]. This is due to the wide-ranging potential applications of SPPs in areas such as high-resolution microscopy, optical communication, and sensing technologies [4–6]. Surface plasmons, which are collective oscillations of free electrons at the metal surface, can confine light at sub-wavelength scales, making them particularly valuable for nanoscale optical applications. Traditional studies on SPP generation typically focus on plane waves or Gaussian beam excitation, which has been well-documented [7, 8]. However, more recent advancements have introduced alternative approaches to generating SPPs, including the use of non-diffracting beams like Bessel beams [9–11].

Bessel beams, known for their non-diffracting and self-reconstructing properties, have become a subject of interest in the plasmonics community. These beams offer unique advantages for plasmon generation, particularly for applications requiring high stability and precise control of field distributions [12–14]. In contrast to Gaussian beams, Bessel beams can form more localized plasmon fields, potentially enhancing the performance of optical devices. Recent studies have investigated the interaction between Bessel light beams (BLBs) and surface plasmon polaritons, specifically focusing on the generation of Bessel plasmon polaritons (BPPs). These works suggest that BPPs can be generated using Bessel beams with specific polarization, most notably transverse magnetic (TM) polarization [15, 16].

This paper builds upon these findings by exploring the generation of Bessel plasmon polaritons using arbitrarily polarized Bessel beams. While prior research has predominantly focused on TM-polarized Bessel beams, little attention has been given to the role of arbitrary polarizations in the formation of BPPs. This aspect is critical for expanding the range of applications for Bessel plasmons in fields like optical communication and surface-enhanced spectroscopy, where control over beam polarization can enhance system functionality. In this study, we simulate the formation of Bessel plasmon polaritons in a dielectric-metal multilayer structure under excitation by arbitrarily polarized Bessel beams. By analyzing the impact of different polarizations on the generated plasmon field, we aim to provide new insights into the tunability and application potential of Bessel plasmons. This work not only contributes to the understanding of Bessel beam interactions with dielectric-metal interfaces but also opens up possibilities for further research into the practical applications of these unique plasmonic modes.

2. Bessel plasmon-polariton characterization in dielectric-metal structure

Let's consider a vector Bessel light beam

$$\vec{E}(R) = A^{TE} \vec{E}^{TE}(R) + A^{TH} \vec{E}^{TH}(R) \quad (1)$$

incident on the dielectric-metal interface. In expression (1), $R = (\rho, \varphi, z)$ are the cylindrical coordinates with the Z axis orthogonal to the interface between the two media with corresponding dielectric permittivities of ε_1 and ε_m , $\vec{E}^{TE,TH}$ are

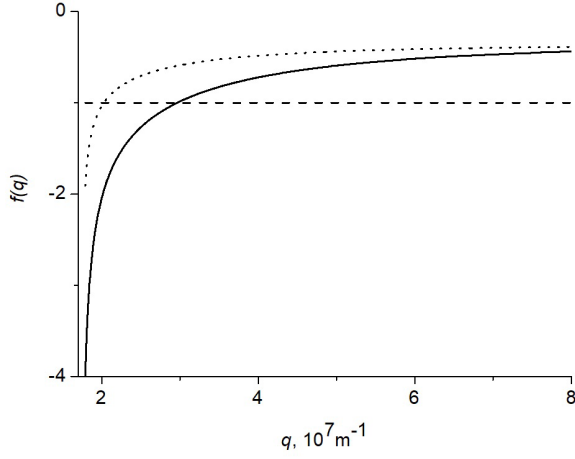


FIG. 1. Dependence $f(q)$ for the structure “optical glass ($n = 1.52$) – silver – air”. The thickness of the silver layer is 16,5 nm (solid line) and 150 nm (dashed line). $\lambda = 550$ nm

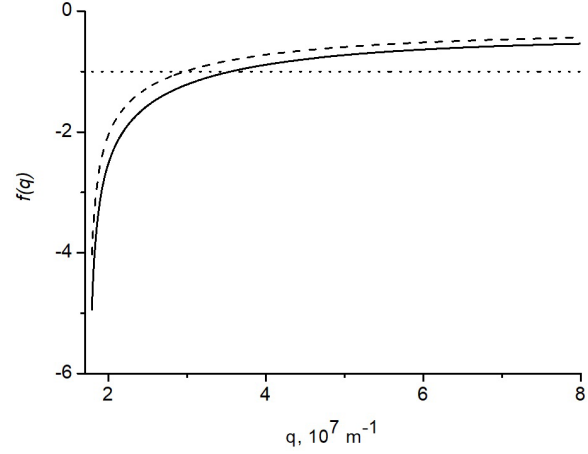


FIG. 2. Dependence $f(q)$ for the structure “optical glass ($n = 1.52$) – metal layer (Na (solid line), Ag (dashed line)) with a thickness of 16.5 nm – air”. $\lambda = 550$ nm

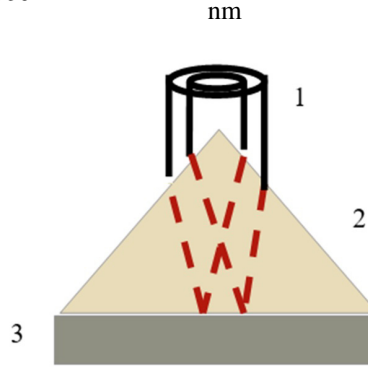


FIG. 3. Bessel plasmon excitation scheme. 1 – ring beam, 2 – axicon, 3 – metal layer

the electric field intensity vector of the TE ($E_z = 0$) and TH ($H_z = 0$) Bessel modes, $A^{TE,TH}$ are the complex constants. In this case, it is possible to generate a surface field for which

$$\begin{aligned} E_{z1,m}^{TE} &= qJ_m(q\rho)/(k_0n_{1,m}) \exp[\pm\chi_{1,m}(q)z + im\varphi], \\ H_{z1,m}^{TE} &= -iqJ_m(q\rho)/(k_0) \exp[\pm\chi_{1,m}(q)z + im\varphi], \end{aligned} \quad (2)$$

where q is the conicity parameter (the transverse component of the wave vector), $q^2 - \chi_{1,m}^2 = k_0^2\varepsilon_{1,m}$, $\varepsilon_{1,m} = n_{1,m}^2$, $k_0 = \omega/c$, $J_m(q\rho)$ is the Bessel function of the m -th order. From the solutions of Maxwell's equations it follows that the transverse component of the formed surface Bessel beam is determined by the following expression:

$$\begin{aligned} \vec{E}_{\perp 1,m}(R) &= \frac{i}{\sqrt{2}} \exp\{i(m-1)\varphi \pm \chi_{1,m}(q)z\} \\ &\times \left\{ A_{1,2}^{TE} [J_{m-1}(q\rho)\vec{e}_+ + J_{m+1}(q\rho) \exp(2i\varphi)\vec{e}_-] \mp iA_{1,2}^{TH} \frac{\chi_{1,m}}{k_0n_{1,m}} [J_{m-1}(q\rho)\vec{e}_+ - J_{m+1}(q\rho) \exp(2i\varphi)\vec{e}_-] \right\}, \\ \vec{H}_{\perp 1,m}(R) &= -\frac{n_{1,m}}{\sqrt{2}} \exp\{i(m-1)\varphi \pm \chi_{1,m}(q)z\} \\ &\times \left\{ A_{1,2}^{TH} [J_{m-1}(q\rho)\vec{e}_+ + J_{m+1}(q\rho) \exp(2i\varphi)\vec{e}_-] \mp iA_{1,2}^{TE} \frac{\chi_{1,m}}{k_0n_{1,m}} [J_{m-1}(q\rho)\vec{e}_+ - J_{m+1}(q\rho) \exp(2i\varphi)\vec{e}_-] \right\}, \end{aligned} \quad (3)$$

where $\vec{e}_{\pm} = (\vec{e}_1 \pm i\vec{e}_2)/\sqrt{2}$. As follows from (3), taking into account the boundary conditions, it is possible to excite only TH polarized surface Bessel modes, the dispersion equation for which has the form:

$$1 + \frac{\chi_1(q)\varepsilon_m(\omega)}{\chi_m(q)\varepsilon_1} = 0. \quad (4)$$

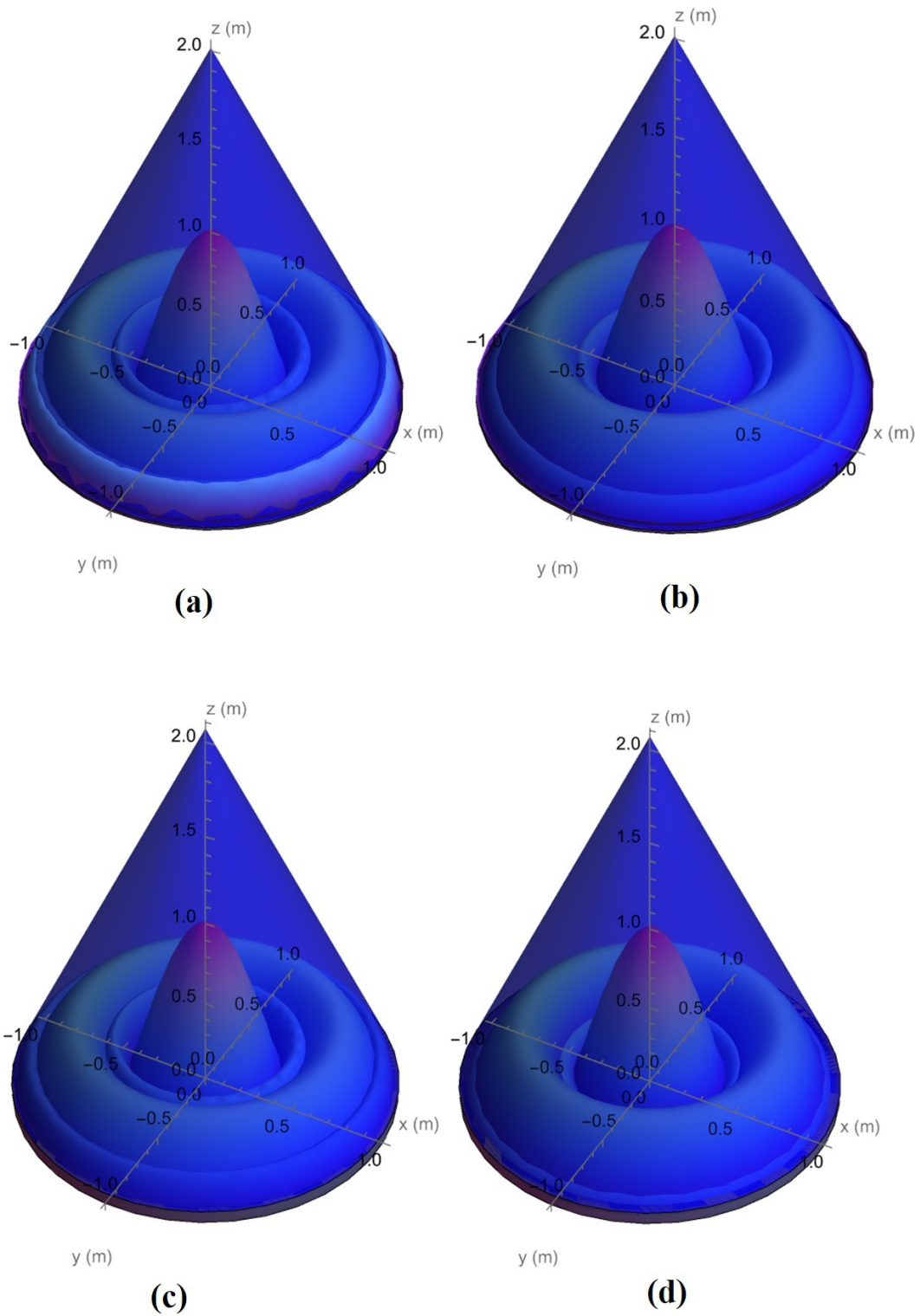


FIG. 4. The formation of the Bessel plasmon-polaritons in the scheme of "axicon-silver layer with a thickness of 16.5 nm (a,b), 70 nm (c,d)" on the surface of the silver layer (a,c), at a depth of 12 nm from the surface of the metal layer (b,d)

From the equation (4), we obtain the following expression:

$$\chi_{1,m} = \sqrt{\frac{\varepsilon_{1,m}^2(\varepsilon_m - \varepsilon_1)}{\varepsilon_1^2 - \varepsilon_m^2}}. \quad (5)$$

As can be seen from (5), the surface Bessel beam exists under the conditions

$$\frac{\varepsilon_m(\omega)}{\varepsilon_1} < 0, \quad |\varepsilon_m| > \varepsilon_1. \quad (6)$$

The dispersion equation (5) coincides in form with the corresponding expression for surface waves in the plane-wave approximation. However, unlike plane waves, this dispersion equation relates the frequency to the conicity parameter of the Bessel light beam:

$$q = k_0 \sqrt{\frac{\varepsilon_1 \varepsilon_m}{\varepsilon_1 + \varepsilon_m}}. \quad (7)$$

Let us now consider the structure “dielectric 1 (ε_1) – metal (ε_m) – dielectric 2 (ε_2)”. As follows from the boundary conditions for fields of type (3), in this case, it is also possible to have only TH- polarized surface Bessel beams (Bessel plasmon-polaritons), the dispersion equation for which has the form:

$$f(q) = \frac{\chi_m^2(q)\varepsilon_1(\omega)\varepsilon_2(\omega)}{\chi_1(q)\chi_2(q)\varepsilon_m^2} + \text{cth}(\chi_m d) \left(\frac{\chi_m^2(q)\varepsilon_2(\omega)}{\chi_2(q)\varepsilon_m} + \frac{\chi_m(q)\varepsilon_1(\omega)}{\chi_1(q)\varepsilon_m} \right) = -1. \quad (8)$$

Here d is the thickness of the metal layer. As the calculation performed in accordance with (7) shows, the radius of the first ring $R_1 = 2,4/q$ of the Bessel plasmon-polariton generated on the surface of a metal film of thickness $d \geq 0,1\lambda$ coincides with that of the Bessel plasmon-polariton generated at the interface of semi-infinite media “dielectric - metal”. The radius of the first ring of the Bessel plasmon-polariton generated in the structure “dielectric - metal layer - dielectric” can be reduced by reducing the thickness of the metal layer (Fig. 1), as well as by using media with permittivities close in absolute value in the structure (Fig. 2). For example, in the structure “optical glass – sodium layer with a thickness of 16,5 nm - air” at a wavelength of 550 nm, a Bessel plasmon with a first ring radius of 65 nm is formed, which allows us to conclude that Bessel plasmon can be used for probing surfaces with subwavelength resolution.

Using (3), it is possible to determine the energy characteristics of the surface Bessel plasmon-polaritons formed in the layered structure. Calculations show that both inside and outside the metal layer, the only non-zero component of the Umov-Poynting vector is the azimuthal component

$$S_{\varphi 1,2} \sim \frac{m}{k_0 \rho} J_m^2(q\rho) \exp(\pm 2\chi_{1,2}z), \quad S_{\varphi} \sim \frac{m}{k_0 \rho} J_m^2(q\rho) \text{ch}(2\chi_m z). \quad (9)$$

In this case, as follows from (9), the directions of rotation of energy inside the layer and outside it coincide.

3. Simulation of the Bessel plasmon-polariton excitation system in the metallic layer

The excitation scheme for the Bessel plasmon-polaritons is illustrated in Fig. 3. A ring-shaped beam (1) is incident on the axicon (2), which has a metal film (3) applied to its lower edge.

In order to simulate the formation of Bessel plasmon-polaritons within the experimental setup consisting of an axicon cone and a silver layer at its base, we employ Wolfram Mathematica 13.1. This software allows us to model the complex interactions and wave dynamics accurately, providing valuable insights into the behavior of plasmon-polaritons under these specific conditions.

Fig. 4 describes the formation of the Bessel plasmon-polaritons in a scheme excited by a zero-order Bessel beam with a wavelength of 550 nm directly incident on a conical axicon with a base radius of 1 μm and a height of 2 μm , adjacent to the silver metal layer. As shown in Fig. 4a,b, the intensity distribution of the Bessel plasmon-polaritons shows a central peak with concentric rings radiating outward. This pattern is characteristic of the Bessel functions. Fig. 4a represents the Bessel plasmon-polariton structure at the surface of the metallic layer ($z = 0$), while Fig. 4b shows the structure at a depth of 12 nm from the surface. At the surface, the intensity distribution is more pronounced with sharper peaks and well-defined concentric rings. This indicates stronger plasmonic interactions at the interface. As we move 12 nm below the surface, the intensity of the plasmon-polaritons decreases. The concentric rings become less distinct, suggesting a damping effect as the plasmonic waves penetrate deeper into the metallic layer. The overall structure of the plasmon-polaritons becomes more diffuse at the 12 nm depth, indicating that the energy is spreading out and the coherence of the plasmonic waves is reducing with depth. At the surface of the metallic layer, the Bessel plasmon-polariton field shows a well-defined pattern with sharp intensity peaks. This is consistent for both 16,5 nm and 70 nm thicknesses.

At a depth of 12 nm, the intensity of the plasmon-polariton field decreases for both thicknesses. However, the field structure for the 70 nm thick layer shows a more pronounced damping effect compared to the 16.5 nm layer. The thicker metallic layer (70 nm) results in a more diffuse plasmon-polariton field at depth, indicating that the energy spreads out more and the coherence of the plasmonic waves reduces more significantly compared to the thinner layer (16,5 nm). The thinner metallic layer (16.5 nm) maintains a relatively higher energy confinement at depth compared to the thicker layer (70 nm), which could be beneficial for applications requiring strong plasmonic interactions close to the surface.

4. Conclusion

In this paper, we have investigated the features of the Bessel plasmon generation at the dielectric-metal interface when excited by beams of arbitrary polarization. The possibility and conditions for obtaining quasi-diffraction-free surface fields with a submicron-sized central maximum are demonstrated. We have proposed and simulated a model for exciting Bessel-plasmon polaritons on the surface of a metal layer. This scheme is significant for applications in plasmonic devices and sensors, where precise control over light-matter interactions is crucial.

References

- [1] Agranovich V.M., Mills D.L. *Surface Polaritons: Electromagnetic Waves at Surfaces and Interfaces*. Amsterdam, North-Holland, 1982, 734 p.
- [2] Boardman A.D. *Electromagnetic Surface Modes*. New York, John Wiley & Sons, 1982, 786 p.
- [3] Zhang P. [et al.]. In-Plane Radiation of Surface Plasmon Polaritons Excited by Free Electrons. *Micromachines*, 2024, **15**(6), 723 p.
- [4] Aftab M., [et al.]. Surface Plasmon Excitation: Theory, Configurations, and Applications. *Plasmonics*, 2024, **19**, P. 1701–1719.
- [5] Rockstuhl C., Fahr S., Lederer F. *Surface Plasmon Polaritons in Metallic Nanostructures: Fundamentals and Their Application to Thin-Film Solar Cells*. Springer Series in Optical Sciences, 2012 (SSOS, volume 165).
- [6] Talles E.M. Marques, [et al.]. Tunable Surface Plasmon-Polaritons Interaction in All-Metal Pyramidal Metasurfaces: Unveiling Principles and Significance for Biosensing Applications. *ACS Appl. Opt. Mater.*, 2024, **2**(7), P. 1374–1381.
- [7] Wang S., Zhao C., Li X. Dynamical Manipulation of Surface Plasmon Polaritons. *Appl. Sci.*, 2019, **9**(16), P. 3297.
- [8] Jiang J.X., Chen Y.G. Generating Surface Plasmon Polariton Airy Beam with Dielectric Relief Holographical Structures. *Plasmonics*, 2020, **15**, P. 1683–1688.
- [9] Qiu P., [et al.]. Polarization Controllable Device for Simultaneous Generation of Surface Plasmon Polariton Bessel-Like Beams and Bottle Beams. *Nanomaterials*, 2018, **8**(12), P. 975.
- [10] Knyazev B.A., [et al.]. Generation of Terahertz Surface Plasmon Polaritons Using Nondiffractive Bessel Beams with Orbital Angular Momentum. *Phys.Rev.Lett.*, 2015, **115**, P. 163901.
- [11] Zhan Q. Evanescent Bessel beam generation via surface plasmon resonance excitation by a radially polarized beam. *Optics Letters*, 2006, **31**, P. 1726–1728.
- [12] Kurilkina S.N., Belyi V.N., Kazak N.S. Features of evanescent Bessel light beams formed in structures containing a dielectric layer. *Optics Communications*, 2010, **283**, P. 3860–3868.
- [13] Jiefeng X., Quing L., Jia W. Numerical simulation of evanescent Bessel beams and apodization of evanescent field in near-field optical virtual probe. *Proceedings of the SPIE*, 2005, **5635**, P. 42–47.
- [14] Novitsky A.V., Barkovsky L.M. Total internal reflection of vector Bessel beams: Imbert–Fedorov shift and intensity transformation. *Journal of Optics A Pure and Applied Optics*, 2008, **10**, P. 075006-1–075006-7.
- [15] Liu L., [et al.]. Nanofocusing of circularly polarized Bessel-type plasmon polaritons with hyperbolic metamaterials. *Mater. Horiz*, 2017, **4**, P. 290–296.
- [16] Carlos J., [et al.]. Nondiffracting Bessel plasmons. *Opt. Expr.*, 2011, **19**(20), P. 19572–19581.

Submitted 5 October 2024; revised 7 October 2024; accepted 8 October 2024

Information about the author:

Nguyen Pham Quynh Anh – Faculty of Electronics and Telecommunications, SaiGon University, 273 An Duong Vuong, Dist. 5, Ho Chi Minh City, Viet Nam; ORCID 0009-0009-4001-4873; npqanh@sgu.edu.vn

Conflict of interest: the author declare no conflict of interest.

Proton beam-induced radiosensitizing effect of $\text{Ce}_{0.8}\text{Gd}_{0.2}\text{O}_{2-x}$ nanoparticles against melanoma cells *in vitro*

Danil D. Kolmanovich^{1,a}, Mikhail V. Romanov^{2,3,b}, Sergey A. Khaustov^{4,c}, Vladimir K. Ivanov^{5,d}, Alexander E. Shemyakov^{1,6,e}, Nikita N. Chukavin^{1,4,f}, Anton L. Popov^{1,4,g}

¹Institute of Theoretical and Experimental Biophysics of the Russian Academy of Sciences, Pushchino, Russia

²Institute of Molecular Theranostics, Sechenov First Moscow State Medical University, Moscow, Russia

³Lopukhin Federal Research and Clinical Center of Physical-Chemical Medicine of Federal Medical Biological Agency, Moscow, Russia

⁴Scientific and Educational Center, State University of Education, Moscow, Russia

⁵Kurnakov Institute of General and Inorganic Chemistry of the Russian Academy of Sciences, Moscow, Russia

⁶Lebedev Physical Institute of the Russian Academy of Sciences, Moscow, Russia

^akdd100996@mail.ru, ^bromanov.mikhail@phystech.edu, ^csergeykhaustov@gmail.com, ^dvan@igic.ras.ru,

^ealshemyakov@yandex.ru, ^fchukavinnik@gmail.com, ^gantonpopovleonid@gmail.com

Corresponding author: A. L. Popov, antonpopovleonid@gmail.com

ABSTRACT Proton beam therapy is being used increasingly to treat melanoma. Meanwhile, proton beam therapy has a number of disadvantages that can be reduced or completely eliminated through the use of modern innovative approaches, including the use of nanoradiosensitizers. Here we showed the possibility of using redox-active dextran-stabilized $\text{Ce}_{0.8}\text{Gd}_{0.2}\text{O}_{2-x}$ nanoparticles ($\text{Ce}_{0.8}\text{Gd}_{0.2}\text{O}_{2-x}$ NPs) as a radiosensitizer to promote mouse melanoma cell death under proton beam irradiation *in vitro*. It has been shown that these $\text{Ce}_{0.8}\text{Gd}_{0.2}\text{O}_{2-x}$ NPs do not reduce the viability and survival rate of both NCTC L929 normal mouse fibroblasts and B16/F10 mouse melanoma cells in a wide range of concentrations. However, $\text{Ce}_{0.8}\text{Gd}_{0.2}\text{O}_{2-x}$ NPs significantly reduce the mitochondrial membrane potential of these cells. Additionally, it has been shown that $\text{Ce}_{0.8}\text{Gd}_{0.2}\text{O}_{2-x}$ NPs are able to effectively reduce the clonogenic activity of B16/F10 melanoma cells under proton beam irradiation. Meanwhile, proton beam irradiation remarkably reduced the clonogenic activity and MMP of melanoma cells. Hence, $\text{Ce}_{0.8}\text{Gd}_{0.2}\text{O}_{2-x}$ NPs act as a radiosensitizer in B16/F10 mouse melanoma cells under proton beam irradiation. We assume that such radiosensitizing effect of $\text{Ce}_{0.8}\text{Gd}_{0.2}\text{O}_{2-x}$ NPs is due to a decrease of the membrane mitochondrial potential. Thus, the use of $\text{Ce}_{0.8}\text{Gd}_{0.2}\text{O}_{2-x}$ NPs in combination with proton beam irradiation is a promising approach for the effective treatment of melanoma.

KEYWORDS gadolinium, cerium oxide nanoparticles, radiosensitization, proton beam irradiation

ACKNOWLEDGEMENTS This research was funded by the Ministry of Science and Higher Education of the Russian Federation (State Assignment: 075-00224-24-03).

FOR CITATION Kolmanovich D.D., Romanov M.V., Khaustov S.A., Ivanov V.K., Shemyakov A.E., Chukavin N.N., Popov A.L. Proton beam-induced radiosensitizing effect of $\text{Ce}_{0.8}\text{Gd}_{0.2}\text{O}_{2-x}$ nanoparticles against melanoma cells *in vitro*. *Nanosystems: Phys. Chem. Math.*, 2024, **15** (5), 675–682.

1. Introduction

Radiation therapy (RT) is a modern medical approach which is being used as a full-fledged treatment of tumors, as well as a palliative therapy to relieve symptoms caused by cancer. Currently, at least 40% of cancer patients receive radiation therapy [1]. One of the main issues of RT is the risk of damage to healthy tissues. The biological effectiveness of irradiation depends on several factors, including linear energy transfer (LET), total dose, fractionation and radiosensitivity of targeted cells and tissues [2]. For instance, low-LET radiation releases relatively small amount of energy, while high-LET radiation releases a lot of energy at the target sites. Despite the fact that irradiation is aimed at killing tumor cells, it inevitably damages healthy cells nearby. Currently, the most commonly used types of radiation for the needs of radiotherapy are X-rays and gamma rays (photon-based radiation). This type of radiation is characterized by low-LET values. Because of this, gamma rays and X-rays are ineffective in the treatment of radioresistant cancers, such as sarcoma, kidney carcinoma, melanoma and glioblastoma [3,4]. In addition, one of the main disadvantages of using photon radiation is the collateral irradiation of healthy tissues along the path of the photon beam, both before and after the tumor site.

The use of proton beam therapy (PBT) makes it possible to reduce the adverse effect of irradiation on healthy tissues and, as a result, decrease the risk of PBT side effects [5]. Also, it is possible to dramatically increase the radiation dose to

the tumor in PBT, while maintaining the side effect on the surrounding healthy tissues within their tolerance limits. These advantages are primarily related to the peculiarities of the physical interaction of protons with the matter: unlike photons, which irradiate everything on their path and lose their energy exponentially, hadrons (protons and also carbon ions) have a finite path length and emit most of their energy at the end of their path [6]. This distribution of hadrons energy along the path of their run is described by the Bregg peak (BP).

In addition to the use of various types of radiation, the selection of optimal irradiation positions and dose, fractionation modes, radiosensitizers of various nature can be used to increase the effectiveness of radiotherapy. Various small organic molecules, peptides, proteins, nucleic acids and other substances can act as radiosensitizers [7, 8]. Nanoparticles based on inorganic components have recently been of the greatest interest in this capacity [9]. Unlike organic preparations, they may have a number of useful properties that extend their use. For example, superparamagnetic substances are used for imaging in MRI and particles with a metal core are used in CT [10]. The radiosensitizing effect of inorganic nanoparticles is due to the generation of secondary radiation when the ionizing beam interacts with these radiosensitizers [11]. In the case of proton beam irradiation, their inelastic Coulomb interactions with nanoparticles can lead either to the formation of free electrons, or even to the destruction of the nuclei of elements in the composition of the radiosensitizer during nuclear reactions [12]. Due to the secondary radiation production, a local dose increase occurs, which makes it possible to expand the therapeutic window. As a result of this effect, it is possible to achieve either an increase in the effectiveness of therapy without changing the administered dose, or to remain at the same treatment level while reducing the administered dose. It was believed that nanoparticles containing elements with a large atomic mass value in their composition are more suitable for radiosensitization purposes, since these elements have more electrons in the outer electron shells, which can be excited by ionizing radiation and therefore emit secondary radiation. However, in a recent study [13], it has been shown that TiO₂ nanoparticles with a relatively low effective atomic number demonstrate a significant radiosensitizing effect when irradiated with photons (150 kV and 6 MV) and protons (100 MeV). This effect may be associated with the pronounced radiocatalytic activity of these nanoparticles, which leads to the formation of hydroxyl radicals. Under proton irradiation conditions, it was found that the generation of reactive oxygen species (ROS) in the presence of TiO₂ is comparable to that in the presence of WO₃ particles and higher than in the presence of HfO₂ nanoparticles. Thus, the use of nanoparticles with radiocatalytic activity in PBT is a promising approach.

Nanodisperse cerium (IV) dioxide (aka CeO₂ NPs) has recently been an object of interest to many researchers [14, 15]. In recent years, it has been found that it exhibits various enzyme-like activities. In particular, it can mimic catalase, superoxide dismutase, oxidase, etc. [16] Its enzyme-like properties are due to incomplete oxidation of cerium, which makes possible the Ce⁺³/Ce⁺⁴ transitions underlying various catalytic processes on the surface of cerium oxide nanoparticles. Depending on the environmental conditions, CeO₂ NPs can exhibit both prooxidant and antioxidant activity. In a low pH environment (6.9 or less), which is typical for tumors, CeO₂ NPs tends to exhibit prooxidant activity. For instance, it has been shown that the co-cultivation of various human cancer cells, such as bronchoavolar [17] and hepatocellular carcinoma [18], with CeO₂ NPs leads to an increase in the intracellular ROS generation and therefore promotes the development of oxidative stress in these cells. Additionally, it has been shown that exposing pancreatic cancer cells loaded with CeO₂ NPs to radiation leads to a more effective reduction in their clonogenic activity, compared to using radiation alone [19]. Due to its unique physicochemical features and noticeable biological activity confirmed by many studies, nanoscale cerium (IV) dioxide can be considered as a promising radiosensitizer. To endow CeO₂ NPs with additional properties, they can be doped with the other elements. Particularly, gadolinium-doped CeO₂ NPs have demonstrated the ability to contrast in MRI [20], which can be used to visualize tumors along with their therapy. In addition, the presence of gadolinium in the composition can increase radiosensitizing properties of CeO₂ NPs. Hence, gadolinium-doped CeO₂ NPs are promising for use as theranostics (substances that have both therapeutic and diagnostic properties).

In this study, we have for the first time demonstrated the potential of using dextran-stabilized Ce_{0.8}Gd_{0.2}O_{2-x} nanoparticles as an effective nanoradiosensitizer in combination with proton beam irradiation for melanoma treatment.

2. Materials and methods

2.1. Synthesis and characterization of Ce_{0.8}Gd_{0.2}O_{2-x} nanoparticles

Ce_{0.8}Gd_{0.2}O_{2-x} NPs were synthesized by the hydrothermal method. Briefly, a solution of mixed of cerium (III) and gadolinium (III) nitrates (0.18 and 0.02 M, respectively) and dextran ($M_r \sim 6000$) was prepared, with the (Ce(NO₃)₃·6H₂O+Gd(NO₃)₃·6H₂O) : dextran ratio being 1 : 2 (wt). To the continuously stirred solution, 1 M aqueous ammonia was added dropwise for 3 hours, maintaining the pH at 7.5–8.0. When the pH became constant, the mixture was stirred, for additional 2 hours, then aqueous ammonia was added to reach pH 12, followed by additional stirring for 8 hours. To the colloidal solution obtained, an excess of isopropanol was added and the mixture was refluxed to form a white precipitate. This precipitate was further washed several times with hot isopropanol and dried in air at 60°C. Ce_{0.8}Gd_{0.2}O_{2-x} NPs colloidal solution was prepared by dispersing the powder in the deionized water. The size and shape of Ce_{0.8}Gd_{0.2}O_{2-x} NPs were determined by transmission electron microscopy (TEM) using a Leo912 AB Omega electron microscope (Carl Zeiss, Germany) equipped with an electron energy loss spectrometer (EELS) operating at an

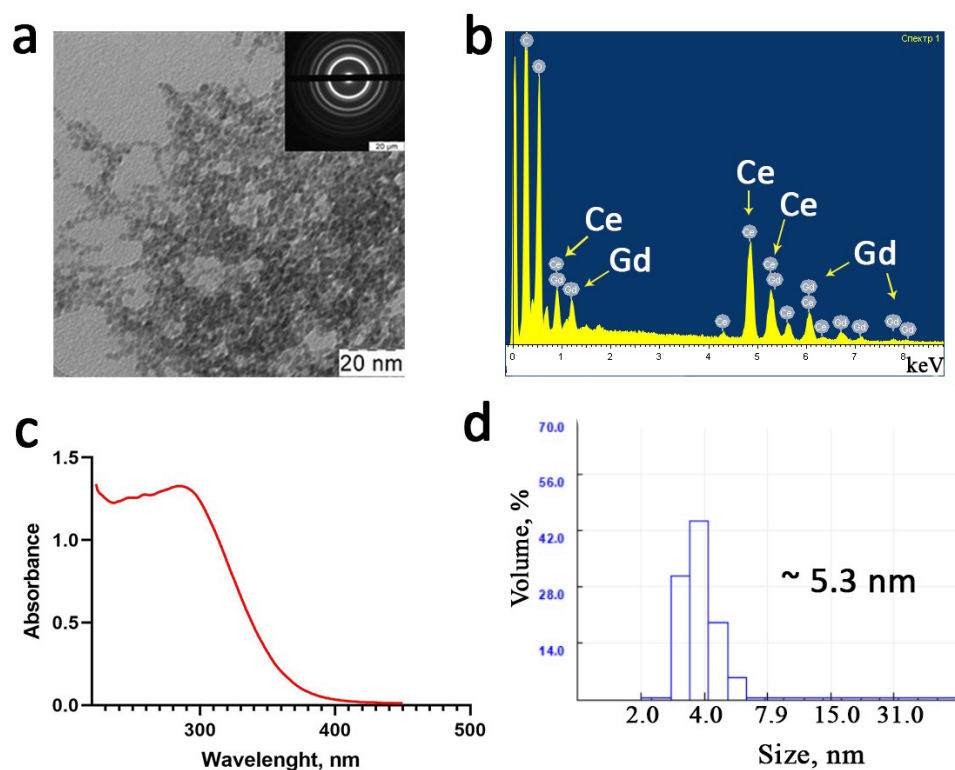


FIG. 1. TEM image with SAED pattern (inset) (a), EDX spectrum (b), UV-visible absorbance spectrum (c) and hydrodynamic diameter distribution (d) of the $Ce_{0.8}Gd_{0.2}O_{2-x}$ NPs

accelerating voltage of 100 kV. The chemical composition of $Ce_{0.8}Gd_{0.2}O_{2-x}$ nanoparticles was analyzed by energy dispersive X-ray analysis (EDX) using a NVision 40 scanning electron microscope (Carl Zeiss, Germany) equipped with an X-MAX detector (80 mm^2) (Oxford Instruments, United Kingdom) at an accelerating voltage of 20 kV. A DS-11+ spectrophotometer (DeNOVIX, USA) was used to measure absorbance of $Ce_{0.8}Gd_{0.2}O_{2-x}$ NPs water sol in the UV-visible range. The hydrodynamic diameter of $Ce_{0.8}Gd_{0.2}O_{2-x}$ nanoparticles in deionized water was measured by dynamic light scattering (DLS) using a N5 submicron particle size analyzer (Beckman Coulter, USA).

2.2. Cell culture

For cell culture experiments, NCTC L929 normal mouse fibroblasts and B16/F10 mouse melanoma cells were obtained from the cryostorage of the Theranostics and Nuclear medicine lab (ITEB RAS, Russia). The cells were cultured in DMEM/F-12 medium (1:1) (PanEco, Russia), containing 2 mM of L-glutamine, 100 U/mL of penicillin and 100 $\mu\text{g}/\text{mL}$ of streptomycin (PanEco, Russia) and 10% of Fetal Bovine Serum (FBS) (HyClone, USA). Cell culture experiments were performed using Neoteric laminar boxes (Lamsystems, Russia). The cells were incubated in CO_2 -incubator D180 (RWD Life Science, China) at 37°C in humidified atmosphere containing 5% CO_2 . As the cells grew and reached subconfluent state, they were treated with a 0.25% trypsin-EDTA (PanEco, Russia) solution and passed into new T12, T25 or T75 cell culture flasks (SPL Life Sciences, Korea) at a ratio of 1:4.

2.3. Proton beam irradiation

T12 cell culture flask, completely filled with the culture medium, was irradiated on the "Prometheus" proton therapy complex (LPI RAS, Russia) in the Bragg peak mode at a beam energy of 160 MeV at the accelerator outlet.

2.4. Cell death analysis

Cell death analysis was performed 24, 48 and 72 hours after co-incubation with $Ce_{0.8}Gd_{0.2}O_{2-x}$ NPs or proton beam irradiation of cells. Briefly, the cell culture medium was replaced with a mixture of fluorescent dyes Hoechst 33342 (Lumiprobe, Russia), which binds to the DNA of all of the cells ($\text{Ex}=350\text{ nm}$, $\text{Em}=460\text{ nm}$), and propidium iodide (PI) (Lumiprobe, Russia), which binds to the DNA of only dead cells ($\text{Ex}=535\text{ nm}$, $\text{Em}=615\text{ nm}$), dissolved in a Hanks' Balanced Salt Solution (HBSS) (PanEco, Russia) at a concentration of 1 μM . After 15 minutes of incubation, the cells were washed twice with HBSS, and then the microphotography of the cells was carried out using ZOE fluorescent cell imager (Bio-Rad, USA). The total number of the cells and the number of dead cells were counted using the ImageJ software. After that, the percentage of dead cells was calculated.

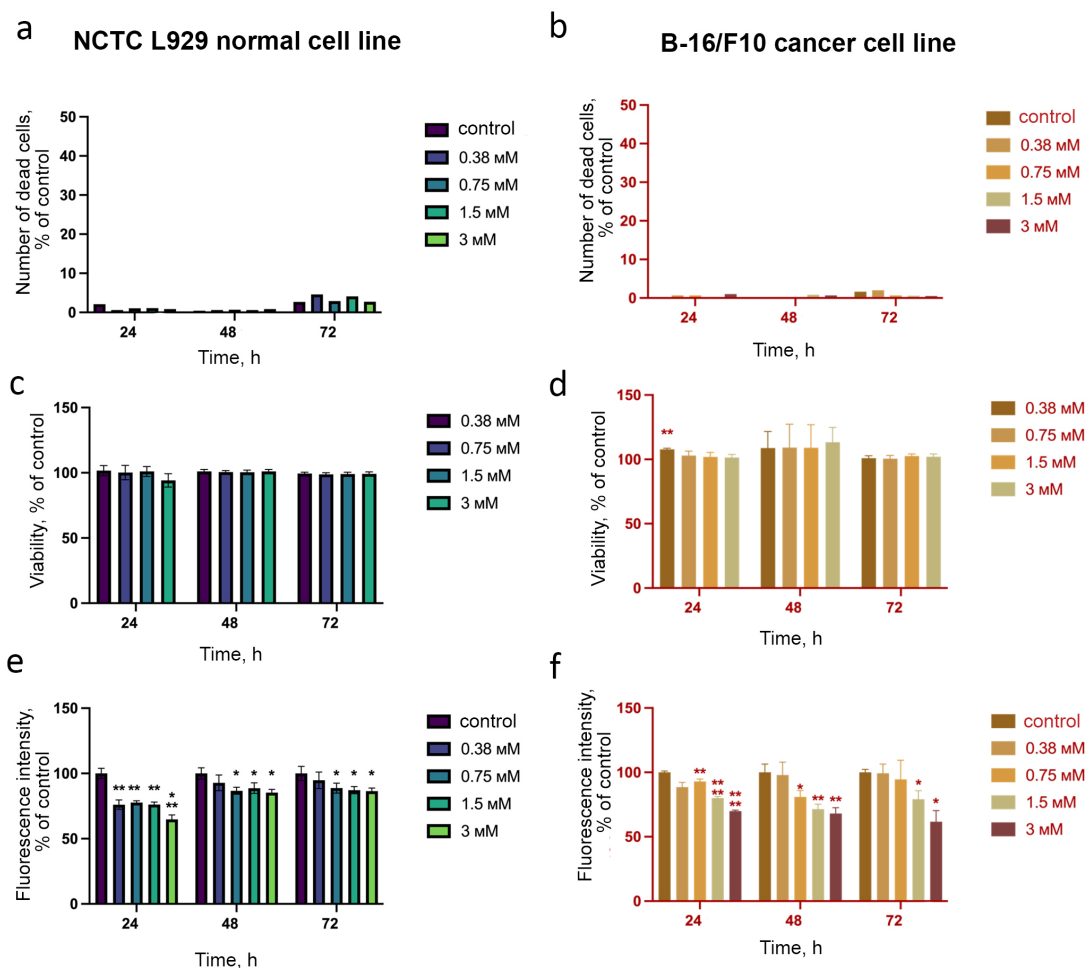


FIG. 2. Percentage of dead cells (a, b), cell viability (c, d) and mitochondrial membrane potential (e, f) of normal (NCTC L929; a, c, e) and tumor (B16/F10; b, d, f) cells after 24, 48 and 72 hours of co-incubation with $Ce_{0.8}Gd_{0.2}O_{2-x}$ NPs at concentration of 0.38–3 mM. The results are presented as a Mean \pm Standard deviation (SD). The significance of the deviations between the experimental and control groups was confirmed using the Welch's t-test with the corresponding p values: $0.01 < p < 0.05$ (*), $0.001 < p < 0.01$ (**), $0.0001 < p < 0.001$ (***) and $p < 0.0001$ (****)

2.5. Cell viability assay

Cell viability was analyzed using routine MTT-assay. Briefly, the cell culture medium was replaced with a solution of MTT (3-(4,5-dimethylthiazole-2-yl)-2,5-diphenyl-tetrazolium bromide) (PanEco, Russia) in a serum-free medium at a concentration of 0.5 mg/mL 24, 48 and 72 hours after co-incubation with $Ce_{0.8}Gd_{0.2}O_{2-x}$ NPs. MTT is being reduced by intracellular NAD(P)H-dependent oxidoreductase enzymes depending on the metabolic activity of cell and, consequently, its viability. After 3 hours of incubation, the MTT solution was replaced with DMSO (PanEco, Russia), and the plate were placed on a plate shaker for 1 minute. After that, the optical density (OD) of the resulted solutions was measured at a wavelength of 570 nm using an INNO-S plate reader (LTek, Korea). The OD values were recalculated as a percentage of the corresponding values from the control groups, the results were presented as a Mean \pm Standard deviation (SD).

2.6. Analysis of mitochondrial membrane potential

Mitochondrial membrane potential (MMP) analysis was performed 24, 48 and 72 hours after co-incubation with $Ce_{0.8}Gd_{0.2}O_{2-x}$ NPs or proton beam irradiation of the cells. Briefly, the cell culture medium was replaced with a TMRE solution (tetramethylrodamine, ethyl ether) (Lumiprobe, Russia), which selectively accumulates in active mitochondria due to their transmembrane potential ($\lambda_{ex}=550$ nm, $\lambda_{em}=575$ nm), in a HBSS at a concentration of 1 μ M. After 15 minutes of incubation, the cells were washed twice with HBSS, and then the microphotography of the cells was carried out using a ZOE fluorescent cell imager (Bio-Rad, USA). The fluorescence intensity of TMRE was measured using the ImageJ program and then were recalculated as a percentage of the corresponding values from the control groups, the results were presented as a Mean \pm Standard deviation (SD).

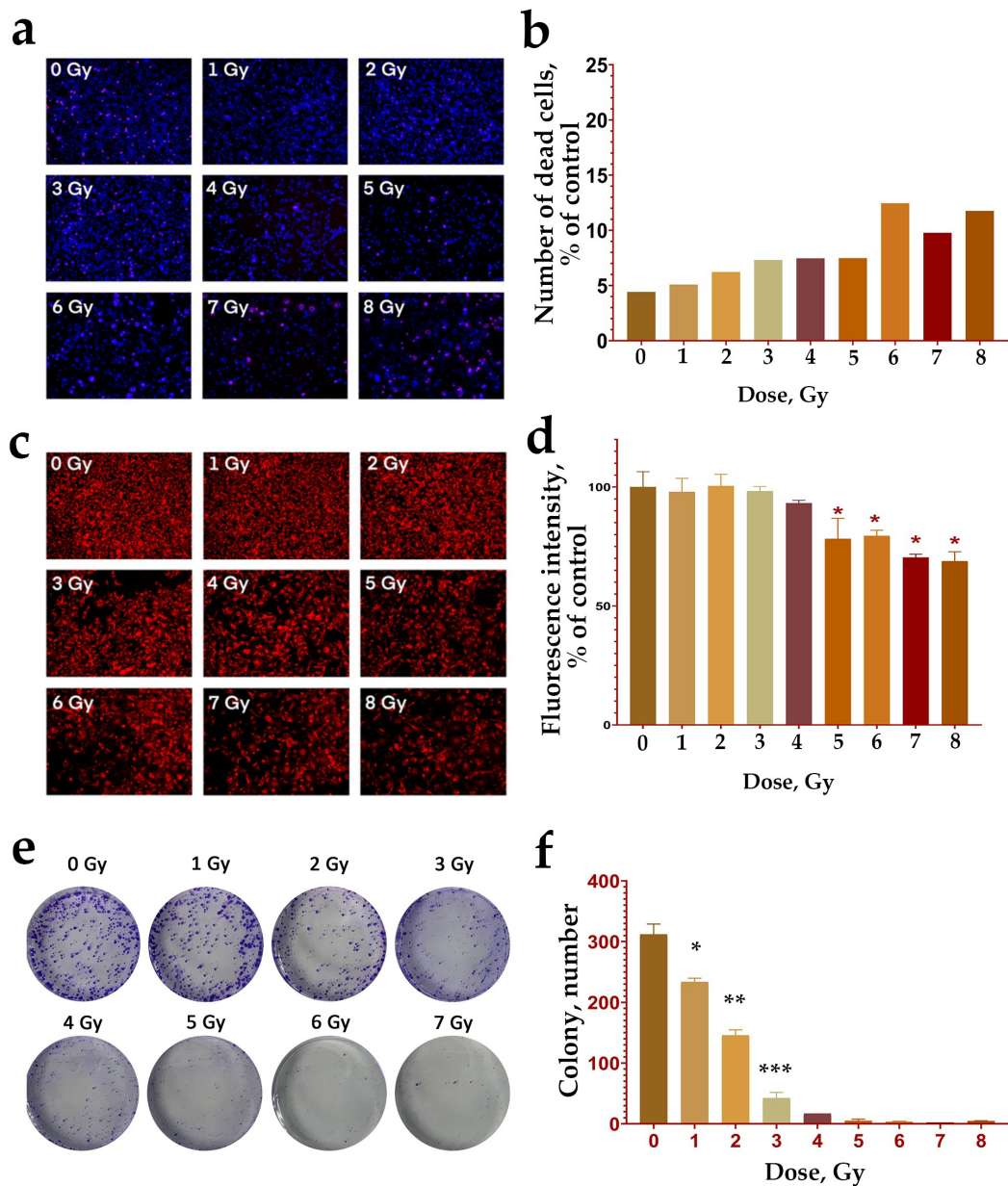


FIG. 3. The effect of proton beam irradiation on the survival (a, b), mitochondrial membrane potential (c, d) and clonogenic activity (e, f) of B16/F10 mouse melanoma cells. The results are presented as a Mean \pm Standard deviation (SD). The significance of the deviations between the experimental and control groups was confirmed using the Welch's t-test with the corresponding p values: $0.01 < p < 0.05$ (*)

2.7. Clonogenic assay

Analysis of cell clonogenic activity was performed immediately after proton beam irradiation. The cells were seeded on a 6-well plate (SPL, Korea) with a density of 1000 cells per well. After 8 days, formed cell colonies were fixed with 4% paraformaldehyde (PanEco, Russia) and stained with 0.1% methylene blue solution (PanEco, Russia). Then cell colonies were counted manually. Colonies were considered to be cellular aggregates of 50 cells or more.

2.8. Statistical analysis

Statistical analysis was performed using a GraphPad Prism software. The significance of the deviations between the experimental and control groups was confirmed using the Welch's t-test with the corresponding p values: $0.01 < p < 0.05$ (*), $0.001 < p < 0.01$ (**), $0.0001 < p < 0.001$ (***) and $p < 0.0001$ (****).

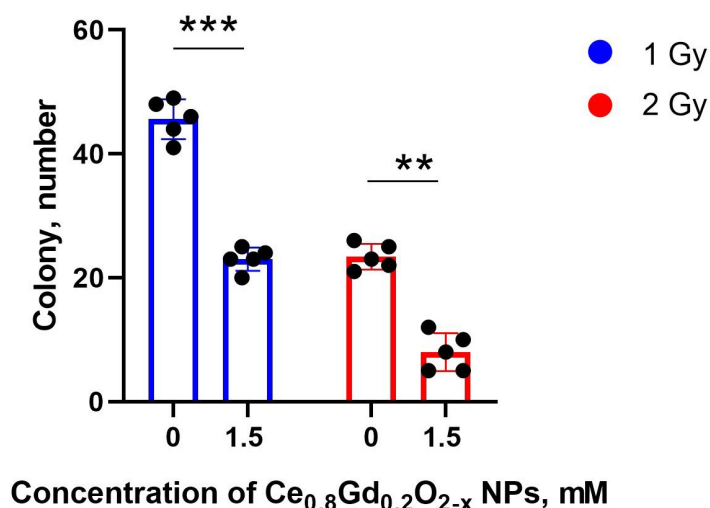


FIG. 4. $\text{Ce}_{0.8}\text{Gd}_{0.2}\text{O}_{2-x}$ NPs nanoparticles at a concentration of 1.5 mM significantly decreased the clonogenic activity of B16/F10 mouse melanoma cells under proton beam irradiation at doses of 1 and 2 Gy. The results are presented as experimental repeats ($n=5$) with Mean \pm Standard deviation (SD). The significance of the deviations between the experimental and control groups was confirmed using the Welch's t-test with the corresponding p values: $0.001 < p < 0.01$ (**) and $0.0001 < p < 0.001$ (***)

3. Results

The synthesized $\text{Ce}_{0.8}\text{Gd}_{0.2}\text{O}_{2-x}$ NPs colloidal solution had no eye-visible opalescence, however it demonstrated an obvious Tyndall effect. According to the transmission electron microscopy data, $\text{Ce}_{0.8}\text{Gd}_{0.2}\text{O}_{2-x}$ NPs have a spherical shape and an ultrasmall size (less than 5 nm) (Figure 1a). Energy dispersive X-ray spectroscopy has shown that the chemical composition of the sample corresponds well to the chemical formula $\text{Ce}_{0.8}\text{Gd}_{0.2}\text{O}_{2-x}$ NPs (Fig. 1b). UV spectrum analysis (Fig. 1c) confirms the characteristic peak of Ce^{4+} . The mean hydrodynamic diameter of $\text{Ce}_{0.8}\text{Gd}_{0.2}\text{O}_{2-x}$ NPs in deionized water is approximately 5.3 ± 3.1 nm (Fig. 1d).

Next, we conducted a comprehensive analysis of the cytotoxicity of $\text{Ce}_{0.8}\text{Gd}_{0.2}\text{O}_{2-x}$ NPs on both normal and tumor cells (Fig. 2). It has been found that $\text{Ce}_{0.8}\text{Gd}_{0.2}\text{O}_{2-x}$ NPs do not promote the death of both NCTC L929 and B16/F10 cells up to a concentration of 3 mM after 72 hours of co-incubation (Fig. 2a,b). It should be noted that the percentage of dead cells did not exceed the value of 5% even at a nanoparticle concentration of 3 mM after 72 hours of incubation. Furthermore, there was no significant decrease in the viability of both normal and tumor cells even at a $\text{Ce}_{0.8}\text{Gd}_{0.2}\text{O}_{2-x}$ NPs concentration of 3 mM after 72 hours of co-incubation (Fig. 2c,d). However, $\text{Ce}_{0.8}\text{Gd}_{0.2}\text{O}_{2-x}$ NPs significantly reduced the MMP of NCTC L929 cells at all of the studied concentrations after 24, 48 and 72 hours of co-incubation (Fig. 2e). Interestingly, there was also a notable MMP decrease in B16/F10 but only at high concentrations of $\text{Ce}_{0.8}\text{Gd}_{0.2}\text{O}_{2-x}$ NPs (0.75–3 mM) after 24, 48 and 72 hours of co-incubation. It is worth noting that $\text{Ce}_{0.8}\text{Gd}_{0.2}\text{O}_{2-x}$ NPs at concentrations of 1.5 mM and 3 mM caused a significant decrease in MMP of melanoma cells (by 30–40%), which was not observed in normal fibroblasts (Fig. 2f).

A comprehensive analysis was further conducted of the effect of proton beam irradiation on the viability parameters of mouse melanoma cells (Fig. 3). This analysis included the determination of the survival rate, MMP and clonogenic activity of B16/F10 cells after proton beam irradiation in the Bragg peak mode in a wide range of doses, ranging from 1 to 8 Gy. A dose-dependent increase in the percentage of dead cells was revealed 72 hours after irradiation at doses of 2 Gy and higher (Fig. 3a,b). It is also worth noting that an increase in the irradiation dose results in an obvious decrease in the overall number of cells seen in micrographs. This phenomenon can be explained by reduced cell proliferation and adhesion after irradiation. Meanwhile, high irradiation doses (6–8 Gy) caused the death of slightly less than 20% of the cells. It has also been demonstrated that irradiation at doses from 1 to 4 Gy did not cause a significant decrease in the MMP of B16/F10 cells (Fig. 3c,d). Nevertheless, irradiation at higher doses (from 5 to 8 Gy) significantly reduced the value of MMP by 25–35% relative to the control. In addition, the clonogenic activity of melanoma cells decreased linearly with an increase in the dose of irradiation (Fig. 3e,f). Starting with a dose of 5 Gy, no colony formation was observed, which indicates a 100% inhibitory effect of proton beam irradiation on B16/F10 cells.

It has also been shown that $\text{Ce}_{0.8}\text{Gd}_{0.2}\text{O}_{2-x}$ NPs at a concentration of 1.5 mM significantly decreased the number of B16/F10 colonies after proton beam irradiation (Fig. 4). It is worth noting that for this concentration of $\text{Ce}_{0.8}\text{Gd}_{0.2}\text{O}_{2-x}$ NPs, we did not observe a reduction in cell viability and survival, but instead observed a decrease in MMP (Fig. 2). Meanwhile, proton beam irradiation at doses of 1 and 2 Gy significantly reduced the clonogenic activity of mouse melanoma cells, and at doses of 5 Gy or above it dramatically declined the MMP of these cells. Therefore, $\text{Ce}_{0.8}\text{Gd}_{0.2}\text{O}_{2-x}$ NPs act

as a radiosensitizer in B16/F10 mouse melanoma cells under proton beam irradiation. We hypothesize that this radiosensitizing effect of $Ce_{0.8}Gd_{0.2}O_{2-x}$ NPs is due to the hypopolarization of mitochondrial membranes, which can be caused in turn by enzyme-like activity of these nanoparticles, and this activity can also be enhanced by proton beam irradiation. Thus, $Ce_{0.8}Gd_{0.2}O_{2-x}$ NPs make it possible to use a lower dose of proton beam irradiation to kill melanoma cells.

4. Discussion

The radioresistance of tumors and the occurrence of side effects due to irradiation of healthy tissues are still urgent problems in the radiotherapy of tumors. The use of hadron therapy instead of classical photon therapy makes it possible to reduce the dose load on healthy tissues, while the use of radiosensitizers significantly increases the therapeutic effect of irradiation, thereby enhancing the effectiveness of treatment. Furthermore, the use of inorganic nanoparticles as radiosensitizers is a promising area of research and development, since such nanomaterials exhibit a wide variety of features inaccessible to organic substances, while their production is neither expensive nor time-consuming. Nanoscale cerium (IV) dioxide has a great potential for use in radiotherapy. Long-term studies on this substance have demonstrated its ability to exhibit selective cytotoxicity against tumor cells as well as to enhance the therapeutic effect of radiotherapy. Our study was aimed at expanding our understanding of the potential of using $Ce_{0.8}Gd_{0.2}O_{2-x}$ NPs in proton therapy of melanoma. We have demonstrated that $Ce_{0.8}Gd_{0.2}O_{2-x}$ NPs are able to dramatically reduce the clonogenic activity of melanoma cells under proton beam irradiation. Also, $Ce_{0.8}Gd_{0.2}O_{2-x}$ NPs promoted a decrease in MMP of these cells. Meanwhile, proton beam irradiation also reduced the clonogenic activity and MMP of melanoma cells. Hence, $Ce_{0.8}Gd_{0.2}O_{2-x}$ NPs act as a radiosensitizer in B16/F10 mouse melanoma cells under proton beam irradiation. We assume that such radiosensitizing effect of $Ce_{0.8}Gd_{0.2}O_{2-x}$ NPs is due to a decrease of the membrane mitochondrial potential, which can be due to enzyme-like activity of these nanoparticles. Moreover, their catalytic activity can also be enhanced by proton beam irradiation. Thus, the use of $Ce_{0.8}Gd_{0.2}O_{2-x}$ NPs in combination with proton beam irradiation is a promising approach for the effective treatment of melanoma. Since this work was conducted only on 2D cell cultures *in vitro*, it seems actual to study the radiosensitizing and MRI-labeling properties of $Ce_{0.8}Gd_{0.2}O_{2-x}$ NPs on both 3D tumor spheroids *in vitro* and mouse tumor model *in vivo* to reveal its theranostic nature.

References

- [1] Ringborg U., Bergqvist D., Brorsson B., Cavallin-ståhl E., Ceberg J., Einhorn N., Frödin J., Järhult J., Lamnevik G., Lindholm C., Littbrand B., Norlund A., Nylén U., Rosén M., Svensson H., Möller T. The Swedish Council on Technology Assessment in Health Care (SBU) Systematic Overview of Radiotherapy for Cancer Including a Prospective Survey of Radiotherapy Practice in Sweden 2001–Summary and Conclusions. *Acta Oncol.* **2003**.
- [2] Baskar R., Lee K.A., Yeo R., Yeoh K.-W. Cancer and Radiation Therapy: Current Advances and Future Directions. *Int. J. Med. Sci.*, 2012, **9**, P. 193–199.
- [3] Yalamarty S.S.K., Filipczak N., Li X., Subhan M.A., Parveen F., Ataide J.A., Rajmalani B.A., Torchilin V.P. Mechanisms of Resistance and Current Treatment Options for Glioblastoma Multiforme (GBM). *Cancers*, 2023, **15**, P. 2116.
- [4] Gregucci F., Beal K., Knisely J.P.S., Pagnini P., Fiorentino A., Bonzano E., Vanpouille-Box C.I., Cisse B., Pannullo S.C., Stieg P.E., et al. Biological Insights and Radiation–Immuno–Oncology Developments in Primary and Secondary Brain Tumors. *Cancers*, 2024, **16**, P. 2047.
- [5] Mohan R. A Review of Proton Therapy – Current Status and Future Directions. *Precis. Radiat. Oncol.*, 2022, **6**, P. 164–176.
- [6] Chen, Z.; Dominello, M.M.; Joiner, M.C.; Burmeister, J.W. Proton versus Photon Radiation Therapy: A Clinical Review. *Front. Oncol.* **2023**, **13**.
- [7] Wang, H.; Mu, X.; He, H.; Zhang, X.-D. Cancer Radiosensitizers. *Trends Pharmacol. Sci.* **2018**, **39**, P. 24–48.
- [8] Gong, L.; Zhang, Y.; Liu, C.; Zhang, M.; Han, S.; Application of Radiosensitizers in Cancer Radiotherapy. *Int J Nanomedicine.* **2021**, **16**, P. 1083–1102. Erratum in: *Int J Nanomedicine.*, 2021, **16**, P. 8139–8140.
- [9] Varzandeh M., Sabouri L., Mansouri V., Gharibshahian M., Beheshtizadeh N., Hamblin M.R., Rezaei N. Application of Nano-Radiosensitizers in Combination Cancer Therapy. *Bioeng. Transl. Med.* **2023**, **8**, P. e10498.
- [10] Laurent S., Mahmoudi M. Superparamagnetic Iron Oxide Nanoparticles: Promises for Diagnosis and Treatment of Cancer. *Int. J. Mol. Epidemiol. Genet.*, **2011**, **2**, P. 367–390.
- [11] Zavestovskaya I.N., Filimonova M.V., Popov A.L., Zelepukin I.V., Shemyakov A.E., Tikhonovski G.V., Savinov M., Filimonov A.S., Shitova A.A., Soldatova O.V., et al. Bismuth Nanoparticles-Enhanced Proton Therapy: Concept and Biological Assessment. *Mater. Today Nano.* 2024, **27**, P. 100508.
- [12] Newhauser W.D., Zhang R. The Physics of Proton Therapy. *Phys. Med. Biol.*, 2015, **60**, P. R155.
- [13] Gerken L.R.H., Gogos A., Starsich F.H.L., David H., Gerdes M.E., Schiefer H., Psoroulas S., Meer D., Plasswilm L., Weber D.C., et al. Catalytic Activity Imperative for Nanoparticle Dose Enhancement in Photon and Proton Therapy. *Nat. Commun.*, 2022, **13**, P. 3248.
- [14] Wei H., Wang E. Nanomaterials with Enzyme-like Characteristics (Nanozymes): Next-Generation Artificial Enzymes. *Chem. Soc. Rev.*, 2013, **42**, P. 6060–6093.
- [15] Wu J., Wang X., Wang Q., Lou Z., Li S., Zhu Y., Qin L., Wei H. Nanomaterials with Enzyme-like Characteristics (Nanozymes): Next-Generation Artificial Enzymes (II). *Chem. Soc. Rev.*, 2019, **48**, P. 1004–1076.
- [16] Popov A.L., Shcherbakov A.B., Zholobak N.M., Baranchikov A.E., Ivanov V.K. Cerium Dioxide Nanoparticles as Third-Generation Enzymes (Nanozymes). *Nanosyst. Phys. Chem. Math.*, **2017**, P. 760–781.
- [17] Lin W., Huang Y., Zhou X.-D., Ma Y. Toxicity of Cerium Oxide Nanoparticles in Human Lung Cancer Cells. *Int. J. Toxicol.*, 2006, **25**, P. 451–457.
- [18] De Marzi L., Monaco A., De Lapuente J., Ramos D., Borrás M., Di Gioacchino M., Santucci S., Poma A. Cytotoxicity and Genotoxicity of Ceria Nanoparticles on Different Cell Lines *In Vitro*. *Int. J. Mol. Sci.*, 2013, **14**, P. 3065–3077.
- [19] Wason M.S., Colon J., Das S., Seal S., Turkson J., Zhao J., Baker C.H. Sensitization of Pancreatic Cancer Cells to Radiation by Cerium Oxide Nanoparticle-Induced ROS Production. *Nanomedicine Nanotechnol. Biol. Med.*, 2013, **9**, P. 558–569.

- [20] Kolmanovich D.D., Chukavin N.N., Savintseva I.V., Mysina E.A., Popova N.R., Baranchikov A.E., Sozarukova M.M., Ivanov V.K., Popov A.L. Hybrid Polyelectrolyte Capsules Loaded with Gadolinium-Doped Cerium Oxide Nanoparticles as a Biocompatible MRI Agent for Theranostic Applications. *Polymers*, 2023, **15**, P. 3840.

Submitted 26 July 2024; accepted 14 October 2024

Information about the authors:

Danil D. Kolmanovich – Institute of Theoretical and Experimental Biophysics of the Russian Academy of Sciences, Pushchino, Russia; ORCID 0000-0003-3391-7889; kdd100996@mail.ru

Mikhail V. Romanov – Institute of Molecular Theranostics, Sechenov First Moscow State Medical University, Moscow, Russia; Lopukhin Federal Research and Clinical Center of Physical-Chemical Medicine of Federal Medical Biological Agency, Moscow, Russia; ORCID 0009-0005-8700-1536; romanov.mikhail@phystech.edu

Sergey A. Khaustov – Scientific and Educational Center, State University of Education, Moscow, Russia; ORCID 0000-0001-9286-3644; sergeykhaustov@gmail.com

Vladimir K. Ivanov – Kurnakov Institute of General and Inorganic Chemistry of the Russian Academy of Sciences, Moscow, Russia; ORCID 0000-0003-2343-2140; van@igic.ras.ru

Alexander E. Shemyakov – Institute of Theoretical and Experimental Biophysics of the Russian Academy of Sciences, Pushchino, Russia; Lebedev Physical Institute of the Russian Academy of Sciences, Moscow, Russia; ORCID 0000-0003-1175-6703; alshemyakov@yandex.ru

Nikita N. Chukavin – Institute of Theoretical and Experimental Biophysics of the Russian Academy of Sciences, Pushchino, Russia; Scientific and Educational Center, State University of Education, Moscow, Russia; ORCID 0000-0001-8431-4485; chukavinnik@gmail.com

Anton L. Popov – Institute of Theoretical and Experimental Biophysics of the Russian Academy of Sciences, Pushchino, Russia; Scientific and Educational Center, State University of Education, Moscow, Russia; ORCID 0000-0003-2643-4846; antonpopovleonid@gmail.com

Conflict of interest: the authors declare no conflict of interest.

Physicochemical properties and biological activity of novel cerium oxide nanoparticles modified with pyrroloquinoline quinone

Elizaveta A. Zamyatina^{1,a}, Olga A. Goryacheva^{2,b}, Nelli R. Popova^{1,c}

¹Institute of Theoretical and Experimental Biophysics of the Russian Academy of Sciences, Pushchino, Russia

²Saratov State University named after N. G. Chernyshevsky, Chemistry Institute, Saratov, Russia

^asonyoru162@gmail.com, ^bolga.goryacheva.93@mail.ru, ^cnellipopovaran@gmail.com

Corresponding author: Nelli R. Popova, nellipopovaran@gmail.com

ABSTRACT Nanoscale cerium oxide (CeO₂) is a bioavailable inorganic nanozyme exhibiting pronounced redox activity and capable of acting as a delivery system for bioactive compounds. We have synthesized and characterized novel CeO₂ nanoparticles modified with pyrroloquinoline quinone (CeO₂@PQQ). TEM analysis revealed the diameter of the CeO₂@PQQ NPs to be approximately 4 nm, with a hydrodynamic diameter of 62 nm (DLS). Furthermore, the zeta potential was found to be –38 mV (ELS), and FTIR analysis confirmed the adsorption of PQQ on the surface of CeO₂ NPs. The results demonstrated that CeO₂@PQQ NPs exhibited no cytotoxic effects on L929 cells within the concentration range of 0.1 – 10 μM and did not adversely affect the mitochondrial function of the cells. It was demonstrated that CeO₂@PQQ NPs exhibited protective effects against L929 cells when induced with oxidative stress (200 μM H₂O₂), leading to preservation of cell mitochondrial potential levels up to 76 % of control and cell viability up to 78 % before and after incubation with CeO₂@PQQ NPs. The results indicate that CeO₂@PQQ NPs can be regarded as a novel hybrid nanosystem that exhibits mitochondrial-directed control of oxidative stress.

KEYWORDS nanoparticles, oxidative stress, reactive oxygen species, antioxidants, nanocrystalline cerium oxide, CeO₂, pyrroloquinoline quinone, PQQ, mitochondria

ACKNOWLEDGEMENTS This research was funded by the Russian Science Foundation, grant No. 22-63-00082. TEM studies were performed using TEM from the Symbioz Center for the Collective Use of Research Equipment of Institute of Biochemistry and Physiology of Plants and Microorganisms (IBPPM RAS).

FOR CITATION Zamyatina E.A., Goryacheva O.A., Popova N.R. Physicochemical properties and biological activity of novel cerium oxide nanoparticles modified with pyrroloquinoline quinone. *Nanosystems: Phys. Chem. Math.*, 2024, **15** (5), 683–692.

1. Introduction

Oxidative stress and mitochondrial dysfunction represent a significant link in the pathogenesis of numerous pathological conditions and the process of ageing [1–4]. Under normal conditions, mitochondria are responsible for the majority of free radical oxidation products generated by the electron transport chain and oxidative phosphorylation, and reactive oxygen species (ROS) are a normal component of numerous metabolic processes within cells [5, 6]. Nevertheless, dysfunctional mitochondria play an important role in the development of oxidative stress, and, as a result, become major targets for ROS [7, 8]. Mitochondrial DNA damage resulting from oxidative stress can lead to impaired energy metabolism and the development of a variety of mitochondrial diseases (Alzheimer's disease, diabetes, muscular dystrophy, cardiomyopathy, etc.) [9–12]. The probability of oxidative stress is contingent upon the level of ROS produced and their relative neutralization by the body's defensive mechanisms, which encompass a complex array of endogenous low molecular weight antioxidants (including superoxide dismutase, catalase, and glutathione peroxidase) [13–16]. When endogenous antioxidant systems are unable to effectively neutralize the increased generation of ROS, exogenous antioxidants can be introduced into biological systems to prevent the development of oxidative stress. The objective is to utilize mitochondrial-directed antioxidant systems to regulate ROS levels and maintain mitochondrial function, while ensuring high biocompatibility and catalytic activity. The utilization of both individual antioxidant compounds and the synthesis of novel combination therapies can be employed for this purpose.

Nanozymes are regarded as a promising platform for the development of new antioxidants that exhibit enhanced characteristics [17, 18]. Nanoparticles that have been functionalized with antioxidants or antioxidant enzymes have the ability to neutralize ROS in a more efficient manner than traditional antioxidants. This is achieved through the enhancement of intrinsic catalytic functions and the promotion of synergistic action with antioxidants [19].

Cerium oxide nanoparticles (CeO₂ NPs) are considered to have promising potential for use as a combined antioxidant due to their distinctive physicochemical properties. In nanoscale particles, the two oxidation states coexist on the nanoparticle's surface, thereby defining a dynamic redox switching process [20,21]. CeO₂ NPs are biocompatible nanozymes that exhibit a range of biomimetic activities, including superoxide dismutase, catalase, glutathione peroxidase, photolyase and phosphatase properties [22]. The mimesis of antioxidant enzymes depends on Ce⁺⁴/Ce⁺³ redox switching on the nanoparticle's surface, which may enable them to act as autoregenerative free radical scavengers [23–28].

Pyroloquinoline quinone (PQQ) is known for its high free radical neutralizing activity [29,30]. Furthermore, recent studies have demonstrated that PQQ may exert a targeted effect on mitochondria, promoting their biogenesis and participating in the regulation of redox processes within the respiratory chain, maintaining the level of intracellular NAD⁺ and stimulating the activity of NAD-dependent enzymes [31–33].

Despite the exceptional properties exhibited by CeO₂ NPs and PQQ, no previous works have demonstrated the properties of the combined action of these two components. In particular, the activity of CeO₂ NPs functionalized with redox-active quinones in biological systems has not been established. It is presumed that the modification of CeO₂ NPs with PQQ can provide a synergistic effect by combining both components in a single material and can therefore be considered as an innovative approach to combat oxidative stress. The nanoparticles exhibit dual functionality, they are capable of neutralizing ROS that cause oxidative stress and simultaneously protecting the mitochondrial function of biological systems.

The development of new nanoparticles allows for the enhancement of the properties of the individual components and for the delivery of a more effective and focused therapeutic intervention. PQQ was selected as an agent capable of synergizing with CeO₂, enhancing the antioxidant functions of CeO₂ and exerting a protective effect on mitochondria, which are the key compartment of ROS formation in the cell.

In this study, we synthesized CeO₂@PQQ NPs, studied the physicochemical properties of the nanoparticles, investigated their cytotoxicity on L929 cells, and examined the protective effects against 200 μM H₂O₂-induced oxidative stress.

2. Materials and methods

2.1. CeO₂@PQQ NPs synthesis

The following reagents were used for the synthesis of CeO₂@PQQ NPs: CeCl₃ · 7H₂O (purity 99 %, Alfa Aesar, USA), PQQ (purity 99 %, Xi'An Horlden Bio Industries Inc, China), KOH (purity ≥ 98 %, Lachema, Czech Republic), NH₄OH (25 %) (Dia-M, Russia). The nanoparticles were obtained via the precipitation method, which is described in brief below: PQQ was added to water and then mixed with a twofold excess of KOH. Subsequently, CeCl₃ · 7H₂O was added to the resulting solution, which was then stirred vigorously on a magnetic stirrer. The developed nanoparticles were then stabilized with 25 % NH₄OH in the requisite quantity until the pH of the solution reached a range of 7.2 – 7.6.

2.2. Characterization of CeO₂@PQQ NPs

The hydrodynamic size and zeta potential values were obtained via dynamic light scattering (DLS) and electrophoretic light scattering (ELS), respectively, using a BeNano Zeta particle size analyzer (BetterSize, Dandong, China). UV-Vis absorption and fluorescence spectra were measured in a quartz cuvette with an optical path length of 10 mm. Absorption spectra were obtained on a Shimadzu UV-1800 spectrophotometer (Shimadzu, Japan). Fluorimeter Cary Eclipse (Agilent Technologies, Australia) was used to obtain fluorescence spectra. Fourier Transform Infrared (FTIR) spectra were recorded from powder samples on a FT-801 FTIR spectrometer (Simex, Russia). To obtain powder, samples were dried in a freeze dryer (Labconco Corp, USA). The size and structural morphology of obtained NPs were observed using a transmission electron microscope (TEM) Libra 120 (Carl Zeiss, Oberkochen, Germany) and scanning electron microscopy (SEM) using a MIRA II LMU instrument (Tescan, Czech Republic) at an operating voltage of 20 kV.

2.3. Cell culture

Mouse fibroblasts (NCTC L929) were obtained from Theranostics and Nuclear Medicine Laboratory cryostorage (ITEB RAS, Pushchino, Russia). L929 cells were cultured in Dulbecco's Modified Eagle's Medium (DMEM)/F12 (1:1), containing 50 μg/mL of penicillin, 50 μg/mL of streptomycin, 1 % of L-glutamine and 10 % of fetal bovine serum (FBS) under 5 % CO₂ at 37 °C. The cells were seeded on 96-well plates at a density of 25000 cells/cm². After the cells had attached, the medium in the wells was replaced with fresh medium containing nanoparticles at concentrations of 0.1 – 100 μM. Cells in the control group were cultured in medium without added nanoparticles.

2.4. MTT assay

The determination of mitochondrial and cytoplasmic dehydrogenases activity in living cells was carried out using a MTT assay based on the reduction of the colorless tetrazolium salt (3-[4,5-dimethylthiazol-2-yl]-2,5-diphenyltetrazolium bromide, MTT, Sigma-Aldrich, USA). Briefly, CeO₂@PQQ NPs were added to cells growing in 96-well plates (for 24, 48 and 72 h at 37 °C in humid air (98 %) containing 5 % CO₂). 3 h prior to the end of the exposure period, the supernatant was removed, and MTT solution in phosphate-buffered saline (0.5 mg/mL, 100 μL/well) was added to the cells for 10 min.

Upon the completion of the exposure period, the supernatant was removed, and a lysis solution containing 0.1 % sodium do-decyl sulfate (Sigma-Aldrich, USA) solution in dimethyl sulfoxide was added. Plates were shaken for 10 min, placed on a microplate spectrophotometer Multiskan FC (Thermo Fisher, USA), and the absorbance was read colorimetrically at 570 nm. Each experiment was repeated three times, with five replications.

2.5. LIVE/DEAD assay

Cell viability after co-incubation with nanoparticles was assessed using a BioRad ZOE Fluorescent Cell Imager. Cells were seeded into 96-well plates and stained with Hoechst 33342 fluorescent dye (absorption – 350 nm, emission – 461 nm) and a propidium iodide (PI) dye (absorption – 493 nm, emission – 636 nm). The dyes were added to the DMEM/F12 without serum (1 μ g/ml) and the plate was placed in a CO₂ incubator for 15 min. Images were captured after washing the cells with a phosphate-buffered saline. Five fields in each well for each cell group were examined. The number of cells (total cells/dead cells) was calculated using the ImageJ software.

2.6. Mitochondrial membrane potential assay

The mitochondrial membrane potential was measured by staining cells with TMRE (tetramethylrhodamine ethyl ester, ThermoFisher, USA) fluorescent dye followed by fluorescence microscopy analysis. After incubating with nanoparticles for 24 hours, the medium was replaced with TMRE solution in Hanks' buffer. The cells were subsequently photographed using a ZOE fluorescence imager. The fluorescence intensity of the TMRE, which is indicative of mitochondrial membrane potential levels in the cells, was quantified using ImageJ software. Three different areas on three separate microphotographs were analyzed for quantitative assessment.

2.7. Measurement of mitochondrial ROS production

For analysis of mitochondrial ROS, cells were treated with 1 μ M MitoSOX (Invitrogen, USA) for 15 min and analyzed using a ZOE fluorescence imager. The fluorescence intensity of reactive oxygen species (ROS) in each of 100 randomly selected cells was quantified using ImageJ software. To ensure the accuracy of the scoring process, the data were scored and analyzed independently by two investigators.

2.8. Oxidative stress model in vitro

The protective action of CeO₂@PQQ NPs was analyzed using experimental model of oxidative stress, whereby the cells were treated with 200 μ M H₂O₂ (30 %, Sigma-Aldrich, USA). In one case, nanoparticles were added to the cell culture, then 24 hours later the cells were treated with H₂O₂ for 60 min. In another case, the cells were immediately incubated with H₂O₂ for 60 min, after which the nanoparticles were added and the cells were incubated for 24 hours. At the end of the incubation period, cytotoxicity tests were performed, including the MTT test and the LIVE/DEAD test, and the level of mitochondrial status was examined by measuring the level of mitochondrial potential. All of the tests were carried out as described in the methodology above.

2.9. Statistical analysis

The data obtained from the MTT test, LIVE/DEAD test, measurement of mitochondrial potential level and mitochondrial ROS level were presented as mean \pm standard deviation. The statistical analysis was performed using Welch's t-test. A p-value of less than 0.05 was considered to be statistically significant between the control and experimental groups.

3. Results and discussion

CeO₂@PQQ NPs were prepared using the precipitation method, the proposed schematic structure of which is shown in Fig. 1. To study the morphology and size of the obtained structures TEM images were analyzed (Fig. 2(D, E)). The obtained samples were compared with CeO₂ NPs (Fig. 2(A, B)), which have been previously obtained by our colleagues and have been well described [34]. From the image, it can be seen that the obtained samples are nanoparticles with the size ranging from 1.6 to 3.9 nm or aggregates of several nanoparticles. FTIR data (Fig. 2(G)) confirmed the similarity of the obtained structures with CeO₂ NPs. The sharpband peak centered at 500 cm⁻¹, which match to Ce–O stretching vibrations, confirmed the formation CeO₂ nanostructures [35].

The SEM and DLS data (Fig. 2(C, F, J)) differed from the TEM image analysis results. This can indicate the formation of complexes or a large layer of adsorbed organic molecules. Nanocluster formation can occur due to the fact that PQQ can bind to the \bar{N} e atom on the surface of CeO₂ NPs in three ways via quinone carbonyl oxygen, pyridine nitrogen, and carboxylate [36]. The zeta potential of the obtained nanoparticles was found to be –38 mV (Fig. 2(K)), which is similar to the zeta potential values of classical citric acid-coated CeO₂ NPs with a zeta potential of around –30 mV [37]. This may indicate that the obtained nanoparticles possess high colloidal stability. PQQ is a multicharged anion, which gives the particles a negative charge, ammonia in turn provides ionization of PQQ and sol stability due to repulsion.

According to infrared spectroscopy, PQQ has a characteristic spectrum from 500 to 1790 cm⁻¹ (Fig. 2(G)). The spectra of CeO₂@PQQ NPs showed a series of characteristic peaks of PQQ. Thus, 1116 cm⁻¹ indicates C–H bond, 1393 cm⁻¹

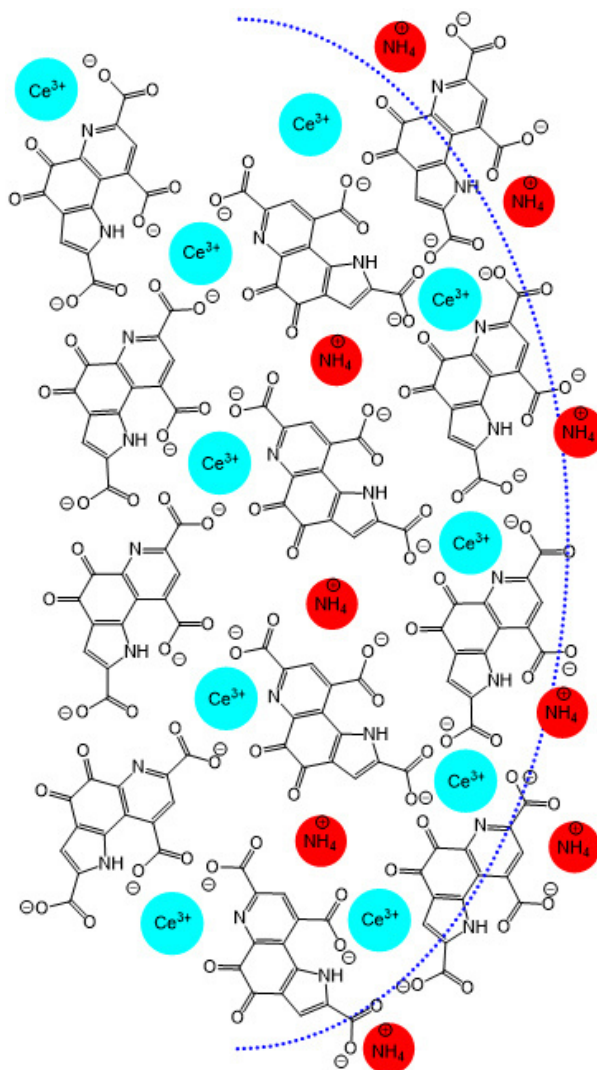


FIG. 1. Schematic representation of the proposed chemical structure of $\text{CeO}_2@PQQ$ NPs. The blue line represents the conditional boundary of the nanoparticle

is characteristic for C–C bond in the aromatic ring [38] and 1543 cm^{-1} band indicates C–N [39] and 1505 cm^{-1} characteristic of the C=O stretching vibrations [40].

A spectrophotometric method was used to evaluate the sorption of PQQ on the surface of CeO_2 NPs. PQQ absorption spectrum is characterized by pronounced maxima at 248, 275 and 333 nm (Fig. 2(I)). During nanoparticles synthesis, the transition of PQQ into anion changed the shape of the spectrum and shifted the maxima. Thus, when the anion PQQ³⁻ appeared in solution, the peak at 275 nm was significantly smoothed and the maximum at 333 nm is shifted to the longer wavelength region [41]. Upon sorption of PQQ on the surface of CeO_2 NPs, there was a significant change in the absorption spectrum of PQQ. The absorption maximum from 248 nm underwent a bathochromic shift to 257 nm. The maximum at 275 nm disappeared, while the peak of the maximum at 333 nm broadened and decreased relative to 257 nm. Similar changes in the absorption spectrum of PQQ were observed upon addition of Eu, another element from the lanthanide group [41]. PQQ has a characteristic fluorescence with a peak maximum at 480 nm (Fig. 2(H)) and the shape of the fluorescence spectrum did not change upon adsorption on the surface of CeO_2 NPs.

L929 mouse fibroblasts are a widely used cell culture for cytotoxicity studies and is frequently utilized as a standard subject for biocompatibility studies of nanomaterials [42]. The cytotoxicity of the $\text{CeO}_2@PQQ$ NPs was evaluated using the MTT assay, which assesses the metabolic activity of cells by measuring the activity of cellular NAD(P)H-dependent oxidoreductases (Fig. 3(A)). The incubation of L929 cells with $\text{CeO}_2@PQQ$ NPs for 24 – 72 hours at concentrations of $0.1 - 2\ \mu\text{M}$ did not result in any significant cytotoxicity. Conversely, the values of metabolic activity exhibited a notable increase, reaching up to 112 %. This effect of increasing cell viability has been demonstrated in other studies involving CeO_2 NPs, where it is presumed that such values can be correlated with the number of mitochondria in cells and the participation of cytosolic enzymes [43]. However, in this study, this effect was only observed for the initial $\text{CeO}_2@PQQ$ NPs investigated ($0.1 - 2\ \mu\text{M}$), at which the differences between the control and the studied groups were not statistically

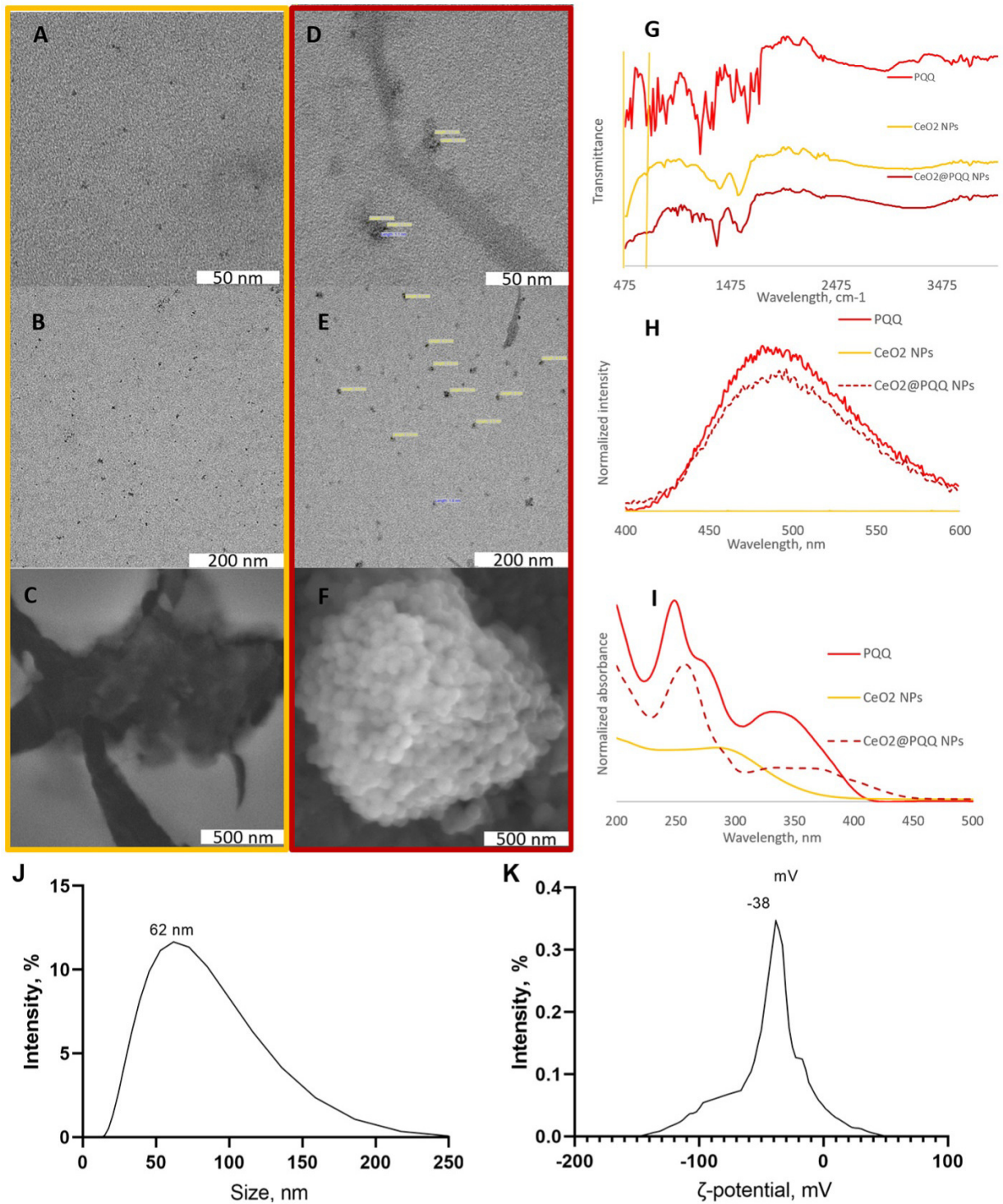


FIG. 2. Transmission electron microscopy images of CeO₂ NPs stabilized with citric acid (A, B) and CeO₂@PQQ NPs (D, E), scanning electron microscopy images of CeO₂ NPs stabilized with citric acid (C) and CeO₂@PQQ NPs (F), FTIR spectra (G), fluorescence spectra (H) and absorption spectra (I) of PQQ, CeO₂ NPs and CeO₂@PQQ NPs, hydrodynamic diameter distribution (J) and zeta potential distribution (K) of CeO₂@PQQ NPs

different. However, the viability of L929 decreased to 46 % when incubated with 10 μM $\text{CeO}_2\text{@PQQ}$ NPs for 24 hours, but this value increased to 65 and 88 % after 48 and 72 hours of incubation, respectively. Incubation of the L929 cells with $\text{CeO}_2\text{@PQQ}$ NPs at concentrations of 20 – 100 μM resulted in a significant reduction in cell metabolic activity. The incubation of L929 cells with $\text{CeO}_2\text{@PQQ}$ NPs at concentrations of 20 – 100 μM resulted in a significant reduction in metabolic activity, with a decrease from 57 to 12 % being observed.

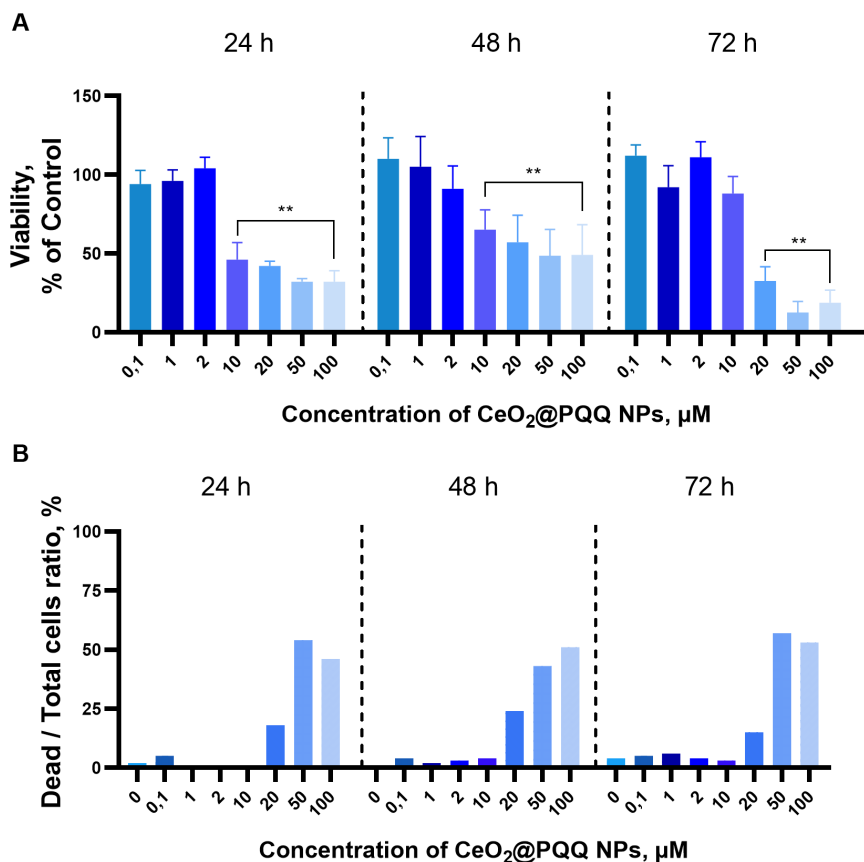


FIG. 3. MTT assay (A) and LIVE/DEAD test (B) results obtained on mouse fibroblasts (L929). The cells were incubated with $\text{CeO}_2\text{@PQQ}$ NPs in concentrations 0.1 – 100 μM . The test was carried out after 24, 48, and 72 hours. Results are represented as a mean \pm SD. The values of the metabolic activity of cells are shown as a percentage of the control. Statistical significance was assumed for P-values < 0.05 : (* $P < 0.05$, ** $P < 0.01$)

A LIVE/DEAD assay was used to visualize the distribution of live and dead cells of the L929. All cells were stained with Hoechst 33342 (blue fluorescence), while dead cells were stained with propidium iodide (PI) (red fluorescence). (Fig. 3(B)). A notable increase in the number of dead cells (approximately 25 %) was observed in the group with a $\text{CeO}_2\text{@PQQ}$ NPs concentration of 20 μM . The number of dead cells exceeded 50 % when L929 was incubated with $\text{CeO}_2\text{@PQQ}$ NPs at concentrations of 50 – 100 μM . Consequently, $\text{CeO}_2\text{@PQQ}$ NPs at concentrations of 0.1 – 10 μM had no pronounced cytotoxic effect on L929, but at concentrations of 20 – 100 μM resulted in decreased metabolic activity and cell death.

Mitochondrial membrane potential was evaluated through assessment of the cationic dye tetramethylrhodamine (TMRE). The accumulation of TMRE within active mitochondria is due to the relative negative membrane potential of these organelles (Fig. 4(A)). The mitochondrial potential values of the cells were obtained following a 24-hour incubation period with $\text{CeO}_2\text{@PQQ}$ NPs at a concentration range of 0.1 to 100 μM . It was demonstrated that a reduction in mitochondrial potential values was observed when $\text{CeO}_2\text{@PQQ}$ NPs were incubated with concentrations of 20 – 100 μM , with a decrease of up to 75 % compared to the intact control.

The fluorescent dye MitoSOX is commonly used to detect ROS in mitochondria, particularly superoxide anions (Fig. 4(B)). Following the incubation of L929 cells with 1 – 100 μM $\text{CeO}_2\text{@PQQ}$ NPs, the superoxide level exhibited no significant changes in comparison to the control. The results demonstrated that $\text{CeO}_2\text{@PQQ}$ NPs at concentrations 1 – 10 μM had no significant impact on mitochondrial function.

The exposure of cell cultures to H_2O_2 is a widely employed method for the induction of oxidative stress [44, 45]. L929 cells were treated with H_2O_2 (200 μM , 60 min) prior to and subsequent to incubation with $\text{CeO}_2\text{@PQQ}$ NPs. The viability of L929 cells incubated with $\text{CeO}_2\text{@PQQ}$ NPs at concentrations of 0.1 – 10 μM was maintained at 63 – 78 %

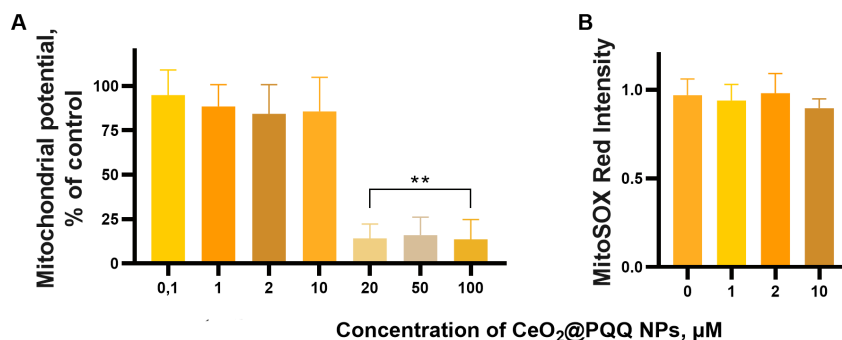


FIG. 4. Mitochondrial membrane potential (A) and mitochondrial ROS levels (B) results were obtained on L929 cells following 24-hour incubation with CeO₂@PQQ NPs at concentrations of 0.1 – 100 μM. Results are represented as a mean ± SD. The values of the mitochondrial potential of cells are shown as a percentage of the control. Statistical significance was assumed for P-values < 0.05: (**P* < 0.05, ***P* < 0.01)

before and after incubation with nanoparticles, as determined by the MTT assay (Fig. 5). Meanwhile, concentrations of CeO₂@PQQ NPs in the range of 20 – 100 μM were found to negatively affect the metabolic activity of cells, reducing cell viability by up to 15 %. The results of the LIVE/DEAD test exhibited a comparable pattern: the number of dead cells in the concentration range of 0.1 – 10 μM CeO₂@PQQ NPs did not exceed 20 %, while 100 % of cells were observed to be dead in the range of 20 – 100 μM (Fig. 6).

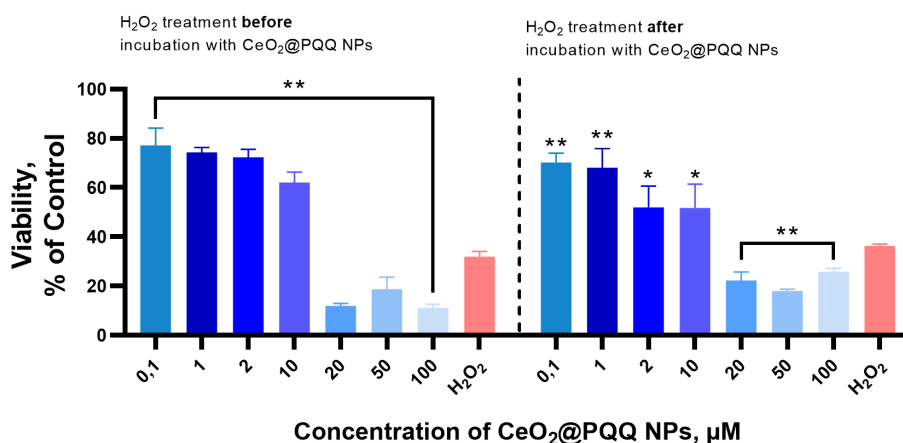


FIG. 5. MTT assay results obtained on mouse fibroblasts (L929). The cells were incubated with CeO₂@PQQ NPs in concentrations 0.1 – 100 μM before and after H₂O₂ treatment. The test was carried out after 24 hours. Results are represented as a mean ± SD. The values of the metabolic activity of cells are shown as a percentage of the control. Statistical significance was assumed for P-values < 0.05: (**P* < 0.05, ***P* < 0.01)

According to TMRE fluorescence, after treatment of cells with H₂O₂, their mitochondrial potential decreased to 37 – 47 % (Fig. 7). Furthermore, following the incubation of cells in the presence of CeO₂@PQQ NPs, a concentration range of 0.1 – 100 μM, mitochondrial potential was maintained at 48 – 76 % of control levels. Upon the introduction of CeO₂@PQQ NPs subsequent to H₂O₂ treatment, effective concentrations capable of inhibiting mitochondrial membrane depolarization were observed to range from 0.1 to 2 μM.

It can be postulated that the CeO₂@PQQ NPs obtained may result in the reduction of H₂O₂-induced oxidative stress in L929 cells. The depolarization of the mitochondrial membrane can be indicative of severe mitochondrial damage, given that mitochondria are a major source of ROS within cells [46]. It is probable that the modification of CeO₂NPs with PQQ will not only enhance their catalytic activity for ROS neutralizing, but also have a beneficial impact on mitochondrial function [33]. The presence of the redox-active cerium ion may potentially accelerate redox reactions involving PQQ. Upon induction of oxidative stress by the incubation of L929 cells with H₂O₂ at a concentration of 200 μM, the nanoparticles under investigation exhibited a preservation of cell viability at 63 – 78 % both before and after nanoparticle application, and of mitochondrial potential at 48 – 76 % of control values across concentrations ranging from 0.1 to 10 μM.

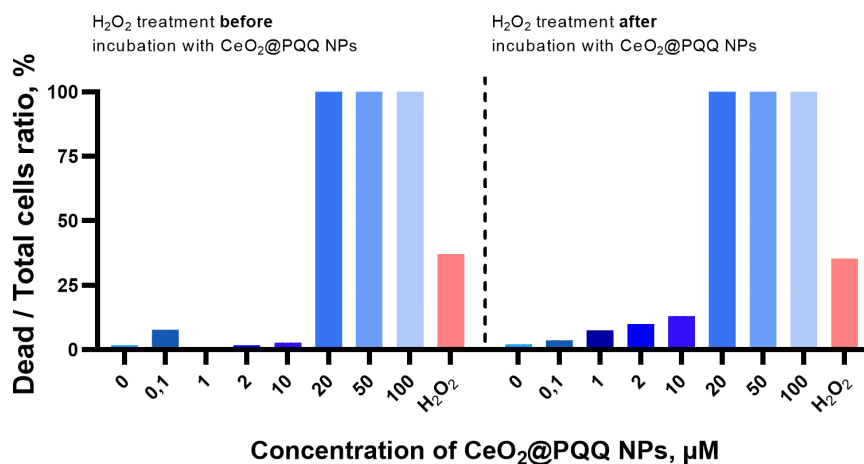


FIG. 6. LIVE/DEAD test results obtained on mouse fibroblasts (L929). The cells were incubated with CeO₂@PQQ NPs in concentrations 0.1 – 100 μM before and after H₂O₂ treatment. The test was carried out after 24 hours. Results are represented as a mean ± SD. The values of the metabolic activity of cells are shown as a percentage of the control. Statistical significance was assumed for P-values < 0.05: (*P < 0.05, **P < 0.01)

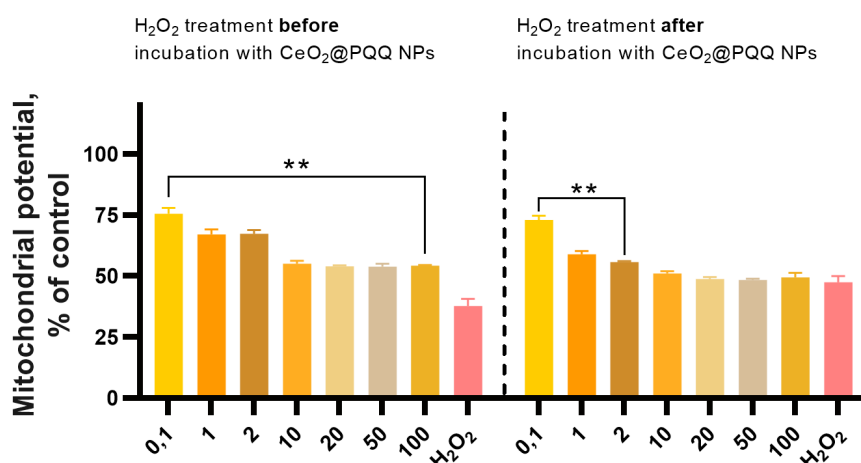


FIG. 7. Mitochondrial membrane potential results were obtained on L929 cells following 24-hour incubation with CeO₂@PQQ NPs at concentrations of 0.1 – 100 μM before and after H₂O₂ treatment. Results are represented as a mean ± SD. The values of the mitochondrial potential of cells are shown as a percentage of the control. Statistical significance was assumed for P-values < 0.05: (*P < 0.05, **P < 0.01)

4. Conclusions

CeO₂@PQQ NPs were successfully obtained by precipitation method. The nanoparticles were characterized by a variety of techniques, including TEM, SEM, DLS, ELS, FTIR and UV-Vis spectroscopy. The morphological study using TEM and SEM revealed that the majority of CeO₂@PQQ NPs exhibited a size range of up to 3.9 nm. The results of the FTIR confirmed the formation of CeO₂ structures and demonstrated the presence of PQQ on the surface of CeO₂ NPs. The results of the DLS analysis indicate that CeO₂@PQQ NPs have an average diameter of 62 nm in solution. The ELS measurements yielded zeta potential of –38 mV, which is indicative of CeO₂@PQQ NPs sufficient colloidal stability. At concentrations up to 20 μM, no reduction in the mitochondrial potential values of L929 was observed. When oxidative stress was induced by treating the L929 cell line with H₂O₂ at a concentration of 200 μM, the nanoparticles under investigation demonstrated the capacity to preserve cell viability at 63 – 78 % before and after nanoparticle addition, as well as to preserve mitochondrial potential at 48 – 76 % of control values at concentrations of 0.1 – 10 μM. Consequently, CeO₂@PQQ NPs may offer new opportunities to combat oxidative stress through their synergistic properties.

References

- [1] Yang S., Lian G. ROS and diseases: role in metabolism and energy supply. *Mol Cell Biochem*, 2020, **467**, P. 1–12.
- [2] Ott M., Gogvadze V., Orrenius S., Zhivotovsky B. Mitochondria, oxidative stress and cell death. *Apoptosis*, 2007, **12**, P. 913–922.
- [3] Jomova K., Raptova R., Alomar S.Y., Alwaseel S.H., Nepovimova E., Kuca K., Valko M. Reactive oxygen species, toxicity, oxidative stress, and antioxidants: chronic diseases and aging. *Arch Toxicol*, 2023, **97**, P. 2499–2574.
- [4] Kowalczyk P., Sulejczak D., Kleczkowska P., Bukowska-Oško I., Kucia M., Popiel M., Wietrak E., Kramkowski K., Wrzosek K., Kaczyńska K. Mitochondrial oxidative stress—A causative factor and therapeutic target in many diseases. *IJMS*, 2021, **22**, 13384.
- [5] Liu Y., Fiskum G., Schubert D. Generation of reactive oxygen species by the mitochondrial electron transport chain. *J. of Neurochemistry*, 2002, **80**, P. 780–787.
- [6] Lennicke C., Cochemé H.M. Redox metabolism: ROS as specific molecular regulators of cell signaling and function. *Molecular Cell*, 2021, **81**, P. 3691–3707.
- [7] Newmeyer D.D., Ferguson-Miller S. Mitochondria. *Cell*, 2003, **112**, P. 481–490.
- [8] Mailloux R.J. An Update on Mitochondrial Reactive Oxygen Species Production. *Antioxidants*, 2020, **9**, 472.
- [9] Filograna R., Mennuni M., Alsina D., Larsson N. Mitochondrial DNA copy number in human disease: the more the better? *FEBS Letters*, 2021, **595**, P. 976–1002.
- [10] Wei W., Chinnery P.F. Inheritance of mitochondrial DNA in humans: implications for rare and common diseases. *J. Intern. Med.*, 2020, **287**, P. 634–644.
- [11] Pereira C.V., Gitschlag B.L., Patel M.R. Cellular mechanisms of mtDNA heteroplasmy dynamics. *Critical Reviews in Biochemistry and Molecular Biology*, 2021, **56**, P. 510–525.
- [12] Mustafa M.F., Fakurazi S., Abdullah M.A., Maniam S. Pathogenic Mitochondria DNA Mutations: Current Detection Tools and Interventions. *Genes*, 2020, **11**, 192.
- [13] Pisoschi A.M., Pop A. The role of antioxidants in the chemistry of oxidative stress: A review. *European J. of Medicinal Chemistry*, 2015, **97**, P. 55–74.
- [14] Elsayed Azab A., Adwas A.A., Ibrahim Elsayed A.S., Adwas A.A., Ibrahim Elsayed A.S., Quwaydir F.A. Oxidative stress and antioxidant mechanisms in human body. *JABB*, 2019, **6**, P. 43–47.
- [15] Nandi A., Yan L.-J., Jana C.K., Das N. Role of Catalase in Oxidative Stress- and Age-Associated Degenerative Diseases. *Oxidative Medicine and Cellular Longevity*, 2019, **2019**, P. 1–19.
- [16] Ighodaro O.M., Akinloye O.A. First line defence antioxidants-superoxide dismutase (SOD), catalase (CAT) and glutathione peroxidase (GPX): Their fundamental role in the entire antioxidant defence grid. *Alexandria J. of Medicine*, 2018, **54**, P. 287–293.
- [17] Li C.-W., Li L.-L., Chen S., Zhang J.-X., Lu W.-L. Antioxidant nanotherapies for the treatment of inflammatory diseases. *Front. Bioeng. Biotechnol.*, 2020, **8**, 200.
- [18] Kim Y.G., Lee Y., Lee N., Soh M., Kim D., Hyeon T. Ceria-based therapeutic antioxidants for biomedical applications. *Advanced Materials*, 2024, **36**, 2210819.
- [19] Khalil I., Yehye W.A., Etxeberria A.E., Alhadi A.A., Dezfooli S.M., Julkapli N.B.M., Basirun W.J., Seyfoddin A. Nanoantioxidants: Recent trends in antioxidant delivery applications. *Antioxidants*, 2019, **9**, 24.
- [20] Celardo I., Pedersen J.Z., Traversa E., Ghibelli L. Pharmacological potential of cerium oxide nanoparticles. *Nanoscale*, 2011, **3**, 1411.
- [21] Popov A.L., Andreeva V.V., Khohlov N.V., Kamenskikh K.A., Gavriluk V.B., Ivanov V.K. Comprehensive cytotoxicity analysis of polysaccharide hydrogel modified with cerium oxide nanoparticles for wound healing application. *Nanosystems: Phys. Chem. Math.*, 2021, **12**, P. 329–335.
- [22] Li F., Yang L., Zou L., Wu Y., Hu C., He J., Yang X. Decreasing crystallinity is beneficial to the superoxide dismutase-like activity of ceria nanoparticles. *ChemNanoMat*, 2022, **8**, e202100466.
- [23] Shcherbakov A.B., Reukov V.V., Yakimansky A.V., Krasnopeeva E.L., Ivanova O.S., Popov A.L., Ivanov V.K. CeO₂ Nanoparticle-containing polymers for biomedical applications: A Review. *Polymers*, 2021, **13**, 924.
- [24] Filippova A.D., Baranchikov A.E., Ivanov V.K. Enzyme-like activity of cerium dioxide colloidal solutions stabilized with L-Malic acid. *Colloid J.*, 2023, **85**, P. 782–794.
- [25] Ge X., Cao Z., Chu L. The antioxidant effect of the metal and metal-oxide nanoparticles. *Antioxidants*, 2022, **11**, 791.
- [26] Corsi F., Deidda Tarquini G., Urbani M., Bejarano L., Traversa E., Ghibelli L. The impressive anti-inflammatory activity of cerium oxide nanoparticles: more than redox? *Nanomaterials*, 2023, **13**, 2803.
- [27] Sozarukova M.M., Kozlova T.O., Beshkareva T.S., Popov A.L., Kolmanovich D.D., Vinnik D.A., Ivanova O.S., Lukashin A.V., Baranchikov A.E., Ivanov V.K. Gadolinium Doping Modulates the Enzyme-like Activity and Radical-Scavenging Properties of CeO₂ Nanoparticles. *Nanomaterials*, 2024, **14**, 769.
- [28] Chukavin N.N., Filippova K.O., Ermakov A.M., Karmanova E.E., Popova N.R., Anikina V.A., Ivanova O.S., Ivanov V.K., Popov A.L. Redox-active cerium fluoride nanoparticles selectively modulate cellular response against X-ray irradiation In Vitro. *Biomedicines*, 2023, **12**, 11.
- [29] Akagawa M., Nakano M., Ikemoto K. Recent progress in studies on the health benefits of pyrroloquinoline quinone. *Bioscience, Biotechnology, and Biochemistry*, 2016, **80**, P. 13–22.
- [30] Ikemoto K., Mohamad Ishak N.S., Akagawa M. The effects of pyrroloquinoline quinone disodium salt on brain function and physiological processes. *J. Med. Invest.*, 2024, **71**, P. 23–28.
- [31] Mohamad Ishak N.S., Ikemoto K. Pyrroloquinoline-quinone to reduce fat accumulation and ameliorate obesity progression. *Front. Mol. Biosci.*, 2023, **10**, 1200025.
- [32] Banerjee R., Purhonen J., Kallijärvi J. The mitochondrial coenzyme Q junction and complex III: biochemistry and pathophysiology. *The FEBS Journal*, 2022, **289**, P. 6936–6958.
- [33] Jonscher K.R., Chowanadisai W., Rucker R.B. Pyrroloquinoline-quinone is more than an antioxidant: A vitamin-like accessory factor important in health and disease prevention. *Biomolecules*, 2021, **11**, 1441.
- [34] Popov A.L., Popova N.R., Selezneva I.I., Akkizov A.Y., Ivanov V.K. Cerium oxide nanoparticles stimulate proliferation of primary mouse embryonic fibroblasts in vitro. *Materials Science and Engineering: C*, 2016, **68**, P. 406–413.
- [35] Parimi D., Sundararajan V., Sadak O., Gunasekaran S., Mohideen S.S., Sundaramurthy A. Synthesis of positively and negatively charged CeO₂ nanoparticles: Investigation of the role of surface charge on growth and development of *Drosophila melanogaster*. *ACS Omega*, 2019, **4**, P. 104–113.
- [36] Itoh S., Kawakami H., Fukuzumi S. Development of the active site model for calcium-containing quinoprotein alcohol dehydrogenases. *J. of Molecular Catalysis B: Enzymatic*, 2000, **8**, P. 85–94.
- [37] Tsai Y.-Y., Oca-Cossio J., Agering K., Simpson N.E., Atkinson M.A., Wasserfall C.H., Constantinidis I., Sigmund W. Novel synthesis of cerium oxide nanoparticles for free radical scavenging. *Nanomedicine*, 2007, **2**, P. 325–332.

- [38] Wang L., Roitberg A., Meuse C., Gaigalas A.K. Raman and FTIR spectroscopies of fluorescein in solutions. *Spectrochimica Acta Part A: Molecular and Biomolecular Spectroscopy*, 2001, **57**, P. 1781–1791.
- [39] Smith B.C. Infrared spectroscopy of polymers XII: Polyaramids and slip agents. *Spectroscopy*, 2023, **38** (5), P. 16–18.
- [40] Ibrahim S., Rezk M.Y., Ismail M., Abdelrahman T., Sharkawy M., Abdellatif A., Allam N.K. Coaxial nanofibers outperform uniaxial nanofibers for the loading and release of pyrroloquinoline quinone (PQQ) for biomedical applications. *Nanoscale Adv.*, 2020, **2**, P. 3341–3349.
- [41] Danaf N.A., Kretzschmar J., Jahn B., Singer H., Pol A., Op Den Camp H.J.M., Steudtner R., Lamb D.C., Drobot B., Daumann L.J. Studies of pyrroloquinoline quinone species in solution and in lanthanide-dependent methanol dehydrogenases. *Phys. Chem. Chem. Phys.*, 2022, **24**, P. 15397–15405.
- [42] Ray R.S., Agrawal N., Sharma A., Hans R.K. Use of L-929 cell line for phototoxicity assessment. *Toxicology in Vitro*, 2008, **22**, P. 1775–1781.
- [43] Tumkur P.P., Gunasekaran N.K., Lamani B.R., Nazario Bayon N., Prabhakaran K., Hall J.C., Ramesh G.T. Cerium oxide nanoparticles: synthesis and characterization for biosafe applications. *Nanomanufacturing*, 2021, **1**, P. 176–189.
- [44] Goffart S., Tikkanen P., Michell C., Wilson T., Pohjoismäki J.L.O. The type and source of reactive oxygen species influences the outcome of oxidative stress in cultured cells. *Cells*, 2021, **10**, 1075.
- [45] Ransy C., Vaz C., Lombès A., Bouillaud F. Use of H₂O₂ to cause oxidative stress, the catalase issue. *IJMS*, 2020, **21**, 9149.
- [46] He K., Nukada H., Urakami T., Murphy M.P. Antioxidant and pro-oxidant properties of pyrroloquinoline quinone (PQQ): implications for its function in biological systems. *Biochemical Pharmacology*, 2003, **65**, P. 67–74.

Submitted 28 August 2024; accepted 26 September 2024

Information about the authors:

Elizaveta A. Zamyatina – Institute of Theoretical and Experimental Biophysics of the Russian Academy of Sciences, Institutskaya str., 3, Pushchino, 142290, Russia; ORCID 0000-0002-1275-565X; sonyoru162@gmail.com

Olga A. Goryacheva – Saratov State University named after N. G. Chernyshevsky, Chemistry Institute, Astrakhanskaya 83, Saratov, 410012, Russia; ORCID 0000-0002-0910-7694; Olga.goryacheva.93@mail.ru

Nelli R. Popova – Institute of Theoretical and Experimental Biophysics of the Russian Academy of Sciences, Institutskaya str., 3, Pushchino, 142290, Russia; ORCID 0000-0002-0982-6349; nellipopovaran@gmail.com

Conflict of interest: the authors declare no conflict of interest.

Ceramic materials prepared from nanocrystalline InFeZnO_4 powder: optical and mechanical properties, and evaluation of radiation tolerance

Olga N. Kondrat'eva^{1,a}, Maria N. Smirnova^{1,b}, Galina E. Nikiforova^{1,c},
Alexey D. Yapryntsev^{1,d}, Dmitriy F. Kondakov^{1,e}, Leonid D. Yagudin^{2,f}

¹Kurnakov Institute of General and Inorganic Chemistry of the Russian Academy of Sciences, Moscow, 119991, Russia

²Frumkin Institute of Physical Chemistry and Electrochemistry of the Russian Academy of Sciences, Moscow, 119071, Russia

^aol.kondratieva@gmail.com, ^bsmirnovamn@igic.ras.ru, ^cgen@igic.ras.ru,

^dyapryntsev@igic.ras.ru, ^eoldradio@mail.ru, ^fyagudinld@icloud.com

Corresponding author: O. N. Kondrat'eva, ol.kondratieva@gmail.com

PACS 81.07.Wx, 62.20.Qp, 78.20.-e

ABSTRACT A method for low-temperature synthesis of InFeZnO_4 oxide from an X-ray amorphous precursor formed as a result of the thermal decomposition of dehydration product of a mixture of polyvinyl alcohol and iron, indium, and zinc nitrate solutions has been developed. Using TG/DSC and XRD, the InFeZnO_4 phase has been shown to be formed in the temperature range of 370–420°C. Using the XRD method, after the heat treatment of the precursor at 800°C for 4 hours, nanocrystalline InFeZnO_4 with an average particle size (CSR) of ≈ 36 nm has been found to be formed. According to SEM, they do not have a clear facet and form a homogeneous cellular microstructure of the powder. The absence of organic residues and moisture in it has been confirmed by FTIR spectroscopy. From the DRS data, it has been found that the band gap energy E_g of InFeZnO_4 for the cases of indirect and direct transitions is 1.54 eV and 2.25 eV, respectively. Ceramics produced from nanocrystalline InFeZnO_4 by high-temperature sintering have a density equal to 5160 kg/m³ (≈ 86 % of the theoretical one). Their microhardness, measured by the Vickers method, is 2.12 GPa. The radiation resistance of InFeZnO_4 has been predicted, from which it follows that, when exposed to intermediate and high doses of ionizing radiation, its partial amorphization is the most likely.

KEYWORDS Indium-iron-zinc oxide; rhombohedral crystal structure; X-ray amorphous precursor; nanoscale powders; sintering; ceramics; microhardness; band gap energy; radiation tolerance.

FUNDING This study was performed within the ARIADNA Collaboration operating under the NICA facility as a part of State Assignment of the IGIC RAS “Solving topical problems with NICA charged particle beams” (ref. # 1024050300012-6-1.4.2).

ACKNOWLEDGEMENTS The measurements were performed using the equipment of the JRC PMR IGIC RAS. The microhardness studies were carried out using the equipment of the CKP FMI IPCE RAS.

FOR CITATION Kondrat'eva O.N., Smirnova M.N., Nikiforova G.E., Yapryntsev A.D., Kondakov D.F., Yagudin L.D. Ceramic materials prepared from nanocrystalline InFeZnO_4 powder: optical and mechanical properties, and evaluation of radiation tolerance. *Nanosystems: Phys. Chem. Math.*, 2024, **15** (5), 693–701.

1. Introduction

The development of new, technologically simple and economically advantageous methods for the production of highly dispersed oxides $\text{RMO}_3(\text{M}'\text{O})_m$ (where R = Sc, In, Y, or Er–Lu; M = Fe, Ga, or Al; M' = Zn; m = 1, 2, 3 ...), combining high thermal stability and potentially promising functional properties are of great interest both from a fundamental and practical point of view [1–5]. For example, materials based on $\text{InGaO}_3(\text{ZnO})_m$ (m = 1–4), owing to their unique electro- and thermophysical characteristics, have already been applied as components of displays and sensor devices [6–8]. A number of complex iron, indium, and zinc oxides $\text{InFeO}_3(\text{ZnO})_m$ (where m = 1–19) belong to refractory oxides that have been relatively poorly studied. In particular, Kimizuka et al. established [9] that some of these oxides (m = 1, 2, 3, 7, 9, 11, 13, 15 and 19) remain thermally stable when heated up to 1550°C, and continuous exposure to very high temperatures (7 days at 1250°C) does not cause changes in their phase and/or chemical composition. The results of the thermophysical characteristics of ceramic materials $\text{InFeO}_3(\text{ZnO})_m$ (m = 1–5) showed [10] that InFeZnO_4 oxide has the lowest thermal conductivity in this series (≈ 2.8 W/(m·K) at 25°C). Its value is closely equal to the thermal conductivity of thermal barrier materials that are already in use, such as 7-8 wt. % yttria-stabilized zirconium dioxide

(YSZ) ($\approx 3.0 \text{ W/(m}\cdot\text{K)}$ at 25°C [11]). The low thermal conductivity of InFeZnO_4 oxide in combination with a thermal expansion coefficient ($11.7 \times 10^{-6} \text{ K}^{-1}$ [12]), close in magnitude to YSZ ($10.7 \times 10^{-6} \text{ K}^{-1}$ [13]), makes it potentially suitable for creating special thermal barrier coatings used on the surface of structural materials from which parts and nodes of aerospace equipment are produced [12, 14–16]. Moreover, it is noted in [10] that the relatively low hardness and low friction coefficient make InFeZnO_4 promising in terms of creating abrasion-resistant seal coating materials with high thermal insulation. Doping or the introduction of an additional phase into the material [10, 14, 16] as well as the use of nanoscale precursors for its production can be considered as a strategy to improve the functional characteristics of InFeZnO_4 . On the other hand, it is possible to change (and even significantly improve) the performance of a material by exposing it to high pressures or various doses of high-energy ion irradiation. For example, in [17] it is noted that irradiation of magnesium aluminate with Mg^+ ions with an energy of 2.4 MeV and a fluence of $1.4 \times 10^{21} \text{ ions/cm}^2$ results in an increase in its hardness compared with a non-irradiated sample by 5%, and when irradiated with high doses of neutrons [18] it leads to a noticeable decrease in thermal conductivity.

To date, the general method of obtaining InFeZnO_4 ceramic materials is that of solid-phase interaction. Analysis of literature data [9, 10, 12, 19, 20] showed that a mechanical mixture of In_2O_3 , Fe_2O_3 and ZnO oxides which is subjected to prolonged (up to 5 days) multistage annealing at temperatures in the range of $1300\text{--}1550^\circ\text{C}$ is used to produce it. Furthermore, it is reported in some works that InFeZnO_4 synthesized in such a way contains an admixture of $\text{InFeO}_3(\text{ZnO})_2$ [12] or ZnFe_2O_4 [20]. In particular, an approach as an alternative, energy-efficient method for the production of InFeZnO_4 can be used. It includes the stages of obtaining a composition consisting of a polymer (polyvinyl alcohol (PVA), starch, etc.) and aqueous mixtures of nitrates of the corresponding metals, its thermal decomposition, and subsequent annealing of the resulting X-ray amorphous precursor at relatively low temperatures. It was shown in [21, 22] that using this approach, it is possible to synthesize single-phase, nano- and microcrystalline powders of various complex metal oxides at temperatures of $800\text{--}1000^\circ\text{C}$.

This paper presents for the first time the development results of the low-temperature synthesis basics of InFeZnO_4 oxide from a PVA-nitrate composition, and discusses the structural and physical and mechanical characteristics of a ceramic material made on its basis. Taking into account the potential applications of the material in question, the prediction results of radiation-induced changes occurring in its crystal structure at intermediate and high doses of ionizing radiation are also presented. These data may be of interest in determining the limits of applicability of InFeZnO_4 ceramic materials when operated under radiation conditions, and also when their properties are directionally changed by exposure to various doses of ionizing radiation.

2. Experimental part

2.1. Synthesis of InFeZnO_4 powder

The point of the synthesis method of InFeZnO_4 oxide was to prepare a composition containing a polymer and nitrate solutions of the corresponding metals, its evaporation and thermal decomposition, and subsequent annealing of the resulting solid-phase product. Polyvinyl alcohol ($(\text{CH}_2\text{CHOH})_n$, GOST 10779-78) and aqueous solutions of indium, iron, and zinc nitrates were used as initial reagents. Their quantity was calculated using the reaction equation given below:



To prepare aqueous solutions of metal nitrates, nitric acid (high purity grade, 18-4, GOST 11125-84), zinc (grade Z0, $\omega(\text{Zn}) = 99.975 \text{ wt. \%}$, GOST 3640-94), indium (grade In0, $\omega(\text{In}) = 99.998 \text{ wt. \%}$, GOST 10297-94) and carbonyl iron (high purity grade, 13-2, TS 6-09-05808009-262-92) were used. The metals were dissolved in acid previously diluted with distilled water in a ratio of 1 : 3 by volume. Solutions $\text{In}(\text{NO}_3)_3$, $\text{Fe}(\text{NO}_3)_3$ and $\text{Zn}(\text{NO}_3)_2$ were mixed and then concentrated on a heating plate at 90°C . Evaporating a mixture of salt solutions, PVA was added with constant stirring. The resulting gel-like mass (hereinafter referred to as the gel) was continued to be heated on a plate until a voluminous brown powder was obtained. The resulting powder was thoroughly ground and then annealed at temperatures ranging from 600°C to 1200°C . The heat treatment was carried out in air, and its duration at each temperature was at least 4 hours.

2.2. Production of InFeZnO_4 ceramics

Nanocrystalline powder InFeZnO_4 was used to produce dense ceramics. A few drops of acetone were added to it and carefully ground in an agate mortar. Cylindrical samples with a height of $\approx 5 \text{ mm}$ and a diameter of $\approx 14 \text{ mm}$ were formed from the produced mass by cold uniaxial pressing. Sintering of the samples was carried out in air at 1350°C for 4 hours. The density of ceramics after sintering was estimated by its geometric dimensions and mass. The relative density was expressed as a percentage of the XRD density.

2.3. Thermal analysis

Thermogravimetry and differential scanning calorimetry (TG/DSC) were used to study the processes occurring during gel heating and to establish the temperature range in which the formation of the crystalline phase of InFeZnO_4 occurred. The measurements were carried out on a MOM Derivatograph Q-1500D with an upgraded heater control unit and a

registration system. A gel sample weighing 0.1500 g was heated in a platinum crucible in the temperature range of 25–1000°C with a heating rate of 10°C/min. The sensitivity of thermobalance was 200 mg, and its accuracy was $\pm 0.5\%$. The temperature measurement error did not exceed $\pm 3^\circ\text{C}$.

2.4. Phase composition, microstructure and mechanical properties

The structure and phase composition of the synthesized materials before and after their heat treatment were studied using powder X-ray diffraction (XRD). XRD patterns were recorded at ambient temperature on a Bruker D8 Advance powder diffractometer (X-ray tube with copper anode $\lambda(\text{CuK}\alpha) = 1.5418 \text{ \AA}$) equipped with a LynxEye linear detector and a nickel filter. The measurement results were processed using Bruker DIFFRAC.EVA software. Crystal phases were identified using the electronic diffraction database ICDD PDF-2. Scanning electron microscopy (SEM) was used to determine the structural and morphological characteristics of synthesized materials. SEM images were obtained using an ultra-high resolution scanning electron microscope TESCAN AMBER. The ceramics were tested for microhardness using the Vickers method on a LOMO PMT-3M device. The samples were pre-polished and washed in an aqueous alcohol solution under ultrasound. The measurements were carried out at a load of 0.98 N (100 g), the duration of exposure under load was 10 seconds.

2.5. Optical and spectral properties

The change in the moisture content and carbon-containing impurities in the powders with an increase in annealing temperature was controlled using Fourier-transform infrared spectroscopy (FTIR). A Perkin Elmer Spectrum 65 FT-IR spectrometer was used to register FTIR spectra in the 400–4000 cm^{-1} region.

Diffuse reflectance spectroscopy (DRS) data were used to determine the band gap energy E_g of InFeZnO_4 oxide. Diffuse reflectance spectra (R) were obtained using the Ocean Optics modular optical system (QE65000 detector, HPX-2000 xenon source, integrating sphere ISP-80-8-R with a diameter of 80 mm). Measurements were carried out in the wavelength range from 200 to 1000 nm. The Ocean Optics WS-1 standard from polytetrafluoroethylene was used as a reference sample. The E_g value was calculated using the Tauc plot in coordinates $(F(R) \cdot h\nu)^n - h\nu$, where $F(R)$ is the Kubelka–Munk function equal to $(1-R)^2/2R$, h is Planck's constant, ν is the frequency of incident radiation, n is a constant characterizing the type of transition ($n = 1/2$ and $n = 2$ correspond to indirect and direct transitions, respectively).

3. Results and Discussion

3.1. Results of XRD and FTIR studies of synthesized powders

Fig. 1(a) demonstrates XRD patterns of powders before (profile 1) and after (profiles 2–4) solid-phase product annealing formed as a result of heating and thermal decomposition of an initial reagent mixture. A blurred halo can be noted on the XRD pattern of the unannealed sample (profile 1), observed in the existence region of the main diffraction lines of InFeZnO_4 oxide ($2\theta \approx 28\text{--}38^\circ$). Furthermore, the absence of any diffraction maxima indicates the X-ray amorphous nature of the powder in question. Its FTIR spectrum is shown in Fig. 1(b) (spectrum 1). The absorption bands observed in the region of 1600–1700 cm^{-1} can be attributed to deformation vibrations of the –OH bonds of water molecules, while the wide band at 3355 cm^{-1} can be attributed to valence ones [23]. The presence of these bands in the FTIR spectrum of the X-ray amorphous powder allows us to conclude that there is sorption of water vapor on the surface of its particles. The bands located in the region of 1450–1300 cm^{-1} and at 800 cm^{-1} are related to stretching vibrations of N–O bonds and bending vibrations of the NO_3^- group [23–25]. From the FTIR spectrum of the sample annealed at a temperature of 600°C, the intensity of the absorption bands connected with the presence of moisture and organic impurities can be seen to decrease markedly. In addition, wide diffraction peaks appear on the XRD pattern of this powder (Fig. 1(a), profile 2), indicating a high degree of dispersion and imperfection in the crystalline structure of the formed phase.

An increase in the annealing temperature to 800°C leads to that in the intensity of diffraction maxima relating to the InFeZnO_4 phase (Fig. 1(a), profile 3). Moreover, intense absorption bands (478 cm^{-1} and 532 cm^{-1}) appear on the FTIR spectrum of this powder due to vibrations of metal–oxygen bonds. The bands observed above 1000 cm^{-1} (Fig. 1(b), spectrum 3) disappear completely, indicating dehydration of the sample and the absence of carbon-containing residues in it. Fig. 1(b) (spectrum 4) shows that powder annealing at 1000°C has almost no effect on the shape and position of the bands in the FTIR spectrum. In addition, the diffraction maxima become narrower and more intense (Fig. 1(a), profile 4), which indicates the continuous ordering and improvement of the InFeZnO_4 crystal structure.

3.2. Thermal behavior of the gel

In order to establish the temperature range in which the formation of the crystalline phase of InFeZnO_4 occurs, the features of thermal decomposition of the gel prepared by evaporation of an initial reagent mixture are investigated. The results of TG and DSC of the test sample in the range of 25–1000°C are shown in Fig. 2(a,b). Analysis of the thermogram and its first derivative in temperature (DTG) (Fig. 2(a)) shows that the thermal decomposition of the gel occurs in several stages. At the first stage which is observed in the range of 60–267°C, the test sample loses almost half of its mass (46.82%). This process is accompanied by a complex endothermic effect (63–234°C) with a minimum at 144°C (Fig. 2(b)). The significant mass loss appears to have been caused by the removal of moisture, nitrogen oxides, and gaseous

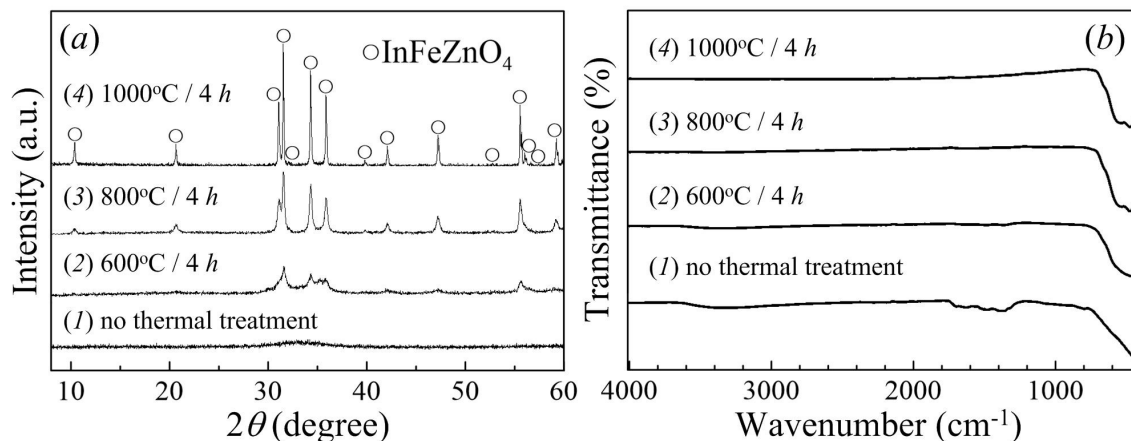


FIG. 1. (a) XRD patterns and (b) FTIR spectra of powders obtained after annealing of a precursor formed as a result of thermal decomposition of the dehydration product of an initial reagent mixture

organic compounds produced as a result of the destruction of organo-inorganic products formed after dehydration of the initial reagent mixture. When there is a further increase in temperature, a less intense exothermic effect appears on the DSC curve ($\approx 370\text{--}420^\circ\text{C}$), having a maximum at 392°C . The mass loss corresponding to this effect occurs in the range of $267\text{--}430^\circ\text{C}$ and is 18.22%. It can be assumed to be related to the continued removal of gaseous decomposition products. Ultrafine particles of InFeZnO_4 begin to form at 370°C alongside with this process. This is supported by the absence of thermal effects above 430°C (Fig. 2(b)) and the results of XRD (Fig. 1(a), profile 2), according to which oxide particles with a CSR size of $\approx 15\text{ nm}$ are formed at temperatures below 600°C . A slight mass loss (2.56%) which completes at a temperature of $\approx 778^\circ\text{C}$ (Fig. 2(a)) is connected with the final removal of carbonaceous residues and surface-adsorbed water, which is confirmed by the results of FTIR spectroscopy (Fig. 1(b), profile 3).

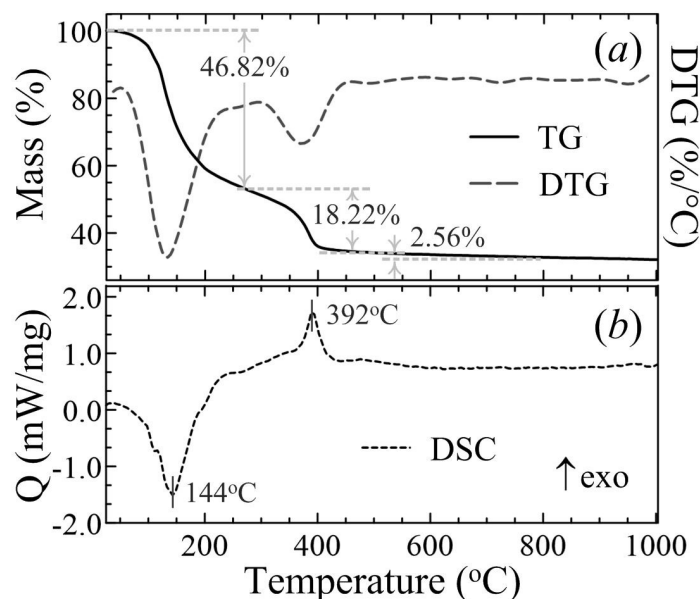


FIG. 2. (a) TG/DTG and (b) DSC curves of the gel

3.3. Microstructural characteristics of InFeZnO_4 powder

SEM images showing the change in the InFeZnO_4 powder microstructure with an increase in the annealing temperature from 800°C to 1200°C are shown in Fig. 3 (a–c). They show that the powder annealed at 800°C for 4 hours (Fig. 3(a)) has a cellular microstructure formed by very small grains without an apparent crystalline cut, which is consistent with XRD data. The average size of the crystalline grain of the InFeZnO_4 phase, which is assumed to be equal to the average size of the CSR, is 36 nm. When the annealing temperature rises to 1000°C , it increases to $\approx 90\text{ nm}$. This correlates with the SEM data (Fig. 3(b)) showing that the grain size of InFeZnO_4 is noticeably enlarged. An increase in the annealing temperature to 1200°C leads to the production of a microcrystalline powder consisting of well-faceted InFeZnO_4 grains

with a size of 2–5 μm (Fig. 3(c)). The XRD pattern of this powder is shown in Fig. 3(d). Its analysis demonstrates that all observed diffraction maxima relate to InFeZnO_4 . The parameters of its unit cell (s.g. R-3m; Z = 3) are: $a = 3.3194(1)$ \AA ; $c = 26.1310(4)$ \AA ; $V = 249.35(1)$ \AA^3 ; $\rho_{XRD} = 5998$ kg/m^3 . Thus, the results of XRD and SEM reveal that an increase in the annealing temperature of the X-ray amorphous powder (Fig. 1(a), profile 1) does not lead to the appearance of secondary phases and is accompanied only by the enlargement of the InFeZnO_4 grains and the improvement of their crystalline faceting.

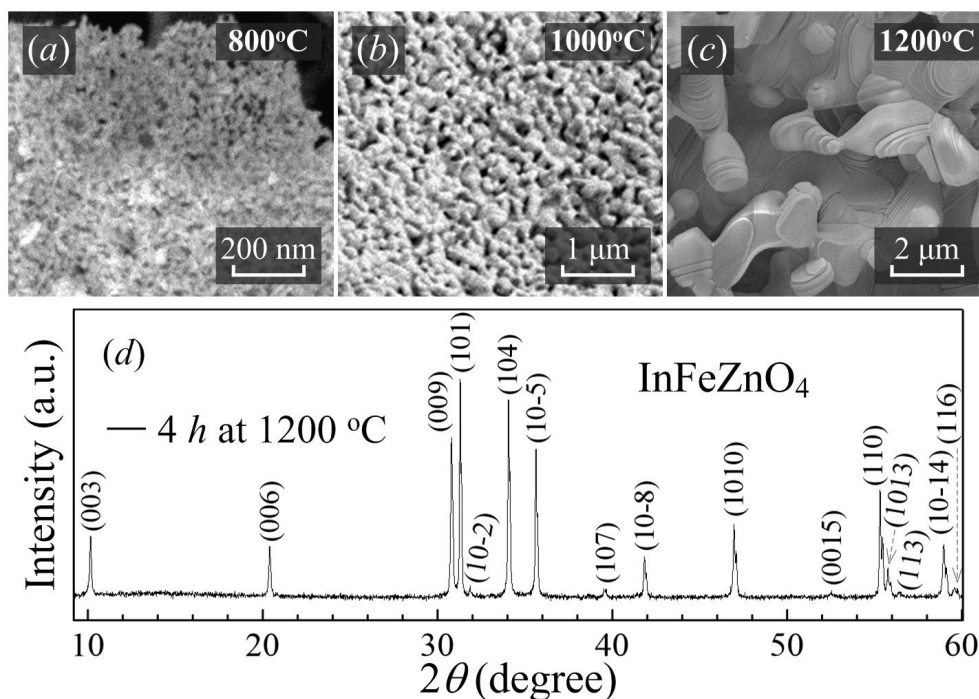


FIG. 3. (a-c) SEM images of InFeZnO_4 powder annealed at temperatures of 800°C, 1000°C and 1200°C for 4 hours in air. (d) XRD pattern of the powder annealed at a temperature of 1200°C

3.4. Structure and mechanical properties of InFeZnO_4 ceramics

It is preferable to use powders with particle sizes varying within a few tens of nanometers for the manufacture of fine-grained and non-porous ceramics. In this regard, a nanocrystalline powder annealed at a temperature of 800°C is used to produce a dense and structurally homogeneous sample of InFeZnO_4 ceramics. A typical image of the ceramics obtained from this powder is shown in Fig. 4(a). It has a uniform dark brown staining, and its surface has no cracks after sintering. SEM images of the cleavage of InFeZnO_4 ceramics at different magnifications are shown in Fig. 4(b,c). The SEM examination also revealed no cracks (Fig. 4(b)), which indicates the correctness of the parameters chosen for the manufacture of ceramics. Fig. 4(c) clearly shows that the ceramic structure is formed by large (up to several tens of micrometers) grains with a layered structure. It can also be noted that single small pores with a diameter of 1–2 microns are visible on the surface of the cleavage, which indicates a quite high density of ceramics. Its density, which is found using the geometric method, is 5160 kg/m^3 , which is $\approx 86\%$ of the theoretically possible one.

The analysis has shown that there are no data on Vickers microhardness for InFeZnO_4 and related oxides in the literature so far. According to the results of testing InFeZnO_4 ceramics for microhardness using the Vickers method, the average value of its microhardness number is found to be 216.3 ± 35.0 (2.12 ± 0.34 GPa). To evaluate the hardness class of InFeZnO_4 , the ratio proposed by Khrushchev [26] was used (Eq. (1)):

$$H_0 = 0.675 \times H^{1/3},$$

where H_0 is the hardness class on a 15–point scale, in which graphite corresponds to 1 and diamond to 15; H is the experimental value of the microhardness number, expressed in kgf/mm^2 . According to the results of calculation using Eq. (1), the hardness class of InFeZnO_4 ceramics on the Khrushchev scale is 4.1, which is comparable in magnitude to H_0 for such minerals as zincite and sphalerite (3.6–4.6) [27]. In terms of classification of minerals and synthetic materials by their hardness numbers [27], InFeZnO_4 can be attributed to materials of medium hardness (1.18–5.40 GPa).

3.5. Calculation of the band gap energy of InFeZnO_4

To date, the optical properties of InFeZnO_4 have not been extensively studied. Narendranath et al. [20] determined the band gap of this oxide from the DRS data under the assumption of an indirect transition ($E_g = 2.85$ eV). However, the

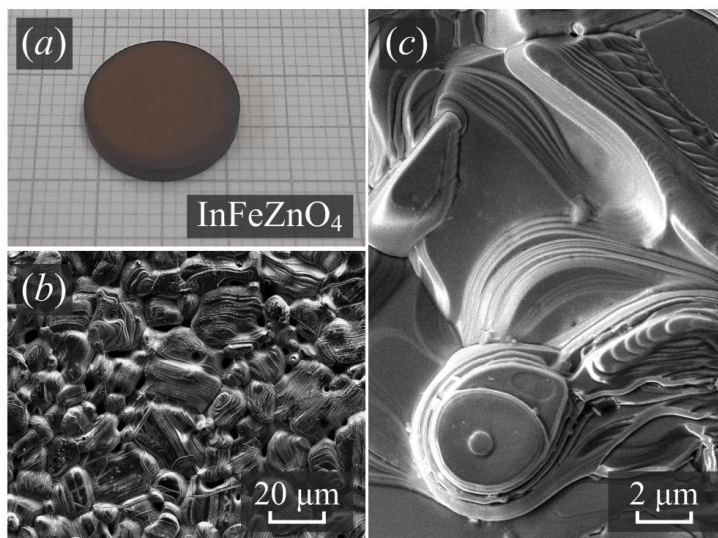


FIG. 4. (a) Digital image of InFeZnO_4 ceramics sintered at a temperature of 1350°C for 4 hours in air. (b, c) SEM images of the cleavage surface obtained at different magnifications

spectrum obtained by the authors contains many bands that can be attributed to both direct and indirect transitions [28]. On the other hand, when determining the E_g value of the isostructural oxides InGaZnO_4 [3] and InGaMgO_4 [29], the analysis was conducted under the assumption of direct transitions, though this choice was not discussed by the authors. Since there is no information about the type of optical transitions in InFeZnO_4 , the data that we obtained from the DRS (Fig. 5(a)) are presented in Tauc plot both under the assumption of direct and indirect transitions (Fig. 5(b)). For both cases, the band gap energy was found by extrapolating the linear section of the graph of the dependence $(F(R)\cdot h\nu)^n$ from $h\nu$ to the abscissa axis. The value of E_g InFeZnO_4 under the assumption of an indirect transition ($n = 1/2$) is 1.54 ± 0.01 eV, and for a direct transition ($n = 2$) it is 2.25 ± 0.01 eV. Both values obtained turn out to be noticeably lower compared to the previously published one in [20]. The reason for this discrepancy is not obvious, however, it can be assumed that the difference in E_g values is due to the fact that InFeZnO_4 samples obtained by different synthesis methods differ in their phase composition, as well as in the degree of dispersion and structural defects. The InFeZnO_4 sample obtained by solid-phase synthesis has a larger particle size compared to that synthesized in this work. Additionally, Narendranath et al. [20] note the presence of ZnFe_2O_4 impurity, which is not observed in our case.

3.6. Evaluation of InFeZnO_4 radiation resistance

Further, we will consider several criteria that allow us to draw a conclusion about the ability of the material to resist ionizing radiation. Structural changes occurring in a solid when exposed to intermediate ($\sim 10^{13} - 10^{16}$ ions/cm²) and high ($\geq 10^{17}$ ions/cm²) doses of high-energy ion irradiation can be reliably predicted using the criteria proposed by Naguib and Kelly [30]. The first of them is that the amorphization of a crystalline solid must occur if the ratio of its crystallization temperature (T_C) to the melting temperature (T_m) exceeds 0.30. The second criterion is based on the fact that the amorphization is most likely if the ionicity of the compound is $f \leq 0.47$. Moreover, compounds with f values in the range from 0.47 to 0.60 may be capable of both amorphization and preservation of their crystal structure under irradiation. The melting point of InFeZnO_4 is unknown, but the authors [9] established that this compound is thermally stable when heated to 1550°C . Therefore, in a rough approximation, this temperature can be assumed to be equal to the melting point. The temperature of the onset of crystallization of InFeZnO_4 , estimated from the DSC data (Fig. 2(b)), is approximately 370°C . The calculated value of the T_C/T_m ratio for the oxide studied is $\approx 0.33 > 0.30$, which indicates the possibility of its amorphization under irradiation. The ionicity of InFeZnO_4 is estimated by the Pauling equation using the electronegativity values of atoms from [31]. According to the calculation results, the ionicity is 0.528. The value obtained falls within the range between 0.47 and 0.60, which does not allow us to draw an unambiguous conclusion about the structural changes that can occur in InFeZnO_4 under irradiation. It can be noted that zinc ferrite ZnFe_2O_4 has the closest f value (0.535) to InFeZnO_4 . Satalkar et al. demonstrated [32] that as a result of irradiation of nanocrystalline ZnFe_2O_4 with $^{16}\text{O}^{6+}$ ions with an energy of 80 MeV and fluence up to 2×10^{14} ions/cm², only a slight increase in the volume of the unit cell (up to 0.64%) and a change in the degree of cationic disordering can be observed. The formation of other phases (crystalline or amorphous) has not been detected [32]. Furthermore, irradiation of a ceramic spinel sample with heavy Xe ions with an energy of the order of several GeV and a fluence of 6×10^{11} ions/cm² results in the formation of amorphous latent tracks [33]. Therefore, it can be concluded that their formation is expected in the case of InFeZnO_4 . Moreover, this oxide can also be assumed to have a higher radiation resistance in the nanocrystalline state. Taking into account the

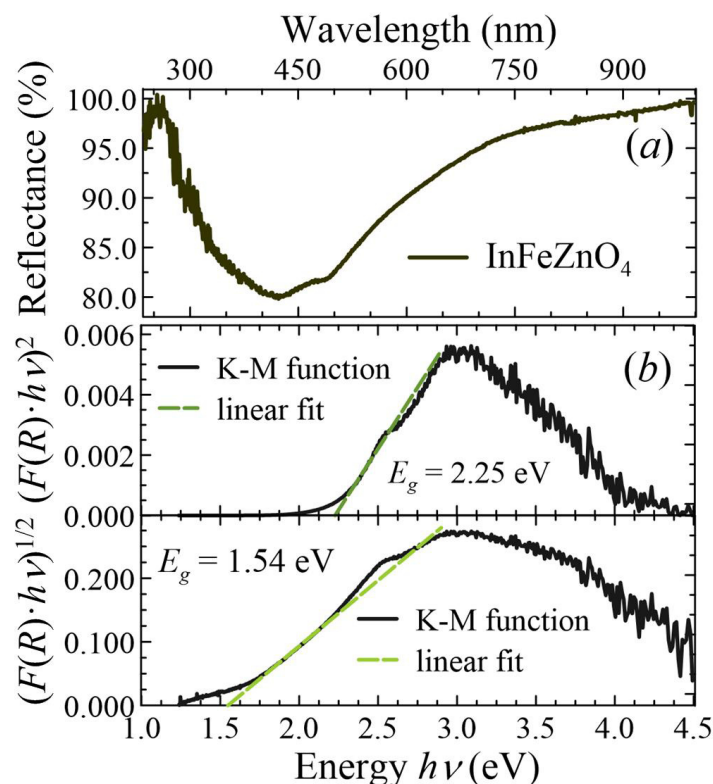


FIG. 5. (a) The diffuse reflectance spectrum of InFeZnO_4 and (b) its representation in Tauc coordinates for the case of indirect ($n = 1/2$) and direct ($n = 2$) transitions

promising thermophysical and mechanical properties of InFeZnO_4 , it can be summed up that nanoscale materials on its base may be suitable for use as radiation-resistant protective coatings with special thermal properties.

4. Conclusions

In this paper, the experimental results on the production of InFeZnO_4 oxide from an X-ray amorphous powder formed during the thermal decomposition of dehydration products of a PVA mixture and metal nitrate solutions are considered. The results of thermal analysis (TG/DSC) of the gel allow us to conclude that the ultrafine phase of InFeZnO_4 is formed in the range of 370–420°C. It is found by XRD that the solid decomposition products are in an X-ray amorphous state, and their annealing at temperatures of 600–800°C gives rise to the formation of a single-phase nanocrystalline powder InFeZnO_4 with a particle size of 15–36 nm. According to SEM data, the powder annealed at 800°C has a homogeneous, cellular microstructure formed by very small and poorly faceted grains, which correlates with the results of X-ray diffraction analysis. The absence of moisture and organic residues in it is confirmed by FTIR spectroscopy. InFeZnO_4 microcrystalline ceramic materials were produced using this powder. Their relative density after sintering at a temperature of 1350°C for 4 hours in air is 86% of the theoretical one. SEM studies have shown that a homogeneous and dense ceramic structure consisting of grains > 10 microns in size are obtained as a result of sintering. The microhardness of InFeZnO_4 ceramics, measured by the Vickers method, is 2.12 GPa. The result obtained makes it possible to classify the manufactured ceramics as materials with medium hardness. According to DRS data, it is revealed that the E_g value of InFeZnO_4 oxide, assuming indirect band transitions, is 1.54 eV, and for direct band transitions it is 2.25 eV. In order to predict structural changes that occur under ionizing radiation, criteria are also calculated, which allowed for the ionicity f of InFeZnO_4 and the ratio of its crystallization and melting temperatures (T_C/T_m). Analysis of the calculated values of f and T_C/T_m allows us to conclude that irradiation of this material with intermediate or high doses of high-energy ions is most likely to result in its partial amorphization. These preliminary conclusions can be taken into account while conducting experiments aimed at changing the functional properties of InFeZnO_4 by high-energy ion irradiation, as well as in the manufacture of coating materials and devices exposed to ionizing radiation, including cosmic radiation.

References

- [1] Kimizuka N., Takayama-Muromachi E., Siratori K. The systems $\text{R}_2\text{O}_3\text{--M}_2\text{O}_3\text{--M/O}$: R is In, Sc, Y or one of the lanthanides, M is Fe, Ga, or Al, and M' is one of the divalent cation elements. *Handbook on the Physics and Chemistry of Rare Earths*, 1990, **13**, P. 283–384.
- [2] Grajczyk R., Subramanian M.A. Structure–property relationships of YbFe_2O_4 - and $\text{Yb}_2\text{Fe}_3\text{O}_7$ -type layered oxides: A bird's eye view. *Progress in Solid State Chemistry*, 2015, **43**(1–2), P. 37–46.

- [3] Préaud S., Byl C., Brisset F., Berardan D. SPS-assisted synthesis of $\text{InGaO}_3(\text{ZnO})_m$ ceramics, and influence of m on the band gap and the thermal conductivity. *Journal of the American Ceramic Society*, 2020, **103**(5), P. 3030–3038.
- [4] Zhang C., Pei Y., Zhao L.-D., Berardan D., Dragoe N., Gong S., Guo H., The phase stability and thermophysical properties of $\text{InFeO}_3(\text{ZnO})_m$ ($m = 2, 3, 4, 5$). *Journal of the European Ceramic Society*, 2014, **34**(1), P. 63–68.
- [5] Katayose S., Miyazaki T., Hayashi Y., Takizawa H. Synthesis of natural superlattice structure in the binary $\text{ZnO}-\text{Fe}_2\text{O}_3$ system by microwave irradiation. *Journal of the Ceramic Society of Japan*, 2010, **118**(1377), P. 387–389.
- [6] Kimizuka N., Yamazaki S. *Physics and Technology of Crystalline Oxide Semiconductor CAAC-IGZO: Fundamentals (Wiley Series in Display Technology)*. John Wiley & Sons, Ltd., 2016, 352 p.
- [7] Costa J.C., Pouryazdan A., Panidi J., Spina F., Anthopoulos T.D., Liedke M.O., Schneider C., Wagner A., Münzenrieder N. Flexible IGZO TFTs and their suitability for space applications. *IEEE Journal of the Electron Devices Society*, 2019, **7**, P. 1182–1190.
- [8] InGaZnO (IGZO) System For Gas Detection at Room Temperature. United States Patent US 20220365022 A1. United States Patent and Trademark Office. Vijjapu M.T., 11 p.
- [9] Kimizuka N., Isobe M., Nakamura M., Mohri T. Syntheses and crystallographic data of the homologous compounds $\text{InFeO}_3(\text{ZnO})_m$ ($m = 1, 2, 3, 7, 11, 13, 15$, and 19) and $\text{Fe}_2\text{O}_3(\text{ZnO})_m$ ($m = 8$ and 9) in the $\text{In}_2\text{O}_3-\text{ZnFe}_2\text{O}_4-\text{ZnO}$ system. *Journal of Solid State Chemistry*, 1993, **103**(2), P. 394–402.
- [10] Qu W.-W., Zhang X.-X., Yuan B.-F., Zhao L.-D. Homologous layered $\text{InFeO}_3(\text{ZnO})_m$: new promising abradable seal coating materials. *Rare Metals*, 2018, **37**, P. 79–94.
- [11] Wu J., Wei X., Pature N.P., Klemens P.G., Gell M., Garcia E., Miranzo P., Osendi M.I. Low-thermal-conductivity rare-earth zirconates for potential thermal-barrier-coating applications. *Journal of the American Ceramic Society*, 2002, **85**(12), P. 3031–3035.
- [12] Zhao L.-D., Pei Y.-L., Liu Y., Berardan D., Dragoe N. InFeZnO_4 as promising thermal barrier coatings. *Journal of the American Ceramic Society*, 2011, **94**(6), P. 1664–1666.
- [13] Pan W., Phillpot S.R., Wan C., Chernatynskiy A., Qu Z. Low thermal conductivity oxides. *MRS Bulletin*, 2012, **37**, P. 917–922.
- [14] Guo H., Zhang C., Pei Y., Guo L., Gong S. Improved thermal barrier properties of InFeZnO_4 ceramics by Gd/Yb doping. *Journal of Alloys and Compounds*, 2014, **585**, P. 404–406.
- [15] Zhang L., Pei Y., Guo H., Gong S. Thermal transport properties of $\text{InFeZnO}_4-\text{YbFeZnO}_4$ solid solutions. *Journal of Alloys and Compounds*, 2015, **623**, P. 203–208.
- [16] Zhao B., Pei Y., Zhang L., Gong S., Zhao L.-D. Thermal and mechanical properties of Yb&Mg co-doped InFeZnO_4 . *Journal of Alloys and Compounds*, 2016, **684**, P. 34–39.
- [17] Zinkle S.J. Hardness and depth-dependent microstructure of ion-irradiated magnesium aluminate spinel. *Journal of the American Ceramic Society*, 1989, **72**(8), P. 1343–1351.
- [18] Fukushima Y., Yano T., Maruyama T. Swelling, thermal diffusivity and microstructural investigation of neutron irradiated single crystals of nonstoichiometric spinel. *Journal of Nuclear Materials*, 1990, **175**(3), P. 203–208.
- [19] Kimizuka N., Mohri T., Matsui Y. Homologous Compounds, $\text{InFeO}_3(\text{ZnO})_m$ ($m = 1-9$). *Journal of Solid State Chemistry*, 1988, **74**(1), P. 98–109.
- [20] Narendranath S.B., Kumar Yadav A., Bhattacharyya D., Nath Jha S., Nandini Devi R. Photocatalytic H_2 evolution from water-methanol system by anisotropic $\text{InFeO}_3(\text{ZnO})_m$ oxides without cocatalyst in visible light. *ACS Applied Materials & Interfaces*, 2014, **6**(15), P. 12321–12327.
- [21] Smirnova M.N., Kondrat'eva O.N., Nikiforova G.E., Khoroshilov A.V. A new approach to prepare LuFeMgO_4 . *Russian Journal of Inorganic Chemistry*, 2023, **68**, P. 507–514.
- [22] Smirnova M.N., Kondrat'eva O.N., Nikiforova G.E., Yapryntsev A.D., Averin A.A., Khoroshilov A.V. Features of synthesis of InGaMgO_4 from nitrate-organic precursors and study of its physical properties. *Russian Journal of Inorganic Chemistry*, 2024, (in press).
- [23] Larkin P.J. *Infrared and Raman Spectroscopy: Principles and Spectral Interpretation*. Elsevier, 2011, 230 p.
- [24] Jain D., Sudarsan V., Patra A.K., Sastry P.U., Tyagi A.K. Effect of local ordering around Th^{4+} ions in glycine-nitrate precursor gel on the powder characteristic of gel-combusted ThO_2 . *Journal of Nuclear Materials*, 2019, **527**, P. 151826.
- [25] Warriar A.V.R., Narayanan P.S. Infrared absorption spectra of single crystals of glycine silver nitrate and monoglycine nitrate. *Proceedings of the Indian Academy of Sciences – Section A*. 1967, **66**, P. 46–54.
- [26] Khrushchev M.M. *Trenie, iznos i mikrotverdost' materialov: Izbrannye raboty (k 120-letiyu so dnya rozhdeniya)*. KRASAND, Moskva, 2012, 512 p.
- [27] Lebedeva S.I. *Opreделение mikrotverdosti mineralov*. Izdatel'stvo akademii nauk SSSR, Moskva, 1963, 124 p.
- [28] Andrade P.H.M., Volkringer C., Loiseau T., Tejeda A., Hureau M., Moissette A. Band gap analysis in MOF materials: Distinguishing direct and indirect transitions using UV-vis spectroscopy. *Applied Materials Today*. 2024, **37**, P. 102094.
- [29] Meng X., Wang Z., Qiu K., Li Y., Liu J., Wang Z., Liu S., Li X., Yang Z., Li P. Design of a novel near-infrared phosphor by controlling cationic coordination environment. *Crystal Growth & Design*, 2018, **18**(8), P. 4691–4700.
- [30] Naguib H.M., Kelly R. Criteria for bombardment-induced structural changes in non-metallic solids. *Radiation Effects*, 1975, **25** (1), P. 1–12.
- [31] Batsanov S.S. The concept of electronegativity. Conclusions and prospects. *Russian Chemical Reviews*, 1968, **37**(5), P. 332–351.
- [32] Satalkar M., Kane S.N., Kulriya P.K., Avasthi D.K. Swift heavy ion irradiated spinel ferrite: A cheap radiation resistant material. *Nuclear Instruments and Methods in Physics Research Section B: Beam Interactions with Materials and Atoms*, 2016, **379**, P. 235–241.
- [33] Studer F., Houpert Ch., Groult D., Yun Fan J., Meftah A., Toulemonde M. Spontaneous magnetization induced in the spinel ZnFe_2O_4 by heavy ion irradiation in the electronic stopping power regime. *Nuclear Instruments and Methods in Physics Research Section B: Beam Interactions with Materials and Atoms*, 1993, **82**(1), P. 91–102.

Submitted 11 October 2024; accepted 15 October 2024

Information about the authors:

Olga N. Kondrat'eva – Kurnakov Institute of General and Inorganic Chemistry of the Russian Academy of Sciences, Leninskii prosp., 31, Moscow, 119991, Russia; ORCID 0000-0003-2508-9868; ol.kondratieva@gmail.com

Maria N. Smirnova – Kurnakov Institute of General and Inorganic Chemistry of the Russian Academy of Sciences, Leninskii prosp., 31, Moscow, 119991, Russia; ORCID 0000-0003-2707-7975; smirnovamn@igic.ras.ru

Galina E. Nikiforova – Kurnakov Institute of General and Inorganic Chemistry of the Russian Academy of Sciences, Leninskii prosp., 31, Moscow, 119991, Russia; ORCID 0000-0002-2892-6054; gen@igic.ras.ru

Alexey D. Yaprntsev – Kurnakov Institute of General and Inorganic Chemistry of the Russian Academy of Sciences, Leninskii prosp., 31, Moscow, 119991, Russia; ORCID 0000-0001-8166-2476; yaprntsev@igic.ras.ru

Dmitriy F. Kondakov – Kurnakov Institute of General and Inorganic Chemistry of the Russian Academy of Sciences, Leninskii prosp., 31, Moscow, 119991, Russia; ORCID 0000-0001-8636-5462; oldradio@mail.ru

Leonid D. Yagudin – Frumkin Institute of Physical Chemistry and Electrochemistry of the Russian Academy of Sciences Leninskii prosp., 31.4, Moscow, 119071, Russia; yagudinld@icloud.com

Conflict of interest: the authors declare no conflict of interest.

Highly dispersed anti-Stokes phosphors based on KGd₂F₇:Yb,Er single-phase solid solutions

Anna S. Zakharova^{1,2,3}, Sergey V. Kuznetsov², Alexander A. Alexandrov^{1,2}, Daria V. Pominova², Valery V. Voronov², Pavel P. Fedorov², Vladimir K. Ivanov¹

¹Kurnakov Institute of General and Inorganic Chemistry of the Russian Academy of Sciences, Moscow, Russia

²Prokhorov General Physics Institute of the Russian Academy of Sciences, Moscow, Russia

³National Research University Higher School of Economics, Moscow, Russia

Corresponding author: Anna S. Zakharova, AnyaZakharova2606@mail.ru

PACS 61.46 Df

ABSTRACT The possibility of doping the KGd₂F₇ matrix with ytterbium and erbium ions by introducing yttrium ions with a concentration of 25 mol.% was confirmed and the conditions were determined for the synthesis of anti-Stokes phosphors based on single-phase KGd₂F₇:Yb,Er solid solutions. The dependences were revealed of the sizes of coherent scattering regions, crystal lattice parameters, and energy yield of luminescence on the temperature and duration of heat treatment. Heat treatment conditions were determined to ensure the achievement of intense anti-Stokes luminescence. As a result, effective phosphors KGd₂F₇:Yb (20.0 mol.%),Er (4.0 mol.%) with an energy yield of up-conversion luminescence of 3.80 % were developed. Disordering of the crystal structure (transition from cubic to tetragonal modification) at a temperature of 600 °C was recorded, corresponding to the rule of Ostwald steps.

KEYWORDS inorganic fluorides, anti-Stokes luminescence, KGd₂F₇, co-precipitation technique, ytterbium, erbium

ACKNOWLEDGEMENTS The study was supported by the Russian Science Foundation (grant No. 22-13-00167). The analysis of the composition, structure and properties of the materials obtained was carried out using the equipment of the JRC PMR IGIC RAS.

FOR CITATION Zakharova A.S., Kuznetsov S.V., Alexandrov A.A., Pominova D.V., Voronov V.V., Fedorov P.P., Ivanov V.K. Highly dispersed anti-Stokes phosphors based on KGd₂F₇:Yb,Er single-phase solid solutions. *Nanosystems: Phys. Chem. Math.*, 2024, **15** (5), 702–709.

1. Introduction

Anti-Stokes phosphors based on fluoride matrices doped with lanthanide ions, due to a combination of unique optical properties, are widely used for the anti-counterfeiting labels [1–7], increasing the efficiency of solar panels [8–11], bioimaging [12–15], and *in vivo* nanothermometry [16–21], sorting of plastic waste [22, 23], etc. Currently, the most widely studied matrices are based on β -NaYF₄ [12, 24–28], β -NaGdF₄ [2, 29, 30], SrF₂ [21, 31–34] and BaF₂ [35]. Solid solutions in the KF–GdF₃ system have been poorly studied [36], but interest in them is due to the fact that matrices based on this system are characterized by lower phonon energy compared to other fluorides, which can lead to an increase in the luminescence quantum yield. One of the key factors determining the efficiency of anti-Stokes luminescence is the size of the coherent scattering regions [29, 30], since it determines the surface/internal volume ratio of crystallites. As a rule, an increase in particle size helps to increase the luminescence intensity. In addition, the effect of the perfection of phosphor particles on the luminescence light output was noted, which manifests itself in the magnitude of microstrains [37]. Thus, optimization of synthesis conditions, including temperature and duration of heat treatment, is an important task to achieve maximum efficiency of anti-Stokes phosphors.

In the present article, we report the results of the investigation of the conditions for the synthesis of anti-Stokes KGd₂F₇:Yb,Er phosphors with a high energy yield and confirm the possibility of doping the KGd₂F₇ matrix with ions of rare earth elements of the yttrium subgroup with a molar concentration of up to 25 %.

2. Materials and methods

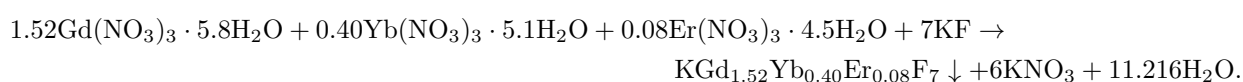
The starting materials were: Gd(NO₃)₃·6H₂O (99.99 mass %, Lanhit), Y(NO₃)₃·6H₂O (99.99 mass %, Lanhit), Yb(NO₃)₃·6H₂O (99.99 mass %, Lanhit), Er(NO₃)₃·5H₂O (99.99 mass %, Lanhit), KF·2H₂O (pure grade, Chemical plant of fluorine salts, Russia), CH₃CH(OH)CH₃ (extra-pure grade, Chimmed) and bidistilled water. The content of crystalline hydrate water in rare-earth elements (REE) nitrates was determined using thermogravimetric analysis, calcining

the initial crystalline hydrates of nitrates of rare earth elements to 1000 °C. Based on the results of the analysis, the content of crystalline hydrate water in nitrates was determined: $\text{Gd}(\text{NO}_3)_3 \cdot 5.8\text{H}_2\text{O}$, $\text{Y}(\text{NO}_3)_3 \cdot 10.7\text{H}_2\text{O}$, $\text{Yb}(\text{NO}_3)_3 \cdot 5.1\text{H}_2\text{O}$, $\text{Er}(\text{NO}_3)_3 \cdot 4.5\text{H}_2\text{O}$. A series of syntheses of a solid solution of the composition $\text{K}(\text{Y}_x\text{Gd}_{1-x})_2\text{F}_7$ was carried out according to the reaction:



REE nitrates were dissolved in 280 ml of bidistilled water to a concentration of 0.08 M and placed in one 500 ml polypropylene reactor. In the second reactor, potassium fluoride was dissolved in 40 ml of bidistilled water, taken with a 25 % excess in comparison with stoichiometry and a molar concentration of 16.4 M, which was added dropwise to the solutions of rare earth nitrates. The resulting suspension was stirred at room temperature on a magnetic stirrer for 2 hours, followed by decantation of the mother liquor. The precipitate was washed twice to remove unreacted salts with a 9:1 mixture of isopropyl alcohol and bidistilled water. The absence of nitrate ions was confirmed by a qualitative reaction with a 1 % solution of diphenylamine in concentrated sulfuric acid. The precipitate was dried at 45 °C. The mass yield of the reaction was 89 %.

The $\text{KGd}_2\text{F}_7\text{:Yb}(20.0 \text{ mol.}\%),\text{Er}(4.0 \text{ mol.}\%)$ phosphors were obtained according to the reaction:



The synthesis technique is similar to the technique used to synthesize $\text{K}(\text{Y}_x\text{Gd}_{1-x})_2\text{F}_7$ solid solutions.

3. Experimental section

The X-ray diffraction patterns were carried out on a Bruker D8 Advance diffractometer with $\text{CuK}\alpha$ radiation. The lattice parameters were calculated using the Topas 4.2 software. The sizes of coherent scattering regions were calculated using the DIFFRAC.EVA V2.1 software. Microphotographs were taken on an Amber GMH scanning electron microscope (Tescan, Czech Republic) at an accelerating voltage of 1 kV using a secondary electron detector. To determine the chemical composition of the samples, an Oxford Instruments X-MAX detector with an accelerating voltage of 20 kV was used. The average diameter of the agglomerates was determined in the ImageJ 1.52a program based on 100 particles. Heat treatment temperatures were selected based on differential scanning calorimetry (Netzsch STA 449 F3 Jupiter, Germany) and thermogravimetric analysis (MOM Q-1500 D). The energy yield (EY, %) of anti-Stokes luminescence was determined using a LESA-01 fiber-optic spectrometer (BIOSPEC, Russia) using an integrating sphere (Avantes, the Netherlands). The error in determining the energy yield of anti-Stokes luminescence was 0.02 %.

4. Results and discussion

When producing phosphors, the practically important concentration of the dopant is the doping of rare earth elements up to 25 mol.%, since a further increase leads to concentration quenching and to the multiphase nature of the sample. The use of yttrium makes it possible to simulate any doping of rare earth elements with the yttrium subgroup. In order to confirm the possibility of doping the KGd_2F_7 matrix with ytterbium and erbium ions with concentrations of 20 and 4 mol.%, respectively, a solid solution was synthesized with the nominal composition $\text{KGd}_{1.5}\text{Y}_{0.5}\text{F}_7$. The X-ray diffraction pattern of the synthesized sample is presented in Fig. 1, the results of calculation of the lattice parameters are given in Table 1. When using a stoichiometric amount of KF for the synthesis of a solid solution (Fig. 1a), two-phase samples are formed: a phase based on $\text{KGd}_{1.5}\text{Y}_{0.5}\text{F}_7$ and GdF_3 . The formation of GdF_3 is associated with the leaching of potassium by water [38]. The lattice parameters are close to the data on the JCPDS card #00-057-0574 for KGd_2F_7 . To prevent potassium leaching, a 25 mol.% excess of KF was used in subsequent syntheses (Fig. 1b), resulting in single-phase samples.

Micrographs of $\text{KY}_{0.5}\text{Gd}_{1.5}\text{F}_7$ sample show spherical agglomerates (Fig. 2a) with an average particle size of 152 nm (Fig. 2b). According to EDX, the sample contains a slightly elevated content of gadolinium ($\text{KY}_{0.47}\text{Gd}_{1.53}\text{F}_7$), which, however, is within the error limits of the chosen method for determining the chemical composition.

As a result, a procedure was determined for the synthesis of single-phase solid solutions $\text{KY}_x\text{Gd}_{1-x}\text{F}_7$, in which the concentration of the doping component was 25 mol.%, which proves the possibility of doping the matrix with ytterbium (20 mol.%) and erbium (4 mol.%) ions.

After confirming the possibility of doping the KGd_2F_7 matrix with yttrium ions with a concentration of 25 mol.%, the single-phase anti-Stokes $\text{KGd}_2\text{F}_7\text{:Yb}(20.0 \text{ mol.}\%),\text{Er}(4.0 \text{ mol.}\%)$ phosphors were synthesized. Since the synthesis was carried out from the aqueous phase, special attention was paid to determining the heat treatment regimes that ensure the removal of physically and chemically bound water. The presence of water and hydroxyl ions leads to quenching of luminescence [43, 44]. According to differential scanning calorimetry and thermogravimetry, smooth weight loss ($\Delta = 0.09 \text{ wt.}\%$) occurs in steps and ends at a temperature of 340 °C (Fig. 3). An exothermic peak is observed on the DSC curve at a temperature of 600 °C, probably corresponding to a phase transition.

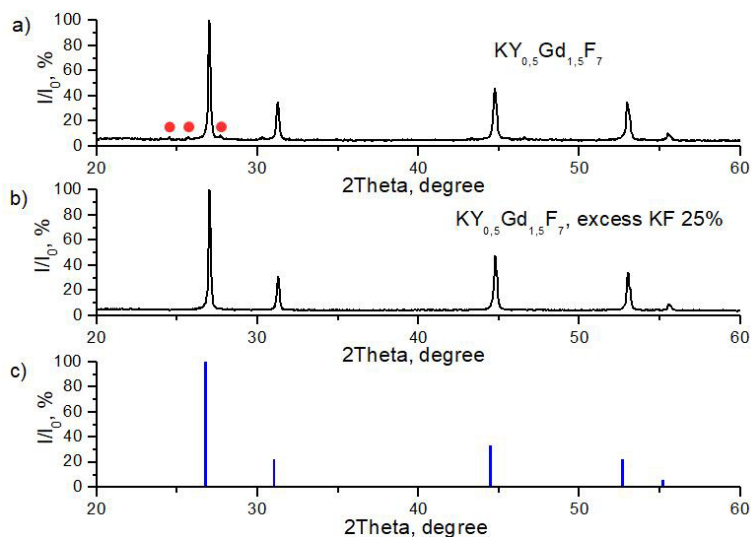


FIG. 1. X-ray diffraction patterns of samples of $\text{KY}_{0.5}\text{Gd}_{1.5}\text{F}_7$ solid solutions: a – $\text{KY}_{0.5}\text{Gd}_{1.5}\text{F}_7$ with a stoichiometric amount of KF; b – $\text{KY}_{0.5}\text{Gd}_{1.5}\text{F}_7$ with a 25 % excess of KF; c – card JCPDS#00-057-0574, corresponding to the KGd_2F_7 phase. The red dot marks the reflections of the GdF_3 phase

TABLE 1. Crystal lattice parameters of $\text{KY}_{0.5}\text{Gd}_{1.5}\text{F}_7$ samples prepared at different potassium fluoride concentrations

Sample code in Fig. 1	Composition	Lattice parameters, Å		Amount of KF
		$\text{K}(\text{Y}_x\text{Gd}_{1-x})_2\text{F}_7$	GdF_3	
a	$\text{KY}_{0.5}\text{Gd}_{1.5}\text{F}_7$	$a = 5.7366(2)$	$a = 6.6513(91)$ $b = 6.9696(51)$ $c = 4.3790(37)$	Stoichiometric amount of KF
b	$\text{KY}_{0.5}\text{Gd}_{1.5}\text{F}_7$	$a = 5.7337(1)$		25 % Excess of KF
c	KGd_2F_7 JCPDS #00-057-0574	$a = 5.762(2)$		

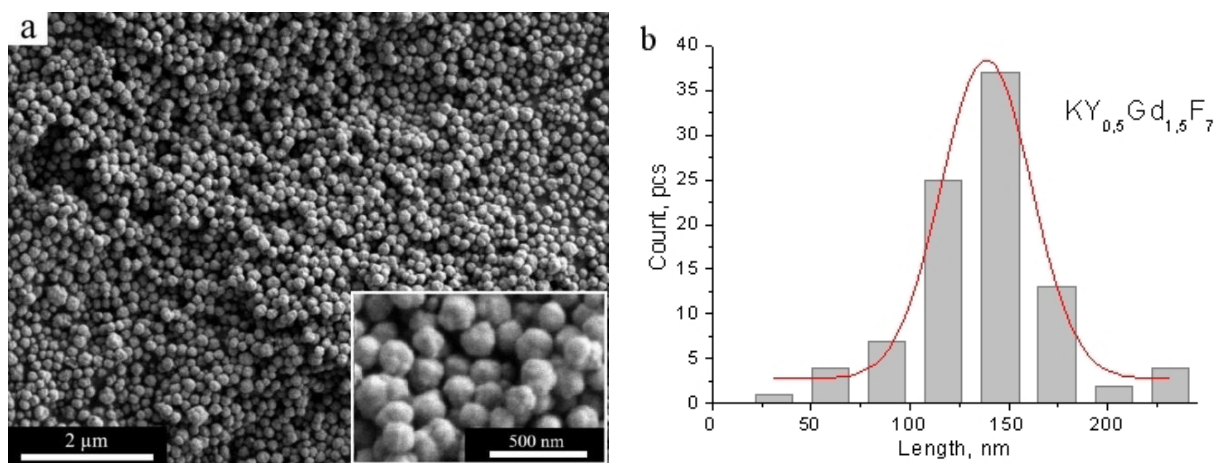


FIG. 2. SEM micrographs (a) and particle size distribution (b) for the sample of $\text{KY}_{0.5}\text{Gd}_{1.5}\text{F}_7$

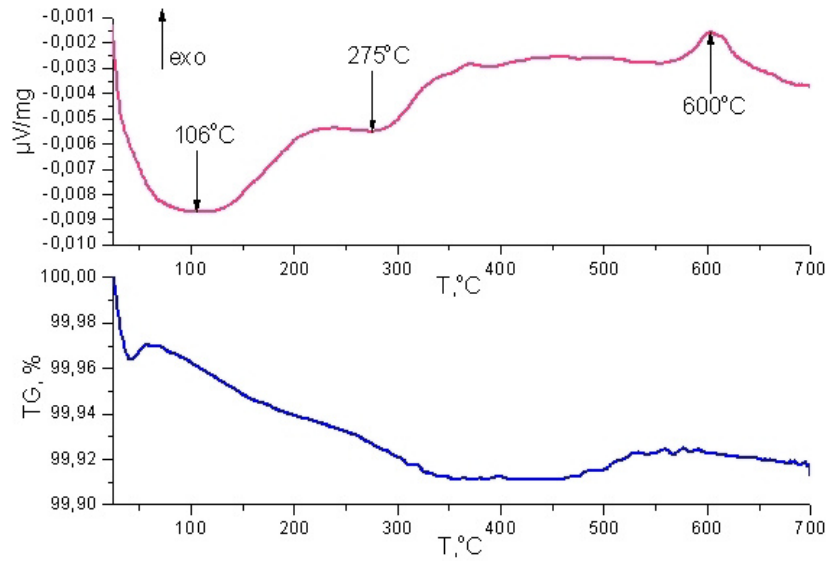


FIG. 3. DSC-TG data for the $\text{KGd}_2\text{F}_7:\text{Yb,Er}$ sample

To identify the nature of the exothermic effect at 600°C and determine the heat treatment temperature that ensures the production of the most effective phosphors of the composition $\text{KGd}_2\text{F}_7:\text{Yb}(20 \text{ mol.}\%), \text{Er}(4 \text{ mol.}\%)$, and taking into account papers [33, 38], we selected the temperatures 500 and 600°C . The heat treatment of anti-Stokes phosphors was carried out using two methods. In the first case, when the specified temperature was reached, the sample was immediately removed from the oven. In the second case, it was kept at this temperature for 4 hours.

X-ray diffraction patterns of $\text{KGd}_2\text{F}_7:\text{Yb}(20 \text{ mol.}\%), \text{Er}(4 \text{ mol.}\%)$ samples after heat treatment at temperatures of 500 and 600°C with exposure for 0 hours and 4 hours are shown in Fig. 4.

For the samples annealed at 500°C (0 h) (Fig. 4a) and 500°C (4 h) (Fig. 4b), the X-ray diffraction patterns correspond to the cubic structure of KGd_2F_7 (JCPDS #00-057-0574) with a slight shift in the X-ray reflections compared to JCPDS #00-057-0574 due to the substitution of gadolinium ions by ytterbium and erbium ions [34], which have smaller radii. After heat treatment at 600°C (0 h) (Fig. 4d), a change in the crystal structure from cubic to tetragonal is observed, which is completed by heat treatment for 4 h (Fig. 4e). This process is explained by the ordering of the structure according to the Ostwald step rule [40]. Calculations of lattice parameters and coherent scattering regions (CSR) are presented in Table 2.

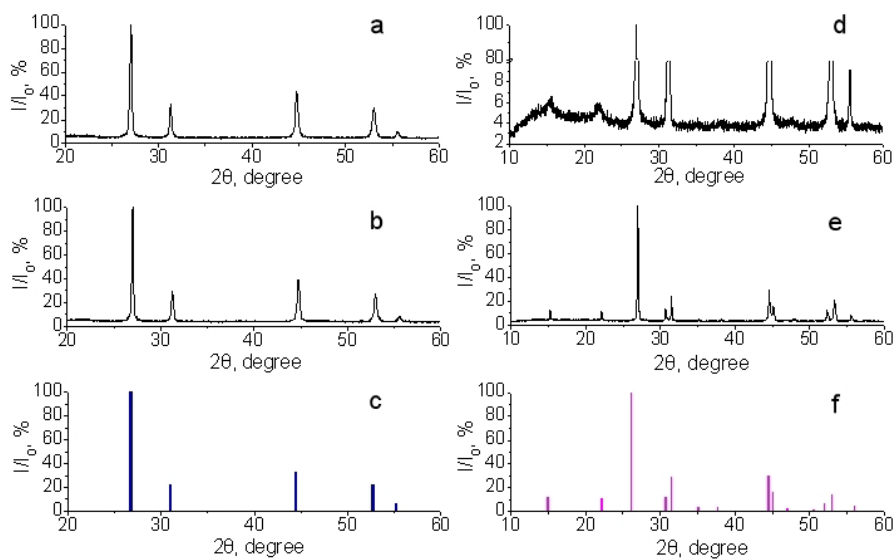


FIG. 4. X-ray diffraction patterns of $\text{KGd}_2\text{F}_7:\text{Yb}(20 \text{ mol.}\%), \text{Er}(4 \text{ mol.}\%)$ powders prepared under different heat treatment conditions: a – 500°C , 0 h; b – 500°C , 4 h; c – JCPDS #00-057-0574; d – 600°C , 0 h; e – 600°C , 4 h; f – X-ray diffraction pattern of sample $\text{K}_{0.33}\text{Gd}_{0.67}\text{F}_{2.33}$ with a tetragonal crystal lattice from the article [39]

TABLE 2. Crystal lattice parameters of KGd₂F₇:Yb (20 mol.%), Er (4 mol.%), samples prepared under different heat treatment conditions

Heat treatment <i>T</i> , °C	Heat treatment duration, h	Sp. group	Lattice parameters, Å	CSR, nm	Composition according to EDX	EY*, %
500	0	<i>Fm</i> -3m	$a = 5.7341(2)$	47	KGd _{1.49} Yb _{0.39} Er _{0.07} F _{6.85}	0.40
500	4	<i>Fm</i> -3m	$a = 5.7382(2)$	56	KGd _{1.48} Yb _{0.38} Er _{0.07} F _{6.79}	0.54
600	0	<i>P4</i> /mmm	$a = 4.0630(4), c = 5.7250(6)$	67	KGd _{1.48} Yb _{0.38} Er _{0.07} F _{6.79}	1.10
600	4	<i>P4</i> /mmm	$a = 4.0242(1), c = 5.8253(3)$	79	KGd _{1.48} Yb _{0.38} Er _{0.07} F _{6.79}	3.80
JCPDS #00-057-0574		<i>Fm</i> -3m	$a = 5.762(2)$			
* [39]		<i>P4</i> /mmm	$a = 4.061, c = 5.853$			

With increasing temperature and time of heat treatment, a slight increase in lattice parameters and CSR values was revealed. DSC-TG and X-ray diffraction data allow us to conclude that the detected exo-effect at 600 °C corresponds to a change in structure from cubic to tetragonal. The X-ray diffraction pattern retains the main X-ray reflections corresponding to the cubic structure, but additional peaks with lower intensity appear which corresponds to the ordering of the crystal lattice. Note that the equilibrium modification KGd₂F₇ is characterized by a tetragonal system, the crystal lattice of which is derived from the fluorite structure [41].

Scanning electron microscopy data for samples subjected to heat treatment under various conditions confirm the results of DSC-TG and XRD. Rounded agglomerates with an average diameter of about 145 nm are visible in the images of samples annealed at a temperature of 500 °C (Fig. 5a,b). In samples that were annealed at 600 °C a change in morphology is observed with simultaneous sintering of agglomerates to micron size.

According to the results of energy dispersive analysis (Table 2), an overestimation (by 3 %) of the potassium content in all samples was revealed compared to the stoichiometric one. The content of ytterbium and erbium, within the error of the determination method, corresponds to the nominal.

For the KGd₂F₇:Yb (20.0 mol.%), Er (4.0 mol.%) samples, anti-Stokes luminescence spectra were recorded (Fig. 6) and the energy yield was estimated using an integrating sphere (Table 1). In the luminescence spectra, characteristic luminescence bands of erbium are observed in the red and green regions of the spectrum, which correspond to the ⁴F_{9/2} → ⁴I_{15/2} and ²H_{11/2}, ⁴S_{3/2} → ⁴I_{15/2} transitions of erbium, respectively. The most intense band was recorded at 670 nm.

The data obtained indicate a significant increase in the efficiency of anti-Stokes luminescence with increasing temperature and time of heat treatment due to an increase in both particle size and ordering of the crystal structure. The highest value of the energy yield of anti-Stokes luminescence (3.80 ± 0.02 %) was recorded for a sample with a tetragonal crystal lattice after annealing for 4 hours at 600 °C. The achieved energy yield of anti-Stokes luminescence is 2.25 times higher than that presented in the literature [33], which is due to the ordering of the crystal structure of the phosphor.

Note that both cubic and tetragonal modifications of KGd₂F₇ should contain clusters of the Gd₆F₃₇ type [42] with a size of about 1.5 nm. The close arrangement of Yb/Er cations in these clusters ensures efficient energy transfer and contributes to obtaining a high light output of anti-Stokes luminescence.

5. Conclusion

A single-phase solid solution with a fluorite structural type of composition KY_{0.5}Gd_{1.5}F₇ was synthesized by using the co-precipitation from aqueous solutions technique while varying various synthesis parameters. An optimized procedure for the synthesis of a solid solution of the specified composition involves a dropwise addition of 25 % excess potassium fluoride to a solution of rare earth nitrates, followed by washing with a 9:1 mixture of isopropyl alcohol and bidistilled water. Using the proposed method anti-Stokes phosphor powders of KGd₂F₇:Yb(20 mol.%),Er(4 mol.%) were synthesized for which an increase in the sizes of coherent scattering regions, lattice parameters, and energy yield of up-conversion luminescence is observed with increasing duration and temperature heat treatment. The heat treatment temperature (600 °C) has been determined at which ordering of the KGd₂F₇:Yb(20 mol.%),Er(4 mol.%) structure occurs, which consists in a change in the structural type from cubic to tetragonal. The highest energy yield of up-conversion luminescence (3.80 %) was recorded for a sample with a tetragonal crystal lattice (*P4*/mmm, $a = 4.024$ Å, $c = 5.825$ Å).

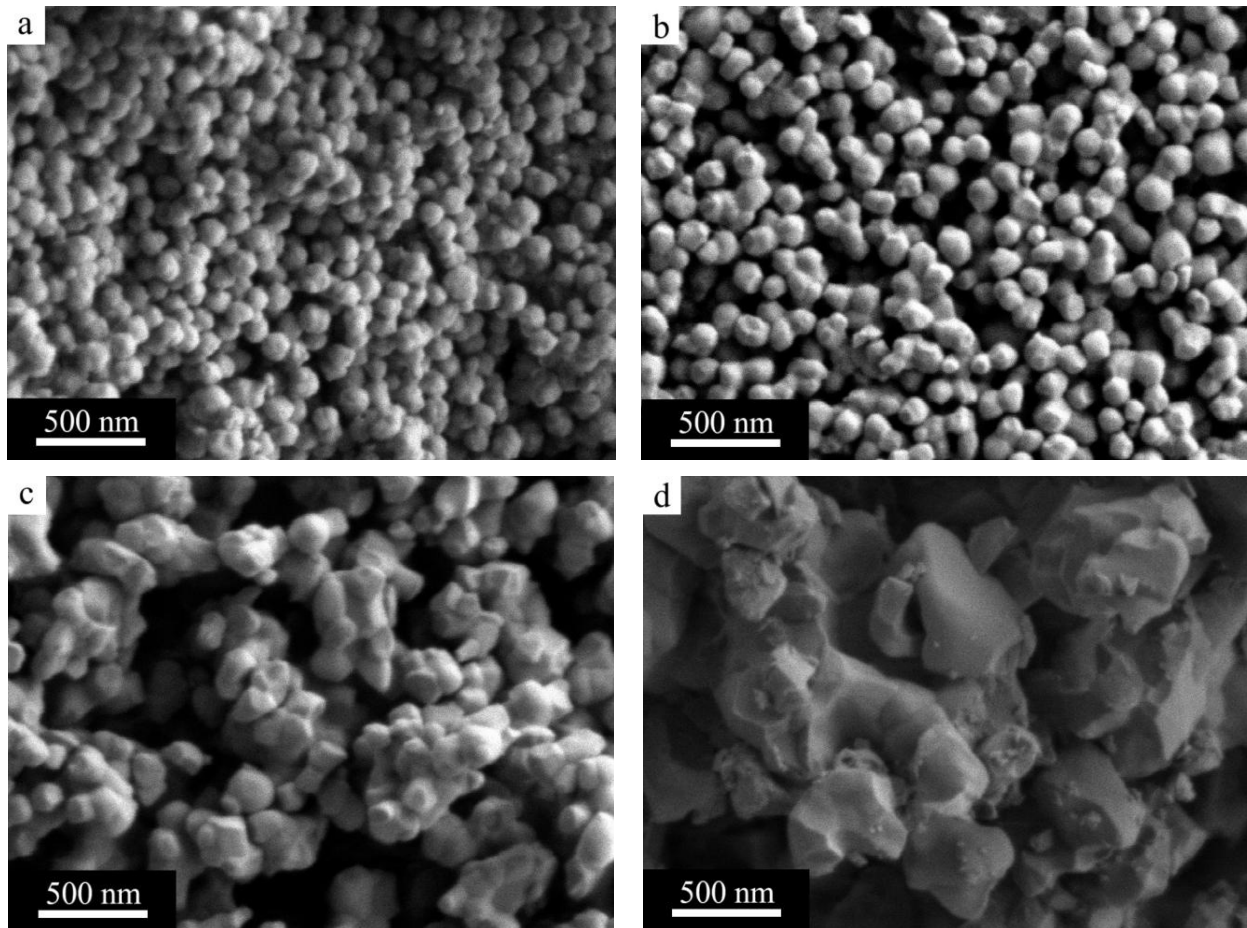


FIG. 5. SEM micrographs of a $\text{KGd}_2\text{F}_7:\text{Yb}$ (20 mol.%),Er(4 mol.%) sample after heat treatment under various conditions: a – 500 °C, 0 h; b – 500 °C, 4 h; c – 600 °C, 0 h; d – 600 °C, 4 h

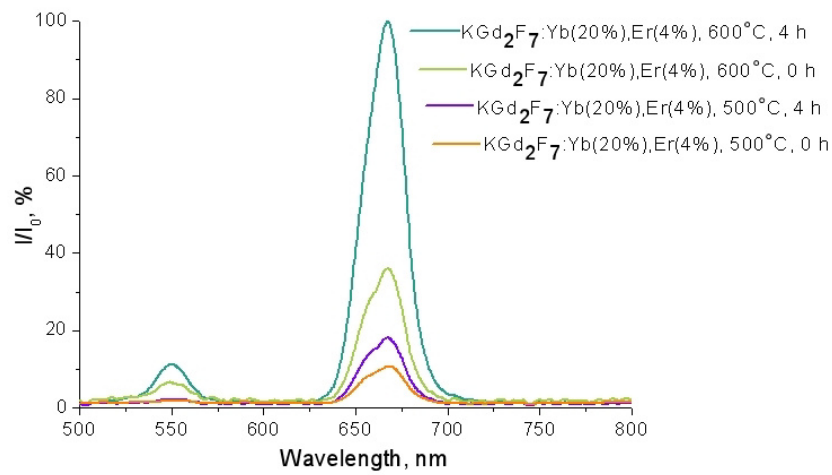


FIG. 6. Luminescence spectra of $\text{KGd}_2\text{F}_7:\text{Yb}$ (20 mol.%),Er(4 mol.%) samples after heat treatment

References

- [1] Kumar A., Prakash Tiwari S., Swart H.C., da Silva J.C.G.E. Infrared interceded $\text{YF}_3:\text{Er}^{3+}/\text{Yb}^{3+}$ upconversion phosphor for crime scene and anti-counterfeiting applications. *Optical Materials*, 2019, **92**, P. 347–351.
- [2] Maturi F.E., Brites C.D.S., Silva R.R., Nigoghossian K., Wilson D., Ferreira R.A.S., Ribeiro S.J.L., Carlos L.D. Sustainable smart tags two-step verification for anticounterfeiting triggered by the photothermal response of upconverting nanoparticles. *Advanced Photonics Research*, 2021, **3**, #2100227.
- [3] Han X., Song E., Zhou B., Zhang Q. Color tunable upconversion luminescent perovskite fluoride with long-/short-lived emissions toward multiple anti-counterfeiting. *J. of Materials Chemistry C*, 2019, **7**, #8226.
- [4] Xie S., Gong G., Song Y., Tan H., Zhang C., Li N., Zhang Y., Xu L., Xu J., Zheng J. Design of novel lanthanide-doped core-shell nanocrystals with dual up-conversion and down-conversion luminescence for anti-counterfeiting printing. *Dalton Transactions*, 2019, **48**, P. 6971–6983.
- [5] Cui E., Xing G., Yuan X., Zhang Y., Artizzu F., Liao X., Tang J., Zhao Y., Zhao P., Liu K., Liu J. Simultaneously excited downshifting/upconversion luminescence from lanthanide-doped core-shell lead-free perovskite nanocrystals for encryption and data storage. *Advanced Functional Materials*, 2024, **8**, P. 2173–2180.
- [6] Suo H., Zhu Q., Zhang X., Chen B., Chen J., Wang F. High-security anti-counterfeiting through upconversion luminescence. *Materials Today Physics*, 2021, **21**, #100520.
- [7] Liu J., Rijckaert H., Zeng M., Haustraete K., Laforce B., Vincze L., Van Driessche I., Kaszmaerek A.M., Van Deun R. Simultaneously from lanthanide-doped core/shell fluoride nanoparticles for multimode anticounterfeiting. *Advanced Functional Materials*, 2018, **28**, #1707365.
- [8] Huang X. Broadband dye-sensitized upconversion: A promising new platform for future solar upconverter design. *J. of Alloys Compounds*, 2017, **690**, P. 356–359.
- [9] Fischer S., Ivaturi A., Jakob P., Kramer K.W., Martin-Rodriges R., Meijerink A., Richards B.S., Golgschmidt J.C. Upconversion solar cell measurements under real sunlight. *Optical Materials*, 2018, **84**, P. 389–395.
- [10] Ghazy A., Safdar M., Lastusaari M., Savin H., Karppinen M. Advances in upconversion enhanced solar cell performance. *Solar Energy and Solar Cell*, 2021, **320**, #111234.
- [11] Fisher S., Favilla E., Tonelli M., Goldschmidt J.C. Record Efficient upconverter solar cell devices with optimized bifacial silicon solar cells and monocrystalline $\text{BaYF}_8:30\%\text{Er}^{3+}$ upconverter. *Solar Energy Materials and Solar Cell*, 2015, **136**, P. 127–134.
- [12] Wang F., Banerjee D., Liu Y., Chen X., Liu X. Upconversion nanoparticles in biological labeling, imaging, and therapy. *Analyst*, 2010, **135**, P. 1839–1854.
- [13] Liu Q., Feng W., Li F. Water-soluble lanthanide upconversion nanophosphors: Synthesis and bioimaging applications in vivo. *Coordination Chemistry Reviews*, 2014, **273**, P. 100–110.
- [14] Tse W.H., Chen L., McCurdy C.M., Tarapaski C.M., Chronik B.A., Zhang J. Development of biocompatible $\text{NaGdF}_4:\text{Er}^{3+},\text{Yb}^{3+}$ upconversion nanoparticles used as contrast agents for bio-imaging. *The Canadian J. of Chemical Engineering*, 2019, **97**, P. 2678–2684.
- [15] Min Y., Li J., Liu F., Padmanabhan P., Yeow E.K.L., Xing B. Recent advance of biological molecular imaging based on lanthanide-doped upconversion-luminescent nanomaterials. *Nanomaterials*, 2014, **4**, P. 129–154.
- [16] Du P., Luo L., Huang X., Yu J.S. Ultrafast synthesis of bifunctional $\text{Er}^{3+}/\text{Yb}^{3+}$ -codoped NaBiF_4 upconverting nanoparticles for nanothermometer and optical heater. *J. of Colloid and Interface Science*, 2018, **514**, P. 172–181.
- [17] Du P., Luo L., Yu J.S. Low-temperature thermometry based on upconversion emission of Ho/Er-codoped $\text{Ba}_{0.77}\text{Ca}_{0.23}\text{TiO}_3$ ceramics. *J. of Alloys and Compounds*, 2015, **632**, P. 73–77.
- [18] Zhou S., Jiang S., Wei X., Chen Y., Duan C.-K., Yin M. Optical thermometry based on upconversion luminescence in $\text{Yb}^{3+}/\text{Ho}^{3+}$ co-doped NaLuF_4 . *J. of Alloys and Compounds*, 2014, **588**, P. 654–657.
- [19] Suo H., Zhao X., Zhang Z., Li T., Goldys E.M., Guo C. Constructing Multifunctional Morphologies of $\text{YF}_3:\text{Er}^{3+}/\text{Yb}^{3+}$ Up-conversion Nano/Micro-crystals towards Sub-tissue Thermometry. *Chemical Engineering J.*, 2017, **313**, P. 65–73.
- [20] Manciniak L., Prorok N., Frances-Soriano L., Perez-Prieto J., Bernarkiewicz A. A broadening temperature sensitivity range with a core-shell YbEr@YbNd double ratiometric optical nanothermometer. *Nanoscale*, 2016, **8**, P. 5037–5042.
- [21] Ryszczynska K., Trejgis K., Manciniak L., Grzyb T. Upconverting $\text{SrF}_2:\text{Er}^{3+}$ Nanoparticles for Optical Temperature Sensors. *Applied Nano Materials*, 2021, **4**, P. 10438–10448.
- [22] Woidsky J., Sander I., Schau A., Moesslein J., Wendler P., Wacker D., Gao G., Kirchenbauer D., Kumar V., Busko D., Howard I.A., Richards B.S., Turshakov A., Wiethoff S., Lang-Koetz C. Inorganic fluorescent marker materials for identification of post-consumer plastic packaging. *Resources, Conservation and Recycling*, 2020, **161**, #104976.
- [23] Howard I.A., Busko D., Gao G., Wendler P., Madirov E., Turshakov A., Moesslein J., Richards B.S. Sorting plastics for a circular economy: Perspectives for lanthanide luminescent markers. *Resources, Conservation and Recycling*, 2024, **205**, #107557.
- [24] Wang F., Deng R., Liu X. $\text{NaYF}_4:\text{Yb},\text{Er}/\text{NaYF}_4$ Core/Shell Nanocrystals with High Upconversion Luminescence Quantum Yield. *Nature Protocols*, 2014, **9**, P. 1634–1644.
- [25] Klier D.T., Kumke M.U. Upconversion Luminescence Properties of $\text{NaYF}_4:\text{Yb},\text{Er}$ Nanoparticles Codoped with Gd^{3+} . *The J. of Physical Chemistry C*, 2015, **119**, P. 3363–3373.
- [26] He L., Zou X., He X., Lei F., Jiang N., Zheng Q., Xu C., Liu Y., Lin D. Reducing Grain Size and Enhancing Luminescence of $\text{NaYF}_4:\text{Yb}^{3+},\text{Er}^{3+}$ Upconversion Materials. *Crystal Growth and Design*, 2018, **18**, P. 808–817.
- [27] Yi G. Synthesis of Hexagonal-Phase $\text{NaYF}_4:\text{Yb},\text{Er}$ and $\text{NaYF}_4:\text{Yb},\text{Tm}$ Nanocrystals with Efficient Up-Conversion Fluorescence. *Advanced Functional Materials*, 2006, **16**, P. 2324–2329.
- [28] Wang L., Li Y. Controlled Synthesis and Luminescence of Doped NaYF_4 Nanocrystals. *Chemistry of Materials*, 2007, **19**, P. 727–734.
- [29] Cheng Q., Sui J., Cai W. Enhanced upconversion emission in Yb^{3+} and Er^{3+} codoped NaGdF_4 nanocrystals by introducing Li^+ ions. *Nanoscale*, 2012, **4**, P. 779–784.
- [30] Maurya S.K., Kushawaha R., Tiwari S.P., Kumar A., Kumar K., Esteves da Silva J.C.G. Thermal decomposition mediated $\text{Er}^{3+}/\text{Yb}^{3+}$ codoped NaGdF_4 upconversion phosphor for optical thermometry. *Materials Research Express*, 2019, **6**, #086211.
- [31] Saleta Reig D., Grauel B., Konyushkin V.A., Nakladov A.N., Fedorov P.P., Brusko D., Howard I.A., Richards B.S., Resch-Genger U., Kuznetsov S.V., Turshakov A., Wurth C. Upconversion properties of $\text{SrF}_2:\text{Yb}^{3+},\text{Er}^{3+}$ single crystals. *J. of Materials Chemistry C*, 2020, **8**, P. 4093–4101.
- [32] Pak A.M., Ermakova J.A., Kuznetsov S.V., Ryabova A.V., Pominova D.V., Voronov V.V. Efficient visible range $\text{SrF}_2:\text{Yb}^{3+},\text{Er}^{3+}$ and $\text{SrF}_2:\text{Yb}^{3+},\text{Tm}^{3+}$ based up-conversion luminophores. *J. of fluorine chemistry*, 2017, **194**, P. 16–22.
- [33] Rozhnova Yu.A., Kuznetsov S.V., Luginina A.A., Voronov V.V., Ryabova A.V., Pominova D.V., Ermakov R.P., Usachev V.A., Kononenko N.E., Baranchikov A.E., Ivanov V.K., Fedorov P.P. New $\text{Sr}_{1-x-z}\text{R}_x(\text{NH}_4)_z\text{F}_{2+x-z}$ ($\text{R}=\text{Yb}, \text{Er}$) solid solution as precursor for high efficiency up-conversion luminophor and optical ceramics on the base of strontium fluoride. *Materials Chemistry and Physics*, 2016, **172**, P. 150–157.

- [34] Ermakova J.A., Madirov E.I., Fedorov P.P., Alexandrov A.A., Kuznetsov S.V. Effect of the fluorinating agent type (NH_4F , NaF , KF) on the particle size and emission properties of $\text{SrF}_2\text{:Yb:Er}$ luminophores. *Mat. Chem. C*, 2024, **12**, P. 1406–1411.
- [35] Madirov E., Kuznetsov S.V., Konyushkin V.A., Nakladov A.N., Fedorov P.P., Bergfeldt Th., Hudry D., Busko D., Howard I.A., Richards B.S., Turshov A. Effect of Yb^{3+} and Er^{3+} concentration on upconversion luminescence of co-doped BaF_2 single crystals. *J. Mater. Chem. C*, 2021, **9**, P. 3493–3503.
- [36] Karbowski M., Mech A., Bednarkiewicz A., Streck W. Structural and luminescent properties of nanostructured $\text{KGdF}_4\text{:Eu}^{3+}$ synthesised by coprecipitation method. *J. Alloys Comp.*, 2004, **380**, P. 321–326.
- [37] Alexandrov A.A., Mayakova M.N., Kuznetsov S.V., Voronov V.V., Pominova D.V., Ivanov V.K., Fedorov P.P. Effect of Structural Perfection of Crystalline $\beta\text{-NaYF}_4\text{:Er}^{3+},\text{Yb}^{3+}$ Phosphor Powders on the Efficiency of Their Upconversion Luminescence. *Inorganic Materials*, 2022, **58** (1), P. 90–96.
- [38] Zakharova A.S., Alexandrov A.A., Pominova D.V., Fedorov P.P., Kuznetsov S.V., Ivanov V.K. Synthesis of $\text{KGd}_2\text{F}_7\text{:Yb:Er}$ luminophores by co-precipitation from aqueous solutions. *J. of Structural Chemistry*, 2024, **65**, P. 138–148.
- [39] Gredin P., Labeguerie J., Pierrard A., Vaulay M.-J., de Kozak A.R.D. Synthesis and structural characterization of $\text{K}_{0.33}\text{Gd}_{0.67}\text{F}_{2.33}(\text{KGd}_2\text{F}_7)$ and $\text{K}_{0.31}\text{Gd}_{0.69}\text{F}_{1.84}\text{O}_{0.27}$. *Solis State Science*, 2004, **6**, P. 1221–1228.
- [40] Ostwald W. Studien über die Bildung und Umwandlung fester Körper. *Zeitschrift für Physikalische Chemie*, 1897, **22**, P. 289–330.
- [41] Fedorov P.P. Systems of alkali and rare-earth metal fluorides. *Russian J. Inorg. Chem.*, 1999, **44** (11), P.1703–1727.
- [42] Le Fur Y., Aleonard S., Gorius M.F., Roux M.T. Structure crystalline de $\text{K}_{0.265}\text{Gd}_{0.735}\text{F}_{2.47}$. *Z. Krist.*, 1988, **182**, P. 281–290.
- [43] Timofeeva E., Orlovskaya E., Popov A., Shaidulin A., Kuznetsov S., Alexandrov A., Uvarov O., Vainer Y., Silaev G., Rähn M., Tamm A., Fedorenko S., Orlovskii Y. The Influence of Medium on Fluorescence Quenching of Colloidal Solution of the $\text{Nd}^{3+}\text{:LaF}_3$ Nanoparticles Prepared with HTMW treatment. *Nanomaterials*, 2022, **12**, 3749.
- [44] Fedorov P.P., Kuznetsov S.V., Osiko V.V. Elaboration of Nanofluorides and Ceramics for Optical and Laser Applications. *Photonic and Electronic Properties of Fluoride Materials*, 2016, P. 7–31.

Submitted 29 August 2024; accepted 26 September 2024

Information about the authors:

Anna S. Zakharova – Kurnakov Institute of General and Inorganic Chemistry of the Russian Academy of Sciences, Moscow, Russia; Prokhorov General Physics Institute of the Russian Academy of Sciences, Moscow, Russia; National Research University Higher School of Economics, Moscow, Russia; ORCID 0000-0003-0976-5192; AnyaZakharova2606@mail.ru

Sergey V. Kuznetsov – Prokhorov General Physics Institute of the Russian Academy of Sciences, Moscow, Russia; ORCID 0000-0002-7669-1106; kouznetzovsv@gmail.com

Alexander A. Alexandrov – Kurnakov Institute of General and Inorganic Chemistry of the Russian Academy of Sciences, Moscow, Russia; Prokhorov General Physics Institute of the Russian Academy of Sciences, Moscow, Russia; ORCID 0000-0001-7874-7284; alexandrov1996@yandex.ru

Daria V. Pominova – Prokhorov General Physics Institute of the Russian Academy of Sciences, Moscow, Russia; ORCID 0000-0002-3634-8709; pominovadv@gmail.com

Valery V. Voronov – Prokhorov General Physics Institute of the Russian Academy of Sciences, Moscow, Russia; ORCID 0000-0001-5029-8560; voronov@lst.gpi.ru

Pavel P. Fedorov – Prokhorov General Physics Institute of the Russian Academy of Sciences, Moscow, Russia; ORCID 0000-0002-2918-3926; ppfedorov@yandex.ru

Vladimir K. Ivanov – Kurnakov Institute of General and Inorganic Chemistry of the Russian Academy of Sciences, Moscow, Russia; ORCID 0000-0003-2343-2140; van@igic.ras.ru

Conflict of interest: the authors declare no conflict of interest.

Synthesis of CdSTe nanoparticles by laser ablation

Maarif A. Jafarov^{1,a}, Vagif M. Salmanov^{1,b}, Rovshan M. Mamedov^{1,c},
Elshan F. Nasirov^{1,d}, Turana A. Mammadova^{1,e}

¹Baku State University, AZ1148 Baku, Azerbaijan

^aMaarif.Jafarov@mail.ru, ^bvagif_salmanov@yahoo.com, ^cpoluprovod@rambler.ru,

^del.nasir@mail.ru, ^eturka.memmedova@gmail.com

Corresponding author: M. A. Jafarov, Maarif.Jafarov@mail.ru

ABSTRACT Synthesis of CdSTe nanoparticles using CdCl₂, Na₂S₂O₃ and TeO₂ solutions under the action of laser radiation was experimentally studied. The radiation source was a pulsed Nd:YAG laser with built-in generators of the 2nd and 3rd harmonics, designed to generate radiation with a wavelength of 1064, 532, and 335 nm. The laser pulse duration was 10 ns with an energy of 135 mJ per pulse. In a colloidal solution, the formation of nanoparticles with a diameter of 10 to 50 nm was observed. X-ray diffraction analysis established that the crystal structure of the nanoparticles is the same as that of the bulk material (hexagonal). It is shown that the photoluminescence emission of the obtained nanoparticles has a green color (~560 nm) and is associated with the radiative recombination of free excitons.

KEYWORDS CdSTe nanoparticles, laser ablation, photoluminescence.

FOR CITATION Jafarov M.A., Salmanov V.M., Mamedov R.M., Nasirov E.F., Mammadova T.A. Synthesis of CdSTe nanoparticles by laser ablation. *Nanosystems: Phys. Chem. Math.*, 2024, **15** (5), 710–715.

1. Introduction

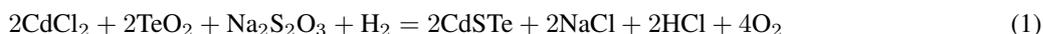
Among the most common semiconductor nanoparticles of groups II–VI, CdSTe nanocrystals are of great interest for applications in optoelectronics, solar cells, LEDs, and biology [1–5]. Due to the developed surface (in a 1 nm particle, almost all atoms are surface atoms) and the manifestation of the quantum confinement effect [6], nanosized semiconductors have unique optical, electronic, catalytic, and other properties that are attractive to researchers. For example, solar cells based on nanosized cadmium telluride demonstrate a record efficiency of solar energy conversion and are currently considered more promising for mass application compared to traditional silicon batteries [7,8]. To obtain nanoclusters and nanostructured materials, various methods are used: gas-dynamic, chemical, plasma, beam [9–18]. CdSTe nanocrystals in solution are most often obtained by chemical synthesis using organometallic “precursors”. These methods provide nearly monodisperse nanocrystals that exhibit narrow photoluminescence emission (up to ~30 nm) as well as high quantum yields. However, in general they require the use of expensive, pyrophoric, hazardous chemical precursors, as well as high temperatures and long reaction times.

One of the most promising methods for the synthesis of clusters is pulsed laser ablation (PLA) [1, 4]. Its main advantage is the ability to exclude the presence of foreign impurities in synthesized nanostructures, which is especially important for applications (one foreign atom in a 2 nm particle corresponds to a defect concentration of $\sim 10^{21} \text{ cm}^{-3}$ and can significantly change its properties). The advantages of the PLA method also include its flexibility and the ability to control the process of cluster growth. The formation of nanoclusters during PLA can occur according to two different scenarios: aggregation of the initial ablation products (atoms, molecules) in an expanding laser plasma and direct emission from the irradiated surface. Recently, significant progress has been made in the PLA synthesis of single-component semiconductor nanoclusters with controlled size, shape, and optical properties [19, 20], as well as in the understanding and quantitative description of the cluster formation process [21–23]. Laser ablation of nanoparticles in a liquid has attracted great interest due to its simplicity, the absence of the need for surfactants, and good control of the size and shape of synthesized nanoparticles [24,25]. In this method, many parameters, such as laser radiation flux density, laser radiation wavelength, pulse duration, and type of colloidal solution, can affect the characteristics of synthesized nanoparticles.

It should be noted that in all the above works devoted to laser ablation, bulk CdSTe crystals grown by the Bridgman method were used as target materials. Laser ablation was carried out either in a vacuum or by immersing the target in various liquids, using ultrashort nano and femtosecond laser pulses. Indeed, the synthesis of CdSTe nanoparticles by laser ablation, as noted, has great advantages over other methods. However, it should be taken into account that this method requires the growth of undoped CdSTe crystals, which is by no means a simple technological problem. In this work, we propose a new method for obtaining nanoparticles, direct interaction of laser radiation with solutions that make up the components of CdSTe nanoparticles. As shown by our experimental studies, the structural characteristics and optical properties of CdSTe nanoparticles are significantly superior to those of nanoparticles obtained using a solid target.

2. Experimental technique

CdSTe nanoparticles were synthesized in solution using the reactive laser ablation method. Highly pure CdCl₂ (99.9 % pure from Sigma Aldrich), Na₂S₂O₃ (99.95 % pure from Sigma Aldrich) and TeO₂ (99.99 % pure from Sigma Aldrich) powders mixed with distilled water were used as initial raw materials. The reaction proceeded according to the following formula:



Immediately after irradiation with a laser pulse, CdSTe nanoparticles were formed. The ablation process was performed by laser radiation with a wavelength of $\lambda = 1064$ nm, with a pulse energy of 135 mJ and an ablation time of ~ 10 min. The radiation source was pulsed Nd:YAG laser with built-in generators of the 2nd and 3rd harmonics, designed to generate radiation with a wavelength of 1064, 532, and 335 nm. The laser pulse duration was 10 ns with a maximum power of ~ 12 MW/cm². The radiation intensity was varied using calibrated neutral light filters. The optical absorption and luminescence spectra of CdSTe nanoparticles were studied using an automatic M833 double dispersion monochromator (spectral resolution ~ 0.024 nm at a wavelength of 600 nm), with computer control and a detector that records radiation in the wavelength range of 350–2000 nm. The scheme of the experimental setup for ablation of CdSTe nanoparticles is shown in Fig. 1.

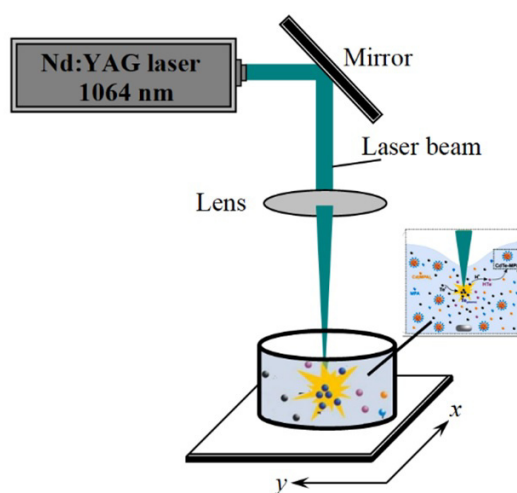


FIG. 1. Scheme of the experimental setup

Fig. 2 shows the diffraction pattern (XRD) of nanoparticles from drops of a colloidal solution of CdSTe dried on a clean glass substrate. CuK α , $\lambda=1.544178$ Å SSFOM: F17-610.0.5.10.60 were used as the radiation source. It is shown that the diffraction planes (111), (200), (220), (311), (222), (400), (331), (422), and (511) at 2θ diffraction angles 23.620, 27.890, 38.970, 45.280, 49.340, 56.750, 63.600, 73.220, and 76.840, respectively, correspond to the cubic (zinc blende) structure of the bulk CdSTe crystal [24], which confirms the crystal structure of the synthesized nanoparticles, which is the same as that of the bulk material. Based on the X-ray diffraction patterns, using the Debye–Scherer formula [21], the sizes of the obtained nanoparticles were calculated:

$$D = \frac{k\lambda}{\beta \cos \theta} \quad (2)$$

where D is the sizes of nanoparticles, $k = 0.9$ is the line shape factor (shape factor), $\beta = 0.035$ Å is the intensity maximum half-width (FWHM- Full Width at Half Maximum), λ is the X-ray wavelength, $\lambda = 1.54$ Å, θ -Bragg angle, $\cos \theta = 0.727$.

Estimates show that the average size of CdSTe crystallites is 27.434 nm (see Table 1).

Morphologists. The surfaces of the synthesized CdSTe nanoparticles were studied using AFM analysis. Fig. 3 shows a 3D AFM image of CdSTe nanoparticles on a glass substrate. As can be seen from the figure, a homogeneous distribution of particles in the presented figure is not observed.

The histogram of particle size distribution is shown in Fig. 4. The average particle size estimated using the software was about 40–50 nm. The particle size value is higher than calculated by X-ray diffraction analysis. This is due to the fact that XRD depends on the free volume of dimensional defects, while AFM directly visualizes the grain without taking into account the degree of defectiveness of the crystal.

The absorption curve from a colloidal solution of CdSTe nanoparticles is shown in Fig. 5a. The onset of absorption at ~ 500 nm is consistent with the absorption of an ensemble of nanoparticles whose maximum diameter is ~ 50 nm. Taking into account that CdSTe is a semiconductor with a direct band gap, from the dependence, the band gap of the

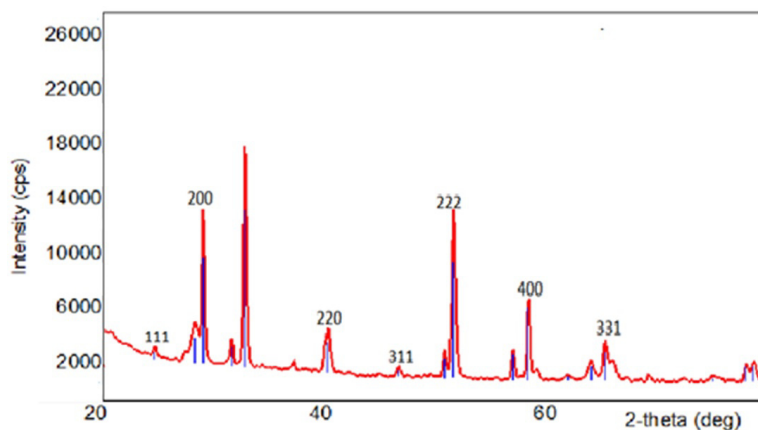


FIG. 2. Diffraction pattern (XRD) of CdSte nanoparticles on a glass substrate

TABLE 1. Crystallite size

2 theta	Crystallite size
23.62(3) 111	28.27 nm
27.891(9) 200	34.91 nm
38.97(3) 220	16.31 nm
45.28(5) 311	23.66 nm
49.347(14) 222	39.72 nm
56.75(8) 400	47.17 nm
63.60(5) 331	20.78 nm
73.2(1) 422	10.87 nm
76.84(3) 511	25.22 nm
average crystallite size:	27.434 nm

studied samples was determined, which turned out to be equal to $E_g = 2.46$ eV (Fig. 5b). This value is 0.97 eV larger than the band gap of a bulk undoped CdSte crystal, (eV (~ 827 nm) [1]. It should be noted that the shift of the red absorption band of nanoparticles to the short-wavelength region of the spectrum compared to a bulk crystal is a characteristic feature of semiconductor nanoparticles, which is related to the quantum size effect.

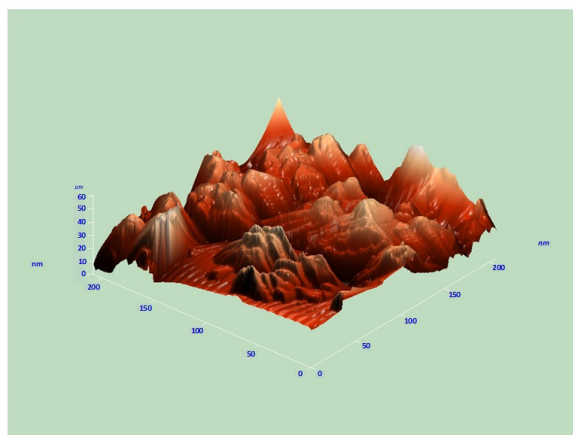


FIG. 3. AFM image of CdSte nanoparticles on a glass substrate

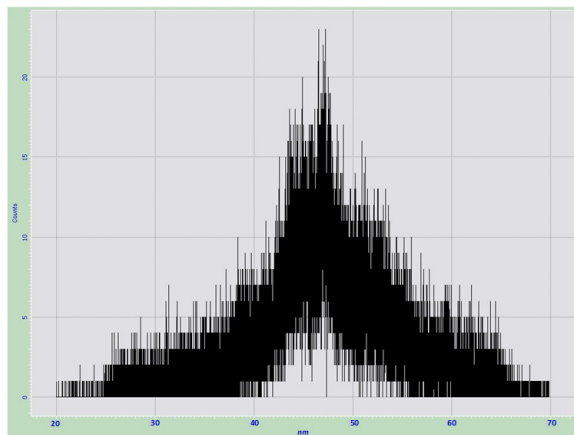


FIG. 4. Histogram of particle size distribution

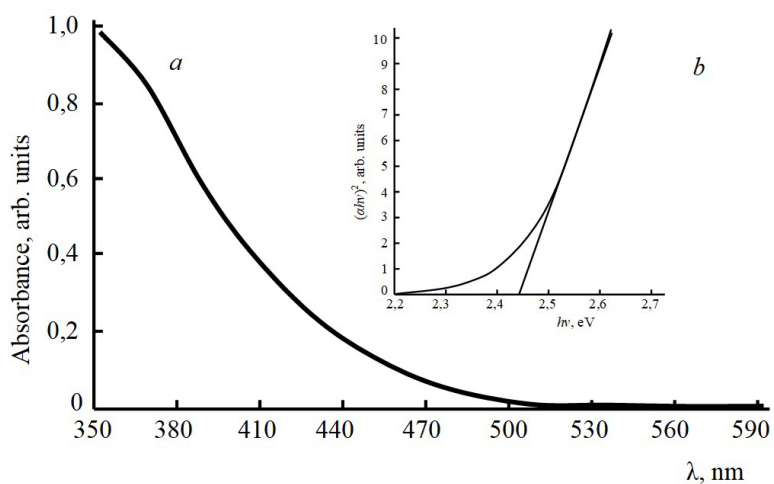


FIG. 5. Optical absorption spectrum (a) and dependence $\alpha^2 \sim f(h\nu)$ (b) of CdSTe nanoparticles obtained in a colloidal solution

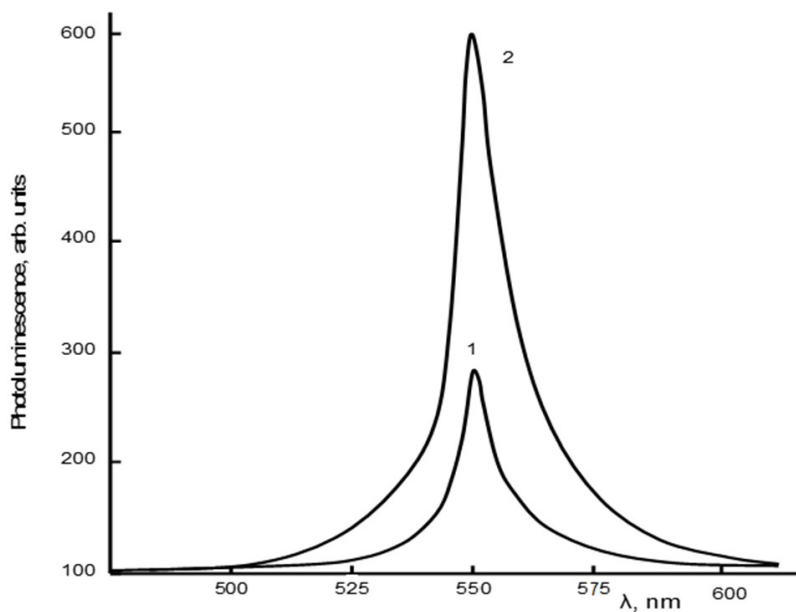


FIG. 6. Photoluminescence spectra of CdSTe nanoparticles at two different excitation powers, the second harmonic of a neodymium laser (eV): 1-1 MW/cm²; 2-10 MW/cm²

Fig. 6 shows the photoluminescence spectra of CdSTe nanoparticles excited by the second harmonic of the Nd:YAG laser (eV). As can be seen from the figure, the emission maximum of nanoparticles corresponds to wavelengths ~ 510 nm (2.43 eV). An increase in the laser light power by 1.2 times does not affect the position of the spectra, but leads to an increase in the radiation intensity by ~ 2.1 times. As regards the nature of the observed radiations, in our opinion they are due to the radiative recombination of free excitons.

Knowing the energy of free excitons in CdSTe (~ 29 meV), it is possible to determine the band gap of nanoparticles, which is equal to 2.46 eV, which is in satisfactory agreement with the value determined from the absorption spectrum.

3. Conclusion

A new method for synthesizing CdSTe nanoparticles by laser radiation is proposed. Highly pure CdCl_2 , $\text{Na}_2\text{S}_2\text{O}_3$ and TeO_2 powders mixed with distilled water were used as initial raw materials. The ablation process was performed by laser radiation with a wavelength of 1064 nm, with a pulse energy of 135 mJ and an ablation time of ~ 10 min. Under these ablation conditions in a colloidal solution, the formation of nanoparticles with diameters from ~ 10 to ~ 50 nm was observed. It is shown that the synthesized nanoparticles retain the crystalline structure of the bulk material and emit photoluminescence at 560 nm associated with the radiative recombination of free excitons.

References

- [1] Semaltianos N.G., Logothetidis S., Perrie W., Romani S., Potter R.J., Sharp M., Dearden G. and Watkins K.G. CdSTe nanoparticles synthesized by laser ablation. *Applied physics letters*, 2009, **95**, P. 033301–033306.
- [2] Jafarov M.A., Nasirov E.F., Jahangirova S.A., Jafarli R. NanoZnS thin films for solar cell. *Nanosystems: physics, chemistry, mathematics*, 2015, **6**(5), P. 644–649.
- [3] Jafarov M.A., Nasirov E.F., Mammadov R., Jafarli R. Fabrication and characterization ZnCdS nanowire. *Nanosystems: physics, chemistry, mathematics*, 2014, **5**(6), P. 796–802.
- [4] Bulgakov A.V., Yevtushenko A.B., Shukhov Yu.Q., Ozerov I., Marin V. *Quantum electronics*, 2010, **40**(11), 1021–1033.
- [5] Jafarov M.A., Nasirov E.F. Nanoscale Structures based on the $\text{Zn}_{1-x}\text{Cd}_x\text{S}$. *Nanosystems: physics, chemistry, mathematics*, 2013, **4**(5), P. 680–689.
- [6] Morales-Acevedo A. Thin film CdS/CdSTe solar cells: research perspectives. *Solar Energy*, 2006, **80**, 675 p.
- [7] Zweibel K. Engineering. The impact of tellurium supply on cadmium telluride photovoltaics. *Science*, 2010, **328**, 699 p.
- [8] Johnston R.L. *Atomic and Molecular Clusters*. London: CRC Press, 2002, 256 p.
- [9] Smirnov B.M. Generation of cluster beams. *Advances in the physical sciences*, 2003, **173**, P. 609.
- [10] Makarov Q.N. Extremal processes in clusters in collision with a solid surface. *Advances in the physical sciences*, 2006, **176**, P. 121.
- [11] Peng Z.A. and Peng X. Formation of High-Quality CdSTe, CdSe, and CdS Nanocrystals Using CdO as Precursor. *J. Am. Chem. Soc.*, 2001, **123**, P. 183.
- [12] Marc-Oliver Piepenbrock M., Tom Stirner, Mary O'Neill and Stephen M. Kelly. Growth dynamics of CdSTe nanoparticles in liquid and crystalline phases. *J. Am. Chem. Soc.*, 2007, **129**, 24, P. 7674.
- [13] Martin Sharp. CdSTe nanoparticles synthesized by laser ablation. *Applied Physics Letters*, 2009, **95**, P. 033302.
- [14] Albert A.R., John A.Y. *Colloids and Surfaces A: Physicochemical and Engineering Aspects*, 2006, **279**, 1-3 P. 121.
- [15] Patrone L., Nelson D., Safarov V.I., Sentis M., Marine W.J. Photoluminescence of silicon nanoclusters with reduced size dispersion produced by laser ablation. *Appl. Phys.*, 2000, **87**, P. 3829.
- [16] Seto T., Orii T., Hirasawa M., Aya N. Fabrication of silicon nanostructured films by deposition of size-selected nanoparticles generated by pulsed laser ablation. *Thin Solid Films*, 2003, **437**, P. 230.
- [17] Lukyanchuk B., Marine W. On the delay time in photoluminescence of Si-nanoclusters, produced by laser ablation. *Appl. Surf. Sci.*, 2000, **314**, P. 154.
- [18] Anisimov S.I., Lukyanchuk B.S. Selected problems of the theory of laser ablation. *Advances in the physical sciences*, 2002, **172**, P. 301.
- [19] Bulgakov A.V., Ozerov I., Marine W. Silicon clusters produced by femtosecond laser ablation: non-thermal emission and gas-phase condensation. *Appl. Phys. A*, 2004, **79**, P. 1591.
- [20] Xu S., Ziegler J., Nann T.J. Rapid synthesis of highly luminescent InP and InP/ZnS nanocrystals. *Mater. Chem.*, 2008, **18**, P. 2653.
- [21] Ozerov I., Nelson D., Bulgakov A.V., Marine W., Sentis M. Synthesis and laser processing of ZnO nanocrystalline thin films. *Appl. Surf. Sci.*, 2003, **349**, P. 212.
- [22] Neretina S., Mascher P., Hughes R.A., Braidly N., Gong W.H., Britten J.F., Preston J.S., Sochinskii N.V., Dippe P. Evolution of wurtzite CdSTe through the formation of cluster assembled films. *Appl. Phys. Lett.*, 2006, **89**, P. 133101.
- [23] JCPDS, International Centre for Diffraction Data, USA, Card Number 15-0770.
- [24] Samuel S. Nanolasers: lasing from nanoscale quantum wires. *Int. J. of Nanotechnology*, 2004, **1**, P. 42–85.

Submitted 7 April 2024; revised 22 August 2024; accepted 26 September 2024

Information about the authors:

Maarif A. Jafarov – Baku State University, AZ1148 Baku, Azerbaijan; ORCID 0000-0001-7483-4882; Maarif.Jafarov@mail.ru

Vagif M. Salmanov – Baku State University, AZ1148 Baku, Azerbaijan; ORCID 0000-0002-8826-4419; vagif_salmanov@yahoo.com

Rovshan M. Mamedov – Baku State University, AZ1148 Baku, Azerbaijan; ORCID 0000-0003-3672-8899; poluprovod@rambler.ru

Elshan F. Nasirov – Baku State University, AZ1148 Baku, Azerbaijan; el.nasir@mail.ru

Turana A. Mammadova – Baku State University, AZ1148 Baku, Azerbaijan; turka.memmedova@gmail.com

Conflict of interest: the authors declare no conflict of interest.

Ionic channel structure in perfluorinated membranes studied by small angle X-ray scattering, optical and Mössbauer spectroscopy

Vasily T. Lebedev^{1,a}, Valery S. Kozlov^{1,b}, Mikhail V. Remizov^{1,c}, Yury V. Kulvelis^{1,d},
Oleg N. Primachenko^{2,e}, Elena A. Marinenko^{2,f}, Georgy S. Peters^{3,g}

¹Petersburg Nuclear Physics Institute named by B. P. Konstantinov of National Research Center “Kurchatov Institute”, Gatchina, Russia

²Institute of Macromolecular Compounds, Russian Academy of Sciences, St. Petersburg, Russia

³National Research Center “Kurchatov Institute”, Moscow, Russia

^alebedev_vt@pnpi.nrcki.ru, ^bkozlov_vs1@pnpi.nrcki.ru, ^cm.remizov97@gmail.com, ^dkulvelis_yv@pnpi.nrcki.ru,
^ealex-prima@mail.ru, ^femarinenkospb@gmail.com, ^ggeorgspeters@gmail.com

Corresponding author: Vasily T. Lebedev, lebedev_vt@pnpi.nrcki.ru

PACS 81.07.Nb, 82.35.Rs

ABSTRACT Small angle X-ray scattering optical and Mössbauer spectroscopy has been used to study ionic channels in perfluorinated Nafion[®]-type membranes. X-ray scattering data have revealed the ordering of ionic groups of polymer chains at nanoscales into extended fine channels for proton conductivity. Then the membranes were saturated with Fe³⁺ ions to probe their interaction with sulfonic groups. This remarkably changed electron properties of copolymer in which the energy of optical gap has decreased. The Mössbauer spectra have confirmed that even at ambient temperature in membrane, Fe³⁺ ions are assembled into antiferromagnetic dimers with water shells and associated with sulfonic groups at the channel surfaces. The applied complementary methods allowed us to examine a short-range order of ionic groups forming a network of channels in membranes that provide their functional properties in hydrogen fuel cells.

KEYWORDS ion, channel, membrane, structure, gamma-spectroscopy

ACKNOWLEDGEMENTS The work was supported by the Russian Science Foundation under Grant No. 23-23-00129. The authors thank Professor V.G. Semenov for methodological help, Engineers I.N. Ivanova, L.I. Lisovskaya for technical assistance.

FOR CITATION Lebedev V.T., Kozlov V.S., Remizov M.V., Kulvelis Yu.V., Primachenko O.N., Marinenko E.A., Peters G.S. Ionic channel structure in perfluorinated membranes studied by small angle X-ray scattering, optical and Mössbauer spectroscopy. *Nanosystems: Phys. Chem. Math.*, 2024, **15** (5), 716–725.

1. Introduction

The crucial problem of hydrogen power industry is related to the creation of solid polyelectrolytes serving as ion-exchange membranes for proton transport in fuel cells [1–3]. Presently these key materials are mainly based on Nafion[®] and Aquvion[®] perfluorinated copolymers which provide necessary functional characteristics of membranes (proton conductivity, strength, mechanical and thermal stability, low fuel crossover) [4–7]. The ways of the following improvement of these materials cannot be found without a detail analysis of their complicated nanostructure [8–11] which is formed as a result of the segregation of nonpolar chain fragments (partially crystallized) from ionic groups forming narrow pores and channels for water and proton transport [12–18].

Despite of various studies [8–18] of membranes based of perfluorinated copolymers, the present knowledge of self-assembly regularities of ionic groups still remains not satisfactory and various models of their package into channel networks are discussed [11]. Mostly these models propose a formation of nano-sized pores (few nanometers) covered with ionic groups and connected via fine channels (~ 1 nm in diameter) occluded by nonpolar chain fragments and partially ordered in polymer matrices [8–11].

To understand the subtle features of molecular ordering in membranes, the X-ray and neutron small angle scattering methods (SAXS, SANS) [9–11] along with electron and atomic force microscopy (TEM, SEM, AFM) are used [19–23]. In addition, the Mössbauer (gamma-resonance) spectroscopy (MS) has been applied [24–26] to examine ion-exchange membranes and search for their channel structure, charge states of ions, local symmetry and nearest environment of ions, their magnetic interactions with neighboring atoms, local mobility when ions are bound to hydrophilic polymer fragments. The MS data makes it possible to judge the local heterogeneity of functional groups distribution, in particular, sulfonic

acid groups, which ensure ion exchange in membrane channels. MS in combination with electron microscopy and X-ray diffraction are indispensable methods for studying the relationship between the structure and functional properties of ionomers as the main materials of proton-conducting membranes – key elements of hydrogen fuel cells. [27–29].

The authors [30] analyzed the chemical state and microstructure of Nafion[®] membranes using EXAFS and MS methods when replacing protons in ionic groups with iron ions by saturating the membranes with iron salts and further drying the samples. The introduction of iron ions (~ 1 wt.%) into membrane films made it possible to perform the MS experiments at low temperatures (80 and 4.2 K) for measuring isomeric shifts and quadrupole splitting of absorption lines showed the oxidation degree of iron cations in membrane channels. The analysis of the spectral profile for the X-ray absorption near edge spectroscopy (XANES) confirmed a local ordering of iron ions surrounded by oxygen shells at the distance of 0.2 nm due to the formation of $\text{Fe}(\text{H}_2\text{O})_6^{2+}$ and $\text{Fe}(\text{H}_2\text{O})_6^{3+}$ complexes when the membranes were saturated with FeSO_4 or FeCl_3 salts. In perfluorinated ionomers with iron additive the MS has revealed the specificity of aggregation of ionogenic groups that led to the formation of conducting channels in membranes and determined their functional properties.

The ionomers in perfluorinated membranes [31] have a complex morphology, since their sulfonic acid groups, together with counterions, form nanoscale aggregates that ensure physical cross-linking of polymer chains [32,33]. For this reason, a cation exchange may significantly modulate chemical, physical and functional properties of ionomers, change their glass transition temperature, Young's modulus, chain mobility [32–38], permeability, transport and gas separation efficiency [39] due to the influence of cations on pristine material [40].

A modification of Nafion[®] membranes by exchanging H^+ ions for Fe^{3+} cations was undertaken [40] to limit the mobility of chain segments with cationic crosslinks, increase its resistance to unwanted plasticization by gas mixtures, and increase the rigidity of chains through ionic interactions between Fe^{3+} cations and sulfonate anions, and ultimately, to improve a diffusion selectivity of material. The MS experiments are able to give a detail information on the structure of channels when introduced ions with Mössbauer [41] serve as tiny local probes to study membranes. Except of fundamental interests, there are some technical reasons to analyze the interactions of polyvalent iron with ion exchange membranes, e.g. to predict their fouling and find strategies to combat it. This motivated authors [42] to study the sorption (desorption) of Fe(III) particles in Nafion[®] membranes by MS. This method is able to deliver really exceptional information on Fe^{2+} , Fe^{3+} ions localization, their environment in Nafion[®] [30] and other ionomer materials [26].

Indeed, there are great prospects to design new ion-exchange nanomaterials for various applications (electrical engineering, electronics, information technologies, biomedicine, hydrogen power) by using a combination of structural methods and MS to analyze charge states, localizations and atomic environments of magnetic iron atoms. This approach allows obtaining a valuable information for targeted synthesis and achieving the desired properties of materials.

The aim of our study was first to analyze the nanostructure of the perfluorinated membranes of Nafion[®]-type copolymer by complementary SAXS, determine the characteristics of ionic channels and their grouping into bunches. At the second stage of work, we tried to search subtle features of membrane ionic channels when saturated them with iron ions to examine their interactions and assembly with copolymer sulfonic groups covering the inner surface of ionic channels in membranes by optical and gamma-resonance absorption (MS) methods which gave the information on the influence of embedded iron ions on the energy of ionomer optical gap and shown the association of these ions with its sulfonic groups.

2. Experimental: samples and methods

We have synthesized perfluorinated Nafion[®]-type copolymer by solution copolymerization of tetrafluoroethylene (TFE) with perfluoro(3,6-dioxo-4-methyl-7-octene)sulfonyl fluoride monomer (FS-141) [43] with equivalent weight of $EW = 900$ g-eq/mol (chain fragment mass per sulfonic group SO_3H) [44]. We used the copolymer in $-\text{SO}_3\text{Li}$ form to produce the membrane films by casting method [45]. The copolymer, dissolved in dimethylformamide (DMF), was applied to a glass substrate. After the film was formed from solution by removing the solvent by heating, it was transferred to $-\text{SO}_3\text{H}$ form by washing in 15 % nitric acid, turning it into a proton-conducting membrane [45]. Then the films (60 μm , capable of water absorbing up to ~ 40 wt.%) were dried and annealed at 100 °C to have stable (equilibrium) structure [45].

The dry membrane films were examined by small angle X-ray scattering (SAXS) using the BioMUR beamline (NRC Kurchatov Institute, Moscow, Russia) [46]. The SAXS intensities distributions $I(q)$ were measured in the range of scattering vector modulus $q = (4\pi/\lambda_p) \sin(\theta) = 0.04 - 4.0 \text{ nm}^{-1}$ for photons with wavelength $\lambda_p = 0.1445 \text{ nm}$ and scattering angle 2θ . The data corrected for background were interpreted in terms of the methodology of SAXS experiments [47].

To perform optical absorption and MS studies we saturated the films with 0.2 M FeCl_3 solution of followed by vacuum drying according to the method [30] to achieve the desirable iron concentration in membranes (2 wt.%). The pristine and modified membranes at ambient temperature (20 °C) were tested in the measurements of the optical density $D(\lambda)$ at light wavelengths $\lambda = 190 - 1100 \text{ nm}$ by the spectrophotometer DU-8600RN(PC) (Drawell Scientific, Yuzhong District, Chongqing, China).

The MS experiments were carried out on the modified samples to search the iron ions arrangement inside the conductive channels coated with SO_3H -groups, determine the ions' charge state and forms of their association with the groups at the conditions which are relatively close to those in hydrogen fuel cells [48]. The MS spectra were recorded on the

original spectrometer built at PNPI in collaboration with the Institute of Chemistry of St. Petersburg State University [49]. We have carried out the transmission measurements in fixed geometry using gamma source ^{57}Co moves in constant acceleration mode (triangular profile of Doppler velocity). We have calibrated the velocity scale against generally accepted $\alpha\text{-Fe}$ standard before the experiments. To process the spectra, we used the MOSSFIT program for Lorentzian line shape description. More details on the spectrometer performance can be found in recent publications [50, 51].

3. Results and discussions

3.1. SAXS studies

SAXS data for Nafion[®]-type copolymer ($EW = 900$ g-eq/mol) in range of scattering vector modulus $q \sim 0.04 - 4.0$ nm⁻¹ (Fig. 1) corresponding to the spatial scales $2\pi/q \sim 10^0 - 10^2$ nm have revealed narrow ionic channels with transversal gyration radius $R_g < 1$ nm which are surrounded by the shells of skeletal chains with partially crystalline order and locally ordered into nanoscale bundles (domains). Indeed, the scattering intensities $I(q)$ increased at $q \leq 0.1$ nm⁻¹ displayed in membrane the presence of polymer domains of $\sim 10^1 - 10^2$ nm in size (Fig. 1). At larger q we detected a local ordering of ionic channels packed into bundles with spatial period of channel arrangement $L_P \sim 2\pi/q_m$ corresponding to the position of the ionomer peak $q_m \sim 2$ nm⁻¹ (Fig. 1).

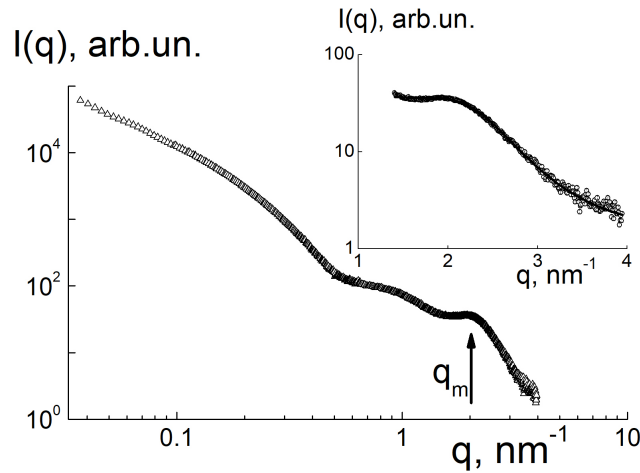


FIG. 1. SAXS intensities $I(q)$ vs. scattering vector modulus for dry Nafion[®] film. Ionomer peak position at q_m is indicated. Insert: ionomer peak fitting by function (1)

We used the model of thin straight ion channels being cylindrical pores with a diameter of $d_{CH} = 2\sqrt{2}R_g \sim 1$ nm much smaller than their length $L \sim 10^1 - 10^2$ nm. In the membrane, such connected linear fragments form a proton-conducting channel network. Locally these fragments are grouped into bundles of several units. This is a generally accepted model confirmed by structural data [10]. In our case, it was a principal interest to determine the structural characteristics of the channels and their mutual ordering at small scales $R \ll L$, comparable with the diameter of the channels and the transverse period of their local packing (L_P), in order to compare the data with the results of Mössbauer experiments characterizing the charge state of the iron ions in the channels when these ions interact with the surrounding sulfonic acid groups.

So, the goal was to find from the ionomer peak parameters the channel diameter corresponding to the radius R_g , their packing period L_P and at last the number in the bundle N_{CH} , which determines the transverse size of the bundle. Bundles of channels in polymer shells are elongated amorphous-crystalline polymer domains. In general, the membrane has a complex structure with alternating crystalline and amorphous regions differing in the packing density of polymer chains at the scales $R \sim 10^1 - 10^2$ nm [10]. Accordingly, on the scattering intensity curve, in addition to the ionomer peak a wide maximum weakly expressed presents at $q \sim 0.7$ nm⁻¹. It should be attributed to the contacts of bundles (domains) at a characteristic distance of $2\pi/q \sim 10$ nm of the order of their width. The length of the domains can be judged from the behavior of the scattering curve at low scattering vectors $q \leq 0.1$ nm⁻¹. In the Guinier approximation, the gyration radius of these objects is $R_G = 36 \pm 1$ nm and their length is approximately $L = \sqrt{12}R_G \approx 125$ nm as for thin rods.

The data treatment for large scattering vectors $q = 1 - 4$ nm⁻¹ allowed us to evaluate the characteristics of ion channels and their arrangement using the scattering function

$$I(q) = \frac{\frac{A}{q} \exp\left[-\frac{(qR_g)^2}{2}\right]}{\left[1 + \frac{(q - q_m)^2}{\Gamma^2}\right]} + \frac{B}{q} \exp\left[-\frac{(qR_g)^2}{2}\right] + Bg, \quad (1)$$

where the first term describes the ionomer peak at $q = q_m$ with the amplitude A , full width at half maximum Γ with the factor $1/q$ which corresponds to the scattering from linear fragments of fine channels having small transversal gyration radius R_g , the second term represents the contribution of the channels when there is no interference in scattering between them and the constant Bq is the background. Note, for our dry membrane with mostly closed pores and squeezed thin ionic channels the scattering at high scattering vectors obeys asymptotic $1/q$ behavior but not $1/q^4$ for smooth (sharp) borders which really absent since in the ionic channels the terminal sulfonic groups of side chains of copolymer are contacted and overlapped that makes the borders of channels very diffuse. In this case, taking into account the atomic structure of scattering particles, using the representation of their correlation function as a sum of δ -functions, leads to the appearance of a constant component in the scattering intensity [47].

The data (Fig. 1) obeyed the function (1) with fitting parameters: $A = 125 \pm 6 \text{ nm}^{-1} \text{ arb.un.}$, $q_m = 2.25 \pm 0.02 \text{ nm}^{-1}$, $\Gamma = 0.64 \pm 0.03 \text{ nm}^{-1}$, $B = 24.1 \pm 5.6 \text{ nm}^{-1} \text{ arb.un.}$, $R_g = 0.59 \pm 0.01 \text{ nm}$, $Bq = 1.58 \pm 0.10 \text{ arb.un.}$ The parameter R_g defines the diameter of channels, $d_{CH} = 2\sqrt{2}R_g = 1.67 \pm 0.03 \text{ nm}$, that is really a characteristic size of ionic channels in such type of membranes [52]. The channels are packed with transversal period $L_P = 2\pi/q_m = 2.79 \pm 0.03 \text{ nm}$ which is the outer diameter of polymer shells around them. Respectively, the difference of the parameters L_C and d_{CH} gives the thickness of polymers shells, $\delta_S = (L_P - d_{CH})/2 = 0.56 \pm 0.02 \text{ nm}$. This magnitude corresponds to the length of folded chain fragment between neighboring ionic groups, $nL_1/2 \approx 0.6 \text{ nm}$, where $n = 4.6$ is the average number of $(\text{CF}_2\text{-CF}_2)$ units and $L_1 \approx 0.25 \text{ nm}$ is their size along chain fragment. Hence, the shells around ionic channels are the assemblies of folded chain fragments like in inverted micelles [11].

As far as the parameter A is a measure of interference in scattering from neighboring channels in bundles, and the parameter B corresponds to individual scattering from linear channel fragments in bundles, the ratio of these characteristics gives the number of channels in a bundle, $N_{CH} = (A/B) + 1 = 6.1 \pm 0.1$. So, parallel channel fragments in membrane are locally gathered into the bundles while each bundle integrates about six channels that is in agreement with the structural modeling [11].

Meanwhile, in the structural analysis it should be understood that in reality, the polymer matrix is an amorphous-crystalline continuum and can only be conditionally divided into bundles (domains) scattering independently. So, the ionomer peak includes contributions not only from channels within individual bundles, but also from the channels in the nearest contacting bundles packed into a common polymer matrix. In view of this, it is not possible to attribute the parameters of the scattering function (A , B) to one or another discrete model of an isolated bundle. As a result, the average degree of channel aggregation was estimated from the found ratio A/B , and the approximate ratio $L_P = 2\pi/q_m$ was used to determine the average period of channel packing. The allocation of discrete structural levels in membranes as a result of local segregation of polar and non-polar fragments of copolymers forming a structure with nanosized amorphous-crystalline regions is conditional and does not allow developing satisfactory quantitative structural models of perfluorinated membranes. The models presented are applicable to well-oriented, highly ordered membranes that may be created in the future.

Since ionic channels with hydrophilic inner surface covered with SO_3H groups can adsorb water, in swollen state this copolymer may provide ionic transport via proton diffusion with water molecules, but protons diffuse also by Grotthuss mechanism by means of short jumps ($\sim 0.05 - 0.07 \text{ nm}$) between polarized water molecules (H_3O^+), that mainly provides proton conductivity [53]. Therefore, it was important to study the ion exchange in diffusion channels of membrane. For this purpose, we saturated it with Fe^{3+} ions and measured optical absorption spectra to detect their interactions with copolymer.

3.2. Optical absorption in membranes

The absorbance spectra $D(\lambda)$ have shown the greater optical density for the membrane saturated with iron ions in the wavelength intervals 370 – 450 and 600 – 900 nm comparative to the data for pristine membrane (Fig. 2). The association of iron ions with copolymer influenced its optical gap energy (E_g). Its original magnitude $E_{g0} = 3.35 \pm 0.01 \text{ eV}$ became smaller by $\sim 5 \%$. For modified material we found the energy $E_{gM} = 3.19 \pm 0.01 \text{ eV}$ using Tauc relation [54] between the photon energy and absorption coefficient. This relation in terms of optical density $D(\lambda)$ vs. reciprocal wavelength is as following,

$$\left[\frac{D(\lambda)}{\lambda} \right]^2 = B \left(\frac{1}{\lambda} - \frac{1}{\lambda_g} \right), \quad (2)$$

where λ_g is the wavelength corresponding to the photon energy E_g , the coefficient B depends on transition probability [55, 56]. A linear approximation of $[D(\lambda)/\lambda]^2$ vs. $1/\lambda$ has given the wavelengths $\lambda_{g0} = 370.4 \pm 0.1 \text{ nm}$ and $\lambda_{gM} = 389.1 \pm 0.2 \text{ nm}$ for original and modified membrane (Fig. 3), and corresponding magnitudes of energy gap (E_{g0} , E_{gM}) were evaluated.

The decrease in energy gap agrees with common trends in the changes of electronic properties of polyelectrolytes, e.g. for Poly(vinyl alcohol) (PVA) doped FeCl_3 [57]. Such kind polymer-metal composites are prospective semiconductive materials for numerous applications (optoelectronic devices, solid-state batteries, solar cells) [57–59]. In these materials, it is of crucial importance to regulate the coordination of metal atoms with ionic groups in polymer matrices. In our case, the information on iron ion assembling with sulfonic groups at channel walls was obtained in the MS experiments.

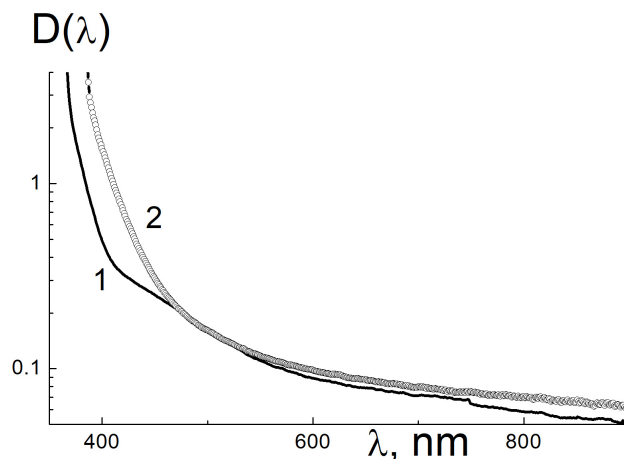


FIG. 2. Absorbance spectra $D(\lambda)$ at wavelengths 300 – 900 nm for pristine (1) and filled with Fe^{3+} membranes (2)

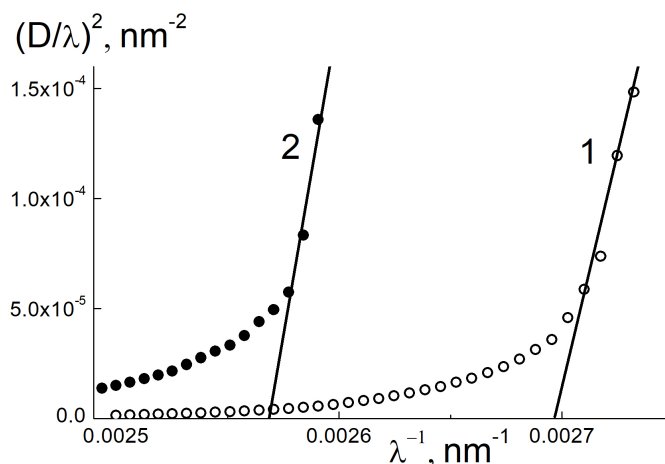


FIG. 3. Absorption data Tauc presentation for pristine (1) and filled with Fe^{3+} membranes (2), data linear approximation to find the energy of material optical gap

3.3. MS spectroscopy of membrane with iron ions

The principal feature of the experiments was a search of resonant gamma absorption in iron doped Nafion[®] type membranes in dry state at ambient temperature (295 K), i.e. not so far from the exploitation conditions for fuel cells. Previously we tested electrochemical properties of unfrozen membranes saturated with water and detected their high proton conductivity (0.1 S/cm). Worth to note, till now the MS spectra for iron modified Nafion[®] were recorded only for the samples cooled down to 80 and 4.2 K [30].

In the experiments, we performed the standard α -Fe calibration and then collected the data for membranes (4 films) gaining high statistics and detecting weak effects of gamma resonance absorption in warm sample (Fig. 4). The sample transmission $Tr(V)$ vs. source speed (V) presented in the form $\Delta Tr = (Tr - 1) = F_1 + F_2 + F_3 + F_4$ is the sum Lorentzian terms (1–4) with fitting parameters (Fig. 4, Table 1),

$$F_1(V) = \frac{A_{m1}}{\left[1 + \left(V - (IS_1 - \frac{QS_1}{2})\right)^2 / \Gamma_{m1}^2\right]}, \quad (3)$$

$$F_2(V) = \frac{A_{m1}}{\left[1 + \left(V - (IS_1 + \frac{QS_1}{2})\right)^2 / \Gamma_{m1}^2\right]}, \quad (4)$$

$$F_3(V) = \frac{A_{m2}}{\left[1 + \left(V - (IS_2 - \frac{QS_2}{2})\right)^2 / \Gamma_{m2}^2\right]}, \quad (5)$$

$$F_4(V) = \frac{A_{m2}}{\left[1 + \left(V - (IS_2 + \frac{QS_2}{2})\right)^2 / \Gamma_{m2}^2\right]}. \quad (6)$$

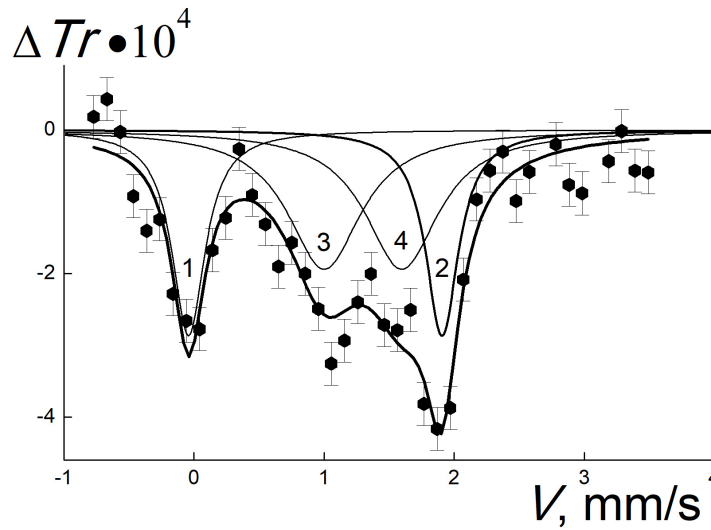


FIG. 4. Transmission data $\Delta Tr \cdot 10^4$ for gamma ray absorption in the sample vs. source speed (V), approximation by the sum of Lorentzian forms (1–4) with fitting parameters (Table 1)

TABLE 1. Spectral parameters for doublets (1,2) of gamma absorption by Fe^{3+} nuclei in membrane channels

No.	$A_m, \%$	$IS, \text{mm/s}^*$	$QS, \text{mm/s}$	$\Gamma_m, \text{mm/s}$	$S, \%$
1	0.029 ± 0.003	0.93 ± 0.02	1.95 ± 0.03	0.31 ± 0.05	39 ± 7
2	0.020 ± 0.003	1.30 ± 0.04	0.60 ± 0.08	0.69 ± 0.14	61 ± 7

* Standard α -Fe calibration used

The data $\Delta Tr = (Tr - 1)$ demonstrated a doublet for Fe^{3+} ions but with low amplitude ($\sim 0.03 \%$) due to iron nuclei thermal motion (Fig. 4). Nevertheless, we definitely detected a quadrupole splitting of $\sim 2 \text{ mm/s}$ which was close to the magnitude $\sim 1.7 \text{ mm/s}$ for cooled Nafion[®] membrane ($EW = 1200 \text{ g-eq/mol}$) [30]. In our case, the observed isomeric shift $\sim 1 \text{ mm/s}$ exceeded a similar effect $\sim 0.6 \text{ mm/s}$ at 80 and 4.2 K [30].

The results obtained for the first time at ambient temperature (295 K) confirmed the stability that Fe^{3+} ions ordering in membrane channels where they organize $[(H_2O)_5Fe-O-Fe(H_2O)_5]^{4+}$ dimers joint with four sulfonic acid groups (Fig. 5) to provide electro-neutrality [30]. This type dimers possess zero spin due to antiferromagnetic ordering of iron ions' spins [60, 61].

Along with the signal for dimers, the additional doublet presents in the spectrum (Fig. 4). Therefore, we fitted the data ΔTr by the sum of Lorentzian forms for doublets with amplitudes $A_{1,2}$, isomeric shifts $IS_{1,2}$, the values of quadrupole splitting $QS_{1,2}$ and linewidths $\Gamma_{1,2}$, which defined the integral contributions of doublets $S_{1,2}$ in the total absorption (Fig. 4, Table 1).

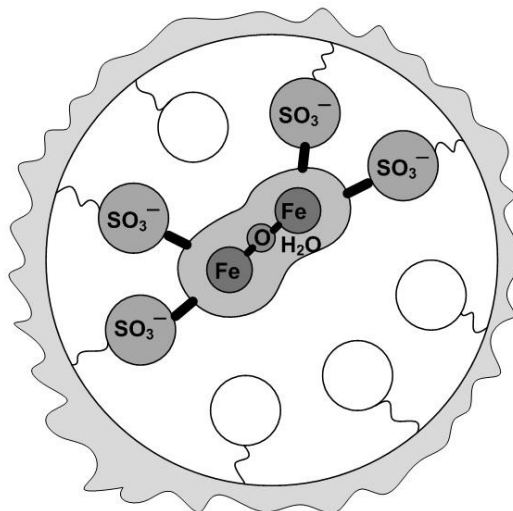


FIG. 5. Hydrated Fe^{3+} dimer associated with sulfonic acid groups in membrane ion channel

The first component has the amplitude A_1 almost one and a half times greater the A_2 for the second term, and the resonance quadrupole splitting QS_1 three times larger the QS_2 for the second signal. However, due to a bigger line width Γ_2 relative to Γ_1 , the second term dominated with the ratio of integral intensities $S_2/S_1 \sim 1.6$ (Table 1). Such deviations in the parameters of the doublets reflected their different structures.

The first doublet indicated the presence of ionic dimers. However, the second doublet was attributed to $\text{Fe}(\text{H}_2\text{O})_6^{3+}$ hydrated ions [62] with weak quadrupole splitting (~ 0.5 mm/s) [30]. At lower temperatures a bulk of them demonstrated paramagnetic hyperfine splitting since they are well separated from each other [30]. Regarding dimers, it should be clarified that in water Fe^{3+} ions are capable to form two types of clusters [30], $[(\text{H}_2\text{O})_4\text{Fe}-(\text{OH})_2-\text{Fe}(\text{H}_2\text{O})_4]^{4+}$ or $[(\text{H}_2\text{O})_5\text{Fe}-\text{O}-\text{Fe}(\text{H}_2\text{O})_5]^{4+}$, through hydroxyls [63] or oxo-bridge [64]. The MS data [63] have shown binuclear Fe(III) oxo complex according to detected quadrupole splitting of ~ 1.7 mm/s exceeding that for the entity with hydroxyls (~ 0.8 mm/s).

As the authors [30] emphasized, in Nafion[®]-type membranes saturated with Fe^{3+} , their dimers have the parameters identical to those in aqueous solutions. In accordance with this, in membranes at 80 and 4.2 K, the quadrupole splitting of 1.65 mm/s has indicated the presence of $[(\text{H}_2\text{O})_5\text{Fe}-\text{O}-\text{Fe}(\text{H}_2\text{O})_5]^{4+}$ dimers. To ensure charge neutrality for dimers, the structural model of their binding to four sulfonate groups, $[(\text{H}_2\text{O})_5\text{Fe}-\text{O}-\text{Fe}(\text{H}_2\text{O})_5]^{4+}[\text{SO}_3^-]_4$, was constructed based on MS and EXAFS data acquired at low temperatures [30]. However, at room temperatures in Nafion[®], the effect was not detected for Fe^{3+} ions, since they were immersed in the aqueous non solid phase [62].

In the MS experiments at 295 K, we established the assembly of Fe^{3+} ions into oxo dimers coordinated with sulfonic acid groups on channel surface. We proved such a stable ionic ordering and the presence of $\text{Fe}(\text{H}_2\text{O})_6^{3+}$ hydrated forms in warm membranes where it is possible proton migration and water diffusion in channels where dimers bridge the groups on the walls of narrow channels.

4. Conclusions

The combination of the methods of X-ray small angle scattering with optical and MS spectroscopy has expanded the experimental capabilities in perfluorinated membranes researches and allowed obtain really new unique information on the ordering of ionic groups in Nafion[®] type copolymer matrix with the formation of fine proton conducting channels gathered into bundles.

The discovered channel structures were based on the arrangement of sulfonic groups covering the inner surface of channels examined by MS using iron ions as tiny local probes creating dimers associated with the groups. This led also to the change in electric properties of copolymer which optical energy gap has decreased due to material modification with iron ions.

The obtained results have revealed exclusive opportunities of applied complementary methods for the examination structural, optical and electrical properties of polyelectrolytes are in demand for various applications including hydrogen power and nuclear technologies in need of effective ion exchange materials for trapping and separating nuclides.

References

- [1] Ahmad S., Nawaz T., Ali A., Orhan M.F., Samreen A., Kannan A.M. An overview of proton-exchange membranes for fuel cells: Materials and manufacturing. *Int. J. of Hydrogen Energy*, 2022, **47** (44), P. 19086–19131.
- [2] Pan M., Pan C., Li C., Zhao J. A review of membranes in proton exchange membrane fuel cells: Transport phenomena, performance and durability. *Renewable and Sustainable Energy Reviews*, 2021, **141** (25), 110771.
- [3] Yaroslavtsev A.B., Stenina I.A. Current progress in membranes for fuel cells and reverse electrodialysis. *Mendeleev Commun.*, 2021, **31**, P. 423–432.
- [4] Yaroslavtsev A.B., Stenina I.A., Golubenko D.V. Membrane materials for energy production and storage. *Pure Appl. Chem.*, 2020, **92** (7), P. 1147–1157.
- [5] Li T., Shen J., Chen G., Guo S., Xie G. Performance Comparison of Proton Exchange Membrane Fuel Cells with Nafion and Aquivion Perfluorosulfonic Acids with Different Equivalent Weights as the Electrode Binders. *ACS Omega*, 2020, **5** (28), P. 17628–17636.
- [6] Mugtasimova K.R., Melnikov A.P., Galitskaya E.A., Kashin A.M., Dobrovolskiy A., Don G.M., Likhomanov V.S., Sivak A.V., Sinityn V.V. Fabrication of Aquivion-type membranes and optimization of their elastic and transport characteristics. *Ionics*, 2018, **24**, P. 3897–3903.
- [7] Dombaycıoğlu Ş., Günşel H., Aydın A.O. Nafion/Aquivion-Based Composite Lithium Ion Exchange Membranes for High Capacity Li–S Batteries. *Chemistry Select*, 2022, **7** (39), e202202910.
- [8] Hsu W.Y., Gierke T.D. Ion transport and clustering in Nafion perfluorinated membranes. *J. of Membrane Science*, 1983, **13** (3), P. 307–326.
- [9] Gebel G., Diat O. Neutron and X-ray scattering: Suitable tools for studying ionomer membranes. *Fuel Cells*, 2005, **5**, P. 261–276.
- [10] Schmidt-Rohr K., Chen Q. Parallel cylindrical water nanochannels in Nafion fuel-cell membranes. *Nature Mater.*, 2008, **7**, P. 75–83.
- [11] Fernandez Bordín S.P., Andrada H.E., Carreras A.C., Castellano G.E., Oliveira R.G., Galván Josa V.M. Nafion membrane channel structure studied by small-angle X-ray scattering and Monte Carlo simulations. *Polymer*, 2018, **155**, P. 58–63.
- [12] Bazaid M., Huang Y., Goddard W.A., Jang S.S. Proton transport through interfaces in nanophase-separation of hydrated aquivion membrane: Molecular dynamics simulation approach. *Colloids and Surfaces A: Physicochemical and Engineering Aspects*, 2023, **676**, Part A, 132187.
- [13] Petrov A.V., Murin I.V. Electronic Structure of SO₃H Functional Groups and Proton Mobility in Nafion and Aquivion Ionomer Membranes. *Russian J. of General Chemistry*, 2019, **89** (3), P. 553–555.
- [14] Agarwal T., Prasad A.K., Advani S.G., Babu S.K., Borup R.L. Infrared spectroscopy for understanding the structure of Nafion and its associated properties. *J. Mater. Chem. A*, 2024, **12**, P. 14229–14244.
- [15] Mbarek S., El Kissi N., Baccouch Z., Iojoiu C. Extrusion of Nafion and Aquivion membranes: environmentally friendly procedure and good conductivities. *Polymer Bulletin*, 2019, **76**, P. 1151–1166.
- [16] Haubold H.-G., Vad T., Jungbluth H., Hiller P. Nano structure of NAFION: a SAXS study. *Electrochimica Acta*, 2001, **46** (10), P. 1559–1563.
- [17] Barbi V., Funari S.S., Gehrke R., Scharnagl N., Stribeck N. Nanostructure of Nafion membrane material as a function of mechanical load studied by SAXS. *Polymer*, 2003, **44**, P. 4853–4861.
- [18] Elliott J.A., Wu D.S., Paddison S.J., Moore R.B. A unified morphological description of Nafion membranes from SAXS and mesoscale simulations. *Soft Matter*, 2011, **7** (15), P. 6820–6827.
- [19] Xue T., Trent J.S., Osseo-Asare K. Characterization of Nafion® membranes by transmission electron microscopy. *J. of Membrane Science*, 1989, **45** (3), P. 261–271.
- [20] Yakovlev S., Balsara N.P., Downing K.H. Insights on the Study of Nafion Nanoscale Morphology by Transmission Electron Microscopy. *Membranes*, 2013, **3**, P. 424–439.
- [21] Yakovlev S., Downing K., Balsara N. Electron Microscopy of Nafion Membrane. *Microscopy and Microanalysis*, 2013, **19** (S2), P. 1652–1653.
- [22] Aleksandrova E., Hink S., Hiesgen R., Roduner E. Spatial distribution and dynamics of proton conductivity in fuel cell membranes: Potential and limitations of electrochemical atomic force microscopy measurements. *J. of Physics: Condensed Matter*, 2011, **23** (23), 234109.
- [23] Hiesgen R., Aleksandrova E., Meichsner G., Andreas Friedrich K. High-resolution imaging of ion conductivity of Nafion (R) membranes with electrochemical atomic force microscopy. *Electrochimica Acta*, 2009, **55**, P. 423–429.
- [24] Tsimbal T.Yu., Chibirova F.Kh., Kostyuchenko I.G. Magnetic relaxation and submicrostructure of iron hydroxide precipitates in ionomer membrane. *J. of Magnetism and Magnetic Materials*, 1994, **136**, P. 197–203.
- [25] Maksimichev A.V., Kostyuchenko I.G., Chibirova F.Kh., Zhilinskaya E.A., Chakulaeva L.N., Timashev S.F. Binding of Fe³⁺ ions to halobacterial purple membranes as studied by Mössbauer spectroscopy. *Membrane & Cell Biology*, 1997, **10** (5), P. 487–501.
- [26] Chibirova F.Kh., Kostyuchenko I.G., Kirsh Yu.E. Specific features of the structure of polymer ion-exchange membranes prepared from sulfocationic aromatic polyamides as studied by Mössbauer spectroscopy. *Russian J. of Physical Chemistry*, 1999, **73** (1), P. 111–116.
- [27] Cui Z., Drioli E., Lee, Y.M. Recent progress in fluoropolymers for membranes. *Progress in Polymer Science*, 2014, **39** (1), P. 164–198.
- [28] Ivanchev S.S., Myakin S.V. Polymer membranes for fuel cells: manufacture, structure, modification, properties. *Russ. Chem. Rev.*, 2010, **79** (2), P. 101–117.
- [29] Primachenko O.N., Marinenko E.A., Odinokov A.S., Kononova S.V., Kulvelis Yu.V., Lebedev V.T. State of the art and prospects in the development of proton-conducting perfluorinated membranes with short side chains: A review. *Polymers for Advanced Technologies*, 2021, **32** (4), P. 1386–1408.
- [30] Pan H.K., Yarusso D.J., Knapp G.S., Pineri M., Meagher A., Coey J.M.D., Cooper S.L. EXAFS and Mössbauer studies of iron neutralized Nafion ionomers. *J. Chem. Phys.*, 1983, **79** (10), P. 4736–4745.
- [31] Chen N., Lee Y.M. Anion exchange polyelectrolytes for membranes and ionomers. *Progress in Polymer Science*, 2021, **113**, 101345.
- [32] Eisenberg A., Hird B., Moore R.B. A new multiplet-cluster model for the morphology of random ionomers. *Macromolecules*, 1990, **23** (18), P. 4098–4107.
- [33] Page K.A., Cable K.M., Moore R.B. Molecular Origins of the Thermal Transitions and Dynamic Mechanical Relaxations In Perfluorosulfonate Ionomers. *Macromolecules*, 2005, **38** (15), P. 6472–6484.
- [34] Wakabayashi K., Register R.A. Morphological origin of the multistep relaxation behavior in semicrystalline ethylene/methacrylic acid ionomers. *Macromolecules*, 2006, **39** (3), P. 1079–1086.
- [35] Weiss R.A., Yu W.C. Viscoelastic Behavior of Very Lightly Sulfonated Polystyrene Ionomers. *Macromolecules*, 2007, **40** (10), P. 3640–3643.
- [36] Mohamed H.F.M., Kobayashi Y., Kuroda C.S., Ohira A. Effects of Ion Exchange on the Free Volume and Oxygen Permeation in Nafion for Fuel Cells. *J. Phys. Chem. B*, 2009, **113** (8), P. 2247–2252.
- [37] Mohamed H.F.M., Kobayashi Y., Kuroda C.S., Ohira A. Free volume and gas permeation in ion-exchanged forms of the Nafion® membrane. *J. Phys. Conf. Ser.*, 2010, **225**, 012038.
- [38] Ruan D., Simmons D.S. Roles of Chain Stiffness and Segmental Rattling in Ionomer Glass Formation. *J. Polym. Sci., Part B: Polym. Phys.*, 2015, **53**, P. 1458–1469.

- [39] Park H.B., Nam S.Y., Rhim J.W., Lee J.M., Kim S.E., Kim J.R., Lee Y.M. Gas-transport properties through cation-exchanged sulfonated polysulfone membranes. *J. Appl. Polym. Sci.*, 2002, **86** (10), P. 2611–2617.
- [40] Mukaddam M., Wang Y., Pinnau I. Structural, Thermal, and Gas-Transport Properties of Fe³⁺ Ion-Exchanged Nafion Membranes. *ACS Omega*, 2018, **3** (7), P. 7474–7482.
- [41] Heitner-Wirguin C. Infra-red spectra of perfluorinated cation-exchanged membranes. *Polymer*, 1979, **20** (3), P. 371–374.
- [42] Chen M., Ma J., Wang Z., Zhang X., Wu Z. Insights into iron induced fouling of ion-exchange membranes revealed by a quartz crystal microbalance with dissipation monitoring. *RSC Adv.*, 2017, **7**, P. 36555–36561.
- [43] Odinkov A.S., Bazanova O.S., Sokolov L.F., Barabanov V.G., Timofeev S.V. Kinetics of copolymerization of tetrafluoroethylene with perfluoro(3,6-dioxo-4-methyl-7-octen)sulfonyl fluoride. *Russian J. of Applied Chemistry*, 2009, **82** (1), P. 112–115.
- [44] Ivanchev S.S., Myakin S.V. Polymer membranes for fuel cells: manufacture, structure, modification, properties. *Russian Chemical Reviews*, 2010, **79** (2), P. 101–117.
- [45] Primachenko O.N., Odinkov A.S., Barabanov V.G., Tyulmankov V.P., Marinenko E.A., Gofman I.V., Ivanchev S.S. Relationship between the Morphology, Nanostructure, and Strength Properties of Aquivion[®] Type Perfluorinated Proton-Conducting Membranes Prepared by Casting from Solution. *Russ. J. Appl. Chem.*, 2018, **91**, P. 101–104.
- [46] Peters G.S., Gaponov Yu.A., Konarev P.V., Marchenkova M., Ilina K., Volkov V.V., Pisarevsky Yu.V., Kovalchuk M.V. Upgrade of the BioMUR beamline at the Kurchatov synchrotron radiation source for serial small-angle X-ray scattering experiments in solutions. *Nuclear Instruments and Methods in Physics Research Section A Accelerators Spectrometers Detectors and Associated Equipment*, 2021, **1025**, 166170.
- [47] Svergun D.I., Feigin L.A. *Structure Analysis by Small-Angle X-ray and Neutron Scattering*. Plenum Press, New York, USA; London, UK, 1987, 335 p.
- [48] Primachenko O.N., Kulvelis Yu.V., Odinkov A.S., Glebova N.V., Krasnova A.O., Antokolskiy L.A., Nechitailov A.A., Shvidchenko A.V., Gofman I.V., Marinenko E.A., Yevlampieva N.P., Lebedev V.T., Kuklin A.I. New Generation of Compositional Aquivion[®]-Type Membranes with Nanodiamonds for Hydrogen Fuel Cells: Design and Performance. *Membranes*, 2022, **12** (9), 827.
- [49] Semenov V.G., Moskvina L.N., Ufimov A.A. Analytical potential of Mössbauer spectroscopy. *Russ. Chem. Rev.*, 2006, **75** (4), P. 317–327.
- [50] Kamzin A.S., Obaidat I.M., Kozlov V.S., Voronina E.V., Narayanaswamy V., Al-Omari I.A. Graphene Oxide/Iron Oxide (GrO/FeOx) Nanocomposites for Biomedicine: Synthesis and Study. *Physics of the Solid State*, 2021, **63** (6), P. 856–865.
- [51] Kamzin A.S., Obaidat I.M., Kozlov V.S., Voronina E.V., Narayanaswamy V., Al-Omari I.A. Magnetic Nanocomposites Graphene Oxide/Magnetite + Cobalt Ferrite (GrO/Fe₃O₄ + CoFe₂O₄) for Magnetic Hyperthermia. *Physics of the Solid State*, 2021, **63**, P. 998–1008.
- [52] Lebedev V.T., Kulvelis Yu.V., Török Gy., Ivankov O.I., Polotskaya G.A., Vinogradova L.V., Vul A.Ya., Primachenko O.N., Marinenko E.A., Odinkov A.S. Structure of diffusive polymer membranes for molecular and ionic transport. *J. of Surface Investigation: X-ray, Synchrotron and Neutron Techniques*, 2021, **15** (5), P. 939–946. ©Pleiades Publishing, Ltd., 2021. ISSN 1027-4510.
- [53] Popov I., Zhu Z., Young-Gonzales A.R., Sacci R.L., Mamontov E., Gainaru C., Paddison S.J., Sokolov A.P. Search for a Grothuss mechanism through the observation of proton transfer. *Commun. Chem.*, 2023, **6**, 77.
- [54] Tauc J., Menth A., Wood D. Optical and Magnetic Investigations of the Localized States in Semiconducting Glasses. *Phys. Rev. Lett.*, 1970, **25**, P. 749–752.
- [55] Dorraniyan D., Abedini Z., Hojabri A., Ghorannevis M. Structural and optical characterization of PMMA surface treated in low power nitrogen and oxygen RF plasmas. *J. of Non-Oxide Glasses*, 2009, **1** (3), P. 217–229.
- [56] Mishjil K.A., Chiad S.S., Abass K., Habubi N.F. Effect of Al doping on structural and optical parameters of ZnO thin films. *Materials Focus*, 2016, **5** (5), P. 471–475.
- [57] Latif D.M.A., Chiad S.S., Erhayief M.S., Abass K.H., Habubi N.F., Hussin H.A. Effects of FeCl₃ additives on optical parameters of PVA. *IOP Conf. Series: J. of Physics: Conf. Series*, 2018, **1003**, 012108.
- [58] Reichmanis E., Donnel J.O. Irradiation of Polymeric Materials, and the Effect of Radiation on High Technology Polymers. *ACS Symposium Series*, 1993, **381** (527), 108.
- [59] Omer M.A.A., Gar-el-nabi M.E.M., Ahmed A.H., Eidam G.A., Khidir N.A.N. Radiochemical Properties of Irradiated PVA/AgNO₃ Film by Electron Beam. *Int. J. of Science and Research*, 2013, **2** (9), P. 361–364.
- [60] Bauminger E.R., Levy A., Labenski de Kanter F., Ofer S., Heitner-Wirguin C. Mössbauer spectra of iron containing Nafion membranes. *J. de Physique. Colloque C1*, 1980, **41** (1), 329.
- [61] Lechan R., Nicolini C., Abeledo C.R., Frankel R.B. Hyperfine Interactions in the Intramolecular Antiferromagnet (Fe salen C1)₂. *J. Chem. Phys.*, 1973, **59** (6), P. 3138–3142.
- [62] Rodmacq B., Pineri M., Coey J.M.D., Meagher A. Mössbauer spectroscopy of Nafion polymer membranes exchanged with Fe²⁺, Fe³⁺, and Eu³⁺. *J. Polym. Sci. Polym. Phys. Ed.*, 1982, **20** (4), P. 603–619.
- [63] Freitknecht W., Giovanoli R., Michaelis W., Müller M. Über die Hydrolyse von Eisen(III)Salzlösungen. I. Die Hydrolyse der Lösungen von Eisen(III)chlorid. *Helv. Chim. Acta*, 1973, **56** (8), P. 2847–2856.
- [64] Knudsen L.M., Larsen E., Moreira J.E., Nielsen O.F. Characterization of Decaqua-mu-oxodi-iron(III) by Mössbauer and Vibrational Spectroscopy. *Acta. Chem. Scand. Sect. A*, 1975, **29** (9), P. 833–839.

Submitted 23 July 2024; revised 1 October 2024; accepted 2 October 2024

Information about the authors:

Vasily T. Lebedev – Petersburg Nuclear Physics Institute named by B. P. Konstantinov of National Research Center “Kurchatov Institute”, 188300, Gatchina, Russia; ORCID 0000-0003-4894-0862; lebedev_vt@npni.nrcki.ru

Valery S. Kozlov – Petersburg Nuclear Physics Institute named by B. P. Konstantinov of National Research Center “Kurchatov Institute”, 188300, Gatchina, Russia; kozlov_vs1@npni.nrcki.ru

Mikhail V. Remizov – Petersburg Nuclear Physics Institute named by B. P. Konstantinov of National Research Center “Kurchatov Institute”, 188300, Gatchina, Russia; m.remizov97@gmail.com

Yury V. Kulvelis – Petersburg Nuclear Physics Institute named by B. P. Konstantinov of National Research Center “Kurchatov Institute”, 188300, Gatchina, Russia; ORCID 0000-0002-3228-3039; kulvelis_yv@pnpi.nrcki.ru

Oleg N. Primachenko – Institute of Macromolecular Compounds, Russian Academy of Sciences, 199004, St. Petersburg, Russia; ORCID 0000-0003-1637-8537; alex-prima@mail.ru

Elena A. Marinenko – Institute of Macromolecular Compounds, Russian Academy of Sciences, 199004, St. Petersburg, Russia; ORCID 0000-0003-2160-2003; emarinenkospb@gmail.com

Georgy S. Peters – National Research Center “Kurchatov Institute”, 123182, Moscow, Russia; ORCID 0000-0003-3597-9370; georgspeters@gmail.com

Conflict of interest: the authors declare no conflict of interest.



NANOSYSTEMS:

PHYSICS, CHEMISTRY, MATHEMATICS

INFORMATION FOR AUTHORS

The journal publishes research articles and reviews, and also short scientific papers (letters) which are unpublished and have not been accepted for publication in other magazines. Articles should be submitted in English. All articles are reviewed, then if necessary come back to the author to completion.

The journal is indexed in Web of Science Core Collection (Emerging Sources Citation Index), Chemical Abstract Service of the American Chemical Society, Zentralblatt MATH and in Russian Scientific Citation Index.

Author should submit the following materials:

1. Article file in English, containing article title, the initials and the surname of the authors, Institute (University), postal address, the electronic address, the summary, keywords, MSC or PACS index, article text, the list of references.
2. Files with illustrations, files with tables.
3. The covering letter in English containing the article information (article name, MSC or PACS index, keywords, the summary, the literature) and about all authors (the surname, names, the full name of places of work, the mailing address with the postal code, contact phone number with a city code, the electronic address).
4. The expert judgement on possibility of publication of the article in open press (for authors from Russia).

Authors can submit a paper and the corresponding files to the following addresses: nanojournal.ifmo@gmail.com, popov1955@gmail.com.

Text requirements

Articles should be prepared with using of text editors MS Word or LaTeX (preferable). It is necessary to submit source file (LaTeX) and a pdf copy. In the name of files the English alphabet is used. The recommended size of short communications (letters) is 4-6 pages, research articles– 6-15 pages, reviews – 30 pages.

Recommendations for text in MS Word:

Formulas should be written using Math Type. Figures and tables with captions should be inserted in the text. Additionally, authors present separate files for all figures and Word files of tables.

Recommendations for text in LaTeX:

Please, use standard LaTeX without macros and additional style files. The list of references should be included in the main LaTeX file. Source LaTeX file of the paper with the corresponding pdf file and files of figures should be submitted.

References in the article text are given in square brackets. The list of references should be prepared in accordance with the following samples:

- [1] Surname N. *Book Title*. Nauka Publishing House, Saint Petersburg, 2000, 281 pp.
- [2] Surname N., Surname N. Paper title. *Journal Name*, 2010, **1** (5), P. 17-23.
- [3] Surname N., Surname N. Lecture title. In: Abstracts/Proceedings of the Conference, Place and Date, 2000, P. 17-23.
- [4] Surname N., Surname N. Paper title, 2000, URL: <http://books.ifmo.ru/ntv>.
- [5] Surname N., Surname N. Patent Name. Patent No. 11111, 2010, Bul. No. 33, 5 pp.
- [6] Surname N., Surname N. Thesis Title. Thesis for full doctor degree in math. and physics, Saint Petersburg, 2000, 105 pp.

Requirements to illustrations

Illustrations should be submitted as separate black-and-white files. Formats of files – jpeg, eps, tiff.



NANOSYSTEMS:

PHYSICS, CHEMISTRY, MATHEMATICS

Журнал зарегистрирован

Федеральной службой по надзору в сфере связи, информационных технологий и массовых коммуникаций

(свидетельство ПИ № ФС 77 - 49048 от 22.03.2012 г.)

ISSN 2220-8054

Учредитель: федеральное государственное автономное образовательное учреждение высшего образования

«Национальный исследовательский университет ИТМО»

Издатель: федеральное государственное автономное образовательное учреждение высшего образования

«Национальный исследовательский университет ИТМО»

Отпечатано в Учреждении «Университетские телекоммуникации»

Адрес: 197101, Санкт-Петербург, Кронверкский пр., 49

Подписка на журнал НФХМ

На первое полугодие 2025 года подписка осуществляется через

ОАО «АРЗИ», подписной индекс Э57385